

Interferometric Synthetic Aperture Radar for slow slip applications

David Peter Sonja Bekaert

Submitted in accordance with the requirements for the degree of
Doctor of Philosophy

The University of Leeds
School of Earth and Environment

October 2015

The candidate confirms that the work submitted is his own, except where work which has formed part of jointly authored publications has been included. The contribution of the candidate and the other authors to this work has been explicitly indicated below. The candidate confirms that appropriate credit has been given within the thesis where reference has been made to the work of others.

The work in Chapter 2 of the thesis has appeared in publication as follows:

Bekaert, D.P.S., A.J. Hooper, and T.J. Wright (2015), *A spatially-variable power-law tropospheric correction technique for InSAR data*, Journal of Geophysical Research, 120, doi:10.1002/2014JB011558.

Part of the research and ideas originate from during my master thesis. During my PhD I refined these ideas and conducted new analysis. I took the experimental approach and developed it towards a mathematical description. Further new work includes the sensitivity testing, implementation in TRAIN, validation, and comparison with the conventional tropospheric correction approaches. I performed the data processing and analysis, and wrote the manuscript, which were improved with comments and suggestions from the co-authors.

The work in Chapter 3 of the thesis has appeared in publication as follows:

Bekaert, D.P.S., R.J. Walters, T.J. Wright, A.J. Hooper, and D.J. Parker(2015), *Statistical comparison of tropospheric correction techniques for InSAR*, Remote Sensing of Environment, doi:10.1016/j.rse.2015.08.035.

The ideas and methodologies used in this paper were developed with the co-authors. I developed the ideas, performed the data processing and analysis, and wrote the manuscript, which were improved with comments and suggestions from the co-authors.

The work in Chapter 4 of the thesis has appeared in publication as follows:

Bekaert, D.P.S., A.J. Hooper, and T.J. Wright (2015), *Reassessing the 2006 Guerrero slow slip event, Mexico: implications for large earthquakes in the Guerrero Gap*, Journal of Geophysical Research, 120, doi:10.1002/2014JB011557.

Part of the research and ideas originate from during my master thesis. During my PhD I refined these ideas, conducted new analysis, and used a more sophisticated modelling approach. Further new work includes the development of the InSAR covariance matrix, and an earthquake hazard analysis for the Guerrero region. I performed the data processing and analysis, and wrote the manuscript, which were improved with comments and suggestions from the co-authors.

The work in Chapter 5 of the thesis is a manuscript under review:

Bekaert, D.P.S., P. Segall, T.J. Wright, and A.J. Hooper (under review), *A Network Inversion Filter combining GNSS and InSAR for tectonic slip modeling*, Journal of Geophysical Research

The ideas and methodologies used in this paper were developed with the co-authors. I developed the ideas, performed the data processing and analysis, and wrote the manuscript, which were improved with comments and suggestions from the co-authors.

This copy has been supplied on the understanding that it is copyright material and that no quotation from the thesis may be published without proper acknowledgement

Copyright © 2015 The University of Leeds and David Peter Sonja Bekaert
The right of David Peter Sonja Bekaert to be identified as Author of this work has been asserted by him in accordance with the Copyright, Designs and Patents Act 1988.

Acknowledgements

This 3-year PhD process, while difficult at times, has been truly enriching in so many ways. My supervisors Tim Wright, Andrew Hooper, and Doug Parker were key in my success. They guided me and supported my ideas, but also allowed me to explore different avenues on my own. Amongst several opportunities, they most notably enabled me to attend the Space Studies Program of the International Space University, and provided support to do a research visit with Paul Segall at Stanford University. I would like to thank Paul and his students for the kind welcome and making my stay more than worthwhile.

Looking back, I am really happy to have completed my PhD at the School of Earth and Environment at the University of Leeds. Working in such a stimulating environment, and meeting great researchers, has shaped me into the researcher I am today. I would like to thank the members of IGT and ICAS, and in particular the InSAR group for being wonderful friends and colleagues. I will surely miss the tea moments, discussions in the coffee area, and awesome group dinners. Thank you to Anna Hogg, and my office mates Ekbal Hussain and Karsten Spaans for the great moments shared together, the hours of badminton, the good food, and your lovely company will not be forgotten. Special thanks to Richard Walters as he was always there when I had a problem or a question, and equally to Richard Rigby and his IT colleagues for their unlimited support and help. My friends from Delft University of Technology have also always been there for me throughout the years, and their support has been invaluable.

As last, I would like to thank my family for their support over my whole academic career. Special words for my lovely wife, Sarah, who was there at my side during my PhD in Leeds. Thank you for your support, and being such a great companion. Now, let us start our next adventure together.

Abstract

Over the last two decades, Slow Slip Events (SSEs) have been observed across many subduction zones, primarily through continuous GNSS networks. SSEs represent shearing of two tectonic plates, at much slower rates than earthquakes but more rapidly than plate motion. They are not dangerous in themselves, but change the stress field and can potentially trigger devastating earthquakes. While highly valuable, GNSS networks at most locations lack the spatial-resolution required to describe the spatial extent of the slow slip at depth. A better constraint of slow slip at depth in combination with other observations from seismology could be essential in addressing key research questions. These include: “Why do slow slip events occurs in some regions and not others?”, “What drives slow slip events?”, “Do slow slip events delay the occurrence of devastating earthquakes?”, and “Can slow slip events trigger devastating earthquakes?”. Interferometric Synthetic Aperture Radar (InSAR) is an established and attractive technique to study surface displacements at high-spatial resolution. Until now, InSAR has not been fully exploited for the study of SSEs. Here, I provide the necessary InSAR methodology, and further demonstrate the use of InSAR for static and time-dependant slow slip modelling. My developments have a direct benefit for various other applications such as earthquake cycle processes.

I Specifically address the following two challenges which limit the wide uptake of InSAR: (1) Decorrelation noise introduced by changing backscattering properties of the surface and a change in satellite acquisition geometry, making it difficult to correctly unwrap meaningful signal. I address this problem by applying existing advanced time-series InSAR processing methods. (2) Atmospheric delays masking the smaller slow slip signal. These are mainly due to spatial and temporal variations in pressure, temperature, and relative humidity in the lower part of the troposphere, which result in an apparent signal in the InSAR data. Different tropospheric correction methods exist, all with their own limitations. Auxiliary data methods often lack the spatial and temporal resolution, while the phase-based methods cannot account for a spatially-varying troposphere. In response, I develop a phase-based power-law representation of tropospheric delay that can be applied in the presence of deformation and which accounts for spatial variation of tropospheric properties. I demonstrate its application over Mexico, where it reduces tropospheric signals both locally (on average by ~ 0.45

cm for each kilometer of elevation) and the long wavelength components. Moreover, I provide to the research community a Toolbox for Reducing Atmospheric InSAR Noise (TRAIN), which includes all the state-of-the-art correction methods, implemented as opensource matlab routines. When comparing these methods, I find spectrometers give the largest reduction in tropospheric noise, but are limited to cloud-free and daylight acquisitions. I also find that all correction methods perform $\sim 10\text{-}20\%$ worse when there is cloud cover. As all methods have their own limitations, future efforts should aim at combining the different correction methods in an optimal manner. Additionally, I apply my InSAR methodology and power-law correction method to the study of the 2006 Guerrero SSE, where I jointly invert cumulative GNSS and InSAR SSE surface displacements. In Guerrero, SSEs have been observed in a “seismic gap”, where no earthquakes have occurred since 1911, accumulating a seismic potential of M_w 8.0-8.4. I find slow slip enters the seismogenic zone and the Guerrero Gap, with ~ 5 cm slip reaching depths as shallow as 12 km, and where the spatial extent of the slow slip collocates on the interface with a highly coupled inter-SSE region as found from an GNSS study. In addition, slow slip decreased the total accumulated moment since the previous SSE (4.7 years earlier) by $\sim 50\%$. Over time and while accounting for SSEs, the moment deficit in the Guerrero Gap increases each year by $M_w \sim 6.8$. Therefore I find that the Guerrero Gap still has the potential for a large earthquake, with a seismic potential of $M_w \sim 8.15$ accumulated over the last century. Finally, I show the application to use InSAR for time-dependant slow slip modelling. From a simulation of the 2006 SSE, I demonstrate that InSAR is able to provide valuable information to constrain the spatial extent of the slow slip signal. With a future perspective of continued high repeat acquisitions of various SAR platforms, my expansion of the Network Inversion Filter with InSAR will become a powerful tool for investigating the spatio-temporal correlation between slow slip and other phenomena such as non volcanic tremor. Moreover, this approach can apply to earthquake cycle processes. Studying the broader earthquake cycle will further our knowledge of seismic hazard and increase our resilience to such events.

Contents

List of Figures	xi
List of Tables	xiii
Nomenclature	xv
1 Introduction	1
1.1 Slow Slip Events	2
1.1.1 Slow Slip Events and their implications for earthquakes	3
1.1.2 Why do Slow Slip Events occur?	4
1.1.3 Scaling laws of SSEs and earthquakes compared	4
1.2 Interferometric Synthetic Aperture Radar	6
1.2.1 Decorrelation noise	8
1.2.2 Tropospheric noise	9
1.2.3 Ionospheric noise	12
1.3 Mexico study area	13
1.3.1 The Guerrero subduction zone	15
1.3.2 Slow slip events in Guerrero	15
1.3.3 Explaining the occurrence of slow slip in Guerrero	16
1.4 Aims and objectives	17
1.5 Thesis Roadmap	17
2 A power-law tropospheric correction technique for InSAR data	29
Abstract	29
2.1 Introduction	30
2.2 Power-law tropospheric correction	32
2.3 Results	35
2.4 Discussion	43
2.5 Conclusions	45
Acknowledgments	45
References	47

3	Statistical comparison of InSAR tropospheric correction techniques	51
	Abstract	51
3.1	Introduction	52
3.2	Tropospheric correction methods for InSAR	54
	3.2.1 Tropospheric delays from weather models	54
	3.2.2 Tropospheric delays from spectrometer observations	55
	3.2.3 Phase-based tropospheric delays	56
3.3	InSAR processing	57
3.4	Background of the test sites	58
3.5	Results and discussion	59
3.6	Conclusions	64
	Acknowledgments	65
	References	66
4	Reassessment of the 2006 Guerrero SSE	71
	Abstract	71
4.1	Introduction	72
4.2	InSAR processing	74
4.3	Time-series InSAR analysis	75
4.4	Error distribution of the surface displacements	77
4.5	Modeling the 2006 SSE	78
4.6	Results	80
	4.6.1 InSAR processing and InSAR time-series estimation	80
	4.6.2 Slow slip modeling	81
4.7	Discussion	87
	4.7.1 Slow slip modeling compared with other studies	87
	4.7.2 Correlation between slow slip, Ultra Slow velocity Layer and Non-Volcanic Tremor	90
	4.7.3 Earthquake hazard	91
4.8	Conclusions	91
	Acknowledgments	93
	Appendix InSAR covariance matrix from bootstrapping	94
	References	96
5	A Network Inversion Filter combining GNSS and InSAR	101
	Abstract	101
5.1	Introduction	102
5.2	Network Inversion Filter	103
	5.2.1 GNSS observation equation	104
	5.2.2 InSAR observation equation	105
	5.2.3 Joint GNSS and InSAR observation and state transition equation	105

5.2.4	Kalman filter and backward smoothing procedure	108
5.2.5	Comparing the NIF with the earlier implementation	109
5.3	Synthetic simulation of the Guerrero SSE	109
5.4	Results	111
5.4.1	GNSS only	113
5.4.2	GNSS and InSAR (neglecting covariance)	115
5.4.3	GNSS and InSAR (including covariance)	118
5.5	Discussion	119
5.6	Conclusions	120
	Overview of Symbols	121
	Acknowledgments	123
	Appendix Time-dependant slow slip simulation	123
	Appendix NIF model for GNSS and multiple InSAR tracks	124
	References	125
6	Discussion and conclusions	129
6.1	Discussion	129
6.2	Conclusions	134
6.3	Recommendations and Future work	137
6.4	Concluding Remarks	141
A	Supplemental material Chapter 2	147
B	Supplemental material Chapter 3	149
C	Supplemental material Chapter 4	157
D	Supplemental material Chapter 5	159
E	Methodology for InSAR feasibility study of slow slip events	163

List of Figures

1.1	Geographic overview of Slow Slip regions	3
1.2	Slow Slip Event and Earthquake empirical scaling laws	7
1.3	Persistent Scatterer pixel simulation	8
1.4	Comparing InSAR and time-series InSAR	9
1.5	Tropospheric delays from balloon sounding data in Mexico	11
1.6	Overview of the Guerrero subduction zone	14
2.1	Tropospheric delays from balloon sounding data	31
2.2	Schematic of the tropospheric delay curve	33
2.3	Seasonal variation of the power-law coefficients	34
2.4	Step-by-step example of the power-law method	36
2.5	Study region overview map	37
2.6	InSAR dataset before and after power-law correction	38
2.6	Continued	39
2.7	Phase-topography slope before and after tropospheric correction	41
2.8	InSAR point time-series before and after power-law correction	42
2.9	Estimated InSAR time-series components	42
2.10	Impact of window size and topography on power-law performance	44
3.1	Fraction of consistent mountain blockage over time for Mexico, Italy, and El Hierro	57
3.2	Overview map of tropospheric study regions	58
3.3	Example of tropospheric delay estimates for different correction methods over Mexico, Italy, and El Hierro	61
3.4	Statistical analysis between different tropospheric correction methods over Mexico, Italy, and El Hierro	62
4.1	Tectonic setting of the 2006 Guerrero Slow Slip Event	72
4.2	Envisat PS-InSAR network of the 2006 Slow Slip Event	74
4.3	Estimated time-series InSAR components	77
4.4	Model of the Guerrero subduction interface	79
4.5	Estimated slow slip displacements before and after tropospheric correction	82

4.6	Maximum a-posteriori slip solution for the 2006 Slow Slip Event	83
4.7	Sampled marginal probability distributions of the model parameters	84
4.7	Continued	85
4.8	Modelled surface displacements for the 2006 Slow Slip Event	86
4.9	Smooth and rough slow slip solutions	88
4.10	Guerrero slip deficit over 4.7 years duration	92
5.1	Overview map of the Guerrero tectonic region	110
5.2	Overview of the simulated GNSS and InSAR data	112
5.3	Likelihood surface (-2L) as function of the smoothing hyperparameters	113
5.4	Comparison of the simulated and NIF inter-SSE locking rate	114
5.5	Comparison of the simulated and NIF cumulative transient slip	115
5.6	Comparison of the simulated and NIF transient slip-rate history	116
5.7	Residuals between simulated and NIF estimated transient slip-rate history	117
6.1	Map overview of slow slip solutions at subduction zones	130
6.2	GNSS station distribution around the Circum-Pacific belt - Ring of Fire	132
6.3	Incremental noise correction for an L-band ALOS interferogram	138
A.1	Weather model analysis of tropospheric delays over Mexico	147
B.1	Mountain wind blockage over Mexico	149
B.2	Mountain wind blockage over Italy	150
B.3	Mountain wind blockage over El Hierro	150
B.4	MODIS recalibration factors estimated from MERIS/MODIS comparison	151
B.5	Power-law spatial band selection for (a) Mexico, (b) Italy, and (c) El Hierro	152
C.1	Inter-SSE velocities before and after tropospheric correction	157
C.2	Experimental variogram estimated from InSAR data	158
D.1	Simulated and NIF estimated observations: GNSS alone	159
D.2	Simulated and NIF estimated observations: GNSS and InSAR neglecting covariance information	160
D.3	Simulated and NIF estimated observations: GNSS and InSAR accounting for covariance information	161
D.4	Transient slip-rate and slip over time	162

List of Tables

2.1	Dataset baseline information	37
2.2	Applied InSAR processing parameters	37
4.1	Dataset baseline information	74
4.2	Applied InSAR processing parameters	75
4.3	Earthquake-like moment magnitude release for the maximum a-posteriori slip solution	87
4.4	Slip deficit after the 2006 SSE	92
6.1	Envisat and Sentinel 1 feasibility for Cascadian SSE	134
B.1	Interferometric Envisat dataset over Mexico (track 255)	153
B.2	Interferometric Envisat dataset over Italy (track 79)	154
B.3	Interferometric TerraSAR-X dataset over El Hierro (track 79)	155
B.3	Continued	156

Nomenclature

List of acronyms

COMET	Centre for the Observation and Modelling of Earthquakes, Volcanoes and Tectonics
DEM	Digital Elevation Model
DORIS	Delft Object-oriented Radar Interferometric Software
Envisat	Environmental satellite
ERS	European Remote-sensing Satellite
ESA	European Space Agency
ETS	Episodic Tremor and Slip
GMT	Generic Mapping Tools
GNSS	Global Navigation Satellite System
InSAR	Interferometric Synthetic Aperture Radar
JPL	Jet Propulsion Laboratory
LOS	Line Of Sight
MASE	Meso-American Subduction Experiment
NERC	Natural Environment Research Council
NVT	Non-Volcanic Tremor
PS	Persistent Scatterer
RADARSAT	RADAR SATellite
ROLPAC	Repeat Orbit Interferometry PACkage
SAR	Synthetic Aperture Radar

SB	Small Baseline
SRTM	Shuttle Radar Topography Mission (DEM)
SSE	Slow Slip Event
StaMPS	Stanford Method of Persistent Scatter
TRAIN	Toolbox for Reducing Atmospheric InSAR Noise
TT	Tectonic Tremor

List of symbols

α	Power-law exponent	
Δd_{tropo}	Relative tropospheric delay	[m]
λ	Wavelength	[m]
TEC	Total Electron Content	[TECU]
θ	Incidence angle	[°]
d_{iono}	Ionospheric delay	[m]
d_{tropo}	Tropospheric delay	[m]
e	Partial pressure of water vapour	[hPa]
f	Radar frequency	[Hz]
h	Height	[m]
h_0	Power-law reference height	[m]
M_w	Moment Magnitude	[-]
N	Refractivity	
n_e	Electron content	[m ⁻³]
P	Total atmospheric pressure	[hPa]
T	Temperature, Temporal baseline	[K,days]
Δf_{DC}	Absolute Doppler centroid baseline	[Hz]
ϕ_{iono}	Ionospheric phase delay	[rad]
ϕ_{tropo}	Tropospheric phase delay	[rad]

$K_{\Delta\phi}, K'_{\Delta\phi}$	Constant relating the interferometric tropospheric phase to topography	
$\Delta\phi_{\text{tropo}}$	Interferometric tropospheric phase delay	[rad]
B_{perp}	Perpendicular baseline	[m]

Chapter 1

Introduction

Since the year 2000, more than 800000 people have lost their lives due to the occurrence of earthquakes and tsunamis (USGS). Getting a better understanding “why” and “when” earthquakes occur requires a better understanding of all the processes involved in the earthquake cycle (e.g. [Avouac, 2015](#)). This includes interseismic loading, during which the energy is built-up, coseismic events, in which energy is released through instantaneous earthquakes, postseismic relaxation, consisting of multiple mechanisms including viscous relaxation of the lower crust and upper mantle, pore-fluid flow, and afterslip; as well as any other aseismic processes such as slow slip events, which further release energy without generating significant seismic waves. All these processes change the stress field and have implications for the occurrence of future earthquakes (e.g. [Segall, 2010](#)).

We can't solve problems by
using the same kind of thinking
we used when we created them.

ALBERT EINSTEIN

This thesis will focus on the use of Interferometric Synthetic Aperture Radar (InSAR) to observe slow slip events (SSEs). In fact, SSEs are one of most poorly understood processes of the earthquake cycle, as they were only discovered two decades ago from GNSS continuous observations ([Hirose et al., 1999](#), [Dragert et al., 2001](#)). Unfortunately, these GNSS networks often lack the spatial resolution to resolve the slow slip extent on the subducting interface (e.g. [Brudzinski et al., 2007](#), [Beroza and Ide, 2011](#)). InSAR offers a potential alternative to address this major issue of spatial resolution, but requires the development of novel methodologies and techniques to detect slow slip surface displacements (e.g. [Hooper et al., 2012](#)). InSAR observations in combination with GNSS, have the potential to provide unprecedented insight into the spatial extent and temporal evolution of SSEs, and could reveal their true role in the earthquake cycle.

In this chapter I will provide background information on SSEs, the rationale and challenges involved in using InSAR, as well as an overview of the selected study area (i.e. Guerrero, Mexico). Finally, I present aims and objectives along with a roadmap of this thesis.

1.1 Slow Slip Events

Slow Slip Events (SSEs) were discovered from GNSS time-series anomalies about two decades ago in Bungo Channel in Japan by *Hirose et al. (1999)*, and independently in Cascadia by *Dragert et al. (2001)*. Over time, and with further deployment of continuous GNSS stations, SSEs have been observed at many subduction zones including Mexico (e.g. *Lowry et al., 2001, Kostoglodov et al., 2003, Larson et al., 2007*), Alaska (e.g. *Wei et al., 2012, Fu and Freymueller, 2013*), New Zealand (e.g. *Douglas et al., 2005, Bartlow et al., 2014*), Costa Rica (e.g. *Jiang et al., 2012, Dixon et al., 2014*), but also away from subduction zones, along the San Andreas fault (e.g. *Linde et al., 1996, Wei et al., 2013*) and in Hawaii (e.g. *Cervelli et al., 2002, Brooks et al., 2006*) (see Figure 1.1).

Slow Slip Events like regular earthquakes release elastic energy, but differ in terms of their duration. While earthquakes occur in seconds to minutes, SSEs can last from a few days, to a week (e.g. Japan and Cascadia: *Ito et al., 2013, Bartlow et al., 2011*), a month (e.g. Japan, New Zealand and Guerrero: *Ito et al., 2013, Bartlow et al., 2014, Frank et al., 2015b*), a year (e.g. Japan and Guerrero: *Hirose et al., 1999, Vergnolle et al., 2010*), or longer (e.g. 1.5 years in New Zealand (*Wallace and Beavan, 2006*), 3 years in Alaska (*Fu and Freymueller, 2013*), and potentially 15 years in Sumatra (*Tsang et al., 2015*)). A detailed overview of global SSEs and their characteristics can be found in *Schwartz and Rokosky (2007)*, *Beroza and Ide (2011)*.

Slow slip is also referred to as Episodic Tremor and Slip (ETS), in those occasions when SSEs are accompanied by an increase of low frequency (< 5 Hz) seismic signals (i.e. Non-Volcanic Tremor (NVT) or Tectonic Tremor (TT)). The main hypothesis for NVT is that it relates to fluid migration as a result of slab dehydration (e.g. *Obara, 2002*). This is also supported from observations such as P and S wave tomography in Japan (e.g. *Shelly et al., 2006*) and high reflection zones along the Cascadia margin (e.g. *Kao et al., 2005*). While ETS has been observed in Japan (e.g. *Obara et al., 2004*) and Cascadia (e.g. *Rogers and Dragert, 2003, Kao et al., 2005, Bartlow et al., 2011*), other slow slip regions like those in New Zealand (*Bartlow et al., 2014*) and Guerrero are updip from the NVT/TT region, and therefore only labelled SSEs.

Potentially, regions currently labeled as SSEs might actually be ETS events. A longer observation period of SSEs worldwide is required as our list of SSEs and tremor locations are likely to be incomplete due to limited observation sensitivity. For example, recently *Frank et al. (2015b)* discovered a new and smaller set of Guerrero (Mexico)

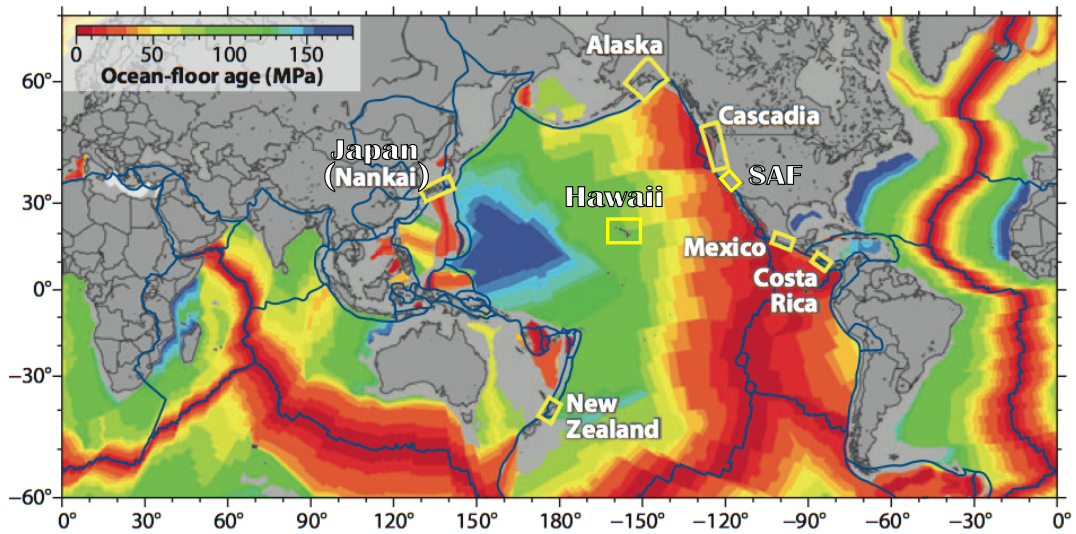


Figure 1.1: A geographic overview of slow slip regions around the world. While most SSEs have been observed at subduction zones, observations have also been made along the San Andreas Fault in California, and at the Kilauea volcano in Hawaii. Figure modified from [Beroza and Ide \(2011\)](#).

SSEs (with duration of approximately a month and repeating every 3 months), which occurs down-dip of the large SSEs and just updip of the tremor zone. These new SSEs are too small to observe with the conventional geodetic techniques, and were only uncovered after careful analysis of low frequency earthquakes and their correlation with stacked GNSS observations. In addition, the Meso-America Subduction Experiment (MASE) was operated from January 2005 to June 2007 ([MASE, 2007](#)), limiting the ETS investigation to the period covering the 2006 Guerrero SSE. Other Guerrero SSEs might exhibit a slightly different NVT pattern.

1.1.1 Slow Slip Events and their implications for earthquakes

The slip rate associated with a SSE is much lower than that of a regular earthquake. So small in fact that it does not result in significant shaking of the Earth. While the SSE in itself does not, therefore, pose a direct hazard to society, it will change the stress field in the surrounding regions and potentially affect the timing of a real earthquake. Over time SSEs can release as much energy as large magnitude earthquakes, e.g. M_w 7.4 in Mexico (e.g [Larson et al., 2007](#)).

Two end-member scenarios can be thought of for the relation between SSEs and earthquakes. In scenario (1), a SSE occurs in the transition zone, downdip of the seismogenic zone and above the free-slipping aseismic region. This changes the stress field near the seismogenic zone, which could trigger a devastating earthquake ([Dragert et al., 2004](#)). While no direct observation has been made of a large earthquake being triggered by a SSE, studies of the 2011 Tohoku-Oki earthquake have shown that the

M_w 7.3 foreshock was preceded by two SSEs of magnitude $M_w \sim 7$ (e.g. [Ito et al., 2013](#)). In Oaxaca, the 2011/2012 SSE has been reported to have migrated into the source region of the 2012 M_w 7.4 Ometepepec earthquake, ending a month before it occurred ([Graham et al., 2014](#)). [Graham et al. \(2014\)](#) found small positive stress changes associated with the Oaxaca SSE for the source region of the Ometepepec earthquake, supporting the scenario of a SSE triggering an earthquake, but they found their results were insufficient to test if this was merely a coincidence. In the Boso Peninsula in Japan, seismic swarms with the largest magnitude $M_w \sim 5$ have reported to occur during a SSE ([Ozawa et al., 2007](#)).

For scenario (2), slow slip enters the seismogenic zone and releases stress, delaying a future earthquake. In Guerrero, Mexico, SSEs have been reported to enter the seismogenic zone (e.g. [Radiquet et al., 2011](#)). [Radiquet et al. \(2012\)](#) found that the accumulated slip deficit where the SSEs enter the seismogenic zone to be 1/3 of those without slow slip, indicating a clear release of energy due to SSEs. Also in Costa Rica SSEs have been reported to extend into the seismogenic zone (e.g. [Dixon et al., 2014](#)). Studies over both locations highlight the importance of SSEs decreasing the earthquake potential and hence having a large impact on the earthquake cycle.

1.1.2 Why do Slow Slip Events occur?

SSEs are often observed in the transition zone between the seismogenic zone, which is assumed to be velocity weakening, and the freely slipping aseismic zone, which is assumed to be velocity strengthening (e.g. [Dragert et al., 2001](#), [Segall, 2010](#)). Friction between the subducting and overriding plate decreases with increasing temperature (depth) (e.g. [Wech and Creager, 2011](#)), as well as with increasing pore fluid pressures (e.g. [Audet et al., 2009](#)). The latter can be the result of metamorphic slab dehydration processes giving rise to fluids (e.g. [Julian, 2002](#)). It has been suggested that a permeability contrast across the Moho traps these dehydrated fluids in the mantle wedge (e.g. [Audet et al., 2009](#), [Katayama et al., 2012](#)), which increases pore-fluid pressure and thus decreases the effective normal stress. Low effective normal stresses along the plate interface in combination with a fault instability could result in repeated SSEs (e.g. [Katayama et al., 2012](#), [Frank et al., 2015a](#)), as also suggested from theoretical rate and state friction modelling (e.g. [Liu and Rice, 2007](#), [Segall et al., 2010](#)). In Mexico, for example, SSEs are co-located with an Ultra Slow Velocity Layer ([Song et al., 2009](#)), which is supported by observations of a large V_p/V_s ratio ([Kim et al., 2010](#)) and findings from a local magnetotelluric study ([Jödicke et al., 2006](#)).

1.1.3 Scaling laws of SSEs and earthquakes compared

Scaling laws for SSEs can be useful as they help to understand the physical mechanism involved and differences with earthquakes ([Gao et al., 2012](#)). Multiple studies of slow

slip scaling laws have been developed over the last decade (e.g. [Ide et al., 2007](#), [Schwartz and Rokosky, 2007](#), [Brodsky and Mori, 2007](#), [Meade and Loveless, 2009](#), [Peng and Gombert, 2010](#), [Obara, 2010](#), [Gao et al., 2012](#)). [Gao et al. \(2012\)](#) indicate a lack of data for events ranging from minutes to a couple of days. The empirically derived relationships will become better constrained with more observations of SSEs over time. Part of the current observation gap is related to a lack of sensitivity in our observation methods. The surface deformation associated with a SSE needs to be large enough to be observed from geodesy, and therefore often relates to larger and longer lasting SSEs. Alternative observations from strain and tilt meters can bridge this, but they are typically more challenging to install and maintain, and therefore are a more sparse dataset. Seismology on the other hand does not provide further direct observations for SSEs, as no significant seismic waves are radiated. However, one can use the spatial and temporal observations from NVT ([Bartlow et al., 2014](#)) or LFEs ([Frank et al., 2015b](#)) to investigate in their potential collocation with SSEs. Until now, numerical modeling of SSEs through rate and state friction laws ([Tse and Rice, 1986](#)) have not been used to expand the catalogue of SSE observations, as further validation is required with geodetic observations of SSEs ([Gao et al., 2012](#)) for the different friction mechanisms: velocity weakening (e.g. [Liu and Rice, 2007](#)), velocity cutoff (e.g. [Hawthorne and Rubin, 2013](#)), and velocity weakening with dilatant strengthening (e.g. [Segall et al., 2010](#)).

Figure 1.2 provides an overview of the worldwide SSE and earthquake observations together with the fitted empirical relations. Key points include:

- The relation between the **fault length**, L , and the **width**, W , affected during regular earthquakes is similar to that of SSEs ($L \sim 2W$), Figure 1.2(a).
- The relation between the **seismic moment** and the **stress-drop**, $\Delta\sigma$, is found to be nearly constant for both regular earthquakes and SSEs. However, for SSEs, the stress-drop is 1-2 orders of magnitude smaller than for regular earthquakes, Figure 1.2(b).
- In case of conventional earthquakes the **seismic moment**, M_o , is proportional to the **duration**, T , cubed ($M_o \sim T^3$) ([Furumoto and Nakanishi, 1983](#)). This is different for SSEs, where the duration is linearly related to seismic moment ($M_o \sim T$), Figure 1.2(c).
- As expected the **seismic moment** and the average event **rupture propagation velocity**, V_{rp} , behave different for SSEs and earthquakes. The average rupture propagation velocity for SSEs are found to range from tens of km/day to hundreds of m/day ($\text{Log}V_{rp} \sim (-0.5 \pm 0.05) \text{Log}M_o$), versus 1-10 km/s for earthquakes, Figure 1.2(d).
- **Event duration**, T , was found to be less than three times the **event rise time**, τ , for SSEs. For earthquakes this is much larger than 3, Figure 1.2(e). The event

rise size was defined to be 95% of the total event deformation (*Gao et al., 2012*).

1.2 Interferometric Synthetic Aperture Radar

Surface displacements associated with SSEs are primarily observed using networks of continuous GNSS stations. The spatial resolution at which the slow slip signal is resolved is limited by the station distribution. Interferometric Synthetic Aperture Radar (InSAR) has the potential to provide worldwide observations of slow slip surface displacements at high spatial resolution (every few meters), assuming a coherent signal is maintained.

InSAR refers to the phase difference between two Synthetic Aperture Radar (SAR) acquisitions over the same region but which were acquired at different times. Typically the first acquisition is referred to as master, while the second acquisition is labeled slave. As the SAR data is defined as a complex number, the InSAR operation becomes a multiplication between the master and the complex conjugate of the slave. Prior to InSAR computation, the slave SAR images needs to be aligned with that of the master. This is achieved through a two-step coregistration procedure (e.g. *Brown, 1992, Gabriel and Goldstein, 1988, Hanssen, 2001*). During coarse-coregistration, large correlation windows are used to estimate the slave image translation offsets with respect to the master (accuracy up to few pixels). This is followed by a fine-coregistration in which the slave is resampled to the master grid using subpixel offset estimation and a polynomial transformation.

To extract the change in surface displacements, the phase contribution from the “flat-earth” and terrain needs to be accounted for (e.g. *Hanssen, 2001*). The flat-earth refers to the phase signal introduced by reference surface (e.g. WGS84) and change in viewing geometry between the master and slave. It is estimated using the precise satellite orbit information and the formulation of the reference surface. The terrain is accounted for by radar-coding a Digital Terrain Model (DEM), e.g. the Shuttle Radar Topography Mission (SRTM) DEM (*Farr et al., 2007*), and combining this with the satellite viewing geometry to compute the phase signal related to a change in elevation.

Different InSAR processors are available to perform the steps described above such as ROIPAC (*Rosen et al., 2004*), GAMMA, and DORIS (*Kampes et al., 2003*). I used the latter throughout my thesis to compute interferograms.

Historically, two major challenges have prevented the widespread uptake of InSAR: (1) decorrelation noise, introduced by a change in satellite acquisition geometry and surface scattering properties (e.g. *Zebker, 1992*), and (2) atmospheric noise signals (e.g. *Zebker et al., 1997, Hanssen, 2001*). The latter include noise from the ionosphere, introduced by free electron concentration variations, and for the troposphere, introduced by water vapour, pressure and temperature variations. Atmospheric noise typically masks the much smaller slow slip surface displacements (e.g. *Hooper et al., 2012, Cavalie*

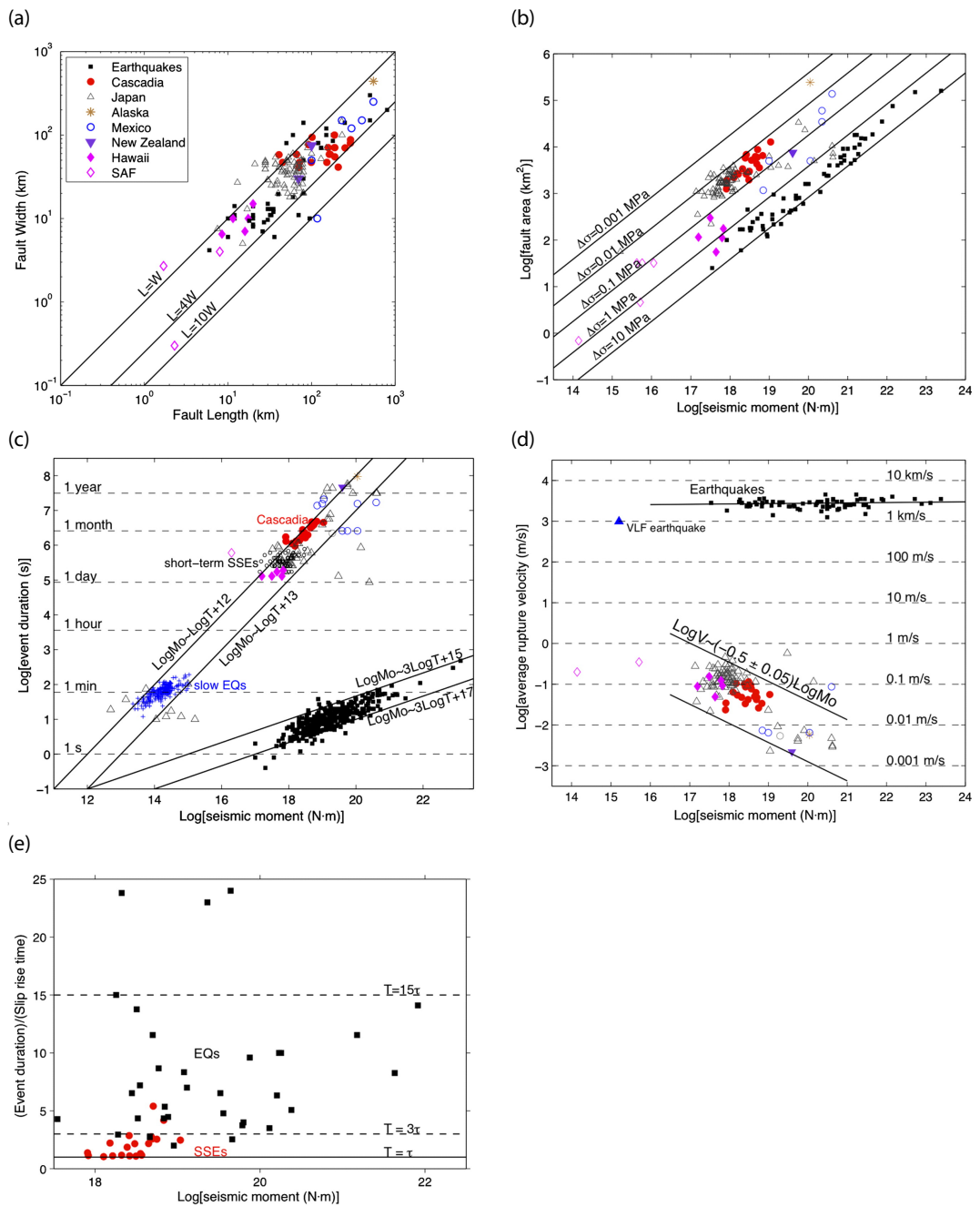


Figure 1.2: A comparison of SSE and earthquake empirical scaling relationships, figures taken from *Gao et al. (2012)*. Logarithmic scaling laws are estimated from a global ensemble SSEs (see legend for locations) and earthquakes. (a) gives the relationship between fault width and fault length, (b) seismic moment and fault area, (c) seismic moment and duration, (d) seismic moment and rupture propagation velocity, and (e) seismic moment and the ratio between event duration and rise time.

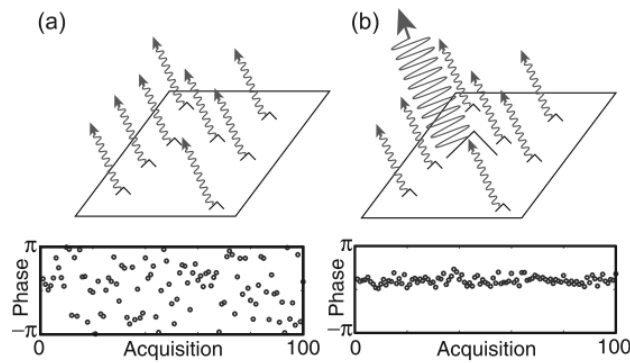


Figure 1.3: Simulation of the phase in case of (a) a distributed scatterer pixel, and (b) a Persistent Scatterer (PS) pixel. For the PS pixel, a dominant scatterer over time results in a stable phase over time. This figure has been taken from [Hooper et al. \(2007\)](#).

[et al., 2013](#)). Therefore, a critical step in the InSAR processing chain lies in reducing atmospheric noise.

Below I elaborate on these individual challenges and how they can be overcome.

1.2.1 Decorrelation noise

One drawback to InSAR measurements is the level of measurement error. This can be reduced by applying state-of-the-art time series InSAR methods, which are typically split into the Persistent Scatterer methods (e.g. [Hooper et al., 2004](#), [Perissin and Ferretti, 2007](#), [Hooper et al., 2007](#)), and the Small Baselines methods (e.g. [Berardino et al., 2002](#), [Lanari et al., 2004](#), [Hooper, 2008](#), [Biggs et al., 2007](#)), or a combination of both ([Hooper, 2008](#)).

These time-series methods go back to the definition of the phase for each pixel, being the coherent sum of all scatterers within the ground resolution cell. When the scattering characteristics vary within this ground cell over time, the coherent sum of the phase will also appear random, and the pixel will appear to be decorrelated (e.g. [Hooper et al., 2007](#)), see the simulation of a distributed scatterer pixel in Figure 1.3(a). However in the case of a bright scatterer - such as a building, tree-trunk, or large rock - the phase value will be dominated by the phase of this bright scatterer and will not appear random over time (e.g. [Hooper et al., 2007](#)), simulation in Figure 1.3(b). Such a pixel is referred to as a Persistent Scatterer (PS) pixel. The aim of time-series InSAR is to find the subset of these PS pixels, such the effects of decorrelation noise can be reduced. Therefore a time-series interferogram will have fewer pixels than that of conventional InSAR.

Throughout my thesis, I apply the Stanford Method for Persistent Scatterer (StaMPS) (e.g. [Hooper, 2008](#), [Hooper et al., 2012](#)). A detailed description of the StaMPS PS approach can be found in [Hooper et al. \(2004\)](#). StaMPS selects the PS pixels based on the phase noise characteristics over time. To limit the computation effort and processing

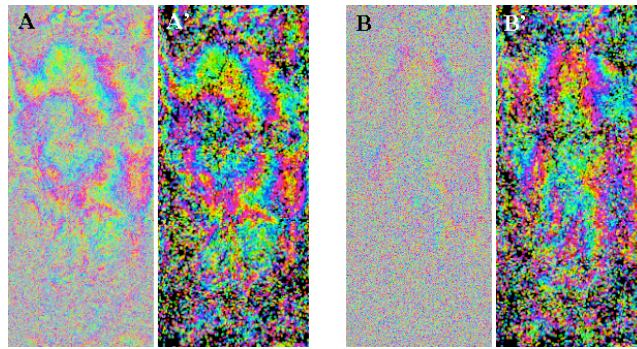


Figure 1.4: Comparing InSAR and time-series InSAR. This example shows 2 Envisat interferograms (a) and (b) processed using the conventional InSAR approach. Strong decorrelation noise can be observed in (b). By performing a time-series analysis (StaMPS) of 19 interferograms, where interferograms are combined over time to select only those pixels with stable phase-characteristics, the noise can be decreased significantly (b'). For (a) which was less subjected for decorrelation, the improvement by applying time-series InSAR (a') is less significant.

time, the interferograms are first split into patches with an initial PS candidate selection based on the amplitude dispersion threshold. The phase noise for each candidate is then estimated using an iterative approach. Once completed, a further reduction of the candidates is made by keeping only a percentage of random pixels per area, controlled through the density random threshold. The PS selection on the candidates follows after the weeding procedure, where the phase noise of neighboring candidate pixels are compared. Those pixels for which the noise standard deviation with its neighbors does not meet the weed standard deviation are rejected. In addition, also candidates with noise levels that exceeds the weed maximum noise threshold will be rejected. Lastly, the different patches are merged back together, either at full resolution or at a preferred merge resolution. When specifying a coarse merge resolution, additional weeding can be done when the noise standard deviation of the resampled PS pixel fails the merge standard deviation threshold. At the same time as the merging step an estimate of the DEM errors are removed. These are errors that correlate with the perpendicular baseline. Some residual spatially-correlated DEM errors will remain due to inaccuracy of the estimation procedure (*Hooper et al., 2004*). However, these residuals can be further reduced after the unwrapping procedure, during the time-series inversion by estimating a component that correlates with the perpendicular baseline. An example comparing conventional InSAR and time-series InSAR is shown in Figure 1.4. Interferogram (b) which shows large signs of decorrelation is improved significantly by combining 19 interferograms over time using the StaMPS PS-InSAR approach. This dataset has been processed using the parameters described in table 4.2.

1.2.2 Tropospheric noise

Variations of temperature, pressure, and relative humidity lead to a spatially varying tropospheric delay signal, which partly correlates with topography. A phase delay

through the troposphere can be characterized by the refractivity, N_{tropo} , (*Smith and Weintraub, 1953, Thayer, 1974, Davis et al., 1985*), and is typically split into a hydrostatic, wet, and liquid components. Below I neglect the liquid component, as it is expected to be small and will only become significant in case of a saturated atmosphere (*Hanssen, 2001*).

$$N_{\text{tropo}} = \left(k_1 \frac{P}{T} \right)_{\text{hydr}} + \left(k_2' \frac{e}{T} + k_3 \frac{e}{T^2} \right)_{\text{wet}}, \quad (1.1)$$

where P indicates total atmospheric pressure, T the temperature and e the partial pressure of water vapour. The coefficients k_1 , k_2' and k_3 are constants estimated in literature as $k_1 = 77.6 \text{ KhPa}^{-1}$, $k_2' = 23.3 \text{ KhPa}^{-1}$ and $k_3 = 3.75 \cdot 10^5 \text{ K}^2 \text{hPa}^{-1}$ (*Smith and Weintraub, 1953, Thayer, 1974*). The tropospheric phase delay (2-way), ϕ_{tropo} , at a specific height, $h = h_1$, corresponds to the integration of the tropospheric refractivity between h_1 and the top of the troposphere h_{top} along the radar line-of-sight (*Hanssen, 2001*).

$$d_{\text{tropo}} = 10^{-6} (\cos\theta)^{-1} \int_{h=h_1}^{h=h_{\text{top}}} N_{\text{tropo}}(h) dh \quad (1.2)$$

$$\phi_{\text{tropo}} = \frac{-4\pi}{\lambda} d_{\text{tropo}} \quad (1.3)$$

where d_{tropo} is the tropospheric delay (1-way), θ the incidence angle, λ the radar wavelength, and $-4\pi/\lambda$ a conversion factor to convert from pseudorange increase to phase delay.

Sounding measurements made during ascents of large inflated hydrogen or helium balloons provide a detailed vertical profile of atmospheric properties (e.g. pressure, temperature, relative humidity, and wind speed), which can be used to calculate refractivity, and when integrated according to equation (1.2) gives the tropospheric delay (Figure 1.5(a)). It can be observed that delays increase at lower altitudes as the signal has travelled further through the troposphere. With an interferogram being the phase difference between two SAR acquisitions, the atmospheric delay depends on the change in refractivity rather than the total refractivity. Figure 1.5(b) shows the relative tropospheric delays, i.e. the difference between all pairs of tropospheric delays shown in Figure 1.5(a), with the darker color indicating more overlapping delay curves. Variations in interferograms in flat regions, are mainly due to the wet component of the refractivity, i.e. the water vapour; the hydrostatic component often appears as a smooth signal due to the large spatial scale of high and low pressure fields (*Hanssen, 2001*). In regions with significant topography, the hydrostatic component will also cause a correlation between the phase and topography (*Elliott et al., 2008*).

Different approaches have been documented to estimate the tropospheric noise in InSAR data, for example by using weather models (e.g. *Wadge et al., 2002, Liu et al.,*

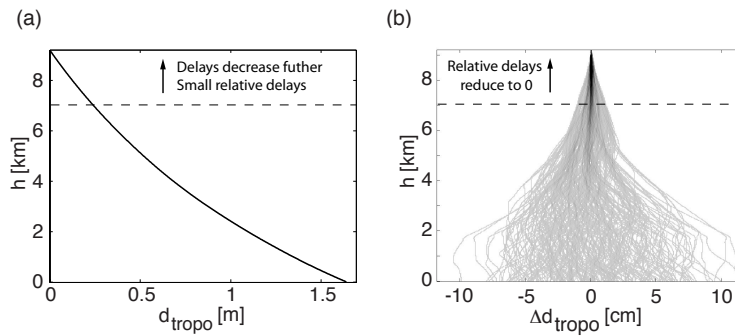


Figure 1.5: (a) Tropospheric delays d_{tropo} computed from balloon sounding data for 24 days (12 UTC) between Jan-Feb 2014 in Southern Mexico. Delays are computed by integrating the refractivity from height h upwards (to 9 km) and projecting to the Envisat radar line-of-sight, with the black solid line indicating the mean delay. Only few soundings extend above 9 km. (b) Relative tropospheric delays Δd_{tropo} , showing all (276) possible combinations of the difference between tropospheric delay at two different days. The darker the color, the more the curves overlap, i.e. black all 276 relative delays overlap. All sounding data is provided by the department of Atmospheric Science of the University of Wyoming.

2009, *Doin et al.*, 2009, *Jolivet et al.*, 2011, *Grandin et al.*, 2012, *Walters et al.*, 2014, *Jolivet et al.*, 2014), GNSS data (e.g. *Onn and Zebker*, 2006, *Williams et al.*, 1998), multi-spectral observations (e.g. from the Medium Resolution Imaging Spectrometer (MERIS) onboard the Envisat satellite; or the Moderate Resolution Imaging Spectroradiometer (MODIS) onboard the Terra and Aqua satellites) (*Li et al.*, 2006, 2009a,b), or GNSS in combinations with spectrometer data (e.g. *Li et al.*, 2005, *Puysségur et al.*, 2007). While all of these techniques can, under certain conditions, reduce the tropospheric signal, they are often limited by the lower spatial resolution of the auxiliary data. Alternatively, tropospheric signals can be estimated from the correlation between the interferometric phase and the topography over the whole interferogram (e.g. *Cavalié et al.*, 2008), in a non-deforming area (*Wicks et al.*, 2002), a spatial frequency band insensitive to deformation (*Lin et al.*, 2010), or by removing a preliminary estimate of the deformation displacements prior to the estimation (*Elliott et al.*, 2008). The assumption of a single relationship between phase and topography over the whole interferogram does not account for the spatial variation of the tropospheric properties. This can be significant over large areas (>10s of km), especially when the area includes different climatic zones. All the above methods are corrections applied to individual interferograms. In the presence of a time series of interferograms, other approaches can be used as well, either stand-alone or in combination with those described earlier. This includes stacking (e.g. *Zebker et al.*, 1997), spatial and temporal filtering (e.g. *Hanssen*, 2001), and time-series methods (e.g. *Hooper et al.*, 2012, *Elliott et al.*, 2008, *Doin et al.*, 2015). Both the stacking and filtering methods assume the atmosphere to be spatially correlated and random in time. The challenges for all these methods lie in separating the atmospheric noise from other signal contributions such as deformation,

orbit errors, and DEM errors.

1.2.3 Ionospheric noise

Ionospheric phase noise in InSAR is introduced when the radar interacts with free electrons in the ionosphere (between 100 and 1000 km altitude). The interaction between the radar signal and the free electrons can be described through the ionospheric refractivity as ([Hanssen, 2001](#)):

$$N_{\text{iono}} = -4.028 \times 10^7 \frac{n_e}{f^2}, \quad (1.4)$$

where n_e is the electron content, and f is the radar frequency. The ionospheric phase delay (2-way), ϕ_{iono} , corresponds to the integration of the ionospheric refractivity along the travelled path as:

$$d_{\text{iono}} = 10^{-6} (\cos\theta)^{-1} \int N_{\text{iono}} dh = -40.28 (\cos\theta)^{-1} \frac{\text{TEC}}{f^2} \quad (1.5)$$

$$\phi_{\text{iono}} = \frac{-4\pi}{\lambda} d_{\text{iono}} \quad (1.6)$$

where d_{iono} is the ionospheric delay (1-way), θ is the radar look angle, λ the radar wavelength, TEC the Total Electron Content for a square meter vertical column, and $-4\pi/\lambda$ a conversion factor to convert from pseudorange increase to phase delay. The TEC varies with latitude, time of day, orientation of the earth magnetic field, and solar activity (e.g [Snoeij et al., 2001](#)).

The ionospheric delay is inversely proportional to the radar frequency f and correlated with the Total Electron Content (TEC) in the ionosphere. Therefore L-band SARs ($\lambda=23$ cm), such as ALOS 1/2 and the future US-India NISAR mission, are more subjected to ionospheric delays than C-band SARs ($\lambda=5.6$ cm), such as ERS 1/2, Envisat, and the RADARSAT constellation.

Ionospheric noise artefacts can be estimated from auxiliary data like GNSS (e.g. [Misra and Enge, 2010](#)) and potentially from ionospheric weather models, but these are often limited by their low spatial resolution (tens of km to hundreds of km) in comparison with high-resolution InSAR data.

Alternatively, relative TEC variations can be estimated from the radar data using azimuth shift (e.g. [Meyer et al., 2006](#)) or split-spectrum methods (e.g. [Rosen et al., 2010](#)). For the azimuth shift method, azimuth displacements from offset tracking, or more accurately from Spectral Diversity (also known as Multi-Aperture Interferometry) (e.g. [Jung et al., 2013](#), [Jung and Lee, 2015](#)), are related to the azimuth derivative of the ionospheric effects. For the range split-spectrum methods, the dispersive relation is used to separate ionospheric noise from a non-dispersive component (troposphere and tectonic signals). Both approaches require a coherent interferogram, and have their

own limitations. The azimuth shift method assumes negligible azimuth deformation compared to the ionospheric delay (up to 5 m) and works well when there are no isolated regions in the interferogram. The split spectrum method is applied to unwrapped interferograms, and requires a high degree of smoothing due to strong noise scaling.

1.3 Mexico study area

The study area of my PhD research is Guerrero in Southern Mexico, Figure 1.6. Here, the Cocos plate subducts beneath the North American plate at a rate of ~ 6.1 cm/year (DeMets *et al.*, 2010), leading to sporadic large thrust earthquakes (gray shaded polygons). Although seismicity is observed over a large depth range, large devastating thrust earthquakes in Guerrero are mainly observed in the locked seismogenic zone between 10-25 km depths, where the subducting and overriding plates are strongly coupled (Kostoglodov *et al.*, 2001, Larson *et al.*, 2004). A M_w 8.0 earthquake in 1985 caused more than 10,000 deaths in Mexico City and 3-4 billion U.S. dollars of damage (USGS). However, there is a region with a seismic gap (Figure 1.6, red line between 101.2°W - 99.2°W) where no earthquake has occurred since the $M_w=7.6$ earthquake in 1911 (e.g. Kostoglodov *et al.*, 2003). The largest slip deficit is assumed to be located on the northwestern section of the Gap (dashed red line between 101.2°W - 100.4°W) (Kostoglodov *et al.*, 1996), as some slip is thought to have been released on the south-eastern section by the M_w 7.7 earthquake in 1957, and the M_w 7.1 and 7.0 earthquakes in 1962 (Ortiz *et al.*, 2000). Singh and Mortera (1991) estimated that a rupture of the Guerrero Gap today could result in an earthquake of M_w 8.2-8.4.

Considering the seismic potential of the Guerrero Gap, the region has been a focus of much research effort. Through repeat leveling observations, Kostoglodov *et al.* (2001) observed an opposite sense of tilting inside compared to outside the Guerrero Gap. They suggested that this could be caused by a change in the geometry of the locked zone and perhaps the occurrence of a SSE, as discovered in Cascadia and Japan (Hirose *et al.*, 1999, Dragert *et al.*, 2001). In the same year, Lowry *et al.* (2001) confirmed the occurrence of the 1998 Guerrero SSE, by using the observations of a single continuous GNSS site, close to the coast (CAYA), and a few campaign sites.

Puzzled by this interesting observation, further questions arose regarding SSEs, including (1) what is their recurrence, (2) what is their spatial extent on the subducting interface, (3) what is their relation with the Guerrero Gap, (4) how do they fit in with the earthquake cycle, and (5) how do they impact the seismic hazard for the surrounding cities and the densely populated capital of Mexico? Even now, two decades later, a lot of opportunities exist to make future contributions to these questions.

The following sections provide information on the Guerrero subduction zone, current SSE observations and modelling results, as well as the latest view on how slow slip events occur and interplay with tremor in the Guerrero region.

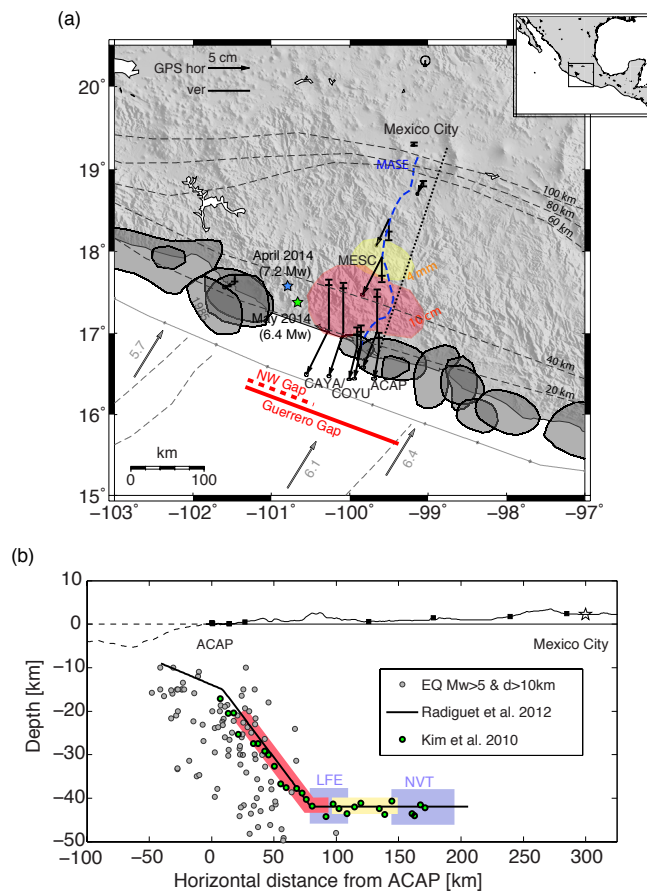


Figure 1.6: Overview of the Guerrero subduction zone. (a) Tectonic setting of Guerrero. The gray arrows indicate the MORVEL relative plate motion of the Cocos and the North America Plate (*DeMets et al., 2010*), with depth contours of the subducting slab indicated every 20 km (*Pardo and Suárez, 1995, Melgar and Pérez-Campos, 2011, Pérez-Campos and Clayton, 2014*). Gray polygons represent rupture areas of major earthquakes (*Kostoglodov et al., 2003*). The rupture of the 1985 earthquake is indicated, as well as the recent 2014 Guerrero earthquakes (stars), which occurred on the western edge of the gap. The red shaded polygon gives the approximate location of the large SSEs, repeating approximately every 4 years, and where the polygon represents the 10 cm slip contour of the 2006 SSE (*Radiguet et al., 2011*). The yellow shaded polygon shows the location of the small SSEs that repeat every 3 months, and where the polygon gives an average location of the 4 mm slip contour of all the small SSEs together (*Frank et al., 2015b*). Plotted GNSS displacements corresponds to the surface displacements of the 2006 SSE (*Vergnolle et al., 2010*), with error bars representing 2σ . The dotted black line represents the transect of the subduction interface as shown in (b) and assumed in many of the Guerrero SSE studies (e.g. *Radiguet et al., 2012, Cavalieri et al., 2013*). Topography information as well as the GNSS stations locations (black square markers) are plotted with respect to the distance to the coastal ACAP GNSS station, located in Acapulco. Interface as determined from Receiver Function tomography of teleseismic earthquakes using the MASE network (*Kim et al., 2010*; blue dashed line in (a)) is shown by the green markers, while gray markers show the seismicity. After *Frank et al. (2015b)*, large and small magnitude SSEs are shown on the subducting interface, together with the approximate location of increased activity of Low Frequency Earthquakes (LFE) and Non Volcanic Tremor (NVT). Ocean bottom topography data has been extracted from the GEBCO_08 Grid (version 20091120, <http://www.gebco.net>), while for the elevations I made use of the SRTM DEM.

1.3.1 The Guerrero subduction zone

The structure of the Guerrero subduction interface is interesting, being different from most subduction zones, as it has a sub-horizontal stage (Figure 1.6(b)). The Pacific plate subducts beneath the North America plate about 66 km south-southwest off the coastal city of Acapulco with a dip angle of 15° and becomes sub-horizontal at a depth of 40 km, approximately 80 km north-northeast from Acapulco. The interface remains horizontal until about 230-250 km from the coast, after which it dips steeply below the Trans-Mexican Volcanic Belt, at an angle of 75° (Kim *et al.*, 2010, Chen and Clayton, 2012). The interface geometry has been estimated from a variety of data, including seismicity and focal mechanics (Singh and Pardo, 1993, Pardo and Suárez, 1995), geologic records and volcanic features (Ferrari, 2004), and from the analysis of the MASE broadband seismic network (Pérez-Campos *et al.*, 2008, Kim *et al.*, 2010).

1.3.2 Slow slip events in Guerrero

Analyses of GNSS data have indicated the Mexican subduction zone to be very active in terms of SSEs, with a repeat interval of approximately 3-5 years. SSEs have been documented to occur in 1995 (Larson *et al.*, 2004, Vergnolle *et al.*, 2010), 1998 (Lowry *et al.*, 2001, Larson *et al.*, 2004, Vergnolle *et al.*, 2010), 2001/2002 (Kostoglodov *et al.*, 2003, Iglesias *et al.*, 2004, Vergnolle *et al.*, 2010), 2006 (Larson *et al.*, 2007, Correa-Mora *et al.*, 2009, Vergnolle *et al.*, 2010, Radiguet *et al.*, 2011, Bekaert, 2011, Hooper *et al.*, 2012, Cavalié *et al.*, 2013), 2009/2010 (Walpersdorf *et al.*, 2011), and recently in 2014/2015 (Vladimir Kostoglodov and Erwan Pathier, personal communication, October 2014).

The slow slip surface displacements are the largest near the coast (average accumulated uplift of ~ 4 -5 cm), and extend from the coast to Mexico City, 300 km inland. Typically, the surface displacements decrease inland with GNSS sites at ~ 100 -130 km distance from the coast showing a subsidence signal, and with displacements decreasing to zero beyond 250-300 km. The cumulative horizontal displacements for most of the sites are in a southwesterly direction.

Slip modelling shows that SSEs reach an average peak slip of ~ 15 -20 cm, located just up-dip of the sub horizontal stage (e.g. Kostoglodov *et al.*, 2003, Vergnolle *et al.*, 2010; Figure 1.6(a) red polygon). The Guerrero SSEs are some of the largest observed around the world (Cotte *et al.*, 2009) with equivalent earthquake magnitudes between M_w 7-7.5 (e.g. Kostoglodov *et al.*, 2003, Larson *et al.*, 2004, Vergnolle *et al.*, 2010). Most of the slow slip occurs along the subducting interface within the transition zone (25-40 km depths). However, some slow slip is found to enter the locked part of the seismogenic zone (< 25 km) where typically large thrust earthquakes occur (e.g. Radiguet *et al.*, 2012). Radiguet *et al.* (2012) found that over a 12-year period SSEs reduced the slip deficit within the Guerrero Gap to 1/4 the slip deficit outside the Gap. While SSEs

decrease the seismic potential in the Guerrero Gap, the question arises to what extent slow slip modifies the stresses at the edges of the slow slip region. This question is under investigation after two earthquakes (M_w 6.4 and 7.2) occurred on the western edge of the Guerrero Gap, blue and green star in Figure 1.6, during the most recent 2014 SSE.

In the last year, a set of smaller magnitude SSEs were discovered by *Frank et al.* (2015b), which have an average magnitude $M_w \sim 6.4$, a duration of about a month, and repeat every 3 months. These SSEs were not observed using the typical GNSS methods, but were revealed by aligning and stacking of GNSS observations with the occurrence of Low Frequency Earthquakes. Modelling results show that these smaller magnitude SSEs, Figure 1.6(a) yellow polygon, occur on the subhorizontal stage, down-dip of the region with the large SSEs, and just up-dip of the NVT “Sweet Spot”, Figure 1.6(a) blue polygon. The average accumulated slip is ~ 6 mm, with associated horizontal surface displacements of maximum ~ 1.5 mm near the coast (*Frank et al.*, 2015b).

1.3.3 Explaining the occurrence of slow slip in Guerrero

The hypothesis on the occurrence of SSEs in Mexico fits in well with the general idea as provided in section 1.1.2. Elevated pore-fluid pressure as a result of slab dehydration decreases the effective normal stress. Those regions of the fault interface with low effective normal stresses can therefore slip when small shear stresses are introduced (*Colella et al.*, 2013). In Mexico, the spatial extent of the slow slip co-locates with an Ultra Slow Velocity Layer (USVL) (*Song et al.*, 2009), supported by observations of a large V_p/V_s ratio (*Kim et al.*, 2010) and findings from a local magnetotelluric study (*Jödicke et al.*, 2006). *Kim et al.* (2013) suggests that the USVL is mainly composed of talc and serpentinites, which can develop a strong anisotropic permeability under shearing (e.g. *Frank et al.*, 2015a). In other regions around the world, such as in Cascadia, NVT and slow slip are correlated in space and time. This is not the case in Mexico, where NVT (*Husker et al.*, 2012) is found down-dip of the slow slip region in an area labeled the NVT “Sweet Spot”, Figure 1.6(b). *Frank et al.* (2013) discovered that within this region also Low Frequency Earthquakes (LFEs) occur. The observational catalogue of NVT and LFEs in Mexico is limited in time by the operational period of the MASE network (blue dashed line in Figure 1.6(a) *MASE*, 2007). Therefore is it only possible to compare NVT activity with the 2006 SSE, for which no increased activity is observed in the Sweet Spot. With the discovery of the smaller magnitude SSEs (*Frank et al.*, 2015b) the spatial gap between the Sweet Spot and slow slip region is further reduced, as illustrated in Figure 1.6(b).

Frank et al. (2014) discovered a new cluster of LFEs in the transition zone, for which the activity correlates in space and time with that of the 2006 SSE. In another study *Frank et al.* (2015a) provides a hypothesis which integrates the occurrence of NVT in the Sweet spot, LFEs in the transition zone and its correlation with SSEs. Their

proposed scenario describes how fluids introduced by slab dehydration are trapped within the Sweet Spot due to the USVL permeability anisotropy, which gives rise to the occurrence of continuous NVT activity. During the occurrence of a slow slip event, shear stresses increase within the LFE transition zone, increasing the LFE activity. The increase in shear stress also re-activates faults, which changes the permeability allowing for fluid migration along the reactivated faults from the Sweet Spot in the updip direction. Once these fluids have moved past the LFE region in the transition zone, the effective normal is increased again decreasing the LFE activity again.

1.4 Aims and objectives

Until now, observations of SSEs have been primarily made from continuous GNSS networks. The spatial resolution of these slow slip surface observations are therefore typically limited by the GNSS station distribution. In many cases this has led to a poorly constrained slow slip solution at the subduction interface. Interferometric Synthetic Aperture Radar (InSAR) can be used to address this problem. Where good coherence is maintained InSAR can provide an observation every ~ 30 m. However, InSAR has its own limitations as was already described in section 1.2.

The aim of my thesis is to get a better understanding of slow slip events by using observations from InSAR. To achieve this I have defined the following objectives.

- Develop and redefine tropospheric correction methods for InSAR.
- Develop a method to extract slow slip surface displacements from InSAR.
- Develop a method to invert static GNSS and InSAR observations of slow slip surface displacements to model slow slip on the subduction interface.
- Develop a joint inversion method of GNSS and InSAR observations to retrieve the slow slip evolution on the subduction interface.

Together these objectives allow for the development of InSAR as an observation tool for slow slip, and its combination with GNSS for high-resolution slip modelling. This will be of particular interest in constraining the spatial and temporal extent of slow slip. Together with observations of seismology this might provide more insight into what causes these slow slip events and how they impact the stress field.

1.5 Thesis Roadmap

In **chapter 2**, I developed a power-law tropospheric correction method for InSAR, which is estimated empirically from the high resolution InSAR data itself (published as [Bekaert et al., 2015a](#)). This method is an improvement above the traditionally applied linear method, as it allows for a spatial variation in tropospheric properties. Here

I present the developed methodology, and present a test-case over Southern Mexico, where I compare the power-law methods with that of the linear method. This chapter is in support of my 1st objective as set within my thesis.

In **chapter 3**, I perform a statistical analysis of the state-of-the-art tropospheric correction methods for InSAR over Southern Mexico, Italy and El Hierro (published as [Bekaert et al., 2015b](#)). Besides my newly developed power-law method, this includes the tropospheric corrections estimated from spectrometers (MERIS and MODIS), a low and high spatial-resolution weather model (ERA-I and WRF), and the conventional linear empirical method. This chapter completes the 1st objective as set within my thesis. Together with the publication of this manuscript, I also released the Toolbox for Reducing Atmospheric InSAR Noise (TRAIN) which can be downloaded at <http://www.davidbekaert.com/#links>). With this toolbox I aim to support the InSAR community and make tropospheric corrections a standard practice in the InSAR processing chain.

In **chapter 4**, I develop and demonstrate the combined usage of InSAR and GNSS to model the cumulative slip as result of the 2006 Guerrero SSE (published as [Bekaert et al., 2015c](#)). This includes the correction of tropospheric delays using the power-law method, as developed in chapter 2, the development of the methodology and estimation of the InSAR slow slip surface displacements, and the slow slip modelling by combining GNSS and InSAR together using full variance-covariance information. This chapter therefore complements the 2nd and 3rd objective as set within my thesis.

In **chapter 5**, I provide the methodology for the time-dependent slip modelling of earthquake cycle processes such as interseismic, coseismic, postseismic and aseismic slip; combining geodetic observations from GNSS and InSAR. This chapter is a manuscript currently under review in the Journal of Geophysical Research. It contains an application of the developed methodology to a simulation of the 2006 Guerrero SSE. This is different from chapter 4, which was a static inversion. The developed method supports the 4th objective as set within my thesis.

References

- Audet, P., M. G. Bostock, N. I. Christensen, and S. M. Peacock (2009), Seismic evidence for overpressured subducted oceanic crust and megathrust fault sealing, *Nature*, *457*(7225), 76 – 78, doi:[10.1038/nature07650](https://doi.org/10.1038/nature07650). 1.1.2
- Avouac, J.-P. (2015), From Geodetic Imaging of Seismic and Aseismic Fault Slip to Dynamic Modeling of the Seismic Cycle, *Annual Review of Earth and Planetary Sciences*, *43*(1), 233 – 271, doi:[10.1146/annurev-earth-060614-105302](https://doi.org/10.1146/annurev-earth-060614-105302). 1
- Bartlow, N. M., S. Miyazaki, A. M. Bradley, and P. Segall (2011), Space-time correlation of slip and tremor during the 2009 Cascadia slow slip event, *Geophys. Res. Lett.*, *38*(18), doi:[10.1029/2011GL048714](https://doi.org/10.1029/2011GL048714). 1.1, 1.1
- Bartlow, N. M., L. M. Wallace, R. J. Beavan, S. Bannister, and P. Segall (2014), Time-dependent modeling of slow slip events and associated seismicity and tremor at the Hikurangi subduction zone, New Zealand, *J. Geophys. Res.*, *119*(1), 734 – 753, doi:[10.1002/2013JB010609](https://doi.org/10.1002/2013JB010609). 1.1, 1.1, 1.1.3
- Bekaert, D. (2011), InSAR Time Series Analysis of the 2006 Slow Slip Event on the Guerrero Subduction Zone, Mexico, M.S. Thesis, Delft University of Technology, Delft, The Netherlands. 1.3.2
- Bekaert, D., A. Hooper, and T. Wright (2015a), A spatially-variable power-law tropospheric correction technique for InSAR data, *J. Geophys. Res.*, *120*, doi:[10.1002/2014JB011558](https://doi.org/10.1002/2014JB011558). 1.5
- Bekaert, D., R. Walters, T. Wright, A. Hooper, and D. Parker (2015b), Statistical comparison of insar tropospheric correction techniques, *Remote Sensing of Environment*, *170*, 40 – 47, doi:<http://dx.doi.org/10.1016/j.rse.2015.08.035>. 1.5
- Bekaert, D., A. Hooper, and T. Wright (2015c), Reassessing the 2006 Guerrero Slow Slip Event, Mexico: implications for large earthquakes in the Guerrero Gap, *J. Geophys. Res.*, *120*, doi:[10.1002/2014JB011557](https://doi.org/10.1002/2014JB011557). 1.5
- Berardino, P., G. Fornaro, R. Lanari, and E. Sansosti (2002), A New Algorithm for Surface Deformation Monitoring Based on Small Baseline Differential SAR Interferograms, *IEEE Transactions on Geoscience and Remote Sensing*, *40*(11). 1.2.1
- Beroza, G. C., and S. Ide (2011), Slow Earthquakes and Nonvolcanic Tremor, *Annual Review of Earth and Planetary Sciences*, *39*(1), 271 – 296, doi:[10.1146/annurev-earth-040809-152531](https://doi.org/10.1146/annurev-earth-040809-152531). 1, 1.1, 1.1
- Biggs, J., T. Wright, Z. Lu, and B. Parsons (2007), Multi-interferogram method for measuring interseismic deformation: Denali Fault, Alaska, *Geophys. J. Int.*, *170*(3), 1165 – 1179, doi:[10.1111/j.1365-246X.2007.03415.x](https://doi.org/10.1111/j.1365-246X.2007.03415.x). 1.2.1
- Brodsky, E., and J. Mori (2007), Creep events slip less than ordinary earthquakes, *Geophys. Res. Lett.*, *34*(16), doi:[10.1029/2007GL030917](https://doi.org/10.1029/2007GL030917). 1.1.3

- Brooks, B. A., J. H. Foster, M. Bevis, L. N. Frazer, C. J. Wolfe, and M. Behn (2006), Periodic slow earthquakes on the flank of Kilauea volcano, Hawaii, *Earth and Planetary Science Letters*, *246*(3 - 4), 207 - 216, doi:<http://dx.doi.org/10.1016/j.epsl.2006.03.035>. 1.1
- Brown, L. G. (1992), A Survey of Image Registration Techniques, *ACM Computing Surveys*, *24*, 325 - 376. 1.2
- Brudzinski, M., E. Cabral-Cano, F. Correa-Mora, C. DeMets, and B. Márquez-Azúa (2007), Slow slip transients along the Oaxaca subduction segment from 1993 to 2007, *Geophys. J. Int.*, *171*(2), 523 - 538, doi:[10.1111/j.1365-246X.2007.03542.x](https://doi.org/10.1111/j.1365-246X.2007.03542.x). 1
- Cavalié, O., C. Lasserre, M.-P. Doin, G. Peltzer, J. Sun, X. Xu, and Z.-K. Shen (2008), Measurement of interseismic strain across the Haiyuan fault (Gansu, China), by InSAR, *Earth and Planetary Science Letters*, *275*(34), 246 - 257, doi:<http://dx.doi.org/10.1016/j.epsl.2008.07.057>. 1.2.2
- Cavalié, O., E. Pathier, M. Radiguet, M. Vergnolle, N. Cotte, A. Walpersdorf, V. Kostoglodov, and F. Cotton (2013), Slow slip event in the Mexican subduction zone: Evidence of shallower slip in the Guerrero seismic gap for the 2006 event revealed by the joint inversion of InSAR and GPS data, *Earth and Planetary Science Letters*, *367*, doi:[10.1016/j.epsl.2013.02.020](https://doi.org/10.1016/j.epsl.2013.02.020). 1.2, 1.6, 1.3.2
- Cervelli, P., P. Segall, K. Johnson, M. Lisowski, and A. Miklius (2002), Sudden aseismic fault slip on the south flank of Kilauea volcano, *Nature*, *414*(6875), 1014 - 1018, doi:[10.1038/4151014a](https://doi.org/10.1038/4151014a). 1.1
- Chen, T., and R. Clayton (2012), Structure of central and southern Mexico from velocity and attenuation tomography, *J. Geophys. Res.*, *117*(B9), doi:[10.1029/2012JB009233](https://doi.org/10.1029/2012JB009233). 1.3.1
- Colella, H. V., J. H. Dieterich, and K. Richards-Dinger (2013), Spatial and temporal patterns of simulated slow slip events on the Cascadia megathrust, *Geophys. Res. Lett.*, *40*(19), 5101 - 5107, doi:[10.1002/grl.50984](https://doi.org/10.1002/grl.50984). 1.3.3
- Correa-Mora, F., C. DeMets, E. Cabral-Cano, O. Diaz-Molina, and B. Marques-Azua (2009), Transient deformation in southern Mexico in 2006 and 2007: Evidence for distinct deep-slip patches beneath Guerrero and Oaxaca, *Geochem. Geophys. Geosyst.*, *10*(2), doi:[10.1029/2008GC002211](https://doi.org/10.1029/2008GC002211). 1.3.2
- Cotte, N., A. Walpersdorf, V. Kostoglodov, M. Vergnolle, J.-A. Santiago, and M. Campillo (2009), Anticipating the next large silent earthquake in Mexico, *Eos, Transactions American Geophysical Union*, *90*(21), 181 - 182, doi:[10.1029/2009EO210002](https://doi.org/10.1029/2009EO210002). 1.3.2
- Davis, J., T. Herring, I. Shapiro, A. Rogers, and G. Elgered (1985), Geodesy by radio interferometry: Effects of atmospheric modeling errors on estimates of baseline length, *Radio Science*, *20*(6), 1593 - 1607, doi:[10.1029/RS020i006p01593](https://doi.org/10.1029/RS020i006p01593). 1.2.2
- DeMets, C., R. Gordon, and D. Argus (2010), Geologically current plate motions, *Geophys. J. Int.*, *181*(1), 1 - 80, doi:[10.1111/j.1365-246X.2009.04491.x](https://doi.org/10.1111/j.1365-246X.2009.04491.x). 1.3, 1.6
- Dixon, T. H., Y. Jiang, R. Malservisi, R. McCaffrey, N. Voss, M. Protti, and V. Gonzalez (2014), Earthquake and tsunami forecasts: Relation of slow slip events to subsequent earthquake rupture, *Proceedings of the National Academy of Sciences*, *111*(48), 17,039 - 17,044, doi:[10.1073/pnas.1412299111](https://doi.org/10.1073/pnas.1412299111). 1.1, 1.1.1
- Doin, M., C. Lasserre, G. Peltzer, O. Cavalié, and C. Doubre (2009), Corrections of stratified tropospheric delays in SAR interferometry: Validation with global atmospheric models, *Journal of Applied Geophysics*, *69*(1), 35 - 50, doi:[10.1016/j.jappgeo.2009.03.010](https://doi.org/10.1016/j.jappgeo.2009.03.010). 1.2.2

- Doin, M.-P., C. Twardzik, G. Ducret, C. Lasserre, S. Guillaso, and S. Jianbao (2015), InSAR measurement of the deformation around Siling Co Lake: Inferences on the lower crust viscosity in central Tibet, *J. Geophys. Res.*, *120*(7), 5290 – 5310, doi:[10.1002/2014JB011768](https://doi.org/10.1002/2014JB011768). 1.2.2
- Douglas, A., J. Beavan, L. Wallace, and J. Townend (2005), Slow slip on the northern Hikurangi subduction interface, New Zealand, *Geophys. Res. Lett.*, *32*(16), doi:[10.1029/2005GL023607](https://doi.org/10.1029/2005GL023607). 1.1
- Dragert, H., K. Wang, and T. James (2001), A Silent Slip Event on the Deeper Cascadia Subduction Interface, *science*, *292*(5521), 1525 – 1528, doi:[10.1126/science.1060152](https://doi.org/10.1126/science.1060152). 1, 1.1, 1.1.2, 1.3
- Dragert, H., K. Wang, and G. Rogers (2004), Geodetic and seismic signatures of episodic tremor and slip in the northern Cascadia subduction zone, *Earth, Planets and Space*, *56*(12), 1143 – 1150, doi:[10.1186/BF03353333](https://doi.org/10.1186/BF03353333). 1.1.1
- Elliott, J., J. Biggs, B. Parsons, and T. Wright (2008), InSAR slip rate determination on the Altyn Tagh Fault, northern Tibet, in the presence of topographically correlated atmospheric delays, *Geophys. Res. Lett.*, *35*(12), doi:[10.1029/2008GL033659](https://doi.org/10.1029/2008GL033659). 1.2.2, 1.2.2
- Farr, T., P. Rosen, E. Caro, R. Crippen, R. Duren, S. Hensley, M. Kobrick, M. Paller, E. Rodriguez, L. Roth, D. Seal, S. Shaffer, J. Shimada, J. Umland, M. Werner, M. Oskin, D. Burbank, and D. Alsdorf (2007), The Shuttle Radar Topography Mission, *Reviews of Geophysics*, *45*(2), doi:[10.1029/2005RG000183](https://doi.org/10.1029/2005RG000183). 1.2
- Ferrari, L. (2004), Slab detachment control on mafic volcanic pulse and mantle heterogeneity in central Mexico, *Geology*, *32*(1), 77 – 80, doi:[10.1130/G19887.1](https://doi.org/10.1130/G19887.1). 1.3.1
- Frank, W., N. Shapiro, A. Husker, M. Campillo, J. Payero, and G. Prieto (2013), Low-frequency earthquakes in the Mexican sweet spot, *Geophys. Res. Lett.*, *40*, 2661 – 2666, doi:[10.1002/grl.50561](https://doi.org/10.1002/grl.50561). 1.3.3
- Frank, W., N. Shapiro, A. Husker, V. Kostoglodov, A. Romanenko, and M. Campillo (2014), Using systematically characterized low-frequency earthquakes as a fault probe in Guerrero, Mexico, *J. Geophys. Res.*, *119*, 7686 – 7700, doi:[10.1002/2014JB011457](https://doi.org/10.1002/2014JB011457). 1.3.3
- Frank, W., N. Shapiro, A. Husker, V. Kostoglodov, H. Bhat, and M. Campillo (2015a), Along-fault pore-pressure evolution during a slow-slip event in Guerrero, Mexico, *Earth and Planetary Science Letters*, *413*, 135 – 143, doi:[10.1016/j.epsl.2014.12.051](https://doi.org/10.1016/j.epsl.2014.12.051). 1.1.2, 1.3.3
- Frank, W. B., M. Radiguet, B. Rousset, N. M. Shapiro, A. L. Husker, V. Kostoglodov, N. Cotte, and M. Campillo (2015b), Uncovering the geodetic signature of silent slip through repeating earthquakes, *Geophys. Res. Lett.*, *42*(8), 2774 – 2779, doi:[10.1002/2015GL063685](https://doi.org/10.1002/2015GL063685). 1.1, 1.1, 1.1.3, 1.6, 1.3.2, 1.3.3
- Fu, Y., and J. T. Freymueller (2013), Repeated large Slow Slip Events at the southcentral Alaska subduction zone, *Earth and Planetary Science Letters*, *375*, 303 – 311, doi:[10.1016/j.epsl.2013.05.049](https://doi.org/10.1016/j.epsl.2013.05.049). 1.1
- Furumoto, M., and I. Nakanishi (1983), Source times and scaling relations of large earthquakes, *J. Geophys. Res.*, *88*(B3), 2191 – 2198, doi:[10.1029/JB088iB03p02191](https://doi.org/10.1029/JB088iB03p02191). 1.1.3
- Gabriel, A., and R. Goldstein (1988), Crossed orbit interferometry: theory and experimental results from SIR-B, *International Journal of Remote Sensing*, *9*(5), 857 – 872, doi:[10.1080/01431168808954901](https://doi.org/10.1080/01431168808954901). 1.2

- Gao, H., D. Schmidt, and R. Weldon (2012), Scaling Relationships of Source Parameters for Slow Slip Events, *Bulletin of the Seismological Society of America*, *102*(1), 352 – 360, doi:[10.1785/0120110096](https://doi.org/10.1785/0120110096). 1.1.3, 1.2
- Graham, S. E., C. DeMets, E. Cabral-Cano, V. Kostoglodov, A. Walpersdorf, N. Cotte, M. Brudzinski, R. McCaffrey, and L. Salazar-Tlaczani (2014), GPS constraints on the 2011/2012 Oaxaca slow slip event that preceded the 2012 March 20 Ometepepec earthquake, southern Mexico, *Geophys. J. Int.*, *197*(3), 1593–1607, doi:[10.1093/gji/ggu019](https://doi.org/10.1093/gji/ggu019). 1.1.1
- Grandin, R., M.-P. Doin, L. Bollinger, B. Pinel-Puysségur, G. Ducret, R. Jolivet, and S. N. Sapkota (2012), Long-term growth of the Himalaya inferred from interseismic InSAR measurement, *Geology*, *40*(12), 1059–1062, doi:[10.1130/G33154.1](https://doi.org/10.1130/G33154.1). 1.2.2
- Hanssen, R. F. (2001), Remote Sensing and Digital Image Processing, in *Radar Interferometry: Data interpretation and error analysis, Earth and Environmental Science*, vol. 2, edited by F. van der Meer, Kluwer Academic Publishers, Dordrecht, The Netherlands. 1.2, 1.2.2, 1.2.2, 1.2.2, 1.2.2, 1.2.3
- Hawthorne, J. C., and A. M. Rubin (2013), Tidal modulation and back-propagating fronts in slow slip events simulated with a velocity-weakening to velocity-strengthening friction law, *J. Geophys. Res.*, *118*(3), 1216 – 1239, doi:[10.1002/jgrb.50107](https://doi.org/10.1002/jgrb.50107). 1.1.3
- Hirose, H., K. Hirahara, F. Kimata, N. Fujii, and S. Miyazaki (1999), A slow thrust slip event following the two 1996 Hyuganada earthquakes beneath the Bungo Channel, southwest Japan, *J. Geophys. Res.*, *26*(21), 3237 – 3240, doi:[10.1029/1999GL010999](https://doi.org/10.1029/1999GL010999). 1, 1.1, 1.3
- Hooper, A. (2008), A multi-temporal InSAR method incorporating both persistent scatterer and small baseline approaches, *Geophys. Res. Lett.*, *35*(16), doi:[10.1029/2008GL034654](https://doi.org/10.1029/2008GL034654). 1.2.1, 1.2.1
- Hooper, A., H. Zebker, P. Segall, and B. Kampes (2004), A new method for measuring deformation on volcanoes and other natural terrains using InSAR persistent scatterers, *Geophys. Res. Lett.*, *31*(23), doi:[10.1029/2004GL021737](https://doi.org/10.1029/2004GL021737). 1.2.1, 1.2.1
- Hooper, A., P. Segall, and H. Zebker (2007), Persistent scatterer interferometric synthetic aperture radar for crustal deformation analysis, with application to Volcán Alcedo, Galápagos, *J. Geophys. Res.*, *112*(B7), doi:[10.1029/2006JB004763](https://doi.org/10.1029/2006JB004763). 1.3, 1.2.1
- Hooper, A., D. Bekaert, K. Spaans, and M. Arikani (2012), Recent advances in SAR interferometry time series analysis for measuring crustal deformation, *Tectonophysics*, *514*517, 1 – 13, doi:<http://dx.doi.org/10.1016/j.tecto.2011.10.013>. 1, 1.2, 1.2.1, 1.2.2, 1.3.2
- Husker, A., V. Kostoglodov, V. Cruz-Atienza, D. Legrand, N. Shapiro, J. Payero, M. Campillo, and E. Huesca-Pérez (2012), Temporal variations of non-volcanic tremor (NVT) locations in the Mexican subduction zone: Finding the NVT sweet spot, *Geochem. Geophys. Geosyst.*, *13*(3), Q03011, doi:[10.1029/2011GC003916](https://doi.org/10.1029/2011GC003916). 1.3.3
- Ide, S., G. Beroza, D. Shelly, and T. Uchide (2007), A scaling law for slow earthquakes, *Nature*, *447*, 76 – 79, doi:[10.1038/nature05780](https://doi.org/10.1038/nature05780). 1.1.3
- Iglesias, A., S. Singh, A. Lowry, M. Santoyo, V. Kostoglodov, K. Larson, S. Franco-Sánchez, and T. Mikumo (2004), The silent earthquake of 2002 in the Guerrero seismic gap, Mexico (Mw = 7.6): inversion of slip on the plate interface and some implications, *Geofísica Internacional*, *43*(3), 309 – 317. 1.3.2
- Ito, Y., R. Hino, M. Kido, H. Fujimoto, Y. Osada, D. Inazu, Y. Ohta, T. Iinuma, M. Ohzono, S. Miura, M. Mishina, K. Suzuki, T. Tsuji, and J. Ashi (2013), Episodic slow slip events in the Japan subduction zone before the 2011 Tohoku-Oki earthquake, *Tectonophysics*, *600*, 14 – 26, doi:[10.1016/j.tecto.2012.08.022](https://doi.org/10.1016/j.tecto.2012.08.022). 1.1, 1.1.1

- Jiang, Y., S. Wdowinski, T. H. Dixon, M. Hackl, M. Protti, and V. Gonzalez (2012), Slow slip events in Costa Rica detected by continuous GPS observations, 20022011, *Geochem. Geophys. Geosyst.*, *13*(4), doi:[10.1029/2012GC004058](https://doi.org/10.1029/2012GC004058). 1.1
- Jödicke, H., A. Jording, L. Ferrari, J. Arzate, K. Mezger, and L. Rüpke (2006), Fluid release from the subducted Cocos plate and partial melting of the crust deduced from magnetotelluric studies in southern Mexico: Implications for the generation of volcanism and subduction dynamics, *J. Geophys. Res.*, *111*(B8), doi:[10.1029/2005JB003739](https://doi.org/10.1029/2005JB003739). 1.1.2, 1.3.3
- Jolivet, R., R. Grandin, C. Lasserre, M. Doin, and G. Peltzer (2011), Systematic InSAR tropospheric phase delay corrections from global meteorological reanalysis data, *Geophys. Res. Lett.*, *38*(17), doi:[10.1029/2011GL048757](https://doi.org/10.1029/2011GL048757). 1.2.2
- Jolivet, R., P. S. Agram, N. Lin, M. Simons, M. Doin, G. Peltzer, and Z. Li (2014), Improving InSAR geodesy using Global Atmospheric Models, *J. Geophys. Res.*, *119*(3), 23242341, doi:[10.1002/2013JB010588](https://doi.org/10.1002/2013JB010588). 1.2.2
- Julian, B. (2002), Seismological Detection of Slab Metamorphism, *science*, *296*(5573), 1625 – 1626, doi:[10.1126/science.1072602](https://doi.org/10.1126/science.1072602). 1.1.2
- Jung, H.-S., and W.-J. Lee (2015), An Improvement of Ionospheric Phase Correction by Multiple-Aperture Interferometry, *Geoscience and Remote Sensing, IEEE Transactions on*, *53*(9), 4952 – 4960, doi:[10.1109/TGRS.2015.2413948](https://doi.org/10.1109/TGRS.2015.2413948). 1.2.3
- Jung, H.-S., D.-T. Lee, Z. Lu, and J.-S. Won (2013), Ionospheric Correction of SAR Interferograms by Multiple-Aperture Interferometry, *Geoscience and Remote Sensing, IEEE Transactions on*, *51*(5), 3191 – 3199, doi:[10.1109/TGRS.2012.2218660](https://doi.org/10.1109/TGRS.2012.2218660). 1.2.3
- Kampes, B., R. Hanssen, and Z. Perski (2003), Radar interferometry with public domain tools, *Proceedings Fringe 2003*, p. 6. 1.2
- Kao, H., S.-J. Shan, H. Dragert, G. Rogers, J. F. Cassidy, and K. Ramachandran (2005), A wide depth distribution of seismic tremors along the northern Cascadia margin, *Nature*, *436*(7052), 841 – 844, doi:[10.1038/nature03903](https://doi.org/10.1038/nature03903). 1.1
- Katayama, I., T. Terada, K. Okazaki, and W. Tanikawa (2012), Episodic tremor and slow slip potentially linked to permeability contrasts at the Moho, *Nature Geoscience*, *5*(10), 731 – 734, doi:[10.1038/NNGEO1559](https://doi.org/10.1038/NNGEO1559). 1.1.2
- Kim, Y., R. Clayton, and J. Jackson (2010), Geometry and seismic properties of the subducting Cocos plate in central Mexico, *J. Geophys. Res.*, *115*(B6), doi:[10.1029/2009JB006942](https://doi.org/10.1029/2009JB006942). 1.1.2, 1.6, 1.3.1, 1.3.3
- Kim, Y., R. W. Clayton, P. D. Asimow, and J. M. Jackson (2013), Generation of talc in the mantle wedge and its role in subduction dynamics in central Mexico, *Earth and Planetary Science Letters*, *384*, 81 – 87, doi:<http://dx.doi.org/10.1016/j.epsl.2013.10.006>. 1.3.3
- Kostoglodov, V., W. Bandy, J. Domínguez, and M. Mena (1996), Gravity and seismicity over the Guerrero seismic gap, Mexico, *Geophys. Res. Lett.*, *23*(23), 3385 – 3388, doi:[10.1029/96GL03159](https://doi.org/10.1029/96GL03159). 1.3
- Kostoglodov, V., R. Valenzuela, A. Gorbato, J. Mimiaga, S. Franco, J. Alvarado, and R. Peláez (2001), Deformation in the Guerrero seismic gap, Mexico, from leveling observations, *Journal of Geodesy*, *75*(1), 19 – 32, doi:[10.1007/s001900000144](https://doi.org/10.1007/s001900000144). 1.3, 1.3
- Kostoglodov, V., S. Singh, J. Santiago, S. Franco, K. Larson, A. Lowry, and R. Bilham (2003), A large silent earthquake in the Guerrero seismic gap, Mexico, *Geophys. Res. Lett.*, *30*(15), doi:[10.1029/2003GL017219](https://doi.org/10.1029/2003GL017219). 1.1, 1.3, 1.6, 1.3.2

- Lanari, R., O. Mora, M. Manunta, J. Mallorqui, P. Berardino, and E. Sansosti (2004), A small-baseline approach for investigating deformations on full-resolution differential SAR interferograms, *Geoscience and Remote Sensing, IEEE Transactions on*, 42(7), 1377 – 1386, doi:[10.1109/TGRS.2004.828196](https://doi.org/10.1109/TGRS.2004.828196). 1.2.1
- Larson, K., A. Lowry, V. Kostoglodov, W. Hutton, O. Sánchez, K. Hudnut, and G. Suárez (2004), Crustal deformation measurements in Guerrero, Mexico, *J. Geophys. Res.*, 109(B4), doi:[10.1029/2003JB002843](https://doi.org/10.1029/2003JB002843). 1.3, 1.3.2
- Larson, K. M., V. Kostoglodov, S. Miyazaki, and J. Santiago (2007), The 2006 aseismic slow slip event in Guerrero, Mexico: New results from GPS, *Geophys. Res. Lett.*, 34(13), doi:[10.1029/2007GL029912](https://doi.org/10.1029/2007GL029912). 1.1, 1.1.1, 1.3.2
- Li, Z., J. Muller, P. Cross, and E. Fielding (2005), Interferometric synthetic aperture radar (InSAR) atmospheric correction: GPS, Moderate Resolution Imaging Spectroradiometer (MODIS), and InSAR integration, *J. Geophys. Res.*, 110(B3), doi:[10.1029/2004JB003446](https://doi.org/10.1029/2004JB003446). 1.2.2
- Li, Z., J. Muller, P. Cross, P. Albert, J. Fischer, and R. Bennartz (2006), Assessment of the potential of MERIS near infrared water vapour products to correct ASAR interferometric measurements, *International Journal of Remote Sensing*, 27(2), 349 – 365, doi:[10.1080/01431160500307342](https://doi.org/10.1080/01431160500307342). 1.2.2
- Li, Z., E. Fielding, P. Cross, and R. Preusker (2009a), Advanced InSAR atmospheric correction: MERIS/MODIS combination and stacked water vapour models, *International Journal of Remote Sensing*, 30(13), 3343 – 3363, doi:[10.1080/01431160802562172](https://doi.org/10.1080/01431160802562172). 1.2.2
- Li, Z., E. Fielding, and P. Cross (2009b), Integration of InSAR Time-Series Analysis and Water-Vapor Correction for Mapping Postseismic Motion After the 2003 Bam (Iran) Earthquake, *IEEE Transactions on Geoscience and Remote Sensing*, 47(9), 3220 – 3230, doi:[10.1109/TGRS.2009.2019125](https://doi.org/10.1109/TGRS.2009.2019125). 1.2.2
- Lin, Y., M. Simons, E. Hetland, P. Muse, and C. DiCaprio (2010), A multiscale approach to estimating topographically correlated propagation delays in radar interferograms, *Geochem. Geophys. Geosyst.*, 11(9). 1.2.2
- Linde, A. T., M. T. Gladwin, M. J. S. Johnston, R. L. Gwyther, and R. G. Bilham (1996), A slow earthquake sequence on the San Andreas fault, *Nature*, 383(6595), 65 – 68, doi:[10.1038/383065a0](https://doi.org/10.1038/383065a0). 1.1
- Liu, S., R. Hanssen, and A. Mika (2009), On the value of high-resolution weather models for atmospheric mitigation in sar interferometry, in *Geoscience and Remote Sensing Symposium, 2009 IEEE International, IGARSS 2009*, vol. 2, pp. II-749 – II-752, doi:[10.1109/IGARSS.2009.5418199](https://doi.org/10.1109/IGARSS.2009.5418199). 1.2.2
- Liu, Y., and J. Rice (2007), Spontaneous and triggered aseismic deformation transients in a subduction fault model, *J. Geophys. Res.*, 112(B9), doi:[10.1029/2007JB004930](https://doi.org/10.1029/2007JB004930). 1.1.2, 1.1.3
- Lowry, A., K. Larson, V. Kostoglodov, and R. Bilham (2001), Transient fault slip in Guerrero, southern Mexico, *J. Geophys. Res.*, 28(19), 3753 – 3756, doi:[10.1029/2001GL013238](https://doi.org/10.1029/2001GL013238). 1.1, 1.3, 1.3.2
- MASE (2007), Meso america subduction experiment, Caltech, Dataset, doi:[10.7909/C3RN35SP](https://doi.org/10.7909/C3RN35SP). 1.1, 1.3.3
- Meade, B., and J. Loveless (2009), Predicting the geodetic signature of MW > 8 slow slip events, *Geophys. Res. Lett.*, 36(1), doi:[10.1029/2008GL036364](https://doi.org/10.1029/2008GL036364). 1.1.3
- Melgar, D., and X. Pérez-Campos (2011), Imaging the moho and subducted oceanic crust at the isthmus of tehuantepec, mexico, from receiver functions, *Pure and Applied Geophysics*, 168(8-9), 1449 – 1460, doi:[10.1007/s00024-010-0199-5](https://doi.org/10.1007/s00024-010-0199-5). 1.6

- Meyer, F., R. Bamler, N. Jakowski, and T. Fritz (2006), The Potential of Low-Frequency SAR Systems for Mapping Ionospheric TEC Distributions, *Geoscience and Remote Sensing Letters, IEEE*, 3(4), 560 – 564, doi:[10.1109/LGRS.2006.882148](https://doi.org/10.1109/LGRS.2006.882148). 1.2.3
- Misra, P., and P. Enge (2010), *Global Positioning System: Signals, Measurements and Performance*, revised second edition ed., Lincoln, MA: Ganga-Jamuna Press. 1.2.3
- Obara, K. (2002), Nonvolcanic Deep Tremor Associated with Subduction in Southwest Japan, *Science*, 296(5573), 1679–1681, doi:[10.1126/science.1070378](https://doi.org/10.1126/science.1070378). 1.1
- Obara, K. (2010), Phenomenology of deep slow earthquake family in southwest Japan: Spatiotemporal characteristics and segmentation, *J. Geophys. Res.*, 115(B00A25), doi:[10.1029/2008JB006048](https://doi.org/10.1029/2008JB006048). 1.1.3
- Obara, K., H. Hirose, F. Yamamizu, and K. Kasahara (2004), Episodic slow slip events accompanied by non-volcanic tremors in southwest Japan subduction zone, *Geophys. Res. Lett.*, 31(23), doi:[10.1029/2004GL020848](https://doi.org/10.1029/2004GL020848). 1.1
- Onn, F., and H. Zebker (2006), Correction for interferometric synthetic aperture radar at-mospheric phase artifacts using time series of zenith wet delay observations from a GPS network, *J. Geophys. Res.*, 111(B9), doi:[10.1029/2005JB004012](https://doi.org/10.1029/2005JB004012). 1.2.2
- Ortiz, M., S. Singh, V. Kostoglodov, and J. Pacheco (2000), Source areas of the Acapulco-San Marcos, Mexico earthquakes of 1962 (M 7.1; 7.0) and 1957 (M 7.7), as constrained by tsunami and uplift records, *Geofísica Internacional*, 39(4), 337 – 348. 1.3
- Ozawa, S., H. Suito, and M. Tobita (2007), Occurrence of quasi-periodic slow-slip off the east coast of the Boso peninsula, Central Japan, *Earth, Planets and Space*, 59(12), 1241 – 1245, doi:[10.1186/BF03352072](https://doi.org/10.1186/BF03352072). 1.1.1
- Pardo, M., and G. Suárez (1995), Shape of the subducted Rivera and Cocos Plates in southern Mexico: Seismic and tectonic implications, *J. Geophys. Res.*, 100(B7), 12,357 – 12,373, doi:[10.1029/95JB00919](https://doi.org/10.1029/95JB00919). 1.6, 1.3.1
- Peng, Z., and J. Gombert (2010), An integrated perspective of the continuum between earthquakes and slow-slip phenomena, *Nature Geoscience*, 3(9), 599 – 607, doi:[10.1038/ngeo940](https://doi.org/10.1038/ngeo940). 1.1.3
- Pérez-Campos, X., and R. W. Clayton (2014), Interaction of cocos and rivera plates with the upper-mantle transition zone underneath central mexico, *Geophys. J. Int.*, 197(3), 1763 – 1769, doi:[10.1093/gji/ggu087](https://doi.org/10.1093/gji/ggu087). 1.6
- Pérez-Campos, X., Y. Kim, A. Husker, P. Davis, R. Clayton, A. Iglesias, J. Pacheco, S. Singh, V. Manea, and M. Gurnis (2008), Horizontal subduction and truncation of the Cocos Plate beneath central Mexico, *Geophys. Res. Lett.*, 35(18), doi:[10.1029/2008GL035127](https://doi.org/10.1029/2008GL035127). 1.3.1
- Perissin, D., and A. Ferretti (2007), Urban-Target Recognition by Means of Repeated Spaceborne SAR Images, *Geoscience and Remote Sensing, IEEE Transactions on*, 45(12), 4043 – 4058, doi:[10.1109/TGRS.2007.906092](https://doi.org/10.1109/TGRS.2007.906092). 1.2.1
- Puysségur, B., R. Michel, and J. Avouac (2007), Tropospheric phase delay in interferometric synthetic aperture radar estimated from meteorological model and multi-spectral imagery, *J. Geophys. Res.*, 112(B5), doi:[10.1029/2006JB004352](https://doi.org/10.1029/2006JB004352). 1.2.2
- Radiguet, M., F. Cotton, M. Vergnolle, M. Campillo, B. Valette, V. Kostoglodov, and N. Cotte (2011), Spatial and temporal evolution of a long term slow slip event: the 2006 Guerrero Slow Slip Event, *Geophys. J. Int.*, 184(2), 816 – 828, doi:[10.1111/j.1365-246X.2010.04866.x](https://doi.org/10.1111/j.1365-246X.2010.04866.x). 1.1.1, 1.6, 1.3.2

- Radiguet, M., F. Cotton, M. Vergnolle, M. Campillo, A. Walpersdorf, N. Cotte, and V. Kostoglodov (2012), Slow slip events and strain accumulation in the Guerrero gap, Mexico, *J. Geophys. Res.*, *117*(B4), doi:[10.1029/2011JB008801](https://doi.org/10.1029/2011JB008801). [1.1.1](#), [1.6](#), [1.3.2](#)
- Rogers, G., and H. Dragert (2003), Episodic Tremor and Slip on the Cascadia Subduction Zone : The Chatter of Silent Slip, *Science*, *300*(5627), 1942 – 1943, doi:[10.1126/science.1084783](https://doi.org/10.1126/science.1084783). [1.1](#)
- Rosen, P., S. Henley, G. Peltzer, and M. Simons (2004), Updated Repeat Orbit Interferometry Package Released, *Eos Trans. AGU*, *85*(5), 47 – 47, doi:[10.1029/2004EO050004](https://doi.org/10.1029/2004EO050004). [1.2](#)
- Rosen, P., S. Hensley, and C. Chen (2010), Measurement and mitigation of the ionosphere in L-band Interferometric SAR data, in *Radar Conference, 2010 IEEE*, pp. 1459 – 1463, doi:[10.1109/RADAR.2010.5494385](https://doi.org/10.1109/RADAR.2010.5494385). [1.2.3](#)
- Schwartz, S., and J. Rokosky (2007), Slow slip events and seismic tremor at circum-pacific subduction zones, *Review of Geophysics*, *45*(3), doi:[10.1029/2006RG000208](https://doi.org/10.1029/2006RG000208). [1.1](#), [1.1.3](#)
- Segall, P. (2010), *Earthquake and Volcano Deformation*, Princeton University Press. [1](#), [1.1.2](#)
- Segall, P., A. M. Rubin, A. M. Bradley, and J. R. Rice (2010), Dilatant strengthening as a mechanism for slow slip events, *J. Geophys. Res.*, *115*(B12), doi:[10.1029/2010JB007449](https://doi.org/10.1029/2010JB007449). [1.1.2](#), [1.1.3](#)
- Shelly, D., G. Beroza, S. Ide, and S. Nakamura (2006), Low-frequency earthquakes in Shikoku, Japan, and their relationship to episodic tremor and slip, *Nature*, *442*(7099), 188 – 191, doi:[10.1038/nature04931](https://doi.org/10.1038/nature04931). [1.1](#)
- Singh, S. K., and F. Mortera (1991), Source Time Functions of Large Mexican Subduction Earthquakes, Morphology of the Benioff Zone, Age of the Plate, and Their Tectonic Implications, *J. Geophys. Res.*, *96*(B13), 21,487 – 21,502, doi:[10.1029/91JB02047](https://doi.org/10.1029/91JB02047). [1.3](#)
- Singh, S. K., and M. Pardo (1993), Geometry of the Benioff Zone and state of stress in the overriding plate in central Mexico, *Geophys. Res. Lett.*, *20*(14), 1483 – 1486, doi:[10.1029/93GL01310](https://doi.org/10.1029/93GL01310). [1.3.1](#)
- Smith, E., and S. Weintraub (1953), The Constants in the Equation for Atmospheric Refractive Index at Radio Frequencies, *Proceeding of the IRE*, *41*(8), 1035 – 1037, doi:[10.1109/JRPROC.1953.274297](https://doi.org/10.1109/JRPROC.1953.274297). [1.2.2](#), [1.2.2](#)
- Snoeiij, P., N. van der Valk, E. Boom, and D. Hoekman (2001), Effect of the ionosphere on P-band spaceborne SAR images, in *Geoscience and Remote Sensing Symposium, 2001. IGARSS '01. IEEE 2001 International*, vol. 1, pp. 132 – 134, doi:[10.1109/IGARSS.2001.976080](https://doi.org/10.1109/IGARSS.2001.976080). [1.2.3](#)
- Song, T., D. Helmberger, M. Brudzinski, R. Clayton, P. Davis, X. Peérez-Campos, and S. Singh (2009), Subducting Slab Ultra-Slow Velocity Layer Coincident with Silent Earthquakes in Southern Mexico, *Science*, *324*(5926), 502 – 506, doi:[10.1126/science.1167595](https://doi.org/10.1126/science.1167595). [1.1.2](#), [1.3.3](#)
- Thayer, G. (1974), An improved equation for the radio refractive index of air, *Radio Science*, *9*(10), 803 – 807, doi:[10.1029/RS009i010p00803](https://doi.org/10.1029/RS009i010p00803). [1.2.2](#), [1.2.2](#)
- Tsang, L. L. H., A. J. Meltzner, B. Philiposian, E. M. Hill, J. T. Freymueller, and K. Sieh (2015), A 15 year slow-slip event on the sunda megathrust offshore sumatra, *Geophys. Res. Lett.*, doi:[10.1002/2015GL064928](https://doi.org/10.1002/2015GL064928), 2015GL064928. [1.1](#)
- Tse, S. T., and J. R. Rice (1986), Crustal earthquake instability in relation to the depth variation of frictional slip properties, *J. Geophys. Res.*, *91*(B9), 9452 – 9472, doi:[10.1029/JB091iB09p09452](https://doi.org/10.1029/JB091iB09p09452). [1.1.3](#)

- Vergnolle, M., A. Walpersdorf, V. Kostoglodov, P. Tregoning, J. Santiago, N. Cotte, and S. Franco (2010), Slow slip events in Mexico revised from the processing of 11-year GPS observations, *J. Geophys. Res.*, *115*(B8), doi:[10.1029/2009JB006852](https://doi.org/10.1029/2009JB006852). [1.1](#), [1.6](#), [1.3.2](#)
- Wadge, G., P. Webley, I. James, R. Bingley, A. Dodson, S. Waugh, T. Veneboer, G. Puglisi, M. Mattia, D. Baker, S. Edwards, S. Edwards, and P. Clarke (2002), Atmospheric models, GPS and InSAR measurements of the tropospheric water vapour field over Mount Etna, *Geophys. Res. Lett.*, *29*, doi:[10.1029/2002GL015159](https://doi.org/10.1029/2002GL015159). [1.2.2](#)
- Wallace, L. M., and J. Beavan (2006), A large slow slip event on the central Hikurangi subduction interface beneath the Manawatu region, North Island, New Zealand, *Geophys. Res. Lett.*, *33*(11), doi:[10.1029/2006GL026009](https://doi.org/10.1029/2006GL026009). [1.1](#)
- Walpersdorf, A., N. Cotte, V. Kostoglodov, M. Vergnolle, M. Radiguet, J. A. Santiago, and M. Campillo (2011), Two successive slow slip events evidenced in 20092010 by a dense GPS network in Guerrero, Mexico, *Geophys. Res. Lett.*, *38*(15), doi:[10.1029/2011GL048124](https://doi.org/10.1029/2011GL048124). [1.3.2](#)
- Walters, R., B. Parsons, and T. Wright (2014), Constraining crustal velocity fields with InSAR for Eastern Turkey: Limits to the block-like behaviour of Eastern Anatolia, *J. Geophys. Res.*, *119*(6), 5215 – 5234, doi:[10.1002/2013JB010909](https://doi.org/10.1002/2013JB010909). [1.2.2](#)
- Wech, A. G., and K. C. Creager (2011), A continuum of stress, strength and slip in the Cascadia subduction zone, *Nature Geoscience*, *4*(9), 624 – 628, doi:[10.1038/ngeo1215](https://doi.org/10.1038/ngeo1215). [1.1.2](#)
- Wei, M., J. McGuire, and E. Richardson (2012), A slow slip event in the south central Alaska Subduction Zone and related seismicity anomaly, *Geophys. Res. Lett.*, *39*(15), doi:[10.1029/2012GL052351](https://doi.org/10.1029/2012GL052351). [1.1](#)
- Wei, M., Y. Kaneko, Y. Liu, and J. J. McGuire (2013), Episodic fault creep events in California controlled by shallow frictional heterogeneity, *Nature Geoscience*, *6*(7), 566 – 570, doi:[10.1038/ngeo1835](https://doi.org/10.1038/ngeo1835). [1.1](#)
- Wicks, C., D. Dzurisin, S. Ingebritsen, W. Thatcher, Z. Lu, and J. Iverson (2002), Magmatic activity beneath the quiescent Three Sisters volcanic center, central Oregon Cascade Range, USA, *Geophys. Res. Lett.*, *29*(7), 26–1 – 26–4, doi:[10.1029/2001GL014205](https://doi.org/10.1029/2001GL014205). [1.2.2](#)
- Williams, S., Y. Bock, and P. Fang (1998), Integrated satellite interferometry: tropospheric noise, GPS estimates and implications for interferometric synthetic aperture radar products, *J. Geophys. Res.*, *103*(B11), 27,051 – 27,067, doi:[10.1029/98JB02794](https://doi.org/10.1029/98JB02794). [1.2.2](#)
- Zebker, H. (1992), Decorrelation in interferometric radar echoes, *IEEE Transactions on Geoscience and Remote Sensing*, *30*(5), 950 – 959, doi:[10.1109/36.175330](https://doi.org/10.1109/36.175330). [1.2](#)
- Zebker, H., P. Rosen, and S. Hensley (1997), Atmospheric effects in interferometric synthetic aperture radar surface deformation and topographic maps, *J. Geophys. Res.*, *102*(B4), 7547 – 7563, doi:[10.1029/96JB03804](https://doi.org/10.1029/96JB03804). [1.2](#), [1.2.2](#)

Chapter 2

A spatially-variable power-law tropospheric correction technique for InSAR data

D.P.S. Bekaert^{1,2}, A.J. Hooper^{1,2}, and T.J. Wright¹

¹ *COMET, School of Earth and Environment, University of Leeds, United Kingdom*

² *Formerly, Department of Geoscience and Remote Sensing, Delft University of Technology, Delft, The Netherlands*

Abstract

Microwave signals travelling through the troposphere are subject to delays. These delays are mainly described by spatial and temporal variations in pressure, temperature, and relative humidity in the lower part of the troposphere, resulting in a spatially-varying tropospheric signal in interferometric synthetic aperture radar (InSAR). Tropospheric correction techniques rely either on external data, often limited by spatial and temporal accuracy, or can be estimated from the high-resolution interferometric phase itself. However, current phase-estimated correction techniques do not account for the spatial variability of the tropospheric properties and fail to capture tropospheric signals over larger regions. Here we propose and test a novel power-law correction method that accounts for spatial variability in atmospheric properties and can be applied to interferograms containing topographically-correlated deformation. The power-law model has its reference fixed at the relative top of the troposphere and describes, through a power-law relationship, how the phase delay varies with altitude. We find the power-law model reduces tropospheric signals both locally (on average by ~ 0.45 cm for each kilometer of elevation in Mexico) and the long wavelength components, leading to an improved fit to independent GNSS data. The power-law model can be applied in presence of

deformation, over a range of different time-periods and in different atmospheric conditions, and potentially allows for the detection of smaller magnitude crustal deformation signals with InSAR.

2.1 Introduction

Radar signals propagating through the atmosphere are affected by the medium in which they travel, which can result in a phase delay or advance. This is a major limiting factor when using Interferometric Synthetic Aperture Radar (InSAR) (e.g. [Wright et al., 2001](#), [Hooper et al., 2012](#), [Cavalié et al., 2013](#)). A phase delay through the atmosphere can be characterized by the refractivity, N , ([Smith and Weintraub, 1953](#), [Thayer, 1974](#), [Davis et al., 1985](#)), which can be split into a hydrostatic, wet, liquid and ionospheric components. For the troposphere, variations of temperature, pressure, and relative humidity lead to a spatially-varying tropospheric phase delay, which partly correlates with topography. We focus only on the hydrostatic and wet components of the refractivity, N , as ([Hanssen, 2001](#)) the liquid component is expected to be small and will only become significant in case of a saturated atmosphere, and the ionospheric delays are assumed to be small for C-band, leading to:

$$N = \left(k_1 \frac{P}{T} \right)_{hydr} + \left(k'_2 \frac{e}{T} + k_3 \frac{e}{T^2} \right)_{wet}, \quad (2.1)$$

where P indicates total atmospheric pressure, T the temperature and e the partial pressure of water vapour. The coefficients k_1 , k'_2 and k_3 are constants estimated in literature as $k_1 = 77.6 \text{ KhPa}^{-1}$, $k'_2 = 23.3 \text{ KhPa}^{-1}$ and $k_3 = 3.75 \cdot 10^5 \text{ K}^2 \text{hPa}^{-1}$ ([Smith and Weintraub, 1953](#), [Thayer, 1974](#)). The tropospheric phase delay (2-way), ϕ_{tropo} , at a specific height, $h = h_1$, corresponds to the integration of the refractivity between h_1 and the top of the troposphere h_{top} along the radar line-of-sight ([Hanssen, 2001](#)).

$$d_{tropo} = 10^{-6} (\cos\theta)^{-1} \int_{h=h_1}^{h=h_{top}} N(h) dh \quad (2.2)$$

$$\phi_{tropo} = \frac{-4\pi}{\lambda} d_{tropo} \quad (2.3)$$

where d_{tropo} is the tropospheric delay (1-way), θ the incidence angle, λ the radar wavelength, and $-4\pi/\lambda$ a conversion factor to convert from pseudorange increase to phase delay.

Sounding measurements made during ascents of large inflated hydrogen or helium balloons provide a detailed vertical profile of atmospheric properties (e.g. pressure, temperature, relative humidity, and wind speed). How often these balloons are released, the measurement accuracy and sampling, and the maximum height vary strongly depending on location and operator ([Parker et al., 2008](#)). We use balloon sounding data provided

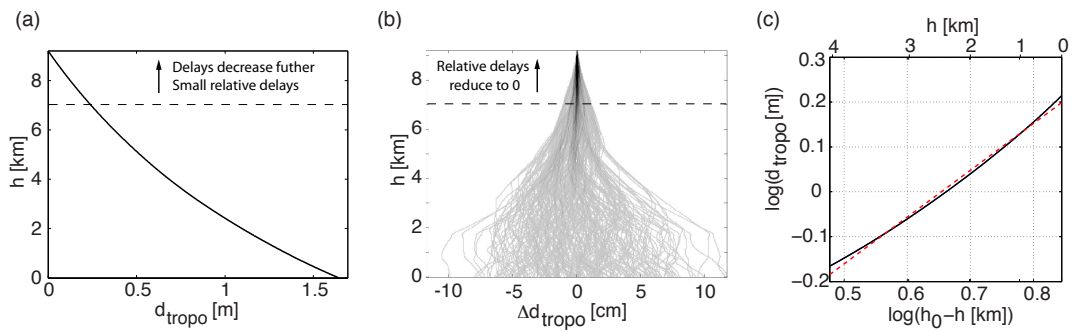


Figure 2.1: (a) Tropospheric delays d_{tropo} computed from balloon sounding data for 24 days (12 UTC) between Jan-Feb 2014. Delays are computed by integrating the refractivity from height h upwards (to 9 km) and projecting to the radar line-of-sight, with the black solid line indicating the mean delay. Only few soundings extend above 9 km. (b) Relative tropospheric delays Δd_{tropo} , showing all (276) possible combinations of the difference between tropospheric delay at two different days. The darker the color, the more the curves overlap, i.e. black all 276 relative delays overlap. Empirically it can be seen that at a specific altitude h_0 the relative delays converge to zero. We set h_0 to the altitude for which the standard deviation of the relative delays is smaller than 0.5 cm. (c) A log-log plot of the mean tropospheric delay d_{tropo} and the topography (h_0-h) for the topographic height range (0-4 km) (black solid line), shows a near-linear behavior, indicating a power-law relationship. The red dashed line shows the best linear fit of the mean tropospheric delay in the log-log domain. All sounding data (Acapulco station) is provided by the department of Atmospheric Science of the University of Wyoming (<http://weather.uwyo.edu/upperair/sounding.html>).

by the University of Wyoming over Acapulco, to calculate refractivity, which when integrated according to equation (2.2) gives the tropospheric delay (Figure 2.1(a)). It can be observed that delays increase at lower altitudes as the signal has travelled further through the troposphere. With an interferogram being the phase difference between two SAR acquisitions, the atmospheric delay depends on the change in refractivity rather than the total refractivity. Figure 2.1(b) shows the relative tropospheric delays, i.e. the difference between all pairs of tropospheric delays shown in Figure 2.1(a), with the darker color indicating more overlapping delay curves. Variations in interferograms in flat regions, are mainly due to the wet component of the refractivity, i.e. the water vapour; the hydrostatic component often appears as a smooth signal due to the large spatial scale of high and low pressure fields (Hanssen, 2001). In regions with significant topography, the hydrostatic component will also cause a correlation between the phase and topography (Elliott et al., 2008).

Different approaches have been documented to estimate the tropospheric signal in InSAR data, e.g. by using weather models (Pinel et al., 2011, Wadge et al., 2002, Walters et al., 2014), GNSS data (Onn and Zebker, 2006, Williams et al., 1998), spectrometer measurements (Li et al., 2006), or by combining weather models and spectrometer data (Walters et al., 2013), or GNSS and spectrometer measurements (Li et al., 2009, Puysségur et al., 2007). While all of these techniques can, under certain conditions, reduce the tropospheric signal, they are often limited by the lower spatial resolution of

the auxiliary data. Alternatively, tropospheric signals can be estimated from the correlation between the interferometric phase and the topography, in a non-deforming area (*Cavalié et al., 2007, Wicks et al., 2002*), or by filtering the InSAR data in space and time (e.g. *Hooper et al., 2012*). The former method assumes a linear relation between the interferometric tropospheric delay and the topography ($\Delta\phi_{tropo} = K_{\Delta\phi}h + \Delta\phi_0$), estimated from data in the non-deforming region. $K_{\Delta\phi}$ is a constant relating the interferometric tropospheric phase to topography, and is used to compute the tropospheric signal throughout the full interferogram. $\Delta\phi_0$ can be neglected as it merely represents a constant shift applied to the whole interferogram.

There are two limitations to this linear height correction technique. Firstly, a non-deforming region is required. To overcome this, *Lin et al. (2010)* developed a multi-scale approach, which also assumes a linear relation, but which can be applied in a deforming region by using a spatial frequency band insensitive to deformation. This method makes use of the fact that the linear relationship holds for all spatial frequencies, but the deformation may only be significant in a certain frequency range. Alternatively, *Elliott et al. (2008)* remove a preliminary estimate of the deformation displacements prior to estimating $K_{\Delta\phi}$. The second limitation follows from the assumption of a single relationship between phase and topography over the whole interferogram, as this does not account for the spatial variation of the tropospheric properties. This can be significant over large areas (>10s of km), especially when the area includes different climatic zones. When applying a linear estimation over multiple small windows, $\Delta\phi_0$ will vary and cannot be neglected. However, $\Delta\phi_0$ is biased by other phase contributions and cannot be estimated from a spatial band insensitive to deformation. An exception may exist for the longest wavelength band, provided it is not contaminated by deformation, but this is not usually the case in areas of tectonic deformation.

In this paper we present a new tropospheric correction technique that can be applied to deforming regions and which allows for a spatially-varying relationship between phase and topography. We apply our power-law methodology to correct the interferograms in a tectonic case study over Mexico, where slow slip deformation is present at the longer spatial wavelengths (~ 150 km), and where the tropospheric signals mask the tectonic signal. The tectonic implications of the results are presented in a companion paper (*Bekaert et al., 2015*).

2.2 Power-law tropospheric correction

Figure 2.2 shows a simplified schematic of the tropospheric delays computed from weather balloon data, shown in Figure 2.1(a) and (b). While the tropospheric delay keeps on decreasing with increasing height, the relative tropospheric variations of the delay curve are important up to a certain altitude h_0 , typically around 7-13 km, after which the relative delays do not differ significantly ($\sigma < 0.5$ cm) and converge to

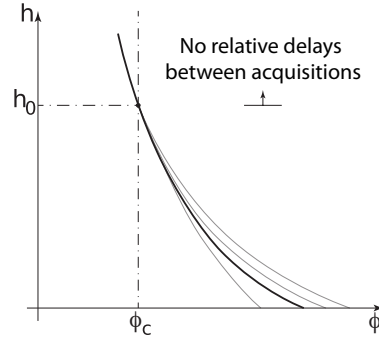


Figure 2.2: Schematic of the tropospheric delay curve. The black line represents the mean delay, while the gray lines show delays at arbitrary times. At h_0 the relative tropospheric delays between different acquisitions converges to zero, while the delay itself continues to decrease with increasing height. This can be observed empirically from the tropospheric delays computed from balloon sounding measurements as shown in Figure 2.1(a) and (b).

zero. Consequently, the interferometric tropospheric phase at this reference height is approximately zero. In other words it is only necessary for the interferometric delays to describe the delay curve up to h_0 , as any delay accumulated at this height ϕ_c will cancel out in the interferometric computation.

By plotting the loglog relationship between the mean tropospheric delay and the topography constrained by the reference height ($h_0 - h$) (black solid line in Figure 2.1(c)), we find the fit to be approximately linear indicating a power-law relationship. We can find the power-law exponent, α , from the slope of this linear fit. We can therefore approximate the tropospheric phase delay ϕ_{tropo} as

$$\phi_{tropo} = K'_\phi (h_0 - h)^\alpha + \phi_c \quad \text{for } h < h_0, \quad (2.4)$$

where ϕ_c is the phase delay at h_0 , α a constant describing the power-law decay estimated from balloon sounding data, and K'_ϕ a coefficient that relates phase to topography and which varies spatially and from acquisition to acquisition. Equation (2.4) is defined for an individual SAR acquisition. The interferometric phase delay, $\Delta\phi_{tropo}$, is the phase difference at the time of the master acquisition ϕ_{tropo}^m and the slave acquisition ϕ_{tropo}^s , results in:

$$\Delta\phi_{tropo} = \phi_{tropo}^m - \phi_{tropo}^s \quad (2.5)$$

So we can rewrite equation (2.4) as,

$$\Delta\phi_{tropo} = K'_{\Delta\phi} (h_0 - h)^\alpha, \quad \text{with } K'_{\Delta\phi} = K'_{\phi_m} - K'_{\phi_s}, \quad \text{and } h < h_0 \quad (2.6)$$

where $K'_{\Delta\phi}$ is a spatially-varying and unknown coefficient, describing the relation between topography and tropospheric phase. Both h_0 and α can be estimated empirically from balloon sounding data or weather model data, and are assumed to be constant for a given area. In time, seasonal and long-term variations can be observed for both

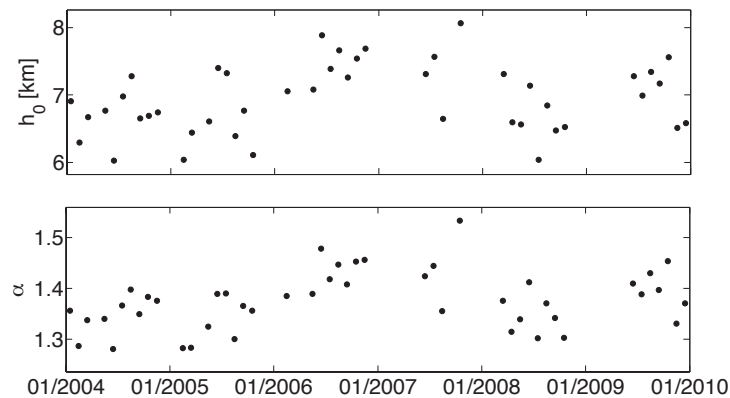


Figure 2.3: Seasonal variation of the reference height h_0 , and the power-law coefficient α . Both coefficients were estimated based on a one month time-window of sounding data. We set h_0 to the altitude for which the standard deviation of the relative delays is smaller than 0.5 cm. All sounding data (Acapulco station) is provided by the department of Atmospheric Science of the University of Wyoming (<http://weather.uwyo.edu/upperair/sounding.html>).

h_0 and α , shown in Figure 2.3 for Acapulco in Mexico. In this study an average over the whole time-period is assumed, alternatively each interferogram can be evaluated using the average h_0 and α for the master and slave acquisition dates. The success of the power-law method is limited to the cases in which the relative delays can be reasonably approximated by a power-law function. From a regional analysis of weather model data for our test region in Mexico (Supplemental Figure A.1), we found that on average $\sim 80\%$ of the relative delay curves can be fit by a power-law function with a correlation coefficient larger than 0.9.

The interferometric phase is a superposition of multiple signals including deformation, tropospheric and ionospheric delays, and errors due to, for example, incorrect orbits and unwrapping errors. Estimating $K'_{\Delta\phi}$ from an interferogram where all these signals are present is not trivial. However, following *Lim et al. (2010)*, we can take advantage of the fact that the tropospheric signal is present at all wavelength scales to estimate $K'_{\Delta\phi}$ from a spatial frequency band relatively insensitive to these other signals. In other words, we can estimate $K'_{\Delta\phi}$ by applying equation (2.6) to band-filtered phase and topography, where the band should be selected such that the contribution from the other signals is negligible. We allow lateral variability by splitting the study area into multiple small windows and estimating $K'_{\Delta\phi}$ locally.

Figure 2.4 shows a step-by-step example of the tropospheric delay estimation for an interferogram over Mexico spanning 31 Dec 2004 - 16 Dec 2005. We used a mean power-law decay, α , of 1.4 and a reference height, h_0 , of 7 km, estimated from sounding data at Acapulco between 2004 and 2010 (<http://weather.uwyo.edu/upperair/sounding.html>), to scale the topography (step 1). We found the mean of h_0 and α estimated at Acapulco to be consistent with estimates of multiple sounding stations at distances up to 1000 km from Acapulco, with h_0 in the range 6.89 ± 0.02 km and α in the range 1.35 ± 0.02 .

This supports our simplification of using a single mean value for h_0 and α over our InSAR region. A 2-8 km bandfilter was chosen to avoid contamination of the tectonic slow slip deformation signal (step 2, Figure 2.4), which from an initial InSAR and GNSS analysis we found to be around 150 km wavelength (*Bekaert et al., 2015*). We estimate $K'_{\Delta\phi}$ locally in approximately 50 km square windows that overlap by 50%. An example of the $K'_{\Delta\phi}$ estimation for an individual window is shown in the scatterplot (step 2, Figure 2.4), where $K'_{\Delta\phi}$ corresponds to the slope of the red dashed line. Once $K'_{\Delta\phi}$ is estimated for each window we interpolate to all points of the interferogram (step 3, Figure 2.4); the interpolated value for each point is calculated as the weighted average of the estimated $K'_{\Delta\phi}$ values, with the weighting being inversely proportional to the uncertainty of the $K'_{\Delta\phi}$ estimate and the distance of the window to the point. The tropospheric signal is then calculated by re-substituting the estimated values into equation (2.6), (step 3, Figure 2.4). Note that in this example the polarity of $K'_{\Delta\phi}$ switches between the center of the image compared to the North and the South. A single $K_{\Delta\phi}$, estimated over the whole interferogram (i.e. the linear method), would not be capable of capturing this variation in space.

2.3 Results

We tested the power-law correction individually on 17 Envisat (C-band) interferograms acquired over Mexico (Figure 2.5), for which the perpendicular, temporal, and Doppler centroid baselines are summarized in Table 2.1; and the unwrapped time-series interferograms are shown in Figure 2.6(a). All SAR data has been focussed using the ROI.PAC software (*Rosen et al., 2004*). Interferometric processing was done using the DORIS software (*Kampes et al., 2003*). We applied time-series InSAR processing using the StaMPS software (*Hooper, 2008, Hooper et al., 2012*) to reduce noise and estimate a DEM correction. Note that time-series processing is not required, as the power-law correction method is applied to individual interferograms. A summary of the applied processing parameters are contained in Table 2.2.

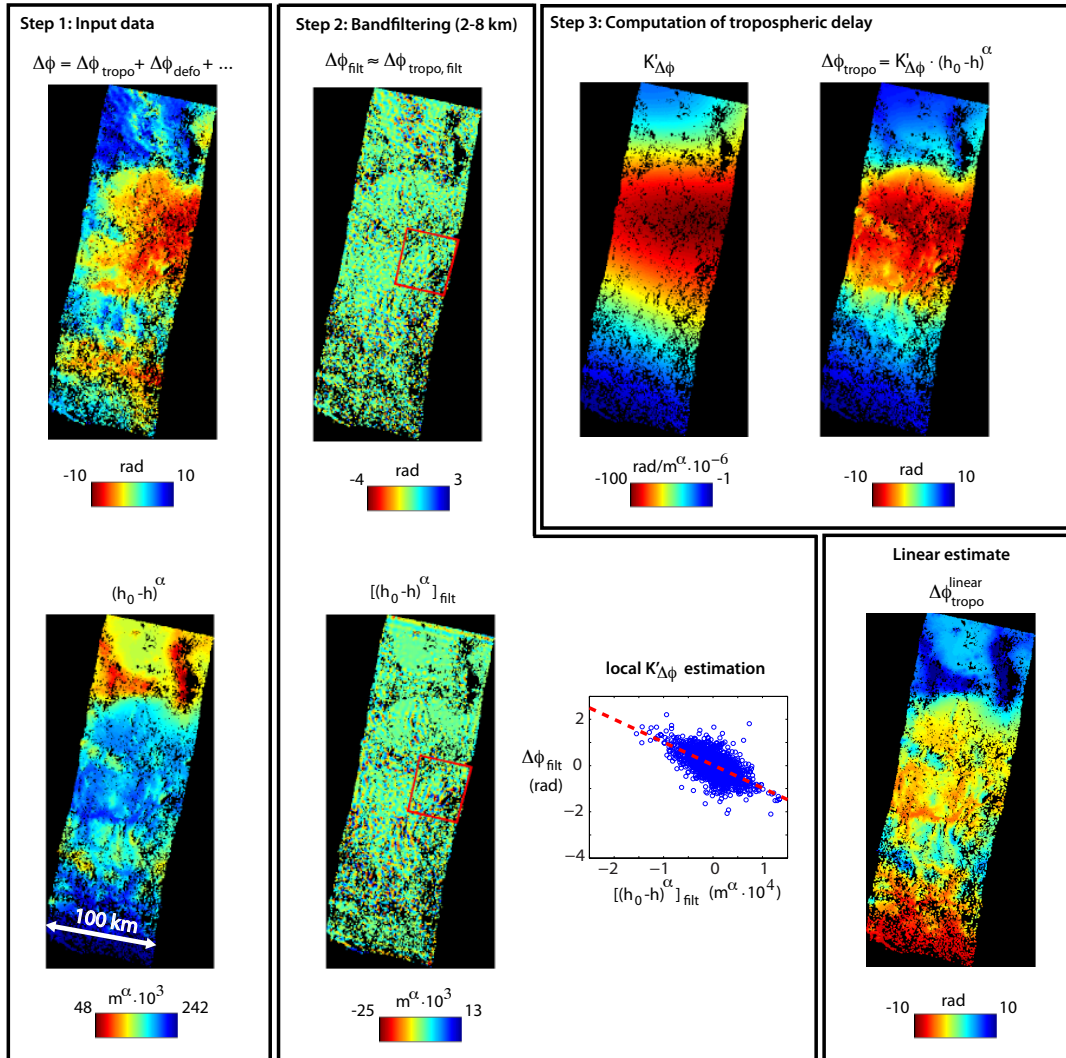


Figure 2.4: Tropospheric delay estimation for the 31 Dec 2004 - 16 Dec 2005 interferogram. (step 1) The original interferometric phase $\Delta\phi$ and the power-law scaled heights $(h_0 - h)^\alpha$. (step 2) shows (step 1) after bandfiltering in the 2-8 km spatial wavelength with a window over which $K'_{\Delta\phi}$ is estimated locally, represented by the slope of the red dashed line. (step 3) Shows the spatial map of $K'_{\Delta\phi}$ obtained after estimation in local windows and extrapolation to all points, and the corresponding tropospheric delay. The last window shows the tropospheric delay estimate when assuming a linear relationship. The input interferogram and the estimated tropospheric delay are referenced with respect to the mean of the whole region.

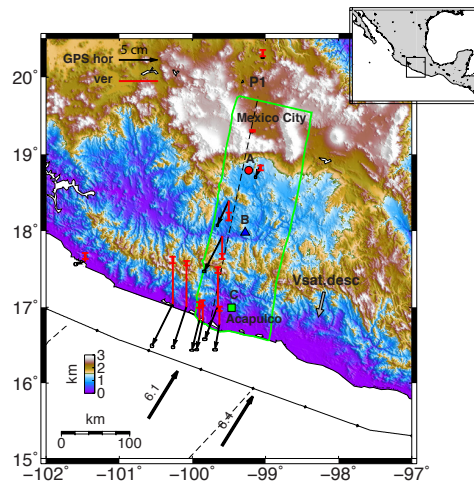


Figure 2.5: Overview of the power-law study region in Guerrero, Mexico. Horizontal (black) and vertical (red) GPS displacements from the 2006 slow slip event are from *Vergnolle et al. (2010)*. The thick arrows indicate the MORVEL (Mid-Ocean Ridge VELOCITY) relative plate motion of the Cocos and the North America Plate (*DeMets et al., 2010*). The green solid line indicates the extent of our SAR data. The SAR sensor is most sensitive to displacements perpendicular to the satellite flight direction. As most of the horizontal displacements are in the flight direction, the SAR is mainly sensitive to the vertical displacement component. The red, blue, and green markers give the location of individual presented InSAR point time-series in Figure 2.8, and P1 refers to the profile in Figure 2.7 and 2.9.

Table 2.1: Dataset baseline information. Perpendicular (B_{perp}), temporal (T) and absolute Doppler centroid (Δf_{DC}) baselines. All interferograms are relative to the master of 16 Dec 2005.

Date	B_{perp} [m]	T [days]	Δf_{DC} [Hz]	Date	B_{perp} [m]	T [days]	Δf_{DC} [Hz]
26 Nov 2004	210	-385	23.4	7 Oct 2005	-110	-70	-4.0
31 Dec 2004	134	-350	24.6	11 Nov 2005	690	-35	0.1
4 Feb 2005	-120	-315	25.9	20 Jan 2006	-864	35	-4.1
11 Mar 2005	283	-280	17.3	24 Feb 2006	-282	70	-1.8
15 Apr 2005	561	-245	21.4	5 Jan 2007	430	385	5.8
20 May 2005	123	-210	26.7	9 Feb 2007	86	420	1.8
24 Jun 2005	700	-175	25.4	16 Mar 2007	349	455	-3.5
29 Jul 2005	305	-140	25.4	9 May 2008	138	875	5.4
2 Sep 2005	652	-105	26.0				

Table 2.2: Applied InSAR processing parameters. DORIS (D) (*Kampes et al., 2003*) and StaMPS (S) (*Hooper et al., 2012*).

Parameter	Value	Parameter	Value
SRTM DEM (D)	90 m	Density random (S)	20 %
Multi-look factor (D)	1x1	Weed max noise (S)	inf
Oversample (D)	no	Weed σ (S)	1
Dispersion threshold (S)	0.4	Unwrap grid size (S)	1000 m
number of patches (S)	144	Merge resample size (S)	1000 m
Processing method (S)	Density	Merge σ (S)	0.45 rad

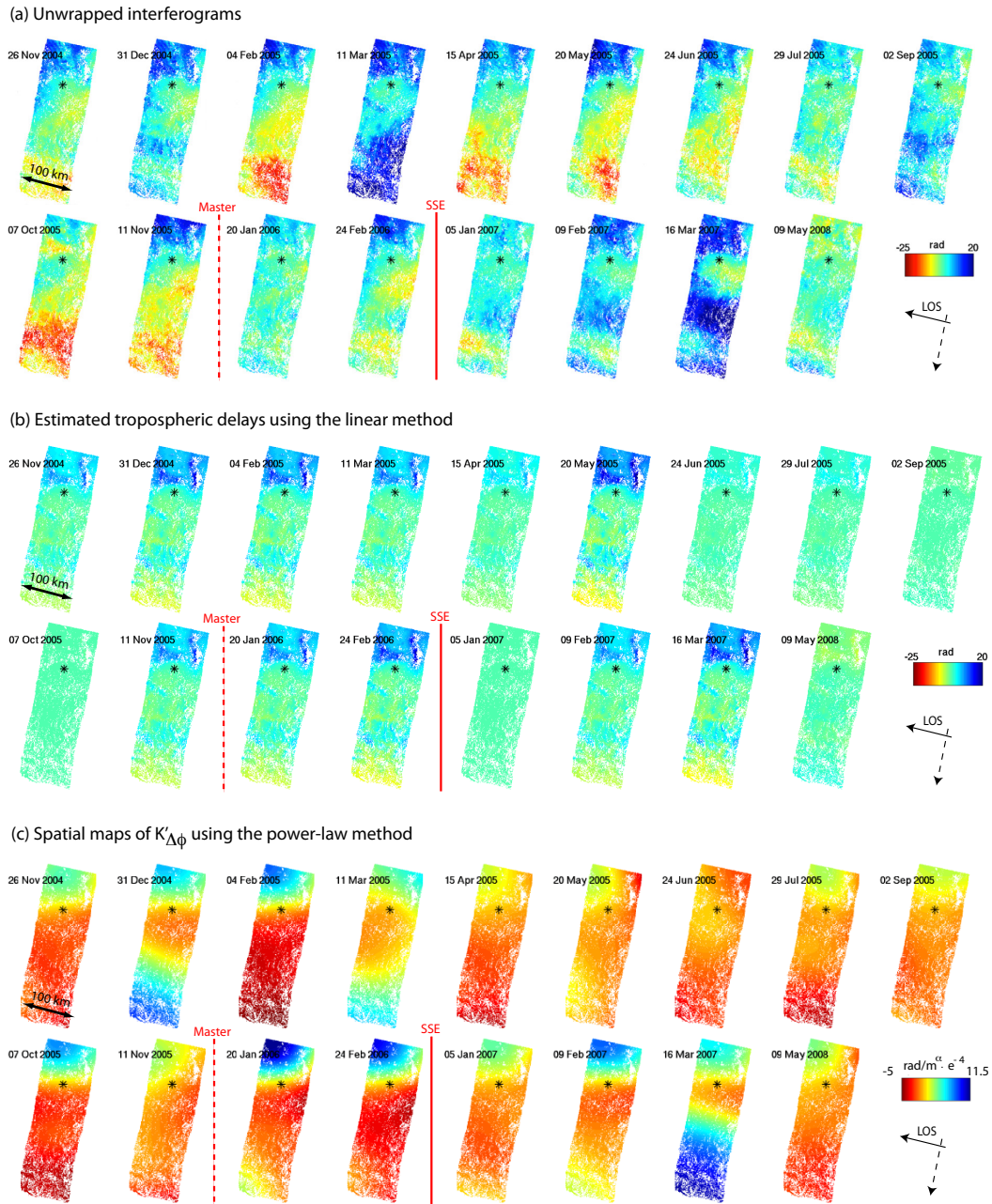


Figure 2.6: Unwrapped (a) time-series InSAR interferograms corrected for DEM errors, containing interseismic and slow slip displacements, (b) the estimated tropospheric delays assuming a linear relation between phase and topography, (c) the estimated maps of $K'_{\Delta\phi}$, (d) the estimated tropospheric delays, and (e) the unwrapped interferogram corrected for DEM errors and the tropospheric delays. The master date (16 Dec 2005) and the slow slip event are indicated by the dashed and solid red line, while the center of the reference area is indicated by the star. A change of 2π radians corresponds to a 2.8 cm displacement in the line-of-sight (LOS). Positive values represent displacements in the LOS direction. The interferograms on 11 Mar 2005 and 16 Mar 2007 show strong spatial correlation with the surface topography, Figure 2.5.

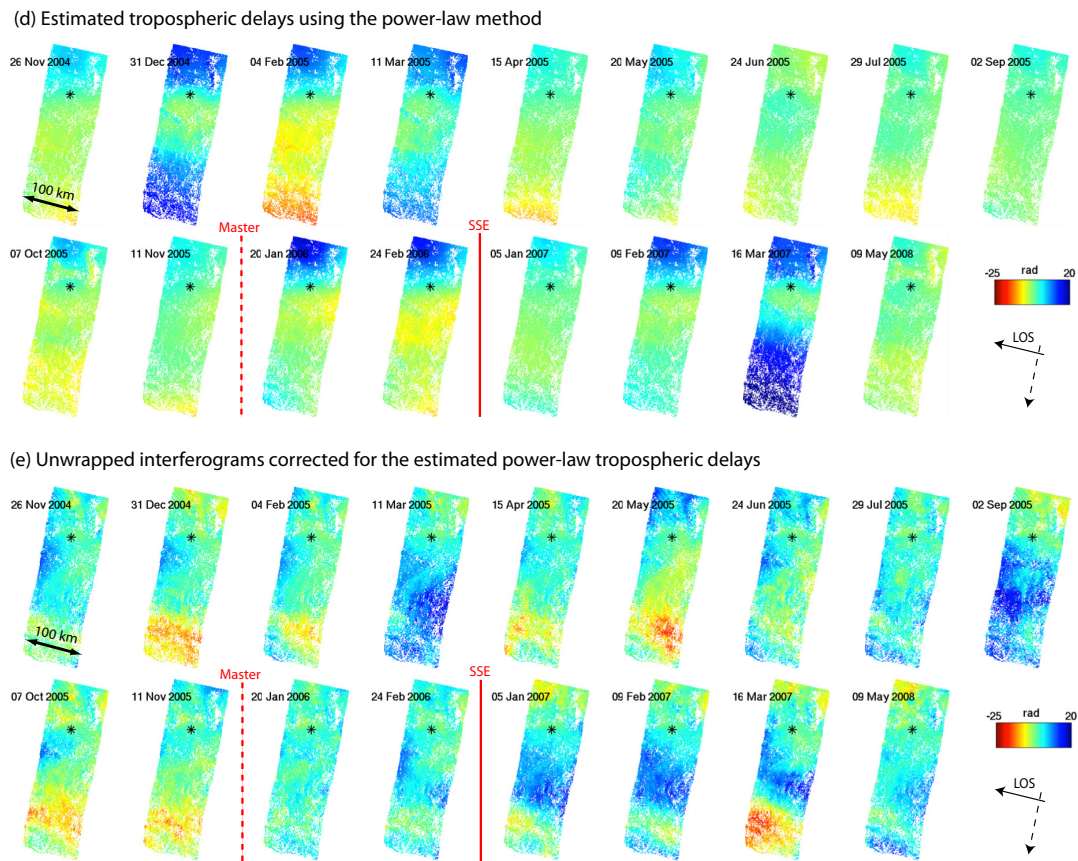


Figure 2.6: (Continued)

Tropospheric delays introduced by water vapour variations in the lower part of the troposphere and topographic variations, up to ~ 3.5 km elevation within our test region, mask the much smaller tectonic slow slip displacement signal (*Hooper et al., 2012*), which should be visible in images acquired after Dec 2006. Figure 2.7 shows the relationship between the unwrapped phase and the topography, with $K_{\Delta\phi}$ estimated in 50 km segments along the satellite flight direction. The relationship varies spatially, and reverses in sign in some cases, indicating the need for a spatially-varying tropospheric correction.

On average we find a strong local relationship $|K_{\Delta\phi}|$ of 2.8 rad/km (1.5 cm/km). The conventional linear tropospheric correction as shown in Figure 2.6(b), was estimated assuming a simple phase-topography relationship for each interferogram, and therefore does not allow for spatial variability. After applying the linear correction, we find that 5 out of 17 interferograms show a decrease in local correlation with topography $\Delta|K_{\Delta\phi}|$ (blue solid line in Figure 2.7). A maximum reduction of 2.5 rad/km (~ 1.13 cm/km) can be observed for 15 Apr 2005, for example. While the linear correction can work well in specific situations, we find that on average it *increases* the local correlation with topography by ~ 0.4 rad/km (~ 0.18 cm/km). While the local correlation increases, the correlation based on the full interferogram and the topogra-

phy on average decreases from 3.3 rad/km before correction to -0.7 rad/km after the linear correction. The increase in local correlation is due to the spatial variation of the troposphere, which cannot be accounted for using the linear method. By applying the power-law correction method locally we are able to account for spatial variation, as can be seen from the variation in the spatial maps of $K'_{\Delta\phi}$ shown in Figure 2.6(c).

The corresponding power-law tropospheric signal we estimate for each interferogram is shown in Figure 2.6(d). For interferograms after tropospheric correction using the power-law method (Figure 2.6(e)), we find an average reduction in local correlation with topography of 1 rad/km (~ 0.45 cm/km) (red solid line in Figure 2.7), about 1/3 of the signal, with the strongest reductions for our 11 Mar 2005 (2.7 rad/km or 1.2 cm/km) and 31 Dec 2004 (2.4 rad/km or 1.1 cm/km) interferograms. In total we find a decrease for 15 interferograms (average decrease of 1.2 rad/km or 0.5 cm/km), while for 2 interferograms a small increase can be observed (average increase of 0.25 rad/km or 0.1 cm/km), outperforming the conventional linear correction method. Based on the whole interferogram, we find the power-law to decrease the correlation with the topography to an average of -0.2 rad/km, 0.5 rad/km better than the linear method. We find that the power-law method does not capture the full signal near the coast, which is possibly due to the smaller topographic height range available to estimate the linear relation between the interferometric phase and the power-law scaled heights. Also, in the north of our study region, rapid subsidence of Mexico City contains deformation in the spatial band of 2-8 km that could contaminate the tropospheric estimates.

After tropospheric correction we find that the Root Mean Square (RMS) residual between the displacements and those predicted by the time-series model decrease (Figure 2.8 with the locations indicated in Figure 2.5), where the time-series model is defined as a linear trend due to interseismic loading, and a jump d_{SSE} at the time of the slow slip event. A detailed description is included in [Bekaert et al. \(2015\)](#). Close to the reference area, A, we find minimal change, as expected, with a slight RMSE increase of ~ 0.1 cm; further away we find a strong decrease in RMSE of ~ 0.6 cm and ~ 1 cm for regions B and C respectively. During the tropospheric correction, we make no a-priori assumptions about the form of the time-series model.

Figure 2.9 (left and middle panel) compares the LOS GNSS and InSAR slow slip estimates from the time-series model along the P1 profile before and after tropospheric correction. With respect to our estimated slow slip displacement signal, we find the gradient α_{SSE} between the slow slip displacements and the topography to decrease on average by 1.1 cm/km (Figure 2.9(c)), where $d_{SSE} = \alpha_{SSE}h + \text{constant}$, especially towards the center and north of our InSAR study region.

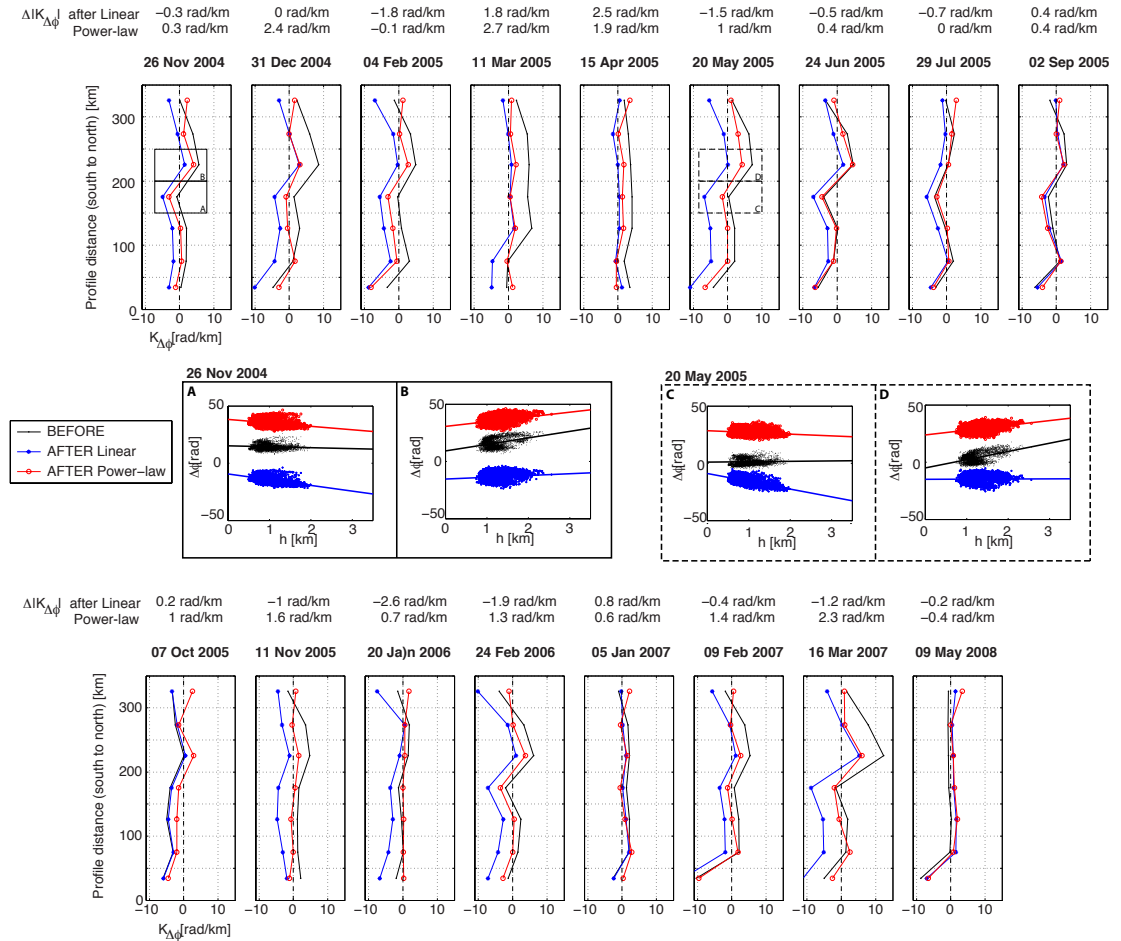


Figure 2.7: Comparing the local slope $K_{\Delta\phi}$, where $\Delta\phi = K_{\Delta\phi}h + \text{constant}$, between the interferograms and the topography, along profile P1 in 50 km segments, using all data. $K_{\Delta\phi}$ is estimated before (black solid line) and after correction for tropospheric signals using both a linear (blue solid line) and power-law (red solid line) correction method (Figure 2.6). For the linear method, 5 out of 17 interferograms show a decrease in local slope $\Delta[K_{\Delta\phi}]$, with a maximum reduction of 2.5 rad/km (~ 1.13 cm/km) on 15 Apr 2005. For the power-law method, 15 out of 17 interferograms show a decrease in slope, with a maximum reduction of 2.7 rad/km (~ 1.2 cm/km) for the 11 Mar 2005 interferogram. On average the linear correction does worse than the power-law with an *increase* in local slope of ~ 0.4 rad/km (~ 0.18 cm/km) compared to a decrease in local slope of 1 rad/km (~ 0.45 cm/km). A-D shows the scatter plots for the local correlation between phase and topography before and after correction for the linear and power-law methods.

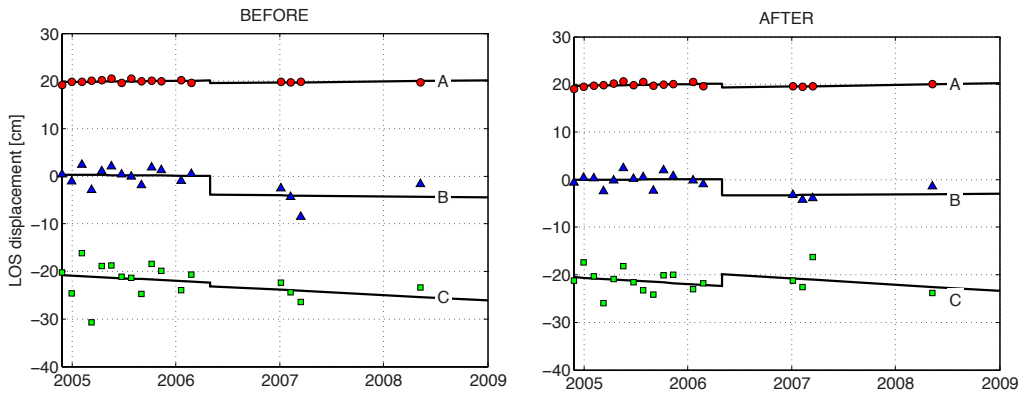


Figure 2.8: InSAR line-of-sight surface displacement time-series for individual locations, as shown in Figure 2.5, before and after the tropospheric correction is applied. Residual master atmosphere and DEM errors are removed. The displacement in time is modelled as an interseismic rate plus a slow slip step (black solid line). Positive displacements refer to motion towards the satellite, comprising mostly of vertical uplift. Offsets on the y-axis are chosen arbitrarily for clarity.

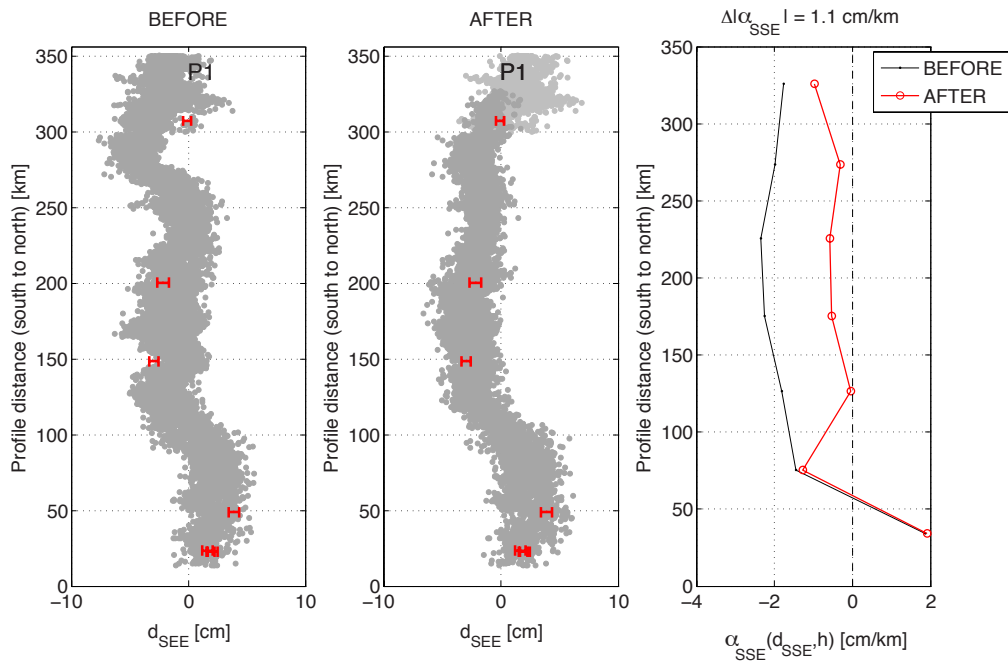


Figure 2.9: Comparison of the estimated slow slip surface displacements, accumulated over 8-9 months, before and after tropospheric correction (left and middle panel) with the estimates from GPS (red 2σ error bars). The right panel gives the local gradient α_{SSE} , where $d_{SSE} = \alpha_{SSE}h + \text{constant}$, between the slow slip deformation signal and topography before and after tropospheric correction, estimated in 50 km segments along profile P1, using all data. Before correction, the estimated slow slip surface displacements are strongly correlated with topography, especially in the middle and north of the InSAR study region. After correction, this local correlation is decreased, with on average a reduction of 1.1 cm/km. Light markers (middle panel) indicate the region around Mexico City, where subsidence contaminates the tropospheric correction estimates at the selected spatial frequency band of 2-8 km, which was chosen to avoid contamination of the long wavelength (~ 150 km) slow slip signal.

2.4 Discussion

Our time-series estimate of the slow slip deformation signal after tropospheric correction compares well with another InSAR study by *Cavalié et al. (2013)*. While the same InSAR track is explored, *Cavalié et al. (2013)* applied a different processing strategy with a stacking of 8 interferograms, spanning the slow slip event, to reduce tropospheric effects. Stacking is limited by the number of independent interferograms, and how uniform the acquisitions are sampled in time; it assumes that the random component of the atmosphere is reduced by averaging of interferograms, with a noise reduction approximately $\sim \sqrt{n}$ for n independent interferograms (*Zebker et al., 1997*).

We define the power-law reference height h_0 to be the lowest height above which the relative delays do not differ significantly ($\sigma < 0.5$ cm). A tighter constraint of σ increases the altitude of h_0 . For example, when using $\sigma < 0.05$ cm we find h_0 and α to be respectively 9 km and 1.5. We investigated the impact of wrongly assumed power-law coefficients, by comparing the estimated power-law delay used in this study ($h_0=7$ km and $\alpha=1.4$) with that estimated from coefficients with a tighter constraint ($h_0=9$ and $\alpha=1.5$). We found the impact to be small, with an average RMS difference between the two corrections of 2 rad or ~ 0.9 cm, similar to the ~ 1 cm line-of-sight accuracy of MERIS (*Walters et al., 2013*).

In order to generalize the proposed power-law relationship for performing tropospheric corrections in InSAR data (individual or time-series) in other study regions, both the reference height, h_0 , and the power-law coefficient, α , should be re-estimated as they might vary somewhat depending on the climate, season, and time of day. While sounding data gives an accurate representation of the atmosphere, it might not always be available near a given study region for a given day. Alternatively, weather model data like the European Centre for Medium-Range Weather Forecasts (ECMWF) ERA-I or the North American Regional Reanalysis (NARR) product can be used. This would also allow for spatial variation of the power-law coefficient, which could further improve the tropospheric delay estimation.

To separate deformation and tropospheric signals, a frequency band insensitive to deformation is required. As the troposphere is present at all spatial wavelength scales, a potential option is to perform a statistical analysis of multiple spatial bands to identify those bands that are consistent and likely to represent the troposphere. Alternatively, one can compare the delay maps as estimated from power-law for each spatial band with an independent estimate from MERIS or weather models to identify the best bands that represent the troposphere. Once identified the bands can be applied throughout the whole dataset. Failing to select a correct frequency band could cause deformation to leak into the estimated atmospheric correction.

The selection of the window size is a balance between spatial variability of the troposphere properties and the reliability of the estimate for $K'_{\Delta\phi}$. Smaller windows are likely

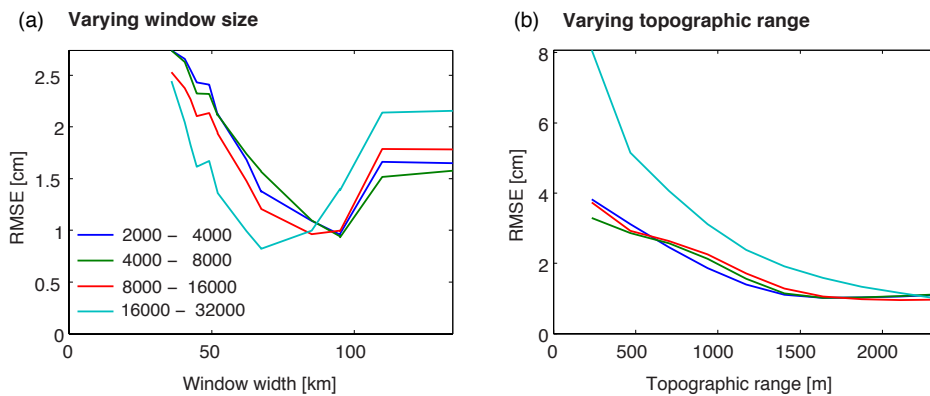


Figure 2.10: Impact of varying window size (a) and topographic relief (b) on the power-law performance. (a) shows that the “optimal” window size is a balance between a window small enough to allow for a spatially varying $K'_{\Delta\phi}$, while large enough to provide a reliable estimate of $K'_{\Delta\phi}$. (b) gives the delays assuming a fixed window size of ~ 90 km and shows that RMSE decreases with increasing topographic range. As input we use a simulated interferogram containing only the tropospheric delay computed from the Weather Research and Forecasting model, at the acquisition time of the 16 Mar 2007 interferogram.

to have a smaller topographic range, making it more difficult to get a robust estimate of $K'_{\Delta\phi}$, while a too large window will not allow $K'_{\Delta\phi}$ to vary in space. The selection of the window size will therefore be specific depending on the region of application. We tested the sensitivity to window size over our study region, by simulating the relative delay for the 16 Mar 2007 interferogram using the Weather Research and Forecasting (WRF) model, and then by estimating the delay from the simulated interferogram using different window sizes. The RMSE between the estimated and simulated delay is plotted in Figure 2.10(a), showing a minimum for a window size of ~ 90 km. Figure 2.10(b) shows the RMSE when the window size is held constant at 90 km, and the topographic range is allowed to vary instead. An increased RMSE can be observed with decreasing topographic range. Note that we assumed the same spatial variability of atmospheric conditions for all topographic ranges, whereas in reality, topography influences the weather conditions.

We did not find clear trends with respect to the band filter size. In general, the largest bandwidth limit is limited by the spatial extent of the study region, while the smallest bandwidth limit is limited by the resolution of the data. In Mexico, the delay differences are dominated by the wet component, which are on average 9.4 cm in the radar line of sight, compared to 0.8 cm for the hydrostatic component. In other regions, it may be possible to include a more complex function that accounts for different scale heights and exponents for the hydrostatic and wet components. This will be at the cost of adding additional degrees of freedom. In doing so, both components would need to be untangled as each of them partially correlate with the topography, and we suspect that this would be challenging in most circumstances.

We compared the power-law with the conventional linear method and found the

power-law to reduce the local correlation with the topography by on average 1 rad/km (~ 0.45 cm/km), compared to an *increase* of ~ 0.4 rad/km (~ 0.18 cm/km) for the linear method. While different tropospheric correction methods exist, each with its own limitations, the integration of multiple tropospheric observations or correction techniques can be used to complement each other. For example, by using the temporal information certain observations can be used to constrain the others. In case of Envisat, GNSS observations and measurements from the Medium Resolution Imaging Spectrometer onboard Envisat can be used to constrain weather models and phase correction methods, while in return the phase-based methods could be used to cope with cloud cover. Alternatively a weighted inversion of the different observations can be used to estimate the tropospheric properties (pressure, temperature, humidity), or a base pressure and an integrated quantity like precipitable water vapour, which then can be used to compute the tropospheric delay.

2.5 Conclusions

Previously, tropospheric corrections estimated from interferometric phase have been estimated over a full interferogram, in local windows in a band insensitive to deformation, or using a non-deforming region. While a local linear correction allows for the estimation of the slope relating interferometric phase and topography, the intercept will be biased by other signals. Failing to include this intercept will lead to an incorrect estimate of the tropospheric delay. We have developed a power-law relationship that can be applied locally, allowing us to estimate a spatially-varying signal from the interferometric phase. Allowing for spatial variation in the tropospheric properties becomes more important for larger spatial datasets (>10 s of km) as pressure, temperature, and relative humidity can change significantly over these length scales. We tested the power-law technique over Mexico, where interseismic and slow-slip deformation occurs on a long wavelength (~ 150 km). After correction, we find a reduction in the topography-correlated signals, and an improved correlation between the GNSS and InSAR estimated slow-slip surface displacements.

Acknowledgments

We acknowledge the Department of Atmospheric Science of the University of Wyoming for providing us the sounding data at Acapulco (downloaded from <http://weather.uwyo.edu/upperair/sounding.html>). Slow slip GNSS estimates were taken from (Vergnolle *et al.*, 2010). Envisat data were provided by the European Space Agency. We acknowledge the Jet Propulsion Laboratory for providing us with ROI-PAC (Rosen *et al.*, 2004), used to focus the raw SAR data, and the SRTM topographic data (Farr *et al.*, 2007), used to correct for the topography in the interferograms. InSAR pro-

cessing was achieved using the DORIS software ([Kampes et al., 2003](#)), developed at Delft University of Technology, and StaMPS software ([Hooper et al., 2012](#)). Some figures were prepared using the public domain GMT software ([Wessel and Smith, 1991](#)). COMET is the NERC Centre for the Observation and Modelling of Earthquakes, Volcanoes and Tectonics. Results can be obtained by contacting the corresponding author (eedpsb@leeds.ac.uk).

References

- Bekaert, D., A. Hooper, and T. Wright (2015), Reassessing the 2006 Guerrero Slow Slip Event, Mexico: implications for large earthquakes in the Guerrero Gap, *J. Geophys. Res.*, *120*, doi:[10.1002/2014JB011557](https://doi.org/10.1002/2014JB011557). 2.1, 2.2, 2.3
- Cavalié, O., M. Doin, C. Lasserre, and P. Briole (2007), Ground motion measurement in the Lake Mead area, Nevada, by differential synthetic aperture radar interferometry time series analysis: Probing the lithosphere rheological structure, *J. Geophys. Res.*, *112*(B3), doi:[10.1029/2006JB004344](https://doi.org/10.1029/2006JB004344). 2.1
- Cavalié, O., E. Pathier, M. Radiguet, M. Vergnolle, N. Cotte, A. Walpersdorf, V. Kostoglodov, and F. Cotton (2013), Slow slip event in the Mexican subduction zone: Evidence of shallower slip in the Guerrero seismic gap for the 2006 event revealed by the joint inversion of InSAR and GPS data, *Earth and Planetary Science Letters*, *367*, doi:[10.1016/j.epsl.2013.02.020](https://doi.org/10.1016/j.epsl.2013.02.020). 2.1, 2.4
- Davis, J., T. Herring, I. Shapiro, A. Rogers, and G. Elgered (1985), Geodesy by radio interferometry: Effects of atmospheric modeling errors on estimates of baseline length, *Radio Science*, *20*(6), 1593 – 1607, doi:[10.1029/RS020i006p01593](https://doi.org/10.1029/RS020i006p01593). 2.1
- DeMets, C., R. Gordon, and D. Argus (2010), Geologically current plate motions, *Geophys. J. Int.*, *181*(1), 1 – 80, doi:[10.1111/j.1365-246X.2009.04491.x](https://doi.org/10.1111/j.1365-246X.2009.04491.x). 2.5
- Elliott, J., J. Biggs, B. Parsons, and T. Wright (2008), InSAR slip rate determination on the Altyn Tagh Fault, northern Tibet, in the presence of topographically correlated atmospheric delays, *Geophys. Res. Lett.*, *35*(12), doi:[10.1029/2008GL033659](https://doi.org/10.1029/2008GL033659). 2.1, 2.1
- Farr, T., P. Rosen, E. Caro, R. Crippen, R. Duren, S. Hensley, M. Kobrick, M. Paller, E. Rodriguez, L. Roth, D. Seal, S. Shaffer, J. Shimada, J. Umland, M. Werner, M. Oskin, D. Burbank, and D. Alsdorf (2007), The Shuttle Radar Topography Mission, *Reviews of Geophysics*, *45*(2), doi:[10.1029/2005RG000183](https://doi.org/10.1029/2005RG000183). 2.5
- Hanssen, R. F. (2001), Remote Sensing and Digital Image Processing, in *Radar Interferometry: Data interpretation and error analysis*, *Earth and Environmental Science*, vol. 2, edited by F. van der Meer, Kluwer Academic Publishers, Dordrecht, The Netherlands. 2.1, 2.1, 2.1
- Hooper, A. (2008), A multi-temporal InSAR method incorporating both persistent scatterer and small baseline approaches, *Geophys. Res. Lett.*, *35*(16), doi:[10.1029/2008GL034654](https://doi.org/10.1029/2008GL034654). 2.3
- Hooper, A., D. Bekaert, K. Spaans, and M. Arikan (2012), Recent advances in SAR interferometry time series analysis for measuring crustal deformation, *Tectonophysics*, *514*517, 1 – 13, doi:<http://dx.doi.org/10.1016/j.tecto.2011.10.013>. 2.1, 2.1, 2.3, 2.2, 2.3, 2.5
- Kampes, B., R. Hanssen, and Z. Perski (2003), Radar interferometry with public domain tools, *Proceedings Fringe 2003*, p. 6. 2.3, 2.2, 2.5

- Li, Z., J. Muller, P. Cross, P. Albert, J. Fischer, and R. Bennartz (2006), Assessment of the potential of MERIS near infrared water vapour products to correct ASAR interferometric measurements, *International Journal of Remote Sensing*, *27*(2), 349 – 365, doi:[10.1080/01431160500307342](https://doi.org/10.1080/01431160500307342). 2.1
- Li, Z., E. Fielding, P. Cross, and R. Preusker (2009), Advanced InSAR atmospheric correction: MERIS/MODIS combination and stacked water vapour models, *International Journal of Remote Sensing*, *30*(13), 3343 – 3363, doi:[10.1080/01431160802562172](https://doi.org/10.1080/01431160802562172). 2.1
- Lin, Y., M. Simons, E. Hetland, P. Muse, and C. DiCaprio (2010), A multiscale approach to estimating topographically correlated propagation delays in radar interferograms, *Geochem. Geophys. Geosyst.*, *11*(9). 2.1, 2.2
- Onn, F., and H. Zebker (2006), Correction for interferometric synthetic aperture radar atmospheric phase artifacts using time series of zenith wet delay observations from a GPS network, *J. Geophys. Res.*, *111*(B9), doi:[10.1029/2005JB004012](https://doi.org/10.1029/2005JB004012). 2.1
- Parker, D., A. Fink, S. Janicot, J. Ngamini, M. Douglas, E. Afiesimama, A. Agusti-Panareda, A. Beljaars, F. Dide, A. Diedhiou, T. Lebel, and J. Polcher (2008), The Amma Radiosonde Program and its Implications for the Future of Atmospheric Monitoring Over Africa, *Bull. Amer. Meteor. Soc.*, *89*(7), 1015 – 1027, doi:[10.1175/2008BAMS2436.1](https://doi.org/10.1175/2008BAMS2436.1). 2.1
- Pinel, V., A. Hooper, S. D. la Cruz-Reyna, G. Reyes-Davila, and M. Doin (2011), The challenging retrieval of the displacement field from InSAR data for andesitic stratovolcanoes: Case study of Popocatepetl and Colima Volcano, Mexico, *J. Volcanol. Geoth. Res.*, *200*(12), 49 – 61, doi:[10.1016/j.jvolgeores.2010.12.002](https://doi.org/10.1016/j.jvolgeores.2010.12.002). 2.1
- Puysségur, B., R. Michel, and J. Avouac (2007), Tropospheric phase delay in interferometric synthetic aperture radar estimated from meteorological model and multi-spectral imagery, *J. Geophys. Res.*, *112*(B5), doi:[10.1029/2006JB004352](https://doi.org/10.1029/2006JB004352). 2.1
- Rosen, P., S. Henley, G. Peltzer, and M. Simons (2004), Updated Repeat Orbit Interferometry Package Released, *Eos Trans. AGU*, *85*(5), 47 – 47, doi:[10.1029/2004EO050004](https://doi.org/10.1029/2004EO050004). 2.3, 2.5
- Smith, E., and S. Weintraub (1953), The Constants in the Equation for Atmospheric Refractive Index at Radio Frequencies, *Proceeding of the IRE*, *41*(8), 1035 – 1037, doi:[10.1109/JRPROC.1953.274297](https://doi.org/10.1109/JRPROC.1953.274297). 2.1, 2.1
- Thayer, G. (1974), An improved equation for the radio refractive index of air, *Radio Science*, *9*(10), 803 – 807, doi:[10.1029/RS009i010p00803](https://doi.org/10.1029/RS009i010p00803). 2.1, 2.1
- Vergnolle, M., A. Walpersdorf, V. Kostoglodov, P. Tregoning, J. Santiago, N. Cotte, and S. Franco (2010), Slow slip events in Mexico revised from the processing of 11-year GPS observations, *J. Geophys. Res.*, *115*(B8), doi:[10.1029/2009JB006852](https://doi.org/10.1029/2009JB006852). 2.5, 2.5
- Wadge, G., P. Webley, I. James, R. Bingley, A. Dodson, S. Waugh, T. Veneboer, G. Puglisi, M. Mattia, D. Baker, S. Edwards, S. Edwards, and P. Clarke (2002), Atmospheric models, GPS and InSAR measurements of the tropospheric water vapour field over Mount Etna, *Geophys. Res. Lett.*, *29*, doi:[10.1029/2002GL015159](https://doi.org/10.1029/2002GL015159). 2.1
- Walters, R., J. Elliott, Z. Li, and B. Parsons (2013), Rapid strain accumulation on the Ashkabad fault (Turkmenistan) from atmosphere-corrected InSAR, *Geophys. Res. Lett.*, *118*, 3674 – 3690, doi:[10.1002/jgrb.50236](https://doi.org/10.1002/jgrb.50236). 2.1, 2.4
- Walters, R., B. Parsons, and T. Wright (2014), Constraining crustal velocity fields with InSAR for Eastern Turkey: Limits to the block-like behaviour of Eastern Anatolia, *J. Geophys. Res.*, *119*(6), 5215 – 5234, doi:[10.1002/2013JB010909](https://doi.org/10.1002/2013JB010909). 2.1

- Wessel, P., and W. Smith (1991), Free Software helps Map and Display Data, *Eos Trans. AGU*, 72(41), 445 – 446, doi:[10.1029/90EO00319](https://doi.org/10.1029/90EO00319). 2.5
- Wicks, C., D. Dzurisin, S. Ingebritsen, W. Thatcher, Z. Lu, and J. Iverson (2002), Magmatic activity beneath the quiescent Three Sisters volcanic center, central Oregon Cascade Range, USA, *Geophys. Res. Lett.*, 29(7), 26–1 – 26–4, doi:[10.1029/2001GL014205](https://doi.org/10.1029/2001GL014205). 2.1
- Williams, S., Y. Bock, and P. Fang (1998), Integrated satellite interferometry: tropospheric noise, GPS estimates and implications for interferometric synthetic aperture radar products, *J. Geophys. Res.*, 103(B11), 27,051 – 27,067, doi:[10.1029/98JB02794](https://doi.org/10.1029/98JB02794). 2.1
- Wright, T., E. Fielding, and B. Parsons (2001), Triggered slip: observations of the 17 August 1999 Izmit (Turkey) earthquake using radar interferometry, *Geophys. Res. Lett.*, 28(6). 2.1
- Zebker, H., P. Rosen, and S. Hensley (1997), Atmospheric effects in interferometric synthetic aperture radar surface deformation and topographic maps, *J. Geophys. Res.*, 102(B4), 7547 – 7563, doi:[10.1029/96JB03804](https://doi.org/10.1029/96JB03804). 2.4

Chapter 3

Statistical comparison of InSAR tropospheric correction techniques

D.P.S. Bekaert^{1,2}, R.J. Walters, T.J. Wright¹, A.J. Hooper¹, and D.J. Parker²

¹ *COMET, School of Earth and Environment, University of Leeds, United Kingdom*

² *ICAS, School of Earth and Environment, University of Leeds, United Kingdom*

Abstract

Correcting for tropospheric delays is one of the largest challenges facing the interferometric synthetic aperture radar (InSAR) community. Spatial and temporal variations in temperature, pressure, and relative humidity create tropospheric signals in InSAR data, masking smaller surface displacements due to tectonic or volcanic deformation. Correction methods using weather model data, GNSS and/or spectrometer data have been applied in the past, but are often limited by the spatial and temporal resolution of the auxiliary data. Alternatively a correction can be estimated from the interferometric phase by assuming a linear or a power-law relationship between the phase and topography. Typically the challenge lies in separating deformation from tropospheric phase signals. In this study we performed a statistical comparison of the state-of-the-art tropospheric corrections estimated from the MERIS and MODIS spectrometers, a low and high spatial-resolution weather model (ERA-I and WRF), and both the conventional linear and new power-law empirical methods. Our test-regions include Southern Mexico, Italy, and El Hierro. We find spectrometers give the largest reduction in tropospheric signal, but are limited to cloud-free and daylight acquisitions. We find the Root Mean Square (RMS) residual after tropospheric correction of interferograms to increase on average by $\sim 10\text{-}20\%$ with increasing cloud cover consistent across methods.

None of the other tropospheric correction methods consistently reduced tropospheric signals over different regions and times. We have released a new software package called TRAIN (Toolbox for Reducing Atmospheric InSAR Noise), which includes all these state-of-the-art correction methods. We recommend future developments should aim towards combining the different correction methods in an optimal manner.

3.1 Introduction

Interferometric Synthetic Aperture Radar (InSAR) is a geodetic tool that is well suited to the observation of crustal deformation processes. However, the use of InSAR to measure small magnitude and long wavelength deformation signals, such as interseismic slip (e.g. [Fournier et al., 2011](#), [Hooper et al., 2013](#), [Béjar-Pizarro et al., 2013](#), [Walters et al., 2013](#)), subduction zone slow slip events (e.g. [Cavalié et al., 2013](#), [Bekaert et al., 2015a](#)), and creep (e.g. [Jolivet et al., 2012](#)) is severely limited by atmospheric contamination of the InSAR data. Separating deformation from atmospheric signals, introduced by the variation of atmospheric properties in space and time, remains one of the major challenges for InSAR ([Hooper et al., 2013](#)).

Atmospheric delays are typically split into ionospheric and tropospheric terms. Ionospheric effects are caused by variations in free electrons along the travel path, resulting in a phase advance of the radar signal that becomes more significant for larger wavelengths, such as for P and L-band SAR (e.g. [Gray et al., 2000](#)). Tropospheric effects are caused by variations in pressure, temperature, and relative humidity in the lower part of the troposphere (<5 km), which cause signals in interferograms of up to 15-20 cm in magnitude, and can often be much larger than the tectonic signals of interest (e.g. [Hooper et al., 2013](#), [Bekaert et al., 2015a](#)). In this study, we focus on the testing and comparison of correction methods for tropospheric noise. Contamination from ionospheric noise in our test-data is minimized as we use C and X-band SAR data only.

The 2-way tropospheric phase delay, ϕ_{tropo} , at a specific height $h = h_1$, corresponds to the integration of the hydrostatic and wet component of the refractivity, N , between h_1 and the top of the troposphere, h_{top} , along the radar line-of-sight as:

$$N = \left(k_1 \frac{P}{T}\right)_{\text{hydr}} + \left(k_2' \frac{e}{T} + k_3 \frac{e}{T^2}\right)_{\text{wet}} = N_{\text{hydr}} + N_{\text{wet}} \quad (3.1)$$

$$\phi_{\text{tropo}} = \frac{-4\pi}{\lambda} \frac{10^{-6}}{\cos\theta} \int_{h_1}^{h_{\text{top}}} (N_{\text{hydr}} + N_{\text{wet}}) dh,$$

where P indicates total atmospheric pressure, T the temperature, e the partial pressure of water vapor, θ the incidence angle, λ the radar wavelength, and $-4\pi/\lambda$ a conversion factor to convert from pseudo-range increase to phase delay ([Hanssen, 2001](#)). The coefficients k_1 , k_2' and k_3 are empirical constants which we take as $k_1 = 77.6 \text{ K hPa}^{-1}$,

$k'_2 = 23.3 \text{ KhPa}^{-1}$ and $k_3 = 3.75 \cdot 10^5 \text{ K}^2\text{hPa}^{-1}$ (*Smith and Weintraub, 1953*). For InSAR, the interferometric tropospheric phase delay $\Delta\phi_{\text{tropo}}$ (from now on referred to as tropospheric phase delay) is the difference between tropospheric delay at the master and slave acquisition times $\Delta\phi_{\text{tropo}} = \phi_{\text{tropo}}^{\text{slv}} - \phi_{\text{tropo}}^{\text{mst}}$, and thus depends on the change in refractivity, rather than the total refractivity.

Tropospheric corrections can be calculated using auxiliary information from weather models (e.g. *Wadge et al., 2002, Liu et al., 2009, Doin et al., 2009, Jolivet et al., 2011, Walters et al., 2014, Jolivet et al., 2014*), GPS measurements (e.g. *Williams et al., 1998, Onn and Zebker, 2006, Li et al., 2006a, Löfgren et al., 2010*), multi-spectral observations (e.g. from the Medium Resolution Imaging Spectrometer (MERIS) onboard the Envisat satellite; or the Moderate Resolution Imaging Spectroradiometer (MODIS) onboard the Terra and Aqua satellites) (*Li et al., 2006b, 2009a,b*), or GPS in combinations with spectrometer data (e.g. *Li et al., 2005, Puysségur et al., 2007*). The estimated corrections are often limited by the spatial and temporal resolution, and the precision of the auxiliary data. GPS stations are often absent or sparsely distributed in many areas around the world. Spectrometers can only provide useful corrections under cloud-free and daylight conditions. Weather models and spectrometer observations that are not acquired simultaneously with SAR data need to be interpolated in time, which can also introduce uncertainties. This is not required for MERIS in combination with Envisat ASAR sensor, as both were operated simultaneously onboard Envisat.

Tropospheric corrections can also be calculated empirically directly from the interferogram. Tropospheric delays $\Delta\phi_{\text{tropo}}$ for an individual interferogram can be estimated by assuming a linear relation, $\Delta\phi_{\text{tropo}} = K_{\Delta\phi}h + \Delta\phi_0$, between topography h and the interferometric phase $\Delta\phi$ in a non-deforming region (*Wicks et al., 2002*) or in a spatial band insensitive to deformation (*Lin et al., 2010*), where $K_{\Delta\phi}$ is the gradient to be estimated, and $\Delta\phi_0$ is a constant that can be neglected as it merely represents a constant shift applied to the whole interferogram. *Elliott et al. (2008)* used a modification of this method and removed a preliminary estimate of the deformation displacements prior to estimating $K_{\Delta\phi}$. Such phase-based methods have been effective in the reduction of tropospheric signals, but are limited as they assume no spatial variability of the tropospheric properties is present. Some authors have attempted to overcome this limitation by applying a piece-wise slope (linear) correction over multiple windows (e.g. *Béjar-Pizarro et al., 2013*). However, this method is technically flawed, as a laterally-varying tropospheric signal requires a common reference between windows, and estimation of the constant $\Delta\phi_0$ within windows is not possible as other phase contributions bias the estimate. Alternatively, *Bekaert et al. (2015b)* developed a power-law model, which unlike the linear approach can account for a spatially-varying tropospheric signal in the presence of deformation.

In this study, we perform a statistical analysis of several different tropospheric correction methods that can be used to correct an individual interferogram. This includes

corrections estimated from (i) MERIS at ~ 1.2 km spatial-resolution, (ii) MODIS at 1 km resolution, (iii) the archived European Center for Medium- Range Weather Forecasts (ECMWF) ERA-I weather model at 80 km resolution (*Dee et al., 2011*), (iv) a locally run Weather Research and Forecasting Model (WRF) (*Michalakes et al., 2004*) nested to a 7 km resolution, and the phase-based empirical (v) linear and (vi) power-law corrections. All these methods are included in **TRAIN**, our open-source Toolbox for Reducing Atmospheric InSAR Noise.

3.2 Tropospheric correction methods for InSAR

Tropospheric signals consist of a short-scale (few km) component, introduced by turbulent as well as coherent dynamics in the troposphere, a longer-scale (10s of km) component, introduced by lateral variation of pressure, temperature and humidity, and a topography-correlated component due to changes of pressure, temperature, and relative humidity with height (e.g. *Hanssen, 2001*). Different correction techniques have different sensitivities for these three components of the tropospheric delay. For example, weather models often have timing issues, which render them unable to correctly resolve the turbulent variation of water vapor (e.g. *Liu et al., 2009*). While the statistical properties of the turbulent component can be representative for the region, the location can be wrong, leading to an adverse effect when removing the estimated tropospheric signal. Unlike water vapor, temperature and pressure are smooth in space, leading to a better-resolved longer wavelength hydrostatic component. Spectrometer measurements only produce an estimate for the wet component of the delay. While a direct comparison is possible between the spectrometer correction and the wet delay as estimated from weather models, the phase-based methods cannot produce separate wet and hydrostatic components of the delay. As the linear and the power-law methods only estimate a topography-correlated component of the delay, they explicitly cannot account for the turbulent and coherent short-scale component.

In the following section we provide more information on the estimation procedure of the different correction methods.

3.2.1 Tropospheric delays from weather models

The output (pressure, temperature, and relative humidity) from local or global weather models can be used with equation (3.1) to compute both hydrostatic and wet tropospheric delay (*Doin et al., 2009, Jolivet et al., 2011*). In this study we used the freely available archived ERA-I global model, and also run our own local high spatial-resolution model using the Weather Research and Forecasting (WRF) model (*Michalakes et al., 2004*).

ERA-I outputs data at a spatial resolution of ~ 80 km, at a 6 hours interval, and on 37 pressure levels (*Dee et al., 2011*). We performed a lateral and vertical spline

interpolation of pressure, temperature, and relative humidity, after which we computed the refractivity and the integration from the surface upwards. To match the SAR acquisition time, we performed a linear interpolation in time.

We modified the WRF set-up to produce outputs at the same 37 pressure levels as ERA-I. We set the boundary of the parent WRF domain using the National Center for Environmental Prediction (NCEP) Climate Forecast System Reanalysis (CFSR) data ([Saha et al., 2010](#)) and NCEP’s Global Forecast System analysis (GFS) ([Unidata et al., 2003](#)). As GFS did not exist prior to 1 November 2006, we used the CFSR data instead for those dates. The impact of changing between CFSR and GFS on the estimated delays is small. We estimate negligible differences in slant total delay between the two methods; the average RMS difference is <1 mm across 15 interferograms for which CFSR and GFS corrections were both available.

3.2.2 Tropospheric delays from spectrometer observations

Both MERIS and MODIS provide products of Precipitable Water Vapor (PWV), the vertically integrated water vapor content of the atmosphere. The MERIS estimate for PWV is computed by comparing the radiance ratio between two closely-spaced infrared frequency bands, of which only one is sensitive to water vapor ([ESA, 2011](#)). A similar approach is used for MODIS but with five near-infrared bands instead ([Gao and Kaufman, 2003](#)). PWV is defined as the equivalent column height of liquid water when integrating all water vapor e from the surface h to the top of the atmosphere ([Bevis et al., 1992](#)):

$$\text{PWV} = \frac{1}{\rho_w R_v} \int_h^\infty \frac{e}{T} dh, \quad (3.2)$$

where ρ_w is the density of water, R_v the specific gas constant of water vapor, and T temperature. The MERIS PWV accuracy has been estimated from continuous GNSS to be ~ 1.1 mm, equivalent to ~ 6.2 mm of zenith wet delay for each epoch ([Li et al., 2006b](#)). For a difference between two epochs this increases by a factor of $\sqrt{2}$ to 8.8 mm. This is equivalent to ~ 1 cm in radar line-of-sight for Envisat with an incidence angle of 23° , obtained by substituting $\text{PWV}=8.8$ mm in the computation of the spectrometer delay, equation (3.5), provided below. We found that MODIS gives at best an accuracy equal to that of MERIS, and at worst twice that of MERIS, further detailed in the results section. MERIS has no bias in PWV retrieval, but MODIS tends to overestimate PWV on average by 5% ([Li et al., 2003](#)). For those SAR dates where PWV from MERIS and MODIS have $\geq 50\%$ mutual pixels after applying a cloud cover mask, we estimated a MODIS recalibration factor α_{MODIS} from a linear relation between both the cloud-free MERIS and MODIS PWV. For the other SAR acquisitions we assumed the calibration factor to be the weighted average of the estimated calibration factors, where weights were estimated from bootstrapping.

The tropospheric delay of equation (3.1) can be rewritten as:

$$\phi_{\text{tropo}}^{\text{wet}} = \frac{-4\pi}{\lambda} \frac{10^{-6}}{\cos\theta} \left(k_2' \int_{h_1}^{h_{\text{top}}} \frac{e}{T} dh + \frac{k_3}{T_m} \int_{h_1}^{h_{\text{top}}} \frac{e}{T} dh \right), \quad (3.3)$$

where T_m is (Davis *et al.*, 1985):

$$T_m = \frac{\int_h^\infty e/T dh}{\int_h^\infty e/T^2 dh}. \quad (3.4)$$

This can now be further rewritten in terms of the spectrometer delay as:

$$\phi_{\text{tropo}}^{\text{wet}} = \frac{-4\pi}{\lambda} \frac{\Pi}{\cos\theta} * \text{PWV}, \quad (3.5)$$

where Π is a conversion factor (Bevis *et al.*, 1992, Niell *et al.*, 2001, Li *et al.*, 2003, 2006b), typically around 6.2, that varies with the temperature of the troposphere, as:

$$\Pi = R_v \rho_w 10^{-6} \left(k_2' + \frac{k_3}{T_m} \right) \quad (3.6)$$

We estimate Π for individual SAR acquisitions using balloon sounding data, provided by the Department of Atmospheric Science of the University of Wyoming.

3.2.3 Phase-based tropospheric delays

The interferometric tropospheric phase $\Delta\phi_{\text{tropo}}$ can be estimated from the relationship between the interferometric phase and the topography as:

$$\Delta\phi_{\text{tropo}} = K_{\Delta\phi} h + \Delta\phi_0, \quad (3.7)$$

for the linear method, and

$$\Delta\phi_{\text{tropo}} = K_{\Delta\phi}' (h_0 - h)^\alpha, \quad \text{with } h < h_0 \quad (3.8)$$

for the power-law method, where $K_{\Delta\phi}$ and $K_{\Delta\phi}'$ are coefficients relating phase to topography. The power-law reference height, h_0 , and the power-law coefficient, α , are constants estimated from balloon sounding data, or weather model data (Bekaert *et al.*, 2015b). Unlike the linear method, the power-law method can account for spatial variation of tropospheric properties by estimating $K_{\Delta\phi}'$ over local windows.

Lateral variation for the lower part of the troposphere is critically controlled by the interaction of air parcels with topographic barriers (Markowski and Richardson, 2010). Whether or not an air parcel will flow around or over a mountain is related to the relative height, the slope of the mountain, the mountain aspect ratio, the horizontal wind speed towards the mountain, and the static stability of the troposphere. The

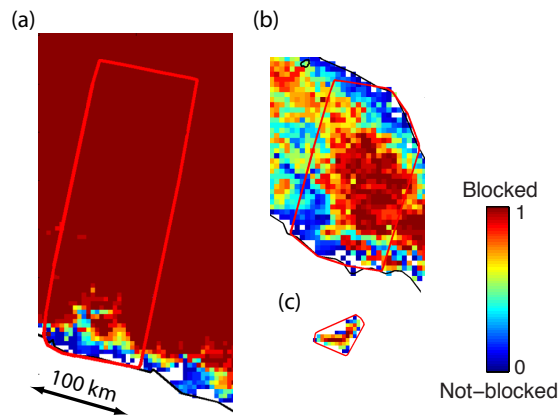


Figure 3.1: Fraction of consistent mountain blockage over time for (a) Mexico, (b) Italy, and (c) El Hierro, using WRF wind velocities at the time and date of the SAR acquisitions. Mountain blockage for individual SAR acquisitions is contained in Figures B.1-B.3 for the different regions.

stagnation height, h_{stag} , or the mountain height for which blockage occurs, can be simplified as:

$$h_{\text{stag}} = \frac{v_m}{f_{\text{bv}}} \quad (3.9)$$

with v_m horizontal wind speed towards the mountain, and f_{bv} the Brunt-Väisälä frequency (*Markowski and Richardson, 2010*), which we fixed to be 0.01 Hz.

The original power-law method (*Bekaert et al., 2015b*) splits the study region into multiple rectangular windows, over which the local phase-topography relation is estimated. This is then interpolated to all data points, by weighting the windows with the distance to the data points, and with the window uncertainty of the estimate. We modified the method to account for disconnected tropospheric regions by specifying a physical boundary, identified from stagnation or mountain blockage, which is used to limit the interpolation to the windows of the same tropospheric region only.

First, we computed the stagnation height for each SAR date using WRF, and compared stagnation height with local topography to identify disconnected regions. Figures B.1-B.3 give a binary representation for all SAR dates whether or not stagnation occurs. Second, we combined the binary information of all SAR dates to compute the fraction of consistent stagnation over time (Figure 3.1), which allows us to identify the physical boundaries that act as barriers persistently through time.

3.3 InSAR processing

We processed InSAR data using ROI-PAC to focus the raw data (*Rosen et al., 2004*), DORIS to form interferograms (*Kampes et al., 2003*), and StaMPS to select stable scatterer pixels (*Hooper et al., 2007*). While a time-series InSAR approach is not required to estimate the tropospheric delay map for each individual interferogram,

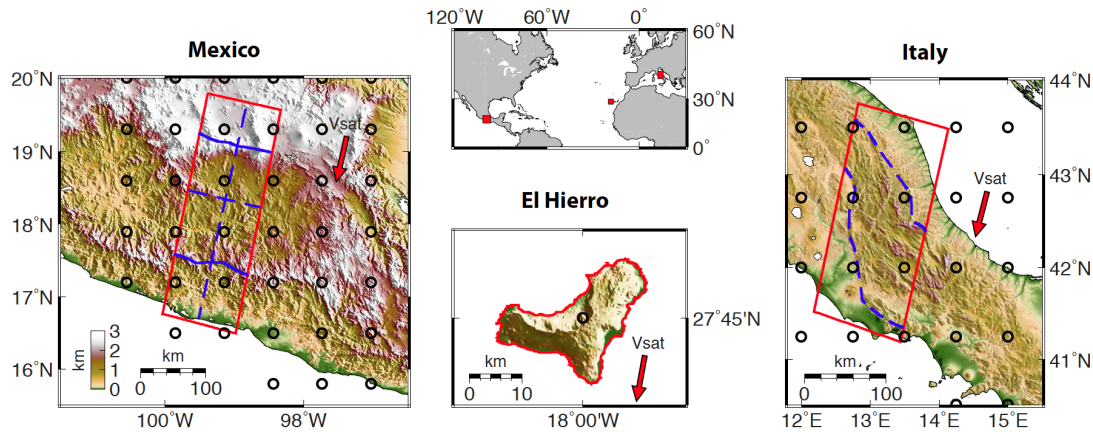


Figure 3.2: Overview map (center) with inserts of our study regions: Mexico, Italy, and El Hierro. Map colors show the local topography from the Shuttle Radar Topography Mission, saturated at 3 km elevation. Red polygons indicate the illuminated ground area of the descending InSAR data. Solid blue lines define a border between different tropospheric regions, as found from consistent wind stagnation over time due to local topography (Figure 3.1). Together, blue solid and blue dashed lines define the local windows as used for the power-law correction method, where windows within a tropospheric region constrain the delay estimation. Black circular markers indicate the location of the ERA-I weather model data points, at ~ 75 km spatial resolution. To avoid clutter, the high resolution WRF model points are not shown; we used a spatial resolution of 7 km over Mexico and Italy, and 2 km over El Hierro.

it allowed us to increase the signal-to-noise ratio, helping the unwrapping process. Moreover, when processed through a small baseline network, it allowed us to validate the unwrapping process. Known phase contributions due to Envisat’s oscillator drift are also removed according to [Marinkovic and Larsen \(2015\)](#).

3.4 Background of the test sites

We investigated the correction capability of the different tropospheric InSAR correction methods over three test sites: Mexico, Italy, and El Hierro in the Canary Islands (Figure 3.2).

Over Mexico we generated a single master network of 19 descending Envisat interferograms (track 255, Table B.1), spanning the period from November 2004 until December 2009, and covering an area of ~ 100 km by 340 km. While no significant earthquakes occurred during our study, interferograms are subjected to long-wavelength (few 100s km) tectonic displacements introduced by the 2006 Guerrero slow slip event, equivalent to $M_w \sim 7.3$ ([Bekaert et al., 2015a](#)), as well as interseismic deformation due to locking on the subduction interface.

The topography ranges from sea-level up to 4.8 km elevation, and includes the valley of Mexico City, and the surrounding Popocatépetl and Iztaccihuatl volcanoes. A mountain range of ~ 2 km elevation, just 100 km inland from the coast, acts as an obstacle for air flow and thus can introduce different atmospheric conditions on either

side of the mountain. Large tropospheric phase delays (>5 cm) have been observed in previous InSAR studies of this region (e.g. [Hooper et al., 2012](#), [Cavalié et al., 2013](#), [Bekaert et al., 2015b](#)).

Over Italy we generated a small baseline network of 49 descending Envisat interferograms (track 79, Table B.2), spanning December 2002 until February 2009. Our study area extends from the western to eastern coastline of peninsular Italy (~ 100 km by 260 km), crossing the Apennines, with a maximum topographic height of ~ 2 km and ridges oriented parallel with the coastline. Within this region six earthquakes of $M_w \geq 5$ occurred, clustered around April 2009, of which the L’Aquila earthquake of 6 April was the largest with M_w 6.3 (e.g. [Walters et al., 2009](#), [Cheloni et al., 2014](#)). Tectonic contamination from long-wavelength (few 100s km) interseismic deformation (extension rate of 6 ± 2 mm/yr ([D’Agostino et al., 2001](#))) is expected to be small, as horizontal deformation is predominately perpendicular to the radar line-of-sight, in which direction InSAR is insensitive.

Over El Hierro we generated a small baseline network of 78 descending TerraSAR-X interferograms (track 79, Table B.3). El Hierro is much smaller (~ 30 km by 25 km) than our Mexico and Italy datasets, and as an island is completely surrounded by water. The local topography is related to the volcanic nature of the island. A sharp cliff ~ 1.5 km high, in combination with the surrounding ocean, allows for complex and highly turbulent tropospheric delays. Our InSAR data covers the period from September 2011 until February 2012, and includes the 13 October 2011 submarine eruption (e.g. [González et al., 2013](#)).

3.5 Results and discussion

Prior to the computation of the MODIS tropospheric delays, we performed a recalibration of MODIS PWV using MERIS as a reference. The left panel of Figure B.4 shows the estimated calibration factors α_{MODIS} for individual SAR acquisitions, with the uncertainty estimated from 1200 bootstrap runs. The average uncertainty for α_{MODIS} is 0.001. The average weighted calibration factor amounts to ~ 0.98 over Italy, based on 13 samples, and ~ 0.95 over Mexico, using only 14 samples, or when combining all samples (Figure B.4 right panel). This value is in agreement with [Li et al. \(2003, 2005\)](#), who found an average recalibration factor of 0.95 when comparing MODIS PWV with GPS observations over Germany and Southern California. On average we found negligible differences between estimated tropospheric delays when applying an individual estimated calibration factor or when assuming a fixed value of 0.95. Therefore we believe it will be sufficient for future studies to estimate a single calibration factor for each region.

The power-law method can be applied in deforming regions by applying the estimation in a spatial band insensitive to the deformation. However, other strong signal

contamination from the turbulent troposphere and orbit errors should also be avoided. While turbulent signals manifest at short spatial scales, and orbit errors are of long wavelength, the selection of the non-deforming band is not always trivial, as it requires *a priori* information about the spatial extent of deformation throughout time.

We selected the spatial band whose correction had the smallest Root Mean Square Error (RMSE) after tropospheric correction of the unwrapped interferograms (Figure B.5). To avoid contamination of deformation, we corrected the interferograms (left panel) for a time-series estimate of tectonic deformation and DEM errors.

We found the mean RMSE to vary more strongly between spatial bands over Mexico (σ_{RMSE} of 0.2 cm) and Italy (σ_{RMSE} of 0.3 cm), than over El Hierro ($\sigma_{\text{RMSE}} < 1$ mm). The 8-16 km spatial band corresponded to the smallest RMSE over Mexico, 16-32 km over Italy, and 4-16 km over El Hierro.

We modified the power-law method from *Bekaert et al. (2015a)* to allow for disconnected tropospheric regions separated by blue solid lines in Figure 3.2, which likely have different tropospheric conditions. To identify these regions we used equation (3.9) to compute the consistency of wind stagnation over time due to topography (Figure 3.1).

Mountain blockage occurs for more than 95% of the time over our Mexican study area, except for the region within ~ 10 km of the Mexican coast, dividing our study area into multiple disconnected tropospheric regions. We did not enforce different disconnected regions over Italy, as the western extent of our study region is only blocked 50-65% of the time. Over El Hierro this analysis is not applicable due to its smaller extent. The identification of different disconnected tropospheric regions (Figure 3.2, blue solid lines), in combination with local subdivision to allow for spatial variation of tropospheric properties (blue dashed lines), leads to a total of eight power-law windows over Mexico, three over Italy, and one over El Hierro.

Figure 3.3(a)-(c) shows two examples of the estimated tropospheric delays for the different correction methods for each test-region. For each of these three regions, the first example (Case 1) shows a scenario where the tropospheric delays are mainly topography-correlated. We find that all methods show both a similar magnitude of the estimated delay and a similar spatial pattern of the delay.

The second example (Case 2) demonstrates a more complex tropospheric delay, with spatial variation of tropospheric properties and with a significant turbulent behavior of the troposphere. Variation can be observed between the different estimated delays, especially over Mexico and Italy. Both MERIS and MODIS estimated delays show a strong resemblance to the original interferograms, whereas the weather model correction shows delays of similar order of magnitude, but not always correctly located (e.g. over Mexico). As the phase-based (linear and power-law) methods are estimated over a region, they are incapable of matching the turbulent signals. Over El Hierro the effect of long wavelength spatial variation is limited due to the small extent of the island, hence

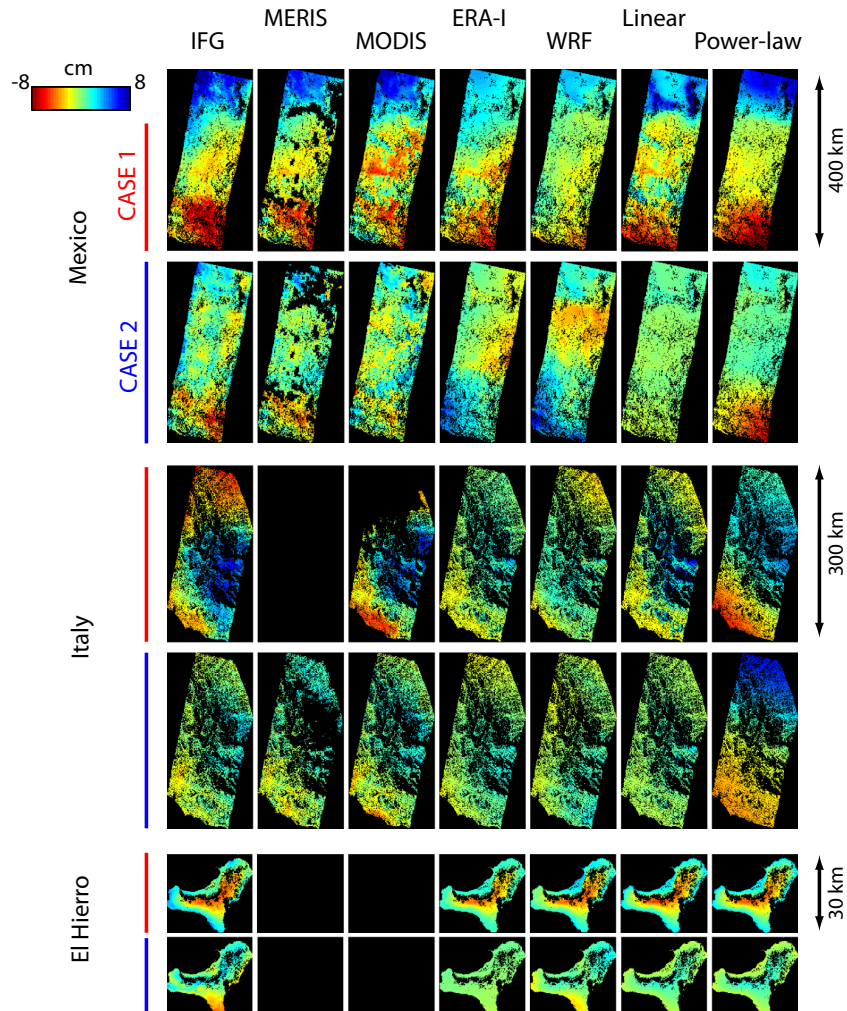


Figure 3.3: Example of tropospheric delay estimates for different correction methods over Mexico, Italy, and El Hierro. Two examples are shown for each region. Case 1 (red) corresponds to an example where the tropospheric delay is mainly correlated with the topography. Case 2 (blue) represents an example with a more complex, turbulent and or spatially-varying tropospheric signal. Columns give from left to right, the unwrapped interferogram, and the estimated tropospheric corrections using MERIS, MODIS, ERA-I, WRF, the linear method, and when using the power-law method. Both MERIS and MODIS spectrometers also have a hydrostatic component of ERA-I included to allow for comparison with the phase-based correction methods. All observations are converted to displacements in the radar line-of-sight.

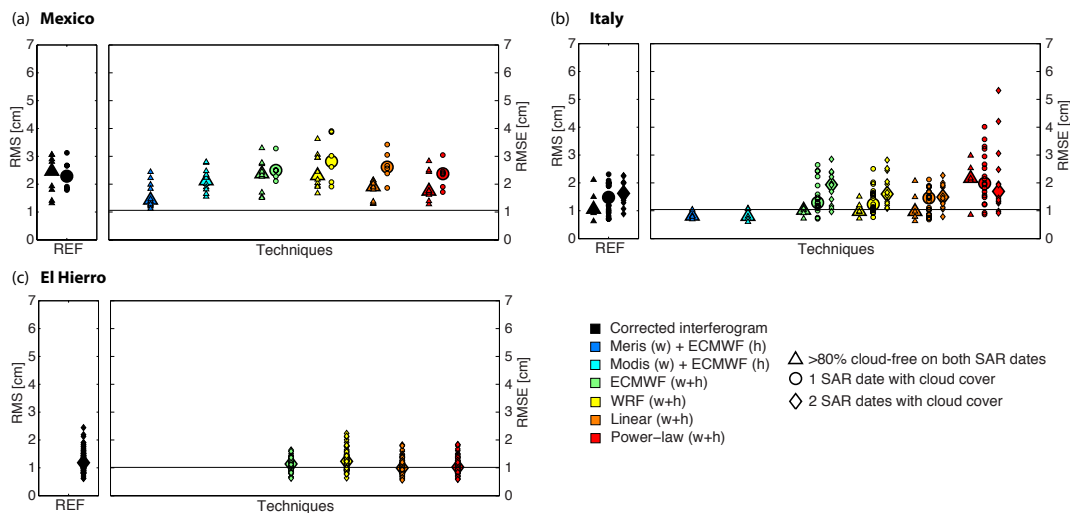


Figure 3.4: Statistical analysis between different tropospheric correction methods over (a) Mexico, (b) Italy, and (c) El Hierro. Left panel, Root Mean Squared (RMS) of the tropospheric signal of the reference technique, corresponding to the unwrapped interferograms corrected for DEM errors and tectonic signals. Right panel, RMS Errors after correction of the reference signal using tropospheric estimates of the power-law for different spatial bands (colored markers). Triangular markers corresponds to interferograms that are more than 80% cloud free, circular markers to interferograms for which one of the SAR dates had more than 20% clouds, and diamond markers where both SAR dates failed the cloud-free threshold. Small colored markers represent individual interferograms, while the thicker marker represents the average of all interferograms. The solid line gives the expected MERIS accuracy level. In the legend, wet delay components are indicated by (w), and hydrostatic components by (h).

the main variation in the tropospheric signal results from the topography-correlated signal and turbulence. While the high-resolution weather model (WRF) is capable of capturing the correct spatial trend over the region, it cannot capture the high gradients in the delay from turbulence (few km). Spectrometer estimates of MERIS and MODIS were not included over El Hierro due to limited amount of data, but when they were available their estimated delays were limited by their lower, ~ 1 km, spatial resolution.

For each region we performed a statistical analysis where we compared all the tropospheric techniques with respect to the unwrapped interferograms (Figure 3.4), similar to the analysis used for the power-law spatial band selection. As before in Figure B.5, the left panel gives the RMS of the unwrapped interferograms, while the right panel gives the RMSE of the different tropospheric correction methods after subtracting the corrections from the unwrapped interferograms.

Assuming the unwrapped interferograms are correctly compensated for signals other than the troposphere, the maximum reduction in RMSE will be limited by the accuracy of the tropospheric correction method under consideration. For MERIS this corresponds to a RMSE level of ~ 1 cm (black line), computed using the measured ~ 1.1 mm PWV accuracy (Li *et al.*, 2006b).

In order not to limit ourselves to cloud free interferograms only, we split our dataset

into three classes: interferograms in which both SAR dates are cloud-free (triangular markers), those in which one of the SAR dates fails our 80% cloud-free threshold (circular markers), and those where both SAR dates fails our cloud-free threshold (diamond markers). By comparing the different classes, we observe all correction methods perform worse as cloud cover increases. On average we find a 22.5% RMSE increase for each additional cloudy SAR date, for all the methods.

Over the different regions, we find MERIS consistently gives the largest RMSE reduction, resulting in RMSE approximately equal to the MERIS ~ 1 cm accuracy level (black line). No uncertainty is introduced through temporal interpolation for MERIS, unlike for MODIS. Over Italy and Mexico, we find MODIS acquisitions are on average within ~ 25 minutes ($\sigma = 18$ minutes) of our SAR acquisition times, with a maximum time difference of around an hour. While both MERIS and MODIS have similar sensitivities, MODIS does not perform as well over Mexico, reducing the RMSE to only ~ 2 cm (twice as bad as the MERIS accuracy), while over Italy MODIS performs similarly to MERIS. While spectrometers are the preferred method in terms of RMSE reduction, the success-rate is limited to cloud-free and daylight acquisitions only. This excludes the use of spectrometer data for the correction of ascending SAR data for satellite systems in a sun-synchronous orbit with night-time ascending acquisitions, such as Envisat (ascending node at 22:00 local time at the equator), ERS 1/2 (22:28 at equator), ALOS (22.00 at equator), and ALOS2 (00:00 at equator). However, for SAR systems which operate in a sun-synchronous dawn-dusk orbit, such as Sentinel 1, Radarsat, Radarsat 2, the future NISAR mission (ascending node at 18:00 for all), and COSMO-SkyMed (ascending node at 06:00), spectrometer-derived corrections can potentially be used for both ascending and descending acquisitions. The application to ascending and descending tracks for these satellites is limited by variation in the length of day over winter and summer seasons, and as such will also be strongly influenced by the latitude of the target.

For Mexico and El Hierro, phase-based methods give a better RMSE reduction than weather models, and in the case of Mexico are also better than the MODIS spectrometer. Over Italy we find that none of the different methods, except for the spectrometers, reduces the RMSE on average.

With large topographic variations over Mexico, the main tropospheric signal contribution results from the topography-correlated component. The phase-based methods, especially designed to resolve the topography-correlated component, therefore are capable of retrieving the tropospheric delay, reducing the RMSE by 0.5 cm to an average RMSE level of 1.9 cm. Over Italy, tropospheric delays are more subject to signals introduced from local weather and turbulent variations, which results in a strongly under estimated tropospheric signal from the linear method with a maximum RMSE reduction of only ~ 0.05 cm on cloud-free interferograms, and 0.3 cm for the complete dataset to an average RMSE level of 1.2 cm. As the power-law is applied locally, it is

more strongly contaminated by the different tropospheric delay components, which are present at different spatial scales, leading to a biased estimation of $K'_{\Delta\phi}$, and an average RMSE increase of ~ 0.2 cm. This is also expressed by the large RMSE across the different power-law spatial bands (Figure B.5). Considering both phase-based methods have the potential to introduce incorrect signals in the presence of turbulence and coherent short-scale tropospheric signals, neither should be applied in those instances. However, for the linear correction method the impact of turbulence appears less severe than for the power-law method.

We do not observe an improvement by running a local high-resolution weather model. This can be observed at El Hierro, where the high-resolution model tries to estimate turbulence, but due to its incorrectly estimated location, is penalized with a larger RMSE. With high-resolution models offering only a minimal improvement and requiring additional computation, online available weather models are more suitable for near real-time InSAR processing.

Preferred correction methods depend on the region of application and the SAR satellite under consideration. However, from our analysis we find that each method has its limitations, which vary with region of application and with time. For future development we suggest that it would be optimal to combine the different correction methods in such a way that they can constrain each other. Further work is needed in order to identify suitable metrics that can be used to weight the different observations.

3.6 Conclusions

We performed a statistical comparison of different tropospheric correction methods with respect to unwrapped interferograms over Mexico, Italy, and El Hierro. Our analysis included methods based on spectrometer measurements, output of weather models, and empirical interferometric phase-based methods. When available and limited to cloud-free and daylight acquisitions only, we found the spectrometers to provide the largest RMSE reduction. We found that the estimated tropospheric delays using MODIS have at best an accuracy equal to that of MERIS, and at worst twice that of MERIS. We found the phase-based methods (linear and power-law) to outperform the weather model methods in regions where tropospheric delays are mainly correlated with topography. For regions over which this is less apparent, due to turbulence in the troposphere and dynamic local weather, weather models can potentially offer better performance. In those instances where weather models mis-estimate the location of turbulent features, they will have a correspondingly higher RMSE. We did not find a significant improvement when using a local high-resolution weather model (7 km and 2 km) instead of the global reanalysis products. With a longer required runtime, local weather model are less suitable for near real-time InSAR application. From a cloud cover analysis, we found the performance of the different correction methods to worsen

with increasing cloud cover, with a $\sim 10\text{-}20\%$ increase in RMSE for each cloudy SAR date.

We confirmed that the different tropospheric correction techniques all have their own limitations, and are not always sensitive to the same component of the tropospheric delay. We did not find any of the tropospheric correction methods to be best in reducing the tropospheric delays consistently over different regions and times. Therefore, we recommend future developments should aim towards combining the different correction methods in an optimal manner.

Together with this paper we release the Toolbox for Reducing Atmospheric InSAR Noise - TRAIN, which contains all the applied correction methods within this study. In future we will further expand this toolbox to include other corrections, such as those from GPS.

Acknowledgments

We acknowledge the Department of Atmospheric Science of the University of Wyoming for providing us the sounding data (downloaded from <http://weather.uwyo.edu/upperair/sounding.html>), JPL for providing us with the Online Services for Correcting Atmosphere in Radar (OSCAR) used to download the MODIS data (<http://oscar.jpl.nasa.gov>), the European Centre for Medium-Range Weather Forecasts (ECMWF) for providing the ERA-I weather model data. Envisat SAR and MERIS data were provided by the European Space Agency. Processed TerraSAR-X interferograms were provided by the Instituto Geográfico Nacional (IGN), Madrid. We acknowledge the Jet Propulsion Laboratory for providing us with ROI_PAC (*Rosen et al., 2004*), used to focus the raw SAR data, and the SRTM topographic data (*Farr et al., 2007*), used to correct for the topography in the interferograms. InSAR processing was achieved using the DORIS software (*Kampes et al., 2003*), and the StaMPS software (*Hooper et al., 2012*). Some figures were prepared using the public domain GMT software (*Wessel and Smith, 1991*). COMET is the NERC Centre for the Observation and Modelling of Earthquakes, Volcanoes and Tectonics. Results can be obtained by contacting the corresponding author (eedpsb@leeds.ac.uk). We thank two anonymous reviewers for their careful and thorough reviews, which helped to improve this manuscript.

References

- Béjar-Pizarro, M., A. Socquet, R. Armijo, D. Carrizo, J. Genrich, and M. Simons (2013), Andean structural control on interseismic coupling in the North Chile subduction zone, *Nature Geoscience*, 6, 462 – 467, doi:[10.1038/NGEO1802](https://doi.org/10.1038/NGEO1802). 3.1, 3.1
- Bekaert, D., A. Hooper, and T. Wright (2015a), Reassessing the 2006 Guerrero Slow Slip Event, Mexico: implications for large earthquakes in the Guerrero Gap, *J. Geophys. Res.*, 120, doi:[10.1002/2014JB011557](https://doi.org/10.1002/2014JB011557). 3.1, 3.4, 3.5
- Bekaert, D., A. Hooper, and T. Wright (2015b), A spatially-variable power-law tropospheric correction technique for InSAR data, *J. Geophys. Res.*, 120, doi:[10.1002/2014JB011558](https://doi.org/10.1002/2014JB011558). 3.1, 3.2.3, 3.2.3, 3.4
- Bevis, M., S. Businger, T. Herring, C. Rocken, R. Anthes, and R. Ware (1992), GPS meteorology: Remote sensing of atmospheric water vapor using the global positioning system, *J. Geophys. Res.*, 97(D14), 15,787 – 15,801, doi:[10.1029/92JD01517](https://doi.org/10.1029/92JD01517). 3.2.2, 3.2.2
- Cavalié, O., E. Pathier, M. Radiguet, M. Vergnolle, N. Cotte, A. Walpersdorf, V. Kostoglodov, and F. Cotton (2013), Slow slip event in the Mexican subduction zone: Evidence of shallower slip in the Guerrero seismic gap for the 2006 event revealed by the joint inversion of InSAR and GPS data, *Earth and Planetary Science Letters*, 367, doi:[10.1016/j.epsl.2013.02.020](https://doi.org/10.1016/j.epsl.2013.02.020). 3.1, 3.4
- Cheloni, D., R. Giuliani, E. D’Anastasio, S. Atzori, R. Walters, L. Bonci, N. D’Agostino, M. Mattone, S. Calcaterra, P. Gambino, F. Deninno, R. Maseroli, and G. Stefanelli (2014), Coseismic and post-seismic slip of the 2009 L’Aquila (central Italy) Mw 6.3 earthquake and implications for seismic potential along the Campotosto fault from joint inversion of high-precision levelling, InSAR and GPS data, *Tectonophysics*, 622, 168 – 185, doi:<http://dx.doi.org/10.1016/j.tecto.2014.03.009>. 3.4
- D’Agostino, N., R. Giuliani, M. Mattone, and L. Bonci (2001), Active crustal extension in the Central Apennines (Italy) inferred from GPS measurements in the interval 1994 - 1999, *Geophys. Res. Lett.*, 28(10), 2121 – 2124, doi:[10.1029/2000GL012462](https://doi.org/10.1029/2000GL012462). 3.4
- Davis, J., T. Herring, I. Shapiro, A. Rogers, and G. Elgered (1985), Geodesy by radio interferometry: Effects of atmospheric modeling errors on estimates of baseline length, *Radio Science*, 20(6), 1593 – 1607, doi:[10.1029/RS020i006p01593](https://doi.org/10.1029/RS020i006p01593). 3.2.2
- Dee, D. P., S. M. Uppala, A. J. Simmons, P. Berrisford, P. Poli, S. Kobayashi, U. Andrae, M. A. Balmaseda, G. Balsamo, P. Bauer, P. Bechtold, A. C. M. Beljaars, L. van de Berg, J. Bidlot, N. Bormann, C. Delsol, R. Dragani, M. Fuentes, A. J. Geer, L. Haimberger, S. B. Healy, H. Hersbach, E. V. Hlm, L. Isaksen, P. Killberg, M. Khler, M. Matricardi, A. P. McNally, B. M. Monge-Sanz, J.-J. Morcrette, B.-K. Park, C. Peubey, P. de Rosnay, C. Tavolato, J.-N. Thpaut, and F. Vitart (2011), The ERA-Interim reanalysis: configuration and performance of the data assimilation system, *Quarterly Journal of the Royal Meteorological Society*, 137(656), 553 – 597, doi:[10.1002/qj.828](https://doi.org/10.1002/qj.828). 3.1, 3.2.1

- Doin, M., C. Lasserre, G. Peltzer, O. Cavalié, and C. Doubre (2009), Corrections of stratified tropospheric delays in SAR interferometry: Validation with global atmospheric models, *Journal of Applied Geophysics*, *69*(1), 35 – 50, doi:[10.1016/j.jappgeo.2009.03.010](https://doi.org/10.1016/j.jappgeo.2009.03.010). 3.1, 3.2.1
- Elliott, J., J. Biggs, B. Parsons, and T. Wright (2008), InSAR slip rate determination on the Altyn Tagh Fault, northern Tibet, in the presence of topographically correlated atmospheric delays, *Geophys. Res. Lett.*, *35*(12), doi:[10.1029/2008GL033659](https://doi.org/10.1029/2008GL033659). 3.1
- ESA (2011), Meris level 2 detailed processing model, *Tech. Rep. PO-TN-MEL-GS-0006*, European Space Agency, issue 8, Rev 0B. 3.2.2
- Farr, T., P. Rosen, E. Caro, R. Crippen, R. Duren, S. Hensley, M. Kobrick, M. Paller, E. Rodriguez, L. Roth, D. Seal, S. Shaffer, J. Shimada, J. Umland, M. Werner, M. Oskin, D. Burbank, and D. Alsdorf (2007), The Shuttle Radar Topography Mission, *Reviews of Geophysics*, *45*(2), doi:[10.1029/2005RG000183](https://doi.org/10.1029/2005RG000183). 3.6
- Fournier, T., M. Pritchard, and N. Finnegan (2011), Accounting for Atmospheric Delays in InSAR Data in a Search for Long-Wavelength Deformation in South America, *IEEE Transactions on Geoscience and Remote Sensing*, *49*(10), 3856 – 3867, doi:[10.1109/TGRS.2011.2139217](https://doi.org/10.1109/TGRS.2011.2139217). 3.1
- Gao, B., and Y. J. Kaufman (2003), Water vapor retrievals using Moderate Resolution Imaging Spectroradiometer (MODIS) near-infrared channels, *J. Geophys. Res.*, *108*(D13), doi:[10.1029/2002JD003023](https://doi.org/10.1029/2002JD003023). 3.2.2
- González, P. J., S. V. Samsonov, S. Pepe, K. F. Tiampo, P. Tizzani, F. Casu, J. Fernández, A. G. Camacho, and E. Sansosti (2013), Magma storage and migration associated with the 2011 - 2012 El Hierro eruption: Implications for crustal magmatic systems at oceanic island volcanoes, *J. Geophys. Res.*, *118*(8), 4361 – 4377, doi:[10.1002/jgrb.50289](https://doi.org/10.1002/jgrb.50289). 3.4
- Gray, A. L., K. E. Mattar, and G. Sofko (2000), Influence of ionospheric electron density fluctuations on satellite radar interferometry, *Geophys. Res. Lett.*, *27*(10), 1451 – 1454, doi:[10.1029/2000GL000016](https://doi.org/10.1029/2000GL000016). 3.1
- Hanssen, R. F. (2001), Remote Sensing and Digital Image Processing, in *Radar Interferometry: Data interpretation and error analysis*, *Earth and Environmental Science*, vol. 2, edited by F. van der Meer, Kluwer Academic Publishers, Dordrecht, The Netherlands. 3.1, 3.2
- Hooper, A., P. Segall, and H. Zebker (2007), Persistent scatterer interferometric synthetic aperture radar for crustal deformation analysis, with application to Volcán Alcedo, Galápagos, *J. Geophys. Res.*, *112*(B7), doi:[10.1029/2006JB004763](https://doi.org/10.1029/2006JB004763). 3.3
- Hooper, A., D. Bekaert, K. Spaans, and M. Arikan (2012), Recent advances in SAR interferometry time series analysis for measuring crustal deformation, *Tectonophysics*, *514*517, 1 – 13, doi:<http://dx.doi.org/10.1016/j.tecto.2011.10.013>. 3.4, 3.6
- Hooper, A., J. Pietrzak, W. Simons, H. Cui, R. Riva, M. Naeije, A. T. van Scheltinga, E. Schrama, G. Stelling, and A. Socquet (2013), Importance of horizontal seafloor motion on tsunami height for the 2011 Mw=9.0 Tohoku-Oki earthquake, *Earth and Planetary Science Letters*, *361*, 469 – 479, doi:[10.1016/j.epsl.2012.11.013](https://doi.org/10.1016/j.epsl.2012.11.013). 3.1
- Jolivet, R., R. Grandin, C. Lasserre, M. Doin, and G. Peltzer (2011), Systematic InSAR tropospheric phase delay corrections from global meteorological reanalysis data, *Geophys. Res. Lett.*, *38*(17), doi:[10.1029/2011GL048757](https://doi.org/10.1029/2011GL048757). 3.1, 3.2.1
- Jolivet, R., C. Lasserre, M. Doin, S. Guillaso, G. Peltzer, R. Dailu, J. Sun, Z. Shen, and X. Xu (2012), Shallow creep on the Haiyuan Fault (Gansu, China) revealed by SAR Interferometry, *J. Geophys. Res.*, *117*(B6), doi:[10.1029/2011JB008732](https://doi.org/10.1029/2011JB008732). 3.1

- Jolivet, R., P. S. Agram, N. Lin, M. Simons, M. Doin, G. Peltzer, and Z. Li (2014), Improving InSAR geodesy using Global Atmospheric Models, *J. Geophys. Res.*, *119*(3), 23242341, doi:[10.1002/2013JB010588](https://doi.org/10.1002/2013JB010588). 3.1
- Kampes, B., R. Hanssen, and Z. Perski (2003), Radar interferometry with public domain tools, *Proceedings Fringe 2003*, p. 6. 3.3, 3.6
- Li, Z., J. Muller, and P. Cross (2003), Comparison of precipitable water vapor derived from radiosonde, GPS, and Moderate-Resolution Imaging Spectroradiometer measurements, *J. Geophys. Res.*, *108*(D20), doi:[10.1029/2003JD003372](https://doi.org/10.1029/2003JD003372). 3.2.2, 3.2.2, 3.5
- Li, Z., J. Muller, P. Cross, and E. Fielding (2005), Interferometric synthetic aperture radar (InSAR) atmospheric correction: GPS, Moderate Resolution Imaging Spectroradiometer (MODIS), and InSAR integration, *J. Geophys. Res.*, *110*(B3), doi:[10.1029/2004JB003446](https://doi.org/10.1029/2004JB003446). 3.1, 3.5
- Li, Z., E. Fielding, P. Cross, and J. Muller (2006a), Interferometric synthetic aperture radar atmospheric correction: GPS topography-dependent turbulence model, *J. Geophys. Res.*, *111*(B2), doi:[10.1029/2005JB003711](https://doi.org/10.1029/2005JB003711). 3.1
- Li, Z., J. Muller, P. Cross, P. Albert, J. Fischer, and R. Bennartz (2006b), Assessment of the potential of MERIS near infrared water vapour products to correct ASAR interferometric measurements, *International Journal of Remote Sensing*, *27*(2), 349 – 365, doi:[10.1080/01431160500307342](https://doi.org/10.1080/01431160500307342). 3.1, 3.2.2, 3.2.2, 3.5
- Li, Z., E. Fielding, P. Cross, and R. Preusker (2009a), Advanced InSAR atmospheric correction: MERIS/MODIS combination and stacked water vapour models, *International Journal of Remote Sensing*, *30*(13), 3343 – 3363, doi:[10.1080/01431160802562172](https://doi.org/10.1080/01431160802562172). 3.1
- Li, Z., E. Fielding, and P. Cross (2009b), Integration of InSAR Time-Series Analysis and Water-Vapor Correction for Mapping Postseismic Motion After the 2003 Bam (Iran) Earthquake, *IEEE Transactions on Geoscience and Remote Sensing*, *47*(9), 3220 – 3230, doi:[10.1109/TGRS.2009.2019125](https://doi.org/10.1109/TGRS.2009.2019125). 3.1
- Lin, Y., M. Simons, E. Hetland, P. Muse, and C. DiCaprio (2010), A multiscale approach to estimating topographically correlated propagation delays in radar interferograms, *Geochem. Geophys. Geosyst.*, *11*(9). 3.1
- Liu, S., R. Hanssen, and A. Mika (2009), On the value of high-resolution weather models for atmospheric mitigation in sar interferometry, in *Geoscience and Remote Sensing Symposium, 2009 IEEE International, IGARSS 2009*, vol. 2, pp. II-749 – II-752, doi:[10.1109/IGARSS.2009.5418199](https://doi.org/10.1109/IGARSS.2009.5418199). 3.1, 3.2
- Löfgren, J., F. Björndahl, A. Moore, F. Webb, E. Fielding, and E. Fishbein (2010), Tropospheric correction for InSAR using interpolated ECMWF data and GPS Zenith Total Delay from the Southern California Integrated GPS Network, in *Geoscience and Remote Sensing Symposium (IGARSS), 2010 IEEE International*, pp. 4503 – 4506, doi:[10.1109/IGARSS.2010.5649888](https://doi.org/10.1109/IGARSS.2010.5649888). 3.1
- Marinkovic, P., and Y. Larsen (2015), On resolving the Local Oscillator drift induced phase ramps in ASAR and ERS1/2 interferometric data - the final solution, in *Fringe 2015 Workshop (ESA SP - 731)*. 3.3
- Markowski, P., and Y. Richardson (Eds.) (2010), *Mesoscale Meteorology in Midlatitudes*, Wiley-Blackwell, Southern Gate, Ghichester, West Succex, UK, edition 1. 3.2.3, 3.2.3
- Michalakes, J., J. Dudhia, D. Gill, T. Henderson, J. Klemp, W. Skamarock, and W. Wang (2004), The weather reseach and forecast model: Software architecture and performance, in *Proceedings of the 11th ECMWF Workshop on the Use of High Performance Computing In Meteorology*, edited by G. Mozdzynski, Reading, United Kingdom. 3.1, 3.2.1

- Niell, A., A. Coster, F. Solheim, V. Mendes, P. Toor, R. Langley, and C. Upham (2001), Comparison of measurements of atmospheric wet delay by radiosonde, water vapor radiometer, GPS, and VLBI, *J. Atmos. Oceanic Technol.*, *18*, 830 – 850. [3.2.2](#)
- Onn, F., and H. Zebker (2006), Correction for interferometric synthetic aperture radar at-mospheric phase artifacts using time series of zenith wet delay observations from a GPS network, *J. Geophys. Res.*, *111*(B9), doi:[10.1029/2005JB004012](#). [3.1](#)
- Puysségur, B., R. Michel, and J. Avouac (2007), Tropospheric phase delay in interferometric synthetic aperture radar estimated from meteorological model and multi-spectral imagery, *J. Geophys. Res.*, *112*(B5), doi:[10.1029/2006JB004352](#). [3.1](#)
- Rosen, P., S. Henley, G. Peltzer, and M. Simons (2004), Updated Repeat Orbit Interferometry Package Released, *Eos Trans. AGU*, *85*(5), 47 – 47, doi:[10.1029/2004EO050004](#). [3.3](#), [3.6](#)
- Saha, S., S. Moorthi, H.-L. Pan, X. Wu, J. Wang, S. Nadiga, P. Tripp, R. Kistler, J. Woollen, D. Behringer, H. Liu, D. Stokes, R. Grumbine, G. Gayno, J. Wang, Y.-T. Hou, H.-Y. Chuang, H.-M. H. Juang, J. Sela, M. Iredell, R. Treadon, D. Kleist, P. Van Delst, D. Keyser, J. Derber, M. Ek, J. Meng, H. Wei, R. Yang, S. Lord, H. van den Dool, A. Kumar, W. Wang, C. Long, M. Chelliah, Y. Xue, B. Huang, J.-K. Schemm, W. Ebisuzaki, R. Lin, P. Xie, M. Chen, S. Zhou, W. Higgins, C.-Z. Zou, Q. Liu, Y. Chen, Y. Han, L. Cucurull, R. W. Reynolds, G. Rutledge, and M. Goldberg (2010), NCEP Climate Forecast System Reanalysis (CFSR) 6-hourly Products, January 1979 to December 2010, [Accessed Dec 2013]. [3.2.1](#)
- Smith, E., and S. Weintraub (1953), The Constants in the Equation for Atmospheric Refractive Index at Radio Frequencies, *Proceeding of the IRE*, *41*(8), 1035 – 1037, doi:[10.1109/JRPROC.1953.274297](#). [3.1](#)
- Unidata, University Corporation for Atmospheric Research and National Centers for Environmental Prediction, National Weather Service, NOAA, U.S. Department of Commerce, and European Centre for Medium-Range Weather Forecasts (2003), Historical Unidata Internet Data Distribution (IDD) Gridded Model Data, December 2002 - current, [Accessed Dec 2013]. [3.2.1](#)
- Wadge, G., P. Webley, I. James, R. Bingley, A. Dodson, S. Waugh, T. Veneboer, G. Puglisi, M. Mattia, D. Baker, S. Edwards, S. Edwards, and P. Clarke (2002), Atmospheric models, GPS and InSAR measurements of the tropospheric water vapour field over Mount Etna, *Geophys. Res. Lett.*, *29*, doi:[10.1029/2002GL015159](#). [3.1](#)
- Walters, R., J. Elliott, , Z. Li, and B. Parsons (2013), Rapid strain accumulation on the Ashkabad fault (Turkmenistan) from atmosphere-corrected InSAR, *Geophys. Res. Lett.*, *118*, 3674 – 3690, doi:[10.1002/jgrb.50236](#). [3.1](#)
- Walters, R., B. Parsons, and T. Wright (2014), Constraining crustal velocity fields with InSAR for Eastern Turkey: Limits to the block-like behaviour of Eastern Anatolia, *J. Geophys. Res.*, *119*(6), 5215 – 5234, doi:[10.1002/2013JB010909](#). [3.1](#)
- Walters, R. J., J. R. Elliott, N. D’Agostino, P. C. England, I. Hunstad, J. A. Jackson, B. Parsons, R. J. Phillips, and G. Roberts (2009), The 2009 L’Aquila earthquake (central Italy): A source mechanism and implications for seismic hazard, *Geophysical Research Letters*, *36*(17), doi:[10.1029/2009GL039337](#). [3.4](#)
- Wessel, P., and W. Smith (1991), Free Software helps Map and Display Data, *Eos Trans. AGU*, *72*(41), 445 – 446, doi:[10.1029/90EO00319](#). [3.6](#)
- Wicks, C., D. Dzurisin, S. Ingebritsen, W. Thatcher, Z. Lu, and J. Iverson (2002), Magmatic activity beneath the quiescent Three Sisters volcanic center, central Oregon Cascade Range, USA, *Geophys. Res. Lett.*, *29*(7), 26–1 – 26–4, doi:[10.1029/2001GL014205](#). [3.1](#)

- Williams, S., Y. Bock, and P. Fang (1998), Integrated satellite interferometry: tropospheric noise, GPS estimates and implications for interferometric synthetic aperture radar products, *J. Geophys. Res.*, *103*(B11), 27,051 – 27,067, doi:[10.1029/98JB02794](https://doi.org/10.1029/98JB02794).
3.1

Chapter 4

Reassessing the 2006 Guerrero slow slip event, Mexico: implications for large earthquakes in the Guerrero Gap

D.P.S. Bekaert^{1,2}, A.J. Hooper^{1,2}, and T.J. Wright¹

¹ *COMET, School of Earth and Environment, University of Leeds, United Kingdom*

² *Formerly, Department of Geoscience and Remote Sensing, Delft University of
Technology, Delft, The Netherlands*

Abstract

In Guerrero, Mexico, slow slip events have been observed in a seismic Gap, where no earthquakes have occurred since 1911. A rupture of the entire Gap today could result in a M_w 8.0-8.4 earthquake. However, it remains unclear how slow slip events change the stress field in the Guerrero seismic region, and what their implications are for devastating earthquakes. Most earlier studies have relied on a sparse network of GNSS measurements. Here we show that Interferometric Synthetic Aperture Radar (InSAR) can be used to improve the spatial resolution. We find slip due to the 2006 slow slip event enters the seismogenic zone and the Guerrero Gap, with ~ 5 cm slip reaching depths as shallow as 12 km. We show that slow slip is correlated with a highly coupled region, and estimate that slow slip events have decreased the total accumulated moment since the end of the 2001/2002 slow slip event (4.7 years) by $\sim 50\%$. Nevertheless, even accounting for slow slip, the moment deficit in the Guerrero Gap increases each year by $M_w \sim 6.8$. The Guerrero Gap therefore still has the potential for a large earthquake, with a slip deficit equivalent to $M_w \sim 8.15$ accumulated over the

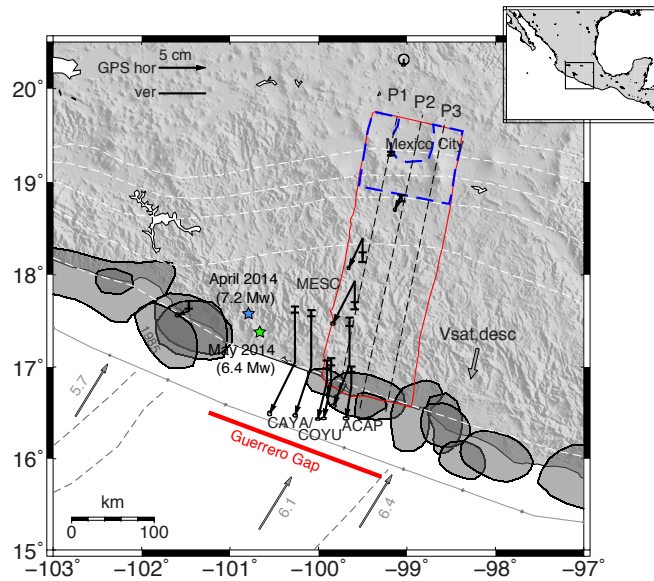


Figure 4.1: Horizontal and vertical displacements for the 2006 SSE from [Vergnolle et al. \(2010\)](#) estimated from GNSS in a North America reference frame. The gray arrows indicate the MORVEL relative plate motion of the Cocos and the North America Plate ([DeMets et al., 2010](#)). Gray polygons represent rupture areas of major earthquakes ([Kostoglodov et al., 2003](#)). The red solid line indicates the extent of our SAR data, while the blue dashed line, in the north of our study area, indicates the extent of the area assumed not to be deforming, used to compute weights of the residual noise and slave atmospheric signal for our time-series model. The SAR sensor is most sensitive to displacements perpendicular to the satellite flight direction. As most of the horizontal displacements are in the flight direction, the SAR is mainly sensitive to the vertical displacement component. P(1-3) refer to the profiles in Figure 4.8. The rupture of the 1985 earthquake is indicated. The recent 2014 Guerrero earthquakes, which occurred on the western edge of the gap, are indicated by the stars.

last century. Correlation between the slow slip region and non-volcanic tremor, and between slow slip and an ultra slow velocity layer supports the hypothesis of a common source potentially related to high pore pressures.

4.1 Introduction

In southern Mexico, the Cocos plate subducts beneath the North America plate at a rate of ~ 6.1 cm/year ([DeMets et al., 2010](#)), posing a huge hazard for coastal cities like Acapulco, and also for nearby Mexico City. A M_w 8.0 earthquake in 1985 caused more than 10,000 deaths in Mexico City and 3-4 billion U.S. dollars of damage (USGS). Since then the city population has swelled to 21 million. Of particular concern is a region of the subduction interface where no significant earthquake has occurred since 1911 ($101.2^\circ\text{W} - 99.2^\circ\text{W}$), referred to as the “Guerrero Gap” (Figure 4.1). The largest slip deficit is assumed to be located on the northwestern section of the Gap ($101.2^\circ\text{W} - 100.4^\circ\text{W}$) ([Kostoglodov et al., 1996](#)), as some slip is thought to have been released on the southeastern section by the M_w 7.7 earthquake in 1957, and the M_w 7.1 and 7.0

earthquakes in 1962 (*Ortiz et al., 2000*). Prior to the discovery of slow slip events by *Lowry et al. (2001)*, *Singh and Mortera (1991)* estimated that a rupture of the Guerrero Gap today could result in an earthquake of M_w 8.2-8.4.

Slow earthquakes, also denoted as slow slip events (SSEs), release strain over days to years. While SSEs are not in themselves hazardous, they alter the stress field and can therefore have an impact on the timing of subsequent, potentially damaging earthquakes. Since 1995 one large event has been observed in Guerrero approximately every 3-5 years; in 1995 (*Larson et al., 2004, Vergnolle et al., 2010*), 1998 (*Lowry et al., 2001, Larson et al., 2004, Vergnolle et al., 2010*), 2001/2002 (*Kostoglodov et al., 2003, Iglesias et al., 2004, Vergnolle et al., 2010*), 2006 (*Larson et al., 2007, Correa-Mora et al., 2009, Vergnolle et al., 2010, Radiguet et al., 2011, Bekaert, 2011, Hooper et al., 2012, Cavalié et al., 2013*), and 2009/2010 (*Walpersdorf et al., 2011*). Of the more recent events, the 2006 SSE started around April 2006 and lasted till December 2006 (*Larson et al., 2007, Correa-Mora et al., 2009*) or perhaps February 2007 (*Vergnolle et al., 2010*). Continuous GNSS observations by *Vergnolle et al. (2010)* (Figure 4.1) show that the surface displacements associated with this SSE are small (maximum ~ 5.6 cm) and extend over a large area. Sites near the coast (CAYA and COYU) uplifted by ~ 5.6 cm, over a period of 9-10 months. About 110 km inland, sites subsided up to ~ 2.6 cm (MESC), with displacements due to the SSE decreasing to zero beyond 250-300 km. The cumulative horizontal displacements for most of the sites are in a southwesterly direction, with the largest displacement reaching approximately 5.5 cm at CAYA. In general, the surface displacements associated with the slow slip events extends from the coast to Mexico City, 300 km inland.

Until very recently, studies of slow slip on the Mexico subduction zone have relied only on a sparse GNSS network only (*Lowry et al., 2001, Kostoglodov et al., 2003, Larson et al., 2004, Iglesias et al., 2004, Larson et al., 2007, Correa-Mora et al., 2009, Vergnolle et al., 2010*), leading to poor spatial resolution of the slow slip itself. In this study, which focuses on the 2006 event, we increase the number of data points by orders of magnitude by including Interferometric Synthetic Aperture Radar (InSAR) data, and perform a joint inversion of the GNSS (*Vergnolle et al., 2010*) and InSAR data for slow slip on the subducting interface. This is an extension of our preliminary work (*Bekaert, 2011, Hooper et al., 2012*). *Cavalié et al. (2013)* also included stacked InSAR data in their recent study, but here we use time-series analysis of the InSAR data, to invert for slip in an optimal way, taking into account the full variance-covariance of the data, and allowing for variable smoothness of slip. We also apply a new method to reduce error contribution from the troposphere, which is described in a companion paper to this study (*Bekaert et al., 2015*). Finally, we use our estimated slow slip solution to estimate the slip deficit accumulated since the end of the 2001/2002 slow slip event till the end of the 2006 slow slip event, and discuss the implications for earthquakes in the Guerrero Gap.

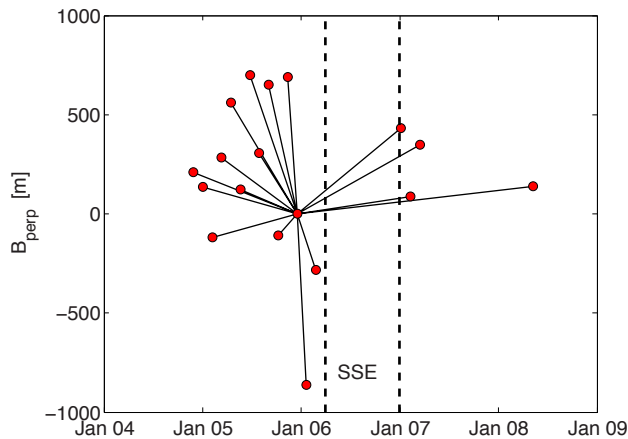


Figure 4.2: Envisat PS-InSAR network showing the perpendicular and temporal baselines. Solid lines indicate interferograms, while the markers show individual SAR acquisitions. All interferograms are with respect to the master SAR image acquired on 16 December 2005. The duration of the 2006 slow slip event is indicated by the dashed vertical lines.

Table 4.1: Dataset baseline information. Perpendicular (B_{perp}), temporal (T) and absolute Doppler centroid (Δf_{DC}) baselines. All interferograms are relative to the master of 16 Dec 2005.

Date	B_{perp} [m]	T [days]	Δf_{DC} [Hz]	Date	B_{perp} [m]	T [days]	Δf_{DC} [Hz]
26 Nov 2004	210	-385	23.4	7 Oct 2005	-110	-70	-4.0
31 Dec 2004	134	-350	24.6	11 Nov 2005	690	-35	0.1
4 Feb 2005	-120	-315	25.9	20 Jan 2006	-864	35	-4.1
11 Mar 2005	283	-280	17.3	24 Feb 2006	-282	70	-1.8
15 Apr 2005	561	-245	21.4	5 Jan 2007	430	385	5.8
20 May 2005	123	-210	26.7	9 Feb 2007	86	420	1.8
24 Jun 2005	700	-175	25.4	16 Mar 2007	349	455	-3.5
29 Jul 2005	305	-140	25.4	9 May 2008	138	875	5.4
2 Sep 2005	652	-105	26.0				

4.2 InSAR processing

We used 18 Envisat (C-band) SAR images to study the 2006 SSE. The images cover an area from the coast to Mexico City, approximately 300 km inland (Figure 4.1), and were acquired during the interseismic period from 2004-2008, before and after the 2006 SSE. Figure 4.2 shows the temporal and perpendicular baselines of the processed single master network. Of the 17 interferograms, 4 span the SSE in time. Exact values, together with the Doppler centroid baselines, are given in Table 4.1.

We focused the data using the ROI-PAC software (*Rosen et al., 2004*), followed by the interferometric processing using the DORIS software (*Kampes et al., 2003*). In our processing we used the 90 m SRTM DEM (*Farr et al., 2007*) to reduce topographic contributions. The change in surface properties between two SAR acquisitions as well

Table 4.2: Applied InSAR processing parameters. DORIS (D) (*Kampes et al., 2003*) and StaMPS (S) (*Hooper et al., 2012*)

Parameter	Value	Parameter	Value
SRTM DEM (D)	90 m	Density random (S)	20 %
Multi-look factor (D)	1x1	Weed max noise (S)	inf
Oversample (D)	no	Weed σ (S)	1
Dispersion threshold (S)	0.4	Unwrap grid size (S)	1000 m
number of patches (S)	144	Merge resample size (S)	1000 m
Processing method (S)	Density	Merge σ (S)	0.45 rad

as the specific satellite acquisition geometry adds decorrelation noise (*Zebker, 1992*). This makes unwrapping more difficult, particularly in the more vegetated regions near the coast. We reduce the noise contribution by applying the StaMPS time-series InSAR technique (*Hooper et al., 2007*), in order to select only those pixels that demonstrate stable phase characteristics in time. A summary of the applied DORIS and StaMPS processing parameters are given in Table 4.2. Spatial-temporal variation in the troposphere leads to an additional signal in the interferograms, with a turbulent component (mostly affecting length scales up to a few km), and a long-wavelength component (>10 km). The turbulent component results from troposphere dynamics, while the long-wavelength component is related to variations in pressure, temperature and relative humidity. Tropospheric delays in interferograms record the integrated delay along the entire travelled path of the radar signal, hence the long-wavelength component exhibits a correlation with the topography. In our study, tropospheric delay masks the smaller slow slip displacement signal (*Hooper et al., 2012*); we observe large tropospheric delays with an average correlation between the unwrapped phase and the topography of $K_{\Delta\phi}=2.8$ rad/km (~ 1.2 cm/km) (*Bekaert et al., 2015*). $K_{\Delta\phi}$ varies spatially and using a single value over a large regions fails to improve the result. Instead, we account for the spatially-varying tropospheric signal by applying a power-law correction technique, assuming an exponent of 1.4 and a reference height of 7 km, both estimated from sounding data for the observed period of time. An in-depth discussion on the tropospheric correction technique and the results used in this study are contained in our companion paper, *Bekaert et al. (2015)*. The wrapped and unwrapped interferograms after time-series processing and correction for tropospheric errors are included in *Bekaert et al. (2015)* and shown in Figure 2.6.

4.3 Time-series InSAR analysis

Once we have corrected the data for the height-dependent tropospheric signal we model the slow slip deformation using elastic dislocation theory. As none of the SAR acquisitions were acquired during the event itself, the time series shows a discrete jump at the time of the SSE corresponding to the slow slip displacement signal d_{SSE} . We

assume the secular velocity v_{sec} to be constant, as was found in the GNSS processing (Vergnolle *et al.*, 2010). In our time-series model d_{SSE} thus represents the cumulative slow slip deformation as the deviation from the secular or inter-SSE velocity, which is consistent with the GNSS estimates from Vergnolle *et al.* (2010) used in this study. In our time-series inversion we estimate d_{SSE} and v_{sec} simultaneously with DEM errors, which correlate with perpendicular baseline B_{perp} , and an atmospheric and noise signal common to all interferograms, referred to as the residual master atmospheric signal, a_m . The linear model describing the change of the interferometric phase $\Delta\phi$ in time, for a single time-series point, is:

$$E\{\Delta\phi\} = \mathbf{A}\mathbf{x} \quad (4.1)$$

$$E\left\{\begin{bmatrix} \Delta\phi_{t_1} \\ \vdots \\ \Delta\phi_{t_{k-1}} \\ \Delta\phi_{t_k} \\ \vdots \\ \Delta\phi_n \end{bmatrix}\right\} = -\frac{4\pi}{\lambda} \begin{bmatrix} \Delta t_1 & 1 & 0 & B_{perp_1} \\ \vdots & \vdots & \vdots & \vdots \\ \Delta t_{k-1} & \vdots & 0 & \vdots \\ \Delta t_k & \vdots & 1 & \vdots \\ \vdots & \vdots & \vdots & \vdots \\ \Delta t_n & 1 & 1 & B_{perp_n} \end{bmatrix} \begin{bmatrix} v_{sec} \\ a_m \\ d_{SSE} \\ c_{topo} \end{bmatrix},$$

where \mathbf{A} is the design matrix and \mathbf{x} is a vector of unknowns. $E\{\cdot\}$ represents the expectation operator, Δt the time between the master and slave acquisition, n the total number of observations in time (interferograms), and $-4\pi/\lambda$ the conversion from the interferometric phase to line-of-sight displacement, as before. All interferograms up to time t_{k-1} are prior to the slip event and thus do not directly include an estimate for d_{SSE} , hence the partial zero column in \mathbf{A} . All interferograms help in constraining the secular velocity. We estimate the unknown parameters by applying weighted least squares, weighted by the inverse variance-covariance matrix of the data $\mathbf{Q}_{\Delta\phi}$. Note that v_{sec} , d_{SSE} , and c_{topo} are independent of the choice of master date; only a_m will change if a different master date is selected, under the assumption that the data are unwrapped correctly.

Correcting for the height-dependent tropospheric signal does not remove all the atmospheric signals. While the impact of the residual atmospheric signal is small on the estimation of the DEM errors and the master atmospheric signal, it strongly affects the estimation of the secular velocity and the slow slip displacement signal. For these we observe large spatial variations near the coast and towards the north of our InSAR study area. We also observe a strong anti-correlation between them (Figure 4.3). To account for this in our stochastic model, we define our diagonal variance-covariance matrix $\mathbf{Q}_{\Delta\phi}$ such that we include the residual noise and slave atmospheric signal. For each interferogram we estimate the data variance, in a non-deforming area (shown by the blue polygon in Figure 4.1), after correction for an initial estimate of the DEM

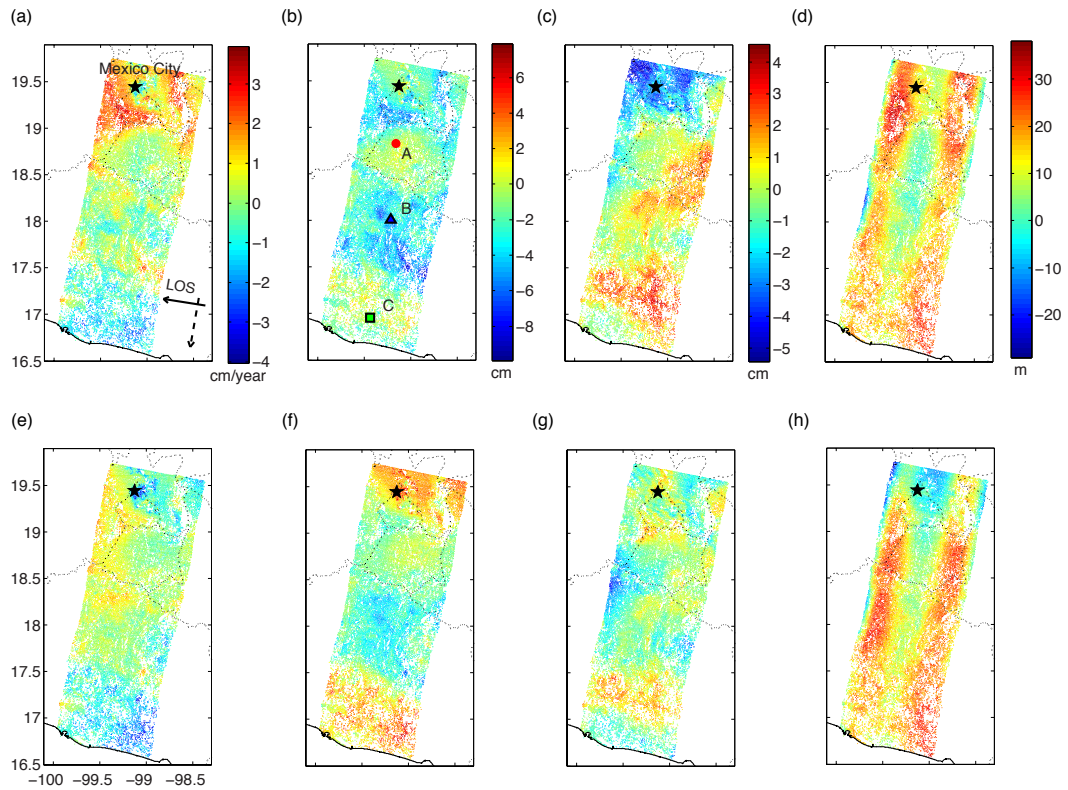


Figure 4.3: Line-of-sight (LOS) estimates for (a,e) the interseismic velocity, (b,f) the slow slip surface displacement, (c,g) the master atmosphere, and (d,h) the DEM converted errors. In absence of a tropospheric correction (top row) a high spatial correlation is observed between the estimated displacements and the surface topography. After tropospheric correction, second row, the signal-topography correlation is reduced, as can also be seen in a lower magnitude of the residual master atmosphere, (d) versus (h). A, B and C in (b) give the location of the individual points for which the surface displacement time-series is shown in Figure 4.5(c).

errors and the master atmospheric signal, estimated assuming uniform weights. The non-deforming area extends over the region where we do not expect LOS displacements associated with the interseismic deformation or the SSE (*Vergnolle et al., 2010*). We also excluded Mexico City due to its large subsidence rate.

4.4 Error distribution of the surface displacements

We determine the error distribution of our model parameters, used for the slow slip modeling on the subduction interface, through the percentile bootstrap method (*Efron and Tibshirani, 1986*). As opposed to the regular algorithm, where n random samples are taken from n observations, we select n_1 and n_2 random samples respectively from the n_1 and n_2 observations (interferograms) before and after the SSE. Using this approach the model design matrix remains invertible for each bootstrap simulation, i.e. there will always be at least one interferogram that spans the slip event. Each bootstrap simulation provides us with an estimate for the unknown model parameters (v_{sec} , a_m ,

d_{SSE} and c_{topo}) at each point.

Estimating the full variance-covariance matrix directly from bootstrapping is not possible, as outliers in the model strongly bias the covariance terms. Moreover, while the variance terms are not strongly biased by outliers, the variance estimate of a point P_i obtained from the bootstrapped data contains, besides its actual variance, also a variance and covariance component of the reference area or point P_j ,

$$\hat{\sigma}_{\Delta ij}^2 = \sigma_i^2 + \sigma_j^2 - 2C_{ij}(x), \quad (4.2)$$

with $\hat{\sigma}_{\Delta ij}^2$ the estimated variance at point P_i computed from the bootstrapped data, σ_i^2 and σ_j^2 respectively the actual variance at P_i and P_j , and $C_{ij}(x)$ the covariance between both P_i and P_j , which varies with separation distance x . Assuming equal point variance P_i and P_j , equation (4.2) can be re-written to the equation of a semi-variogram (*Wackernagel, 2003*); see Appendix 4.8 for a full derivation. We constructed our noise variance-covariance matrix using the covariance function fitted to the semi-variogram of the slow slip displacement residuals ϵ . The latter is calculated as the difference between the bootstrapped estimates of the slow slip displacement signal and the weighted least squares estimate, i.e. $\epsilon = \hat{\mathbf{d}}_{SSE}^{boot} - \hat{\mathbf{d}}_{SSE}$. An example of the estimated semi-variogram is shown in Figure C.2.

4.5 Modeling the 2006 SSE

The position and structure of the Guerrero subduction interface has been previously estimated from a variety of data, including seismicity and focal mechanics (*Singh and Pardo, 1993, Pardo and Suárez, 1995*), geologic records and volcanic features (*Ferrari, 2004*), and from the analysis of the Meso America Subduction Experiment (MASE) broadband seismic network (*Pérez-Campos et al., 2008, Kim et al., 2010*). The Pacific plate subducts beneath the North America plate about 66 km south-southwest off the coastal city Acapulco with a dip angle of 15° and becomes sub-horizontal at a depth of 40 km, approximately 80 km north-northeast from Acapulco (Figure 4.4). The interface remains horizontal until about 230-250 km from the coast, after which it dips steeply below the Trans-Mexican Volcanic Belt, at an angle of 75° (*Kim et al., 2010, Chen and Clayton, 2012*). We use the same subduction geometry as *Radiquet et al. (2012)* and *Cavalié et al. (2013)* (red solid line in Figure 4.4), which correlates with observations from receiver functions (*Kim et al., 2010*) (green markers).

We model the slip event by dividing the fault into 25x25 km dislocation patches and inverting for slip on the interface to fit the slow slip surface displacements. The relationship between slip on the interface and the surface displacement, assuming a homogeneous elastic half-space, is given by the Green's functions in *Okada (1985)*. We assume a Poisson's ratio of 0.25, and use the GNSS and our InSAR displacements

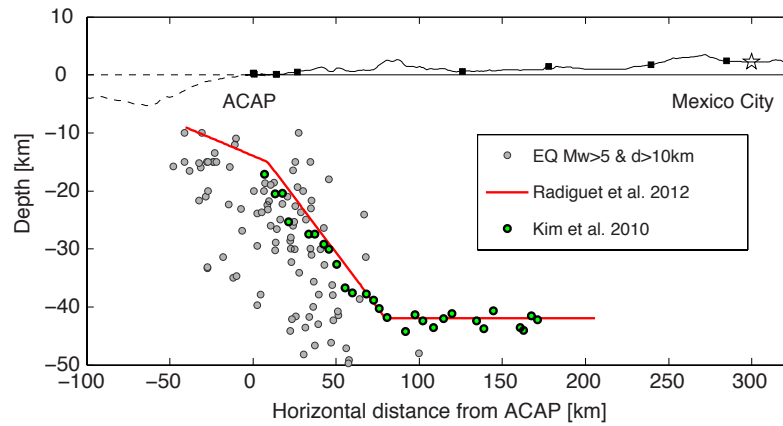


Figure 4.4: Subduction interface model of the Cocos plate (beneath) and the North America plate (above), as used in this study and by *Radiguet et al. (2012)*, *Cavalié et al. (2013)* (solid red). Interface as determined from Receiver Function tomography of teleseismic earthquakes using the MASE network (*Kim et al., 2010*) is shown by the green markers. Topography information as well as the GNSS stations locations (black square markers) are plotted with respect to the distance to the coastal ACAP GNSS station, located in Acapulco. The interface is modelled in 25x25 km dislocation patches, extending 450 km in the strike direction. In total we use 180 patches to model. Ocean bottom topography data has been extracted from the GEBCO_08 Grid (version 20091120, <http://www.gebco.net>), while for the elevations we made use of the SRTM DEM.

during the SSE as our observations, resulting in the following slip model:

$$E \left\{ \begin{bmatrix} \mathbf{d}_{LOS}^{InSAR} \\ \mathbf{d}_N^{GNSS} \\ \mathbf{d}_E^{GNSS} \\ \mathbf{d}_U^{GNSS} \end{bmatrix} \right\} = \begin{bmatrix} \mathbf{G}_{LOS}^{InSAR} & \mathbf{x} & \mathbf{y} & \mathbf{1} \\ \mathbf{G}_N^{GNSS} & \mathbf{0} & \mathbf{0} & \mathbf{0} \\ \mathbf{G}_E^{GNSS} & \mathbf{0} & \mathbf{0} & \mathbf{0} \\ \mathbf{G}_U^{GNSS} & \mathbf{0} & \mathbf{0} & \mathbf{0} \end{bmatrix} \begin{bmatrix} \mathbf{s} \\ \alpha_{pl} \\ \beta_{pl} \\ \gamma_{pl} \end{bmatrix},$$

where \mathbf{d}_{LOS}^{InSAR} is a vector of the estimated InSAR displacements in the line-of-sight, \mathbf{d}^{GNSS} are vectors of the GNSS displacements (3-components), \mathbf{G} are matrices of Green's coefficients relating slip to surface displacement, and \mathbf{s} is a vector of unknown slip values for each patch. A planar correction is included for the InSAR data ($\alpha_{pl}\mathbf{x} + \beta_{pl}\mathbf{y} + \gamma_{pl}$) to correct for the long wavelength orbit errors, where \mathbf{x} and \mathbf{y} are the InSAR coordinates in a local reference frame. The inversion is weighted by the inverse of the variance-covariance matrix \mathbf{Q} , as estimated in section 4.4. Due to the large number of observations and the long spatial wavelength of the slow slip deformation signal, we resampled our initial InSAR observations to a 1 km grid before computing the slow slip surface displacements using weighted least squares, taking care to propagate all errors.

The inverse problem is ill-posed and highly sensitive to measurement noise. We therefore regularize the problem by introducing a prior constraint on smoothness, by including Laplacian smoothness in the inversion. Previous studies of the 2006 slow slip event have relied on smoothing based on trading off roughness and misfit manu-

ally (*Radiguet et al.*, 2011, 2012, *Cavalié et al.*, 2013), except for *Correa-Mora et al.* (2009), who select a smoothness coefficient based on a trade-off between the degrees of freedom in the model and the misfit (*Correa-Mora et al.*, 2008). We apply the method as proposed by *Fukuda and Johnson* (2008), which solves for smoothness in a Bayesian framework, allowing us to estimate the full probability distribution of each slipping patch, taking into consideration all possible smoothness values. We assume the distribution of the model residuals ϵ_d and the Laplacian of the slip $\nabla \mathbf{s}$ have a normal distribution of zero mean, respectively $\sim N(0, \mathbf{Q})$ and $\sim N(0, \alpha^2 \mathbf{I})$. With α^2 an unknown scaling parameter of the Laplacian variance matrix. Unlike, *Fukuda and Johnson* (2008) we assume that our data uncertainties are known, and we do not scale them. The posteriori probability distribution can be written as:

$$p(\mathbf{s}, \alpha_{pl}, \beta_{pl}, \gamma_{pl}, \alpha^2 | d) = K \alpha^{2(-M/2)} \times \exp\left\{-\frac{1}{2} \epsilon_d^T \mathbf{Q}^{-1} \epsilon_d - \frac{1}{2\alpha^2} (\nabla \mathbf{s})^T (\nabla \mathbf{s})\right\}, \quad (4.3)$$

where K is a normalization constant, N the total number of observations (GNSS and InSAR combined), and M the number of dislocation patches. We treat α^2 as unknown and sample its full probability distribution using a Markov chain Monte Carlo method (*Mosegaard and Tarantola*, 1995). We do the same for the unknown InSAR plane coefficients (α_{pl} , β_{pl} and γ_{pl}) as well as the slip and rake of each slipping patch. We fix the slip rake so that it is within 20 degrees of the plate convergence direction. We sample our prior distributions using a variable step size which is evaluated every 10,000 model runs (*Hooper et al.*, 2013).

4.6 Results

4.6.1 InSAR processing and InSAR time-series estimation

As no GNSS tropospheric estimates are available in *Vergnolle et al.* (2010), a direct comparison between GNSS and the estimated InSAR tropospheric delays is not possible. We are however able to compare the estimated tectonic components from InSAR and GNSS before and after tropospheric correction. Figure 4.3 gives the estimated time-series components before (top row) and after (bottom row) tropospheric correction. Before tropospheric correction, spatial patterns correlating with the topography can be observed in the north and middle of our study regions. For the slow slip displacements, the variation of the signal towards the north does not correlate with GNSS (top row, Figure 4.5). After correction, the slow slip signal is consistent with independent estimates from GNSS, and the gradient between the slow slip displacement signal and the local topography decreases by 1.1 cm/km. We find that the RMSE between the displacements and those predicted by our time-series model decreases after tropo-

spheric correction (second row, Figure 4.5). The reduction increases with distance to the InSAR reference area, and has a maximum value of ~ 1 cm (Bekaert *et al.*, 2015).

For the secular velocity, we observe the largest displacement rates near the coast (Figure 4.3(e)). This signal results from coupling between the subducting slab and the continental plate, causing a buckling of the hanging wall block near the coast. As the horizontal motion is almost perpendicular to the radar line-of-sight, the signal reflects the vertical velocity almost exclusively. Further inland, the secular displacement rates decrease.

For the slow slip displacement signal (Figure 4.3(f)), we see the opposite behavior. This is a consequence of the continental plate (hanging wall) slipping back towards the trench, resulting in uplift near the trench, and subsidence further inland. Further inland we see the signal level out and diminish. The estimated slow slip deformation signal near Mexico City is a tropospheric correction artifact, introduced when deformation around Mexico City leaked into the 2-8 km spatial band filter.

For the estimated master atmospheric signal (Figure 4.3(g)), we find signals of up to 10 cm which do not show a clear correlation with topography. Towards the north-west of our study region, we observe ~ 9 km wavelength meso-scale atmospheric features (wave pattern formation).

The DEM errors reveal a smoothly varying signal in along-track with an across-track variation (Figure 4.3(h)). These signals are also present in the wrapped interferograms. We believe this signal to be a focusing artifact, introduced by the zero-Doppler processing within ROI-PAC. We observed a similar feature in another study region, which disappeared with images focused by ESA. The errors introduced during the focusing stage are limited, as they are correlated with perpendicular baseline, and therefore reliably estimated and subtracted.

4.6.2 Slow slip modeling

In total we performed 2.5 million forward models using Markov chain Monte Carlo sampling, to sample the full parameter space for the slip and rake of each slipping patch, the smoothness, and the three InSAR plane coefficients. From all these inversions we kept the maximum a-posteriori solution, which represents the maximum of the 364-dimensional histogram (364 parameters) (Hooper *et al.*, 2013). When inverting GNSS only this reduces by three, as no plane is included. Figure 4.6 and Figure 4.7 give respectively our maximum a-posteriori slip solution and the corresponding marginal probability density distributions for the largest slipping patch. The corresponding modelled observations, residuals, and profiles P1-3 are shown in Figure 4.8. From the GNSS time-series it is unclear if the Oaxaca GNSS sites are solely displaced due to the 2006 Oaxaca SSE, or potentially a combination with the Guerrero 2006 slip event. While the displacements associated with the 2006 Guerrero event are expected to be small, we opted to exclude the Oaxaca GNSS sites (HUAT, PINO, and OAXA). Other

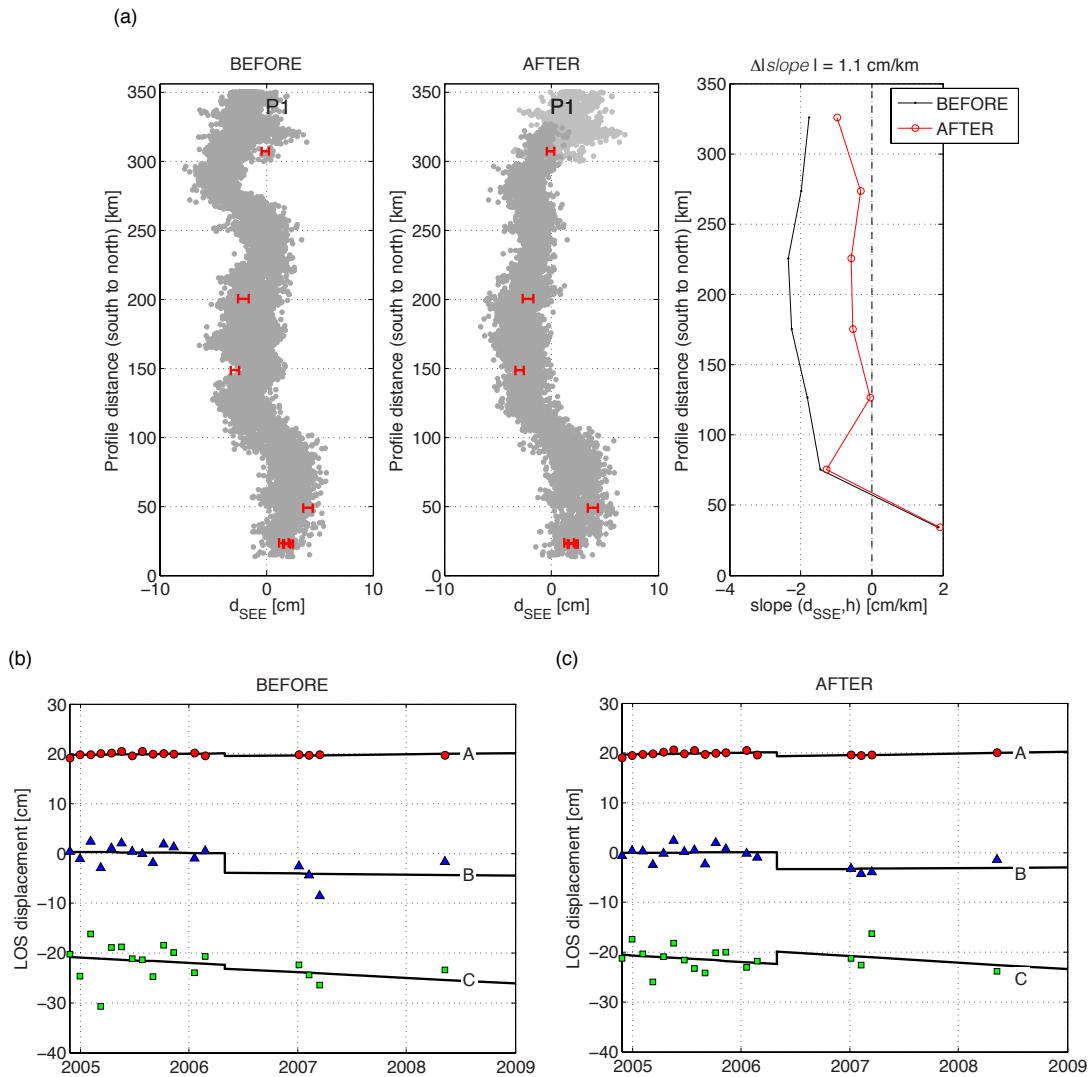


Figure 4.5: Figure from (*Bekaert et al., 2015*). Top row, comparison of the estimated slow slip surface displacements before and after tropospheric correction (left and middle panel). The right panel gives the gradient between the slow slip deformation signal and topography before and after tropospheric correction, estimated in 50 km along track segments using all data in range. Before correction, the signal is strongly correlated in the middle and north of the InSAR study region. After correction, this correlation is decreased, with on average a reduction of 1.1 cm/km. Light markers indicate the region around Mexico City, where subsidence contaminates the tropospheric correction estimates at the selected spatial frequency band of 2-8 km, which was chosen to avoid contamination of the long wavelength (~ 150 km) slow slip signal. This region is neglected in the slow slip modeling. Supplemental Figure C.1 gives the same comparison for the secular velocity. Second row, line-of-sight surface displacement time-series for individual locations, as shown in Figure 4.3, (b) before and (c) after the tropospheric correction is applied. Residual master atmosphere and DEM errors are removed. The displacement in time is modelled as an interseismic rate plus a slow slip step (black solid line). Positive displacements refer to motion towards the satellite, comprising mostly of vertical uplift. Offsets on the y-axis are chosen arbitrarily for clarity.

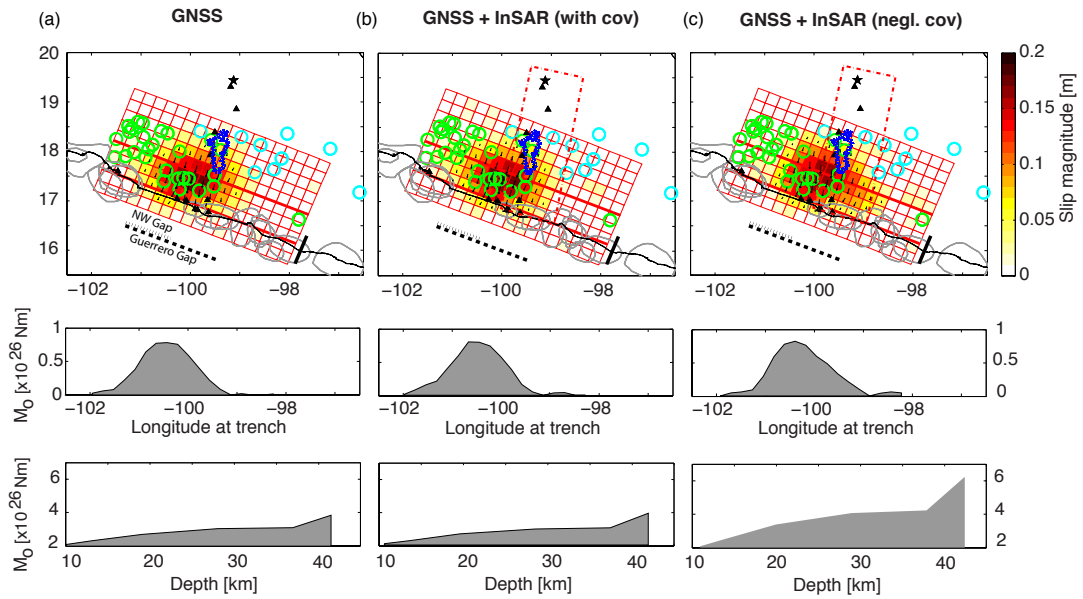


Figure 4.6: Maximum a-posteriori slip solution derived from (a) GNSS only, (b) GNSS and InSAR when including InSAR error covariance, and (c) GNSS and InSAR when neglecting InSAR error covariance. Only significant slip, 95% confidence slip >0 cm, is shown. For each slip solution we find slip in the seismogenic zone (thick solid black line). Inverting for the InSAR variance only, assumes the estimated signal not to be contaminated from residual atmospheric signals. Inverting for the variance only, allows slow slip to extend further eastwards than when using GNSS only. Inclusion of covariance downweights the InSAR towards the GNSS solution, potentially indicating that the InSAR signal is subjected to residual atmospheric signals. Slip extends within the seismogenic zone (10-25 km depths), black solid line, and enters the Guerrero Gap, dashed black line (black dotted line for the northwestern Guerrero Gap). Spatial correlation between the slow slip region and non-volcanic tremor ([Husker et al., 2012](#)) (blue dashed line) correlate with the existence of an ultra slow velocity layer ([Song et al., 2009](#)) (green circles). Absence of an ultra slow velocity layer is shown from the cyan circles ([Song et al., 2009](#)). Rake (black arrows) is within $\sim 10^\circ$ of the updip direction. The second and third rows, show the integrated seismic moment for the longitude at the trench, and for depth. A peak at 40 km depth is introduced by the sub-horizontal character of the interface at this depth.

studies instead force a zero displacement (e.g. [Vergnolle et al., 2010](#), [Radiguet et al., 2012](#), [Cavalié et al., 2013](#)).

We compared the solution found when inverting GNSS data only (first column, Figure 4.6) with those of a combined GNSS and InSAR inversion. We also compared solutions found when including and excluding InSAR covariance (second and third columns).

For the GNSS-only solution, significant slip (slip lower bound of 95% confidence >0 cm) is mostly found within 100 km horizontal distance of the GNSS sites perpendicular to the trench. The slip release corresponds to an equivalent earthquake magnitude of M_w 7.3, with the maximum slip (~ 17 cm) concentrated at depths of 30-40 km. As summarized in Table 4.3, we find most of the slip release ($\sim 76\%$) occurs on the transition zone (25-40 km depths), with the remaining part almost completely ($\sim 23\%$)

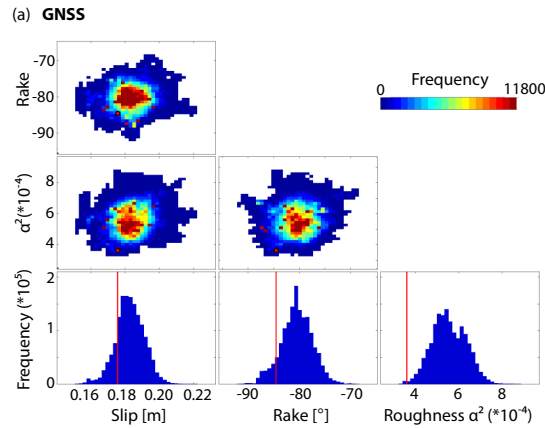


Figure 4.7: Sampled marginal probability distributions of the model parameters. The rake and slip is shown for the largest slipping patch, together with the smoothness, and when using InSAR the planar correction. (a) gives the case when inverting for GNSS alone, (b) the combination between GNSS and InSAR when using the InSAR covariance, and (c) the combined solution ignoring InSAR covariance. The maximum a-posteriori slip solution is highlighted by the red marker and line.

in the locked portion of the seismogenic zone (10-25 km) defined from past large thrust earthquakes and inter-SSE coupling from interseismic studies (e.g. *Kostoglodov et al., 2001, Larson et al., 2004*). The locked portion of the Guerrero Gap (101.2 $^\circ$ W - 99.2 $^\circ$ W) itself accounts for $\sim 22\%$ of the total seismic release in SSE, moment release equivalent to an M_w 6.9 earthquake. For the northwest portion of the gap (101.2 $^\circ$ W - 100.4 $^\circ$ W, no earthquake since 1911) this release is $\sim 13\%$ of the SSE total, equivalent to an M_w 6.7 earthquake.

When including the full InSAR noise variance-covariance information (second column) the InSAR data are downweighted, pushing the solution more towards the GNSS solution on the western side of the InSAR track, while the InSAR still provides a low-level constraint. Including the InSAR data but neglecting covariance (third column) causes the slip solution to extend much more in south-easterly direction. While the maximum slip magnitude and location remains approximately unchanged, we find slip patches of ~ 10 cm slip extending about 80 km more southeast than when using GNSS-alone. As shown in Table 4.3, independent of which data is used, the maximum a-posteriori slip solution has a similar estimated release of M_w 7.3, with $\sim 19-22\%$ being released in the locked Guerrero Gap ($M_w \sim 6.9$), and $\sim 11-13\%$ in the northwest portion of the gap ($M_w \sim 6.7$). Inverting without covariance (but leaving variance) information tends to push the slip solution more down-dip, with $\sim 1.3\%$ more of the total moment released on the transition stage (25-42 km depths).

The maximum a-posteriori solution tends towards the smoother side of the marginal probability distributions shown in Figure 4.7, and does not always coincide with the peaks of the histograms. This can be explained by the fact that the histogram peaks represent the maxima in a 2-dimensional parameter space and neglect all other dimen-

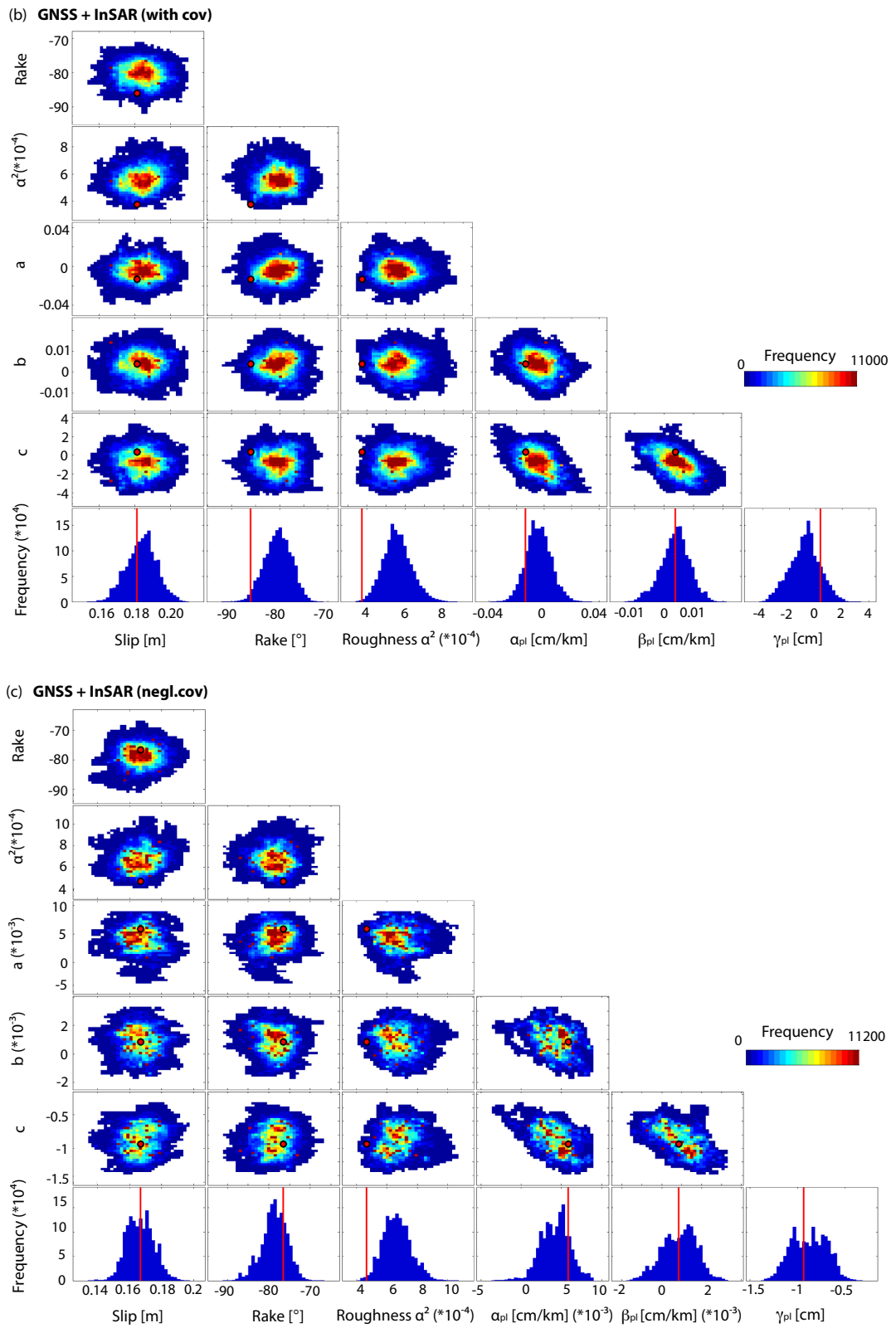


Figure 4.7: (Continued)

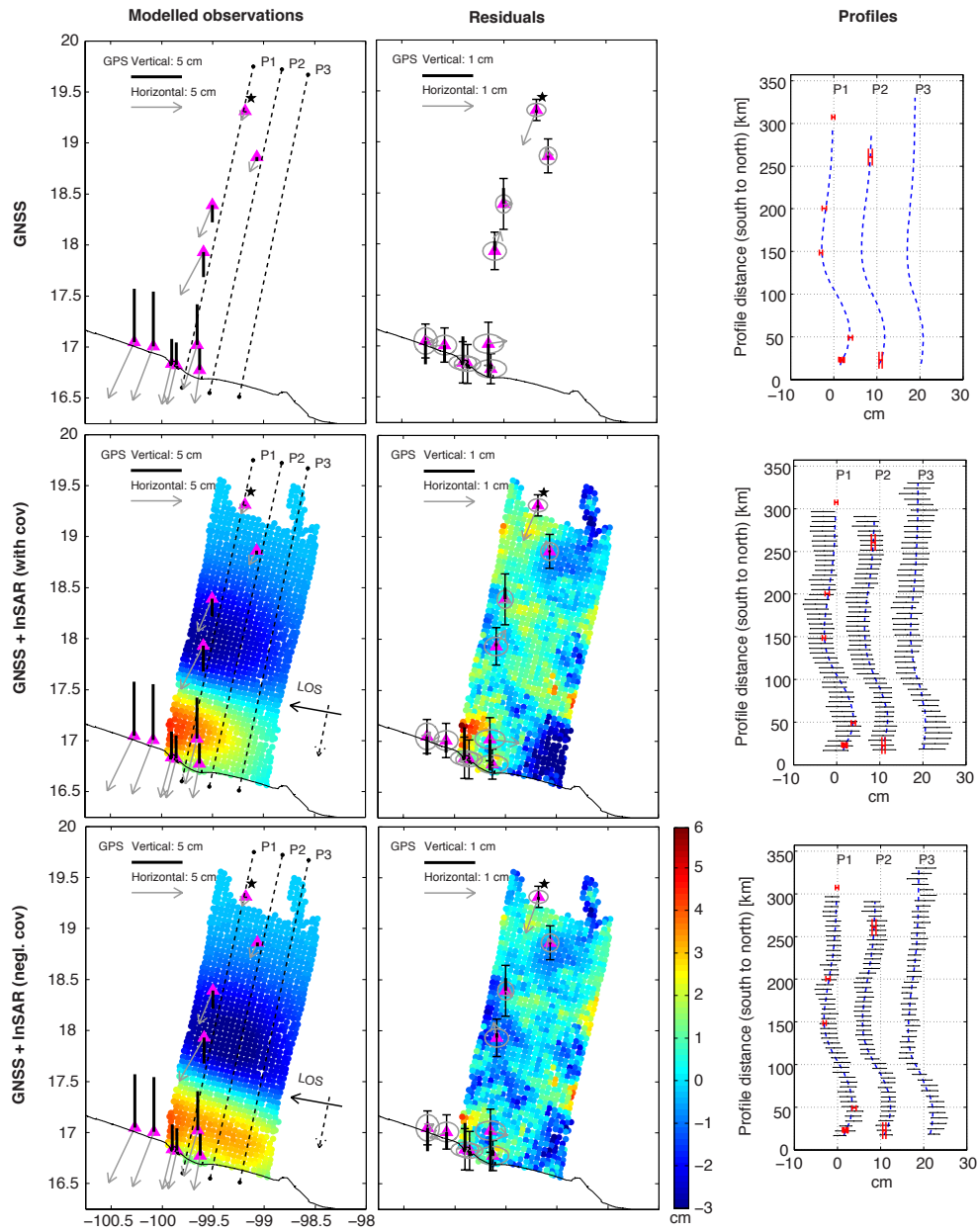


Figure 4.8: Modelled surface displacements (first column) and their residual (second column) together with the surface displacement profiles (P1, P2 and P3) (third column). The first row gives the result when inverting GNSS data alone, middle row, when inverting GNSS together with full co-variance information after tropospheric correction, and bottom row, after tropospheric correction and when ignoring the InSAR covariance information. After tropospheric correction we find the InSAR data to be more consistent with the GNSS observations in the northern region. Near the coast the inclusion of co-variance downweights the InSAR data, pushing it towards the GNSS solution. This is due to residual tropospheric atmosphere near the coastal region. Residuals reveal a misfit for the InSAR at the higher spatial resolution, imposed by the smoothness constrained on the slip. Displayed errors are 2σ . All shown displacements are in the line-of-sight (LOS).

Table 4.3: Earthquake-like moment magnitude release for the maximum a-posteriori slip solution. A comparison is made between the moment release in the locked seismogenic zone (10-25 km depth) and the transition zone (25-42 km depth). Also the moment magnitude release within the locked Guerrero Gap (101.2°W - 99.2°W) and the northwest portion of the gap (101.2°W - 100.4°W) is shown. Rigidity is assumed to be 3×10^{11} dyne/cm² (or 3×10^{10} N/m²).

M_w	GNSS	GNSS & InSAR (negl. COVAR)	GNSS & InSAR (with COVAR)
Total release	7.3 (100.0%)	7.3 (100.0%)	7.3 (100.0%)
Locked seismogenic zone	6.9 (23.4%)	6.9 (22.3%)	6.9 (23.5%)
Transition zone	7.2 (75.8%)	7.3 (77.1%)	7.2 (75.7%)
Guerrero Gap (Locked seismogenic zone)	6.9 (22.4%)	6.9 (18.8%)	6.9 (21.8%)
Northwest Guerrero Gap (Locked seismogenic zone)	6.7 (13.3%)	6.7 (10.7%)	6.7 (12.1%)

sions included in the maximum a-posteriori solution. Each slip solution has a different smoothness value, which is also set by the Markov chain Monte Carlo sampling. Figure 4.9 gives the rougher and smoother slip solutions.

4.7 Discussion

4.7.1 Slow slip modeling compared with other studies

Below, we compare the results when inverting for GNSS alone, and the integration of GNSS and InSAR. For the latter we compare the inversions when using the full InSAR variance covariance matrix, with those ignoring the InSAR covariance, as done by *Cavalié et al. (2013)*. In all our cases we find slip to enter the seismogenic zone (10-25 km depth) and the Guerrero Gap, reaching depths as shallow as 10 km.

GNSS inversion

Our slow slip solution derived using GNSS observations only, Figure 4.6(a), compares well with the overall slip pattern of *Correa-Mora et al. (2009)*, who found a similar spatial extent and magnitude of the slip distribution, and a peak slip of ~ 19 cm compared to our 17 cm. The solution of *Radiquet et al. (2011)*, where smoothness is chosen based on a trade-off between roughness and misfit, is rougher, with a maximum slip just after the down-dip transition on the sub-horizontal section, and a large up-dip asperity near the coastal GNSS sites ACAP and COYA. The asperity is likely introduced to fit the vertical displacements at COYO and ACAP, which differ from surrounding GNSS stations (*Larson et al., 2007*). Our maximum a-posteriori solution fits the GNSS observations well, with an RMSE of 0.3 cm and 0.3 cm for, respectively, the horizontal

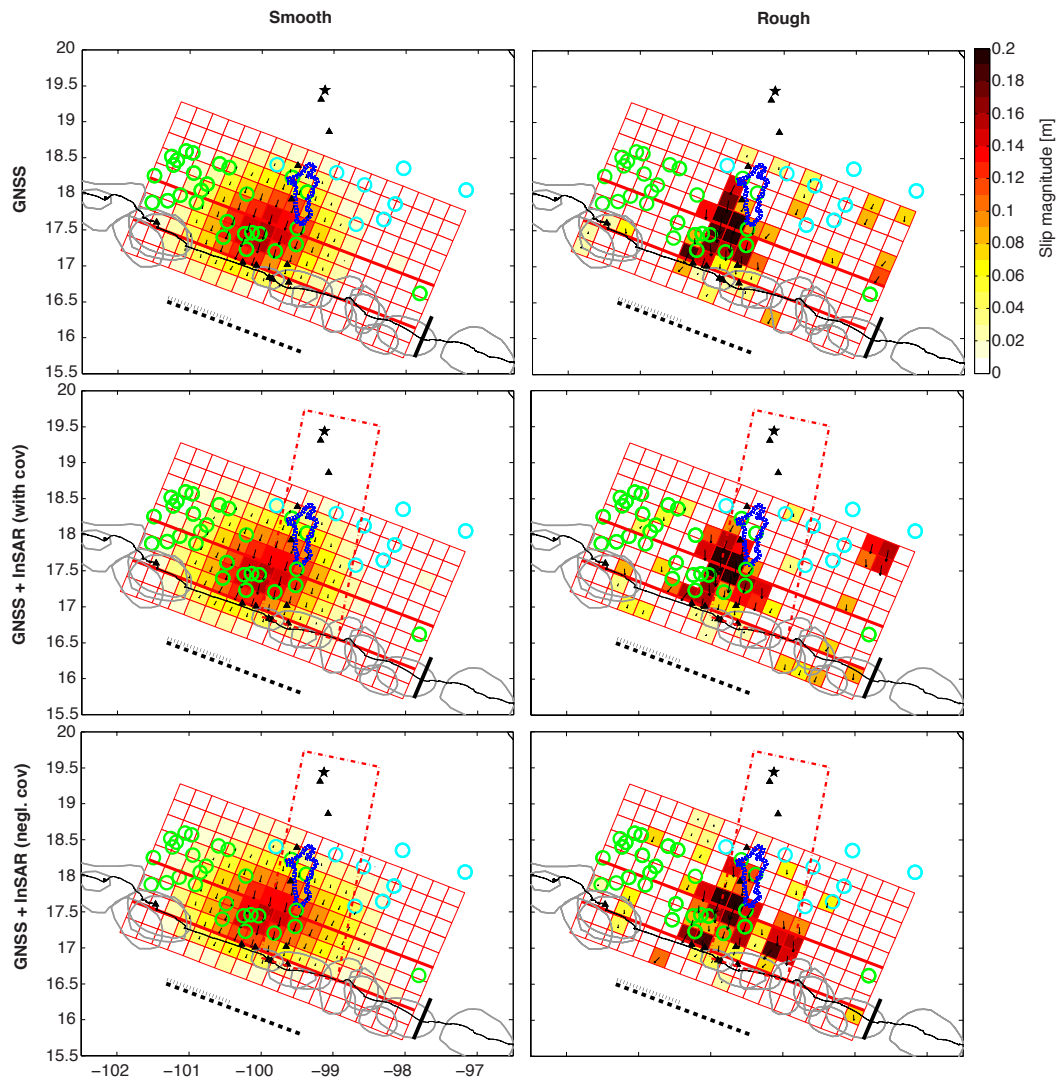


Figure 4.9: Smooth (left column) and rough slip solution (right column) for GNSS (top row), combining GNSS and InSAR with full co-variance information (middle row), and, combining GNSS and InSAR when ignoring co-variance (bottom row). The hyper parameter α^2 is respectively $1e^{-4}$ and 0.025 for the smooth and rough slip solution, both well outside the smoothness marginal probability distribution (Figure 4.7). Only significant slip, 95% confidence slip >0 cm, is shown.

and vertical components. For the two coastal sites COYA and ACAP, we overestimate the vertical by an average of 0.1 cm, while fitting the horizontal displacements. In our rougher solution, shown in Figure 4.9, we are capable of estimating both components without significant residuals, illustrating the impact of smoothness. Compared to [Vergnolle et al. \(2010\)](#), we find a slightly smaller maximum slip (17 cm compared to 22.5 cm) and locate it 10 km further down-dip from the trench. Unlike [Vergnolle et al. \(2010\)](#), we find significant slip extends to depths shallower than 19 km. Inverting with the same interface as [Radiquet et al. \(2012\)](#), we find our peak slip coincides with their down-dip extent of the higher slipping region (~ 17 cm). We do not observe the large up-dip slip of ~ 17 cm just north of the coastal ACAP and COYA GNSS sites, potentially introduced due to a rougher solution to decrease misfit of the observations. We find a smaller magnitude release for the total slip distribution than [Radiquet et al. \(2012\)](#), M_w 7.3 compared to M_w 7.5, as well as the release in the northwestern Guerrero Gap, M_w 6.9 compared to M_w 7.2. The difference in magnitude could be introduced by the difference in the assumed rigidity, which we assumed to be constant in this study, compared to a layered model in [Radiquet et al. \(2012\)](#).

Within our sampled marginal smoothness probability distribution, we find slip of ~ 5 cm reaching depths as shallow as 12 km, which is larger and shallower than previous studies by [Correa-Mora et al. \(2009\)](#) and [Vergnolle et al. \(2010\)](#), but in overall agreement (~ 1 cm larger) with the slip magnitudes by [Radiquet et al. \(2011, 2012\)](#). In agreement with previous studies by [Radiquet et al. \(2011, 2012\)](#), we find slow slip occurs in the locked part of the Guerrero Gap.

GNSS and InSAR (with covariance) combined inversion

Our joint GNSS and InSAR slip solution (Figure 4.6(b)), when including the InSAR data with full covariance information, tends towards the GNSS solution. The region of maximum slip remains west of the InSAR region towards the 40 km depth sub-horizontal transition of the subduction interface. Slip enters the Guerrero Gap, with magnitudes of up to ~ 5 cm reaching depths as shallow as 12 km. The InSAR data are not strongly weighted with the inclusion of the covariance information, as the slow slip signal is correlated on similar length scales to atmospheric noise. Therefore the Bayesian algorithm assigns a higher probability to keeping the slip smooth than fitting the InSAR data perfectly.

GNSS and InSAR (neglecting covariance) combined inversion

When ignoring the InSAR error covariance (Figure 4.6(c)), the long wavelength signal is interpreted as slow slip, which requires more slip northwards on the sub-horizontal, 40 km depth, segment of the interface than the GNSS-only solution, with a maximum slip of ~ 17 cm. This is in agreement with [Cavalié et al. \(2013\)](#), who explored the

same InSAR track, with a different processing approach. However, unlike *Cavalié et al. (2013)*, we find the slip distribution is constrained to be parallel to the subducting trench and we do not find any slip extending in a north-east direction. Care needs to be taken with the eastern extent of the slow slip region. Inverting without covariance assumes implicitly that the residual atmospheric signal is not correlated spatially. If there are correlated residual atmospheric signals, they are assumed to be part of the slow slip displacements in the inversion. When combining GNSS and InSAR, we find a similar magnitude of slip as for GNSS (~ 5 cm), reaching depths as shallow as 12 km.

Cavalié et al. (2013) constructed 8 interferometric pairs spanning the 2006 slow slip event, multi-looked to a ~ 640 m pixel size in order to reduce noise and thus decorrelation. They used a model from GNSS measurements to correct for the interseismic displacement, and corrected orbital effects and long-wavelength errors by removing a planar trend utilizing 5 to 6 GNSS stations, depending on the interferogram. In this study, we used more SAR acquisitions, in a time-series approach, reducing the effects of noise and atmosphere, and allowing us to simultaneously invert for the inter-seismic rates and slow slip displacement signal. We include the uncertainty in orbit and other long wavelength errors in our results, as is the case for the smoothness. *Cavalié et al. (2013)* did not use a dedicated troposphere correction as applied in this study; instead, they applied a simple stacking approach (*Zebker et al., 1997*) using the 8 interferograms. In terms of modeling, we assumed the same subduction interface as *Cavalié et al. (2013)*, but rather than imposing an arbitrary scaling factor between InSAR and GNSS, we let the variance of the observations control the weights. We use approximately the same GNSS observations, except that we exclude the OAXACA GNSS stations (PINO, HUAT and OAXA) rather than forcing them to have zero displacement.

4.7.2 Correlation between slow slip, Ultra Slow velocity Layer and Non-Volcanic Tremor

The coincidence of Non-Volcanic Tremor (NVT) and SSEs in Japan, Cascadia, known as episodic tremor and slip events, gives weight to the hypothesis that NVT and slow slip originates from the same source, or that one initiates the other. We find that our slow slip solution (Figure 4.6) correlates well with the spatial occurrence of the NVT (*Husker et al., 2012*), and the presence of an ultra slow velocity layer (*Song et al., 2009, Kim et al., 2010, Song and Kim, 2012*). As the MASE (Meso-American Subduction Experiment) network is a linear array, approximately perpendicular to the trench, the NVT sensitivity in the direction perpendicular to the array is limited. Increased energy release in NVT has been observed during the 2006 SSE (*Rubinstein et al., 2010, Husker et al., 2012*), with an up-dip trend in NVT locations as the 2006 SSE progresses (*Husker et al., 2012*). In space, we find the NVT region occurs just

down-dip of the maximum slipping region, coinciding with areas slipping by 3-13 cm. The hypothesis of fluid flow and fluid processes at the plate interface generating seismic tremor (*Rubinstein et al., 2010*) is supported by the correlation between an ultra slow velocity layer (*Pérez-Campos et al., 2008, Song et al., 2009*) and the NVT, low electric resistivity from magneto-telluric (*Jödicke et al., 2006*), and seismic velocity tomography (*Huesca-Pérez and Husker, 2012*). The correlation we observe between the slow slip region and the ultra slow velocity layer supports the hypothesis of slow slip related to high pore pressures.

4.7.3 Earthquake hazard

We evaluated the slip deficit introduced from the end of the 2001/2002 SSE till the end of the 2006 SSE, Figure 4.10. This interval of 4.7 years is fairly typical of the time between events, which ranges from 3 to 5 years. To calculate the slip deficit at the Guerrero Gap in the absence of any SSE, we multiplied the MORVEL plate convergence rate of 6.1 cm/year (*DeMets et al., 2010*) over this period (4.7 years) and subtracted the inter-SSE coupling solution by *Radiquet et al. (2012)*, as derived from 12 years of GNSS observations. We then calculated the slip deficit by differencing the slow slip estimate from this. As the rake only deviates by up to $\sim 10^\circ$ from the plate convergence direction at the Guerrero Gap, we do not account for the rake variations. Irrespective of inverting GNSS data alone, or when combining GNSS with InSAR, we find slow slip reduces the total moment within the Guerrero Gap by $\sim 50\%$ (Table 4.4). This leaves a residual slip deficit, build up over 4.7 years, equivalent to an earthquake potential of M_w 7.3 which has been incremented by $M_w \sim 6.8$ each year. In the northwestern section of the Gap, where no earthquake has been observed since 1911, the slip deficit over the same time-period is equivalent to M_w 7-7.1. In agreement with *Radiquet et al. (2012)* we find the slip deficit outside the Guerrero Gap to be higher than inside the Gap, where slow slip occurs. Nevertheless, considering the partial release of slow slip events over time, the slip deficit within the Guerrero Gap can still cause large earthquakes and remains a threat for Mexico City. Assuming all stress release happens through earthquakes and through slow slip, an equivalent $M_w \sim 8$ earthquake has been accumulated in the last century within the Guerrero Gap. Recently, two earthquakes occurred on 18 April 2014 ($M_w \sim 7.2$) and 8 May 2014 ($M_w \sim 6.4$) on western edge of the Guerrero gap. Even if they slipped entirely within the locked portion of the Guerrero Gap, they are too small to have a significant impact on the slip deficit.

4.8 Conclusions

Whether inverting GNSS observations alone, combining GNSS and InSAR while neglecting the covariance information, or while including the full InSAR covariance information, we find the 2006 Guerrero slow slip event to have an equivalent earthquake

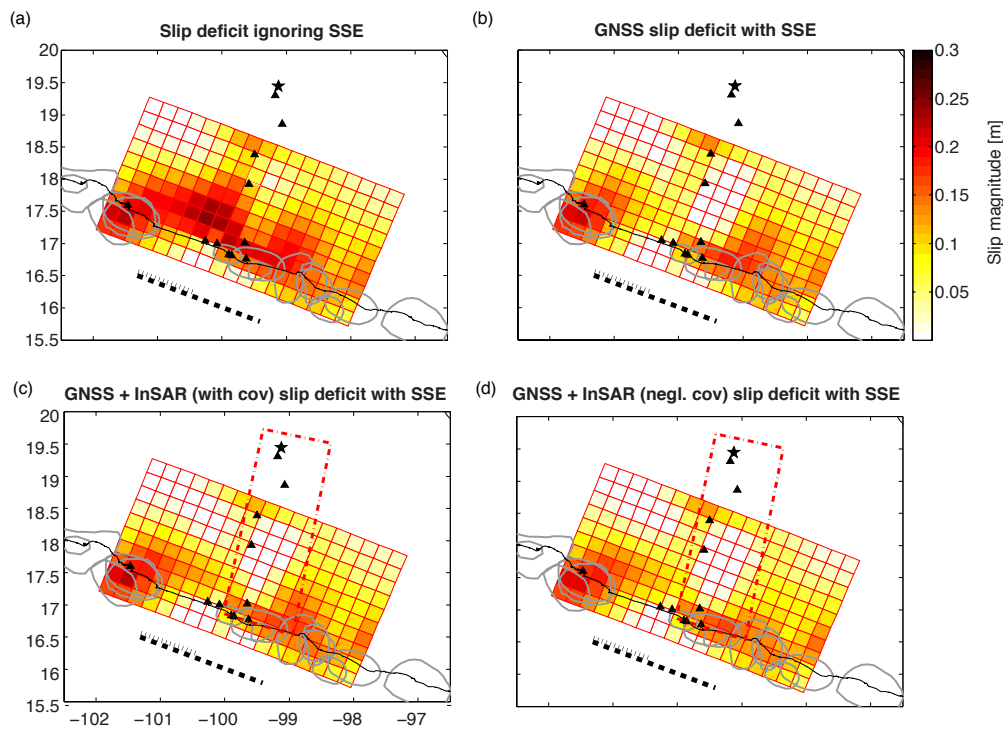


Figure 4.10: Slip deficit over Guerrero in 4.7 years, from the period after the 2001 SSE till the end of the 2006 SSE. (a) Gives the slip deficit estimated assuming a 6.1 cm/year convergence rate at the Guerrero Gap (*DeMets et al., 2010*) and with an inter-SSE coupling derived from GNSS by *Radiguet et al. (2012)*. After removal of the 2006 SSE we find the slip deficit in (b) when inverting for GNSS only, in (c) combining GNSS and InSAR with full covariance information, and in (d) when combining GNSS and InSAR ignoring covariance. In all cases the slow slip release coincides with a high inter-SSE coupled region, reducing the slip deficit by more than 50% (Table 4.4).

Table 4.4: Slip deficit after the 2006 SSE. This is the slip deficit from mid April 2002 (end of the 2001/2002 SSE) till January 2007 (end of the 2006 SSE), approximately 4.7 years. Over this duration and when neglecting the 2006 SSE the slip deficit in Guerrero was equivalent to a M_w 7.5 or a M_w 7/year. For the northwestern Guerrero Gap this corresponds to a deficit of M_w 7.3 or M_w 6.8/year. The slip deficit is computed assuming a MORVEL plate convergence in the Gap of 6.1 cm/year (*DeMets et al., 2010*) with the inter-SSE coupling from GNSS *Radiguet et al. (2012)*. Slip deficit values in the table in addition account for the 2006 SSE. In the calculation rake is neglected as on average it is within 10° of plate convergence direction.

Guerrero Gap	GNSS	GNSS & InSAR (negl. COVAR)	GNSS & InSAR (with COVAR)
Slip deficit equivalent M_w	7.3 (~ 6.8 /year)	7.3 (~ 6.8 /year)	7.3 (~ 6.8 /year)
Seismic moment reduction	51.4%	53.1%	50.8%
Northwest Guerrero Gap	GNSS	GNSS & InSAR (negl. COVAR)	GNSS & InSAR (with COVAR)
Slip deficit equivalent M_w	7.1 (~ 6.6 /year)	7.1 (~ 6.6 /year)	7 (~ 6.6 /year)
Seismic moment reduction	55.2%	51%	54.6%

magnitude of M_w 7.3. This is in agreement with [Correa-Mora et al. \(2009\)](#), but smaller than previous studies, which estimated a $M_w \sim 7.5$. We find larger slip magnitudes (~ 5 cm) in the seismogenic zone (10-25 km depths) in the Guerrero Gap than reported previously. Of the total slow slip moment release we find 19-25% is released in the locked part of the Guerrero Gap (equivalent to $M_w \sim 6.9$). The majority of slip, $\sim 75\%$ of the total moment, is released in the transition zone (25-40 km depths). We allowed for rake variations within 20° of the plate convergence direction, but find most of the slip to be in the dip direction of the subducting interface. As the dip direction is $\sim 10^\circ$ of the plate convergence direction, this suggests some slip partitioning to occur. The remnant strike slip component is not released through slow slip. When inverting the combined observations from GNSS and InSAR, we find the slow slip extends further east, under the InSAR track. In contrast to a previous InSAR and GNSS study ([Cavalié et al., 2013](#)), we find that slip does not extend to the north-east, but remains approximately parallel to the trench. Both non-volcanic tremor and our slow slip region correlate well with the presence of an ultra slow velocity layer, strengthening the hypothesis that both originate from the same process. We find slow slip occurs within a highly inter-SSE coupled region. For the period between the end of the 2001/2002, and the end of the 2006 slow slip event an M_w 7.3 earthquake was accumulated, or equivalent to M_w 6.8 each year. This includes a reduction in total moment by $\sim 51\%$ introduced by slow slip. In the northwestern portion of the Gap, where no earthquake has been observed since 1911, the slip deficit is equivalent to a $M_w \sim 7.1$ earthquake. Assuming stress being released by earthquakes and slow slip, and considering an average 4-year slow slip cycle and absence of a large earthquake in the last 100 years, the Guerrero Gap still has the potential for causing a $M_w \sim 8$ earthquake. The recent April and May 2014 Guerrero earthquakes that occurred on the western edge of the Guerrero Gap are too small to decrease this estimate significantly.

Acknowledgments

We acknowledge the Department of Atmospheric Science of the University of Wyoming for providing us the sounding data at Acapulco (downloaded from <http://weather.uwyo.edu/upperair/sounding.html>). Slow slip GNSS estimates were taken from ([Vergnolle et al., 2010](#)). Envisat data were provided by the European Space Agency. We acknowledge the Jet Propulsion Laboratory for providing us with ROI_PAC ([Rosen et al., 2004](#)), used to focus the raw SAR data, and the SRTM topographic data ([Farr et al., 2007](#)), used to correct for the topography in the interferograms. InSAR processing was achieved using the DORIS software ([Kampes et al., 2003](#)), developed at Delft University of Technology, and StaMPS software ([Hooper et al., 2012](#)). Methodology on the applied power-law correction method is included in a companion paper ([Bekaert et al., 2015](#)). Some figures were prepared using the public domain GMT software ([Wes-](#)

sel and Smith, 1991). COMET is the NERC Centre for the Observation and Modelling of Earthquakes, Volcanoes and Tectonics. Results can be obtained by contacting the corresponding author (eedpsb@leeds.ac.uk).

Appendix InSAR covariance matrix from bootstrapping

We derive the InSAR variance covariance matrix for the errors by applying the percentile bootstrap method (*Efron and Tibshirani, 1986*) and using point-pair combinations of the errors to estimate a covariance function. As opposed to the regular bootstrap algorithm, where n random samples are taken from n observations, we select n_1 and n_2 random samples respectively from the n_1 and n_2 observations (interferograms) before and after the SSE, such that our model design matrix remains invertible for each bootstrap simulation, equation (4.1). We estimate the residuals of the slow slip displacement, ϵ , between each bootstrap simulation $\hat{\mathbf{d}}_{SSE}^{boot}$ and the best estimate from weighted least squares $\hat{\mathbf{d}}_{SSE}$, and use the residuals for the variance-covariance matrix estimation.

$$\epsilon^k = \hat{d}_{SSE}^{boot,k} - \hat{d}_{SSE} \quad (4.4)$$

Where k represents one of the n bootstrap runs. Estimating the covariance matrix directly from all the residuals is not possible as the covariance terms are biased by outliers. For the variance the influence of outliers is less. Using the bootstrapped residuals the estimated variance $\hat{\sigma}_{\Delta ij}^2$ between a point pair P_{ij} follows as:

$$\hat{\sigma}_{\Delta ij}^2 = \sum_k^n \frac{(\epsilon_{\Delta ij}^k)^2}{n-1} \quad (4.5)$$

Which in theory corresponds to:

$$\sigma_{\Delta ij}^2 = \sigma_i^2 + \sigma_j^2 - 2C_{ij} \quad (4.6)$$

With σ_i^2 and σ_j^2 the variance at P_i and P_j , and C_{ij} covariance between both. By assuming the same variance for point P_i and P_j , equation (4.6) becomes $\sigma_{\Delta ij}^2 = 2\sigma_{i/j}^2 - 2C_{ij}$, which reduces to the definition of a semi-variogram (*Wackernagel, 2003*):

$$\gamma(x) = C(0) - C_{ij}(x) \quad (4.7)$$

With $C(0)$ the variance at point P_i and P_j , and with γ representing the dissimilarity of the semi-variogram depending on the separation distance x between the two points. By binning the experimental semi-variogram and by fitting a Gaussian covariance function in combination with a nugget model for the uncorrelated terms, we were able to derive the full variance-covariance matrix for the slow slip displacement. We validated the

variance-covariance matrix for errors by using its inverse to weight a least squares estimation of the point centroid for each bin, and ensuring that each estimated centroid lay within the cloud of points used in the estimation.

References

- Bekaert, D. (2011), InSAR Time Series Analysis of the 2006 Slow Slip Event on the Guerrero Subduction Zone, Mexico, M.S. Thesis, Delft University of Technology, Delft, The Netherlands. [4.1](#)
- Bekaert, D., A. Hooper, and T. Wright (2015), A spatially-variable power-law tropospheric correction technique for InSAR data, *J. Geophys. Res.*, *120*, doi:[10.1002/2014JB011558](#). [4.1](#), [4.2](#), [4.6.1](#), [4.5](#), [4.8](#)
- Cavalié, O., E. Pathier, M. Radiguet, M. Vergnolle, N. Cotte, A. Walpersdorf, V. Kostoglodov, and F. Cotton (2013), Slow slip event in the Mexican subduction zone: Evidence of shallower slip in the Guerrero seismic gap for the 2006 event revealed by the joint inversion of InSAR and GPS data, *Earth and Planetary Science Letters*, *367*, doi:[10.1016/j.epsl.2013.02.020](#). [4.1](#), [4.5](#), [4.4](#), [4.5](#), [4.6.2](#), [4.7.1](#), [4.7.1](#), [4.8](#)
- Chen, T., and R. Clayton (2012), Structure of central and southern Mexico from velocity and attenuation tomography, *J. Geophys. Res.*, *117*(B9), doi:[10.1029/2012JB009233](#). [4.5](#)
- Correa-Mora, F., C. DeMets, E. Cabral-Cano, B. Marquez-Azua, and O. Diaz-Molina (2008), Interplate coupling and transient slip along the subduction interface beneath Oaxaca, Mexico, *Geophys. J. Int.*, *175*(1), 269 – 290, doi:[10.1111/j.1365-246X.2008.03910.x](#). [4.5](#)
- Correa-Mora, F., C. DeMets, E. Cabral-Cano, O. Diaz-Molina, and B. Marques-Azua (2009), Transient deformation in southern Mexico in 2006 and 2007: Evidence for distinct deep-slip patches beneath Guerrero and Oaxaca, *Geochem. Geophys. Geosyst.*, *10*(2), doi:[10.1029/2008GC002211](#). [4.1](#), [4.5](#), [4.7.1](#), [4.8](#)
- DeMets, C., R. Gordon, and D. Argus (2010), Geologically current plate motions, *Geophys. J. Int.*, *181*(1), 1 – 80, doi:[10.1111/j.1365-246X.2009.04491.x](#). [4.1](#), [4.1](#), [4.7.3](#), [4.10](#), [4.4](#)
- Efron, B., and R. Tibshirani (1986), Bootstrap methods for standard errors, confidence intervals, and other measures of statistical accuracy, *Statistical Science*, *1*(1), 54 – 75, doi:[10.1214/ss/1177013815](#). [4.4](#), [4.8](#)
- Farr, T., P. Rosen, E. Caro, R. Crippen, R. Duren, S. Hensley, M. Kobrick, M. Paller, E. Rodriguez, L. Roth, D. Seal, S. Shaffer, J. Shimada, J. Umland, M. Werner, M. Oskin, D. Burbank, and D. Alsdorf (2007), The Shuttle Radar Topography Mission, *Reviews of Geophysics*, *45*(2), doi:[10.1029/2005RG000183](#). [4.2](#), [4.8](#)
- Ferrari, L. (2004), Slab detachment control on mafic volcanic pulse and mantle heterogeneity in central Mexico, *Geology*, *32*(1), 77 – 80, doi:[10.1130/G19887.1](#). [4.5](#)
- Fukuda, J., and K. Johnson (2008), A Fully Bayesian Inversion for Spatial Distribution of Fault Slip with Objective Smoothing, *Bulletin of the Seismological Society of America*, *98*(3), 1128 – 1146, doi:[10.1785/0120070194](#). [4.5](#)

- Hooper, A., P. Segall, and H. Zebker (2007), Persistent scatterer interferometric synthetic aperture radar for crustal deformation analysis, with application to Volcán Alcedo, Galápagos, *J. Geophys. Res.*, *112*(B7), doi:[10.1029/2006JB004763](https://doi.org/10.1029/2006JB004763). 4.2
- Hooper, A., D. Bekaert, K. Spaans, and M. Arikan (2012), Recent advances in SAR interferometry time series analysis for measuring crustal deformation, *Tectonophysics*, *514*517, 1 – 13, doi:<http://dx.doi.org/10.1016/j.tecto.2011.10.013>. 4.1, 4.2, 4.2, 4.8
- Hooper, A., J. Pietrzak, W. Simons, H. Cui, R. Riva, M. Naeije, A. T. van Scheltinga, E. Schrama, G. Stelling, and A. Socquet (2013), Importance of horizontal seafloor motion on tsunami height for the 2011 Mw=9.0 Tohoku-Oki earthquake, *Earth and Planetary Science Letters*, *361*, 469 – 479, doi:[10.1016/j.epsl.2012.11.013](https://doi.org/10.1016/j.epsl.2012.11.013). 4.5, 4.6.2
- Huesca-Pérez, E., and A. Husker (2012), Shallow travel-time tomography below southern Mexico, *Geofísica Internacional*, *51*(3), 281 – 291. 4.7.2
- Husker, A., V. Kostoglodov, V. Cruz-Atienza, D. Legrand, N. Shapiro, J. Payero, M. Campillo, and E. Huesca-Pérez (2012), Temporal variations of non-volcanic tremor (NVT) locations in the Mexican subduction zone: Finding the NVT sweet spot, *Geochem. Geophys. Geosyst.*, *13*(3), Q03011, doi:[10.1029/2011GC003916](https://doi.org/10.1029/2011GC003916). 4.6, 4.7.2
- Iglesias, A., S. Singh, A. Lowry, M. Santoyo, V. Kostoglodov, K. Larson, S. Franco-Sánchez, and T. Mikumo (2004), The silent earthquake of 2002 in the Guerrero seismic gap, Mexico (Mw = 7.6): inversion of slip on the plate interface and some implications, *Geofísica Internacional*, *43*(3), 309 – 317. 4.1
- Jödicke, H., A. Jording, L. Ferrari, J. Arzate, K. Mezger, and L. Rüpke (2006), Fluid release from the subducted Cocos plate and partial melting of the crust deduced from magnetotelluric studies in southern Mexico: Implications for the generation of volcanism and subduction dynamics, *J. Geophys. Res.*, *111*(B8), doi:[10.1029/2005JB003739](https://doi.org/10.1029/2005JB003739). 4.7.2
- Kampes, B., R. Hanssen, and Z. Perski (2003), Radar interferometry with public domain tools, *Proceedings Fringe 2003*, p. 6. 4.2, 4.2, 4.8
- Kim, Y., R. Clayton, and J. Jackson (2010), Geometry and seismic properties of the subducting Cocos plate in central Mexico, *J. Geophys. Res.*, *115*(B6), doi:[10.1029/2009JB006942](https://doi.org/10.1029/2009JB006942). 4.5, 4.4, 4.7.2
- Kostoglodov, V., W. Bandy, J. Domínguez, and M. Mena (1996), Gravity and seismicity over the Guerrero seismic gap, Mexico, *Geophys. Res. Lett.*, *23*(23), 3385 – 3388, doi:[10.1029/96GL03159](https://doi.org/10.1029/96GL03159). 4.1
- Kostoglodov, V., R. Valenzuela, A. Gorbato, J. Mimiaga, S. Franco, J. Alvarado, and R. Peláez (2001), Deformation in the Guerrero seismic gap, Mexico, from leveling observations, *Journal of Geodesy*, *75*(1), 19 – 32, doi:[10.1007/s001900000144](https://doi.org/10.1007/s001900000144). 4.6.2
- Kostoglodov, V., S. Singh, J. Santiago, S. Franco, K. Larson, A. Lowry, and R. Bilham (2003), A large silent earthquake in the Guerrero seismic gap, Mexico, *Geophys. Res. Lett.*, *30*(15), doi:[10.1029/2003GL017219](https://doi.org/10.1029/2003GL017219). 4.1
- Larson, K., A. Lowry, V. Kostoglodov, W. Hutton, O. Sánchez, K. Hudnut, and G. Suárez (2004), Crustal deformation measurements in Guerrero, Mexico, *J. Geophys. Res.*, *109*(B4), doi:[10.1029/2003JB002843](https://doi.org/10.1029/2003JB002843). 4.1, 4.6.2
- Larson, K. M., V. Kostoglodov, S. Miyazaki, and J. Santiago (2007), The 2006 aseismic slow slip event in Guerrero, Mexico: New results from GPS, *Geophys. Res. Lett.*, *34*(13), doi:[10.1029/2007GL029912](https://doi.org/10.1029/2007GL029912). 4.1, 4.7.1
- Lowry, A., K. Larson, V. Kostoglodov, and R. Bilham (2001), Transient fault slip in Guerrero, southern Mexico, *J. Geophys. Res.*, *28*(19), 3753 – 3756, doi:[10.1029/2001GL013238](https://doi.org/10.1029/2001GL013238). 4.1

- Mosegaard, K., and A. Tarantola (1995), Monte Carlo sampling of solutions to inverse problems, *J. Geophys. Res.*, *100*(B7), 12,431 – 12,447, doi:[10.1029/94JB03097](https://doi.org/10.1029/94JB03097). 4.5
- Okada, Y. (1985), Surface deformation due to shear and tensile faults in a half-space, *Bulletin of the Seismological Society of America*, *75*(4), 1135 – 1154. 4.5
- Ortiz, M., S. Singh, V. Kostoglodov, and J. Pacheco (2000), Source areas of the Acapulco-San Marcos, Mexico earthquakes of 1962 (M 7.1; 7.0) and 1957 (M 7.7), as constrained by tsunami and uplift records, *Geofísica Internacional*, *39*(4), 337 – 348. 4.1
- Pardo, M., and G. Suárez (1995), Shape of the subducted Rivera and Cocos Plates in southern Mexico: Seismic and tectonic implications, *J. Geophys. Res.*, *100*(B7), 12,357 – 12,373, doi:[10.1029/95JB00919](https://doi.org/10.1029/95JB00919). 4.5
- Pérez-Campos, X., Y. Kim, A. Husker, P. Davis, R. Clayton, A. Iglesias, J. Pacheco, S. Singh, V. Manea, and M. Gurnis (2008), Horizontal subduction and truncation of the Cocos Plate beneath central Mexico, *Geophys. Res. Lett.*, *35*(18), doi:[10.1029/2008GL035127](https://doi.org/10.1029/2008GL035127). 4.5, 4.7.2
- Radiguet, M., F. Cotton, M. Vergnolle, M. Campillo, B. Valette, V. Kostoglodov, and N. Cotte (2011), Spatial and temporal evolution of a long term slow slip event: the 2006 Guerrero Slow Slip Event, *Geophys. J. Int.*, *184*(2), 816 – 828, doi:[10.1111/j.1365-246X.2010.04866.x](https://doi.org/10.1111/j.1365-246X.2010.04866.x). 4.1, 4.5, 4.7.1
- Radiguet, M., F. Cotton, M. Vergnolle, M. Campillo, A. Walpersdorf, N. Cotte, and V. Kostoglodov (2012), Slow slip events and strain accumulation in the Guerrero gap, Mexico, *J. Geophys. Res.*, *117*(B4), doi:[10.1029/2011JB008801](https://doi.org/10.1029/2011JB008801). 4.5, 4.4, 4.5, 4.6.2, 4.7.1, 4.7.3, 4.10, 4.4
- Rosen, P., S. Henley, G. Peltzer, and M. Simons (2004), Updated Repeat Orbit Interferometry Package Released, *Eos Trans. AGU*, *85*(5), 47 – 47, doi:[10.1029/2004EO050004](https://doi.org/10.1029/2004EO050004). 4.2, 4.8
- Rubinstein, J., D. Shelly, and W. Ellsworth (2010), *New Frontiers in Integrated Solid Earth Sciences*, chap. Non-volcanic Tremor: A Window into the Roots of Fault Zones, pp. 287 – 314, Springer, doi:[10.1007/978-90-481-2737-5](https://doi.org/10.1007/978-90-481-2737-5). 4.7.2
- Singh, S. K., and F. Mortera (1991), Source Time Functions of Large Mexican Subduction Earthquakes, Morphology of the Benioff Zone, Age of the Plate, and Their Tectonic Implications, *J. Geophys. Res.*, *96*(B13), 21,487 – 21,502, doi:[10.1029/91JB02047](https://doi.org/10.1029/91JB02047). 4.1
- Singh, S. K., and M. Pardo (1993), Geometry of the Benioff Zone and state of stress in the overriding plate in central Mexico, *Geophys. Res. Lett.*, *20*(14), 1483 – 1486, doi:[10.1029/93GL01310](https://doi.org/10.1029/93GL01310). 4.5
- Song, T., and Y. Kim (2012), Localized seismic anisotropy associated with long-term slow-slip events beneath southern Mexico, *Geophys. Res. Lett.*, *39*(9), doi:[10.1029/2012GL051324](https://doi.org/10.1029/2012GL051324). 4.7.2
- Song, T., D. Helmberger, M. Brudzinski, R. Clayton, P. Davis, X. Peérez-Campos, and S. Singh (2009), Subducting Slab Ultra-Slow Velocity Layer Coincident with Silent Earthquakes in Southern Mexico, *Science*, *324*(5926), 502 – 506, doi:[10.1126/science.1167595](https://doi.org/10.1126/science.1167595). 4.6, 4.7.2
- Suárez, G., T. Monfret, G. Wittlinger, and C. David (1990), Geometry of subduction and depth of the seismogenic zone in the Guerrero gap, Mexico, *Nature*, *345*(6273), 336 – 338, doi:[10.1038/345336a0](https://doi.org/10.1038/345336a0).
- Vergnolle, M., A. Walpersdorf, V. Kostoglodov, P. Tregoning, J. Santiago, N. Cotte, and S. Franco (2010), Slow slip events in Mexico revised from the processing of 11-year GPS observations, *J. Geophys. Res.*, *115*(B8), doi:[10.1029/2009JB006852](https://doi.org/10.1029/2009JB006852). 4.1, 4.3, 4.3, 4.6.1, 4.6.2, 4.7.1, 4.8

-
- Wackernagel, H. (Ed.) (2003), *Multivariate Geostatistics*, Springer, Springer-Verlag Berlin Heidelberg, edition 3. [4.4](#), [4.8](#)
- Walpersdorf, A., N. Cotte, V. Kostoglodov, M. Vergnolle, M. Radiguet, J. A. Santiago, and M. Campillo (2011), Two successive slow slip events evidenced in 2009/2010 by a dense GPS network in Guerrero, Mexico, *Geophys. Res. Lett.*, *38*(15), doi:[10.1029/2011GL048124](#). [4.1](#)
- Wessel, P., and W. Smith (1991), Free Software helps Map and Display Data, *Eos Trans. AGU*, *72*(41), 445 – 446, doi:[10.1029/90EO00319](#). [4.8](#)
- Zebker, H. (1992), Decorrelation in interferometric radar echoes, *IEEE Transactions on Geoscience and Remote Sensing*, *30*(5), 950 – 959, doi:[10.1109/36.175330](#). [4.2](#)
- Zebker, H., P. Rosen, and S. Hensley (1997), Atmospheric effects in interferometric synthetic aperture radar surface deformation and topographic maps, *J. Geophys. Res.*, *102*(B4), 7547 – 7563, doi:[10.1029/96JB03804](#). [4.7.1](#)

Chapter 5

A Network Inversion Filter combining GNSS and InSAR for tectonic slip modeling

D.P.S. Bekaert¹, P. Segall², T.J. Wright¹, and A.J. Hooper¹

¹ *COMET, School of Earth and Environment, University of Leeds, United Kingdom*

² *Department of Geophysics, Stanford University, United States of America*

Abstract

Studies of the earthquake cycle benefit from long-term time-dependent slip modeling, as it can be a powerful means to improve our understanding on the interaction of earthquake cycle processes such as interseismic, coseismic, postseismic, and aseismic slip. Observations from Interferometric Synthetic Aperture Radar (InSAR) allow us to model slip at depth with a higher spatial resolution than when using GNSS alone. While the temporal resolution of InSAR has typically been limited, the recent fleet of SAR satellites including Sentinel-1, COSMO-SkyMED, and RADARSAT-2 permits the use of InSAR for time-dependent slip modeling, at intervals of a few days when combined. With the vast amount of SAR data available, simultaneous data inversion of all epochs becomes challenging. Here, we expanded the original Network Inversion Filter to include InSAR observations of surface displacements in addition to GNSS. In the NIF framework, geodetic observations are limited to those of a given epoch, with a stochastic model describing slip evolution over time. The combination of the Kalman forward filtering and backward smoothing allows all geodetic observations to constrain the complete observation period. Combining GNSS and InSAR allows modeling of time-dependent slip at unprecedented spatial resolution. We validate the approach with a simulation of the 2006 Guerrero slow slip event. We highlight the importance

of including InSAR covariance information, and demonstrate that InSAR provides an additional constraint on the spatial extent of the slow slip.

5.1 Introduction

For a better understanding of what causes and triggers earthquakes, it is important to study all processes of the earthquake cycle. One aspect of this is the study of the spatial and temporal inter-relation between the interseismic period, coseismic events and related postseismic signals, as well as aseismic slip processes such as slow slip events, which also change the surrounding stress field.

In the last few decades geodetic observations have proliferated with the development of dense permanent GNSS networks such as the GPS Earth Observation NETwork (GEONET) in Japan, the Southern California Integrated GPS Network (SCIGN), the Pacific Northwest Geodetic Array (PANGA), and the Sumatran GPS Array (SuGAR), and the acquisition of Interferometric Synthetic Aperture Radar (InSAR) data from a large variety of satellites. Multiple studies have used the high temporal resolution of continuous GNSS stations to model time-dependent processes including those of slow slip events (e.g. *Cervelli et al., 2002*, *Segall et al., 2006*, *Schmidt and Gao, 2010*, *Radigue et al., 2011*, *Bartlow et al., 2014*), post-seismic slip (e.g. *Hsu et al., 2006*, *Kositsky and Avouac, 2010*), afterslip (e.g. *Miyazaki et al., 2004*, *Bedford et al., 2013*), and transient deformation (e.g. *Mavrommatis et al., 2014*). However, the spatial resolution is dependent on the local GNSS network, and thus GNSS station distribution. In contrast, Interferometric SAR (InSAR) has a much finer spatial resolution, on the order of meters, but is limited to longer time-scales, with acquisitions every few days at best, and is only sensitive to deformation in the direction of the radar line of sight. Because of complementary advantages, GNSS and InSAR are often used in a joint framework (e.g. *Pritchard et al., 2002*, *Simons et al., 2002*, *Wright et al., 2004*).

One way to retrieve the time-dependent history of fault slip is to invert all observations at all epochs simultaneously for slip at depth. This can become data and memory intensive, especially when considering vast amounts of continuous GNSS and InSAR data, the latter of which can be a few millions of observations for a single track and epoch. Strategies exist to decrease the amount of InSAR data but might not be sufficient, e.g. uniform grid resampling (e.g. *Pritchard et al., 2002*), quadtree resampling based on the local variance (e.g. *Jónsson et al., 2002*), curvature-based resampling (e.g. *Simons et al., 2002*), or using resolution-based resampling (*Lohman and Simons, 2005*). Even so, with many acquisitions the data load can become untenable.

Alternatives to the single inversion approach exist, such as the Principal Component Analysis-based Inversion Method (PCA-IM) (*Kositsky and Avouac, 2010*), the Network Inversion Filter (NIF) (*Segall and Matthews, 1997*), and its modification, the Extended Network Inversion Filter (ENIF) (*McGuire and Segall, 2003*). PCA-IM relies on a

principal component analysis in the time domain to resolve the surface deformation time-series. The NIF uses a stochastic description to describe how slip on the fault or subduction zone interface evolves in time using a Kalman filter. This has the advantage that it limits the observations in any single inversion step to those at the current epoch only. Unlike the NIF and the ENIF, PCAIM does not require temporal smoothing to be solved as hyperparameter, as the temporal smoothing follows from the number of selected PCA components, which follows based on the statistical reduced chi-square statistics. However, PCAIM is not capable of estimating specific terms such as the GNSS local station motion or the GNSS reference frame motion. For all these methods, the authors suggest the potential of including InSAR data as observations.

In our study we focus on the extension of the NIF (version by *Bartlow et al. (2014)* which is an expansion of *Segall and Matthews (1997)*) to combine GNSS and InSAR observations. The NIF implementation uses Kalman forward modeling and a backward smoothing operation. After completing both operations, all geodetic observations will provide a constraint on the slip estimates at all epochs. The strength of the NIF thus lies in the complementary InSAR and GNSS datasets, where GNSS provides a high temporal resolution and InSAR gives the high spatial resolution. We describe and implement the methodology required to include InSAR in the NIF, combined with GNSS. We then demonstrate the procedure on a synthetic simulation of the 2006 Guerrero slow slip event.

5.2 Network Inversion Filter

To model time-dependent fault slip using Kalman filtering, the relationship between fault slip, \mathbf{s} , and geodetic observations of surface displacements, \mathbf{d} , is combined with a stochastic description of how slip evolves over time. The relationship between slip and the displacement at the surface follows from elastostatic Green's functions (e.g. *Okada, 1985*, *Thomas, 1993*). However, surface displacements as observed by geodetic techniques will be contaminated by processes including non-tectonic deformation, such as motions introduced by soil compaction. In addition, GNSS reference frame corrections, InSAR orbit errors, and atmospheric delays introduce additional apparent deformation that must be accounted for.

The observation equation at a time (epoch) t_k relates the state vector of unknowns \mathbf{X}_k to the observations \mathbf{d}_k as:

$$\mathbf{d}_k = \mathbf{H}_k \mathbf{X}_k + \boldsymbol{\epsilon}_k, \quad (5.1)$$

where \mathbf{H}_k is the observation matrix, and the observation errors $\boldsymbol{\epsilon}_k \sim \mathcal{N}(0, \mathbf{R}_k)$, with \mathbf{R}_k the data covariance matrix. In addition to geodetic observations from e.g. GNSS and InSAR, pseudo-observations can be included to enforce spatial smoothing, for

example by minimizing the second derivative or Laplacian of the slip as $\min \|\nabla^2 \mathbf{s}\| \sim \mathcal{N}(0, \kappa^2 \mathbf{I})$, where κ is a scalar determining the amount of smoothing (*Segall et al., 2000*).

The state transition equation describes how the state vector, \mathbf{X}_k , at the current epoch, t_k , relates to the state, \mathbf{X}_{k+1} , of the future at epoch, t_{k+1} .

$$\mathbf{X}_{k+1} = \mathbf{T}_{k+1} \mathbf{X}_k + \boldsymbol{\delta}_{k+1}, \quad \text{with } \boldsymbol{\Omega}_{k+1} = \mathbf{T}_{k+1} \boldsymbol{\Omega}_k \mathbf{T}_{k+1}^T + \mathbf{Q}_{k+1} \quad (5.2)$$

where \mathbf{T}_{k+1} is the transition matrix, $\boldsymbol{\delta}_{k+1}$ the process noise $\sim \mathcal{N}(0, \mathbf{Q}_{k+1})$, and $\boldsymbol{\Omega}_{k+1}$ the prediction variance-covariance matrix, all at epoch t_{k+1} . $\boldsymbol{\Omega}_{k+1}$ follows from error propagation and combination of the process noise variance-covariance matrix \mathbf{Q}_{k+1} . The definition depends on the formulation of the inverse problem. In section 5.2.3 we elaborate on this for our application.

The definition of the transition matrix depends on the stochastic model. The Network Inversion Filter (NIF) as proposed by *Segall and Matthews (1997)* is designed to detect the departure of slip from steady state, which we define to be the interseismic rate. The prior assumption is that the slip acceleration is close to zero, and can be modelled as a white noise process, with scale parameter ω as $\sim \mathcal{N}(0, \omega^2)$. This allows cumulative slip s since time t_0 to be written as:

$$s_t = v(t - t_0) + W_t, \quad (5.3)$$

where v is the interseismic slip rate, and W_t the accumulated slip deviated from the interseismic rate. The accumulated transient slip is the integral of a random walk process \dot{W} , or twice the integral of a white noise process with variance ω^2 . The scale parameter ω constrains the temporal smoothing of the slip. \dot{W} is the transient slip rate. For a more complete description of the theoretical basis for the NIF see *Segall and Matthews (1997)*.

Below, we elaborate on the individual observation equations for GNSS (section 5.2.1) and InSAR (section 5.2.2), and describe how the state variables are assumed to change in time. Finally (section 5.2.3), we combine both GNSS and InSAR, and derive the full observation matrix \mathbf{H}_k , the observation variance-covariance matrix \mathbf{R}_k , the state transition matrix \mathbf{T}_{k+1} , and the process noise variance-covariance matrix \mathbf{Q}_{k+1} . These four matrices completely define the linear system.

5.2.1 GNSS observation equation

The GNSS surface displacements, \mathbf{d}^{GNSS} , can be written as (e.g. *Segall and Matthews, 1997*):

$$\mathbf{d}^{\text{GNSS}}(\mathbf{x}, t, t_0^{\text{GNSS}}) = \mathbf{G}(\mathbf{x}) \left[\mathbf{s}_t - \mathbf{s}_{t_0^{\text{GNSS}}} \right] + \mathcal{L}(\mathbf{x}, t) + \mathbf{F}\mathcal{F}(t) + \boldsymbol{\epsilon}^{\text{GNSS}}, \quad (5.4)$$

where \mathbf{x} describes the station location, t_0^{GNSS} is the start of the GNSS time-series, \mathbf{G} are the Green's coefficients relating slip to surface displacements, and \mathcal{L} are the local GNSS benchmark motions for each component (ENU) and every station, modeled as a Brownian random walk with scale τ as $\mathcal{L} = \tau \int_0^t dw$ (*Langbein and Johnson, 1997*). Note, the benchmark motions represent spatially-incoherent GNSS network displacements and therefore should not include displacements related to \mathbf{G} s. $\mathbf{F}\mathcal{F}$ is the GNSS reference frame error, where \mathbf{F} is a linearized Helmert transformation (e.g. *Miyazaki et al., 2003, Mavrommatis et al., 2014*). \mathcal{F} is a vector containing the coefficients of the Helmert transformation (translation, rotation, and scale factors for each component). We assume the latter to be an identity matrix, and let the ζ^2 control the variance. ϵ^{GNSS} are the GNSS observation errors $\sim \mathcal{N}(0, \Sigma^{\text{GNSS}}(t))$, where $\Sigma^{\text{GNSS}}(t)$ is the GNSS observation variance-covariance matrix at time t .

5.2.2 InSAR observation equation

The InSAR surface displacements, $\Delta \mathbf{d}^{\text{InSAR}}$, are the difference in the radar line of sight between two acquisition times, t_0^{InSAR} and t , and for which the observations are with respect to an arbitrary reference area or pixel (e.g. *Hooper et al., 2012, Bekaert et al., 2015*):

$$\begin{aligned} \Delta \mathbf{d}^{\text{InSAR}}(\mathbf{x}, t, t_0^{\text{InSAR}}) &= \mathbf{d}^{\text{InSAR}}(\mathbf{x}, t) - \mathbf{d}^{\text{InSAR}}(\mathbf{x}, t_0^{\text{InSAR}}) \\ &= \mathbf{G}(\mathbf{x}) \left[\mathbf{s}_t - \mathbf{s}_{t_0^{\text{InSAR}}} \right] + \mathbf{P}\mathcal{P}(t) + \epsilon^{\text{InSAR}}, \end{aligned} \quad (5.5)$$

where t_0^{InSAR} refers to the acquisition time of the first SAR image. A planar correction $\mathbf{P}\mathcal{P} = [\mathbf{x}_1, \mathbf{x}_2, \mathbf{1}] [\alpha, \beta, \gamma]^\top$ is included to account for the long wavelength orbit errors in the interferogram between t_0^{InSAR} and t ; \mathbf{x}_1 and \mathbf{x}_2 are the coordinates of the InSAR observations in a local reference frame. The variation of the planar coefficients in time is assumed to be uncorrelated between interferograms. ϵ^{InSAR} are the InSAR observation errors $\sim \mathcal{N}(0, \Sigma^{\text{InSAR}}(t))$, where $\Sigma^{\text{InSAR}}(t)$ is the interferogram observation variance-covariance matrix at time t .

5.2.3 Joint GNSS and InSAR observation and state transition equation

For the derivation of the full observation matrix \mathbf{H}_k , let us assume that the number of GNSS stations, N_s , does not vary in time. Likewise for the number of InSAR pixels, N_p , which is consistent over N_I interferograms. For simplicity we limit the description below to one GNSS network and InSAR track, but expand \mathbf{H}_k to include multiple InSAR tracks in Appendix 5.6. Combining the GNSS observations, equation (5.4), with those of InSAR, equation (5.6), in the observation equation (5.1), including

Laplacian smoothing, at time t_k results in:

$$\begin{bmatrix} \mathbf{d}^{\text{GNSS}} \\ \Delta \mathbf{d}^{\text{InSAR}} \\ \mathbf{0} \\ \mathbf{0} \\ \mathbf{0} \end{bmatrix}_{t_k} = \underbrace{\begin{bmatrix} \mathbf{G}^{\text{GNSS}}(t_k - t_0^{\text{GNSS}}) & \mathbf{G}^{\text{GNSS}} & \mathbf{0} & \mathbf{I} & \mathbf{F} & \mathbf{0} & \mathbf{0} \\ \mathbf{G}^{\text{InSAR}}_{t_k} & \mathbf{G}^{\text{InSAR}} & \mathbf{0} & \mathbf{0} & \mathbf{0} & \mathbf{P} & -\mathbf{G}^{\text{InSAR}} \\ \nabla^2 & \mathbf{0} & \mathbf{0} & \mathbf{0} & \mathbf{0} & \mathbf{0} & \mathbf{0} \\ \mathbf{0} & \nabla^2 & \mathbf{0} & \mathbf{0} & \mathbf{0} & \mathbf{0} & \mathbf{0} \\ \mathbf{0} & \mathbf{0} & \nabla^2 & \mathbf{0} & \mathbf{0} & \mathbf{0} & \mathbf{0} \end{bmatrix}_{t_k}}_{\mathbf{H}_k} \begin{bmatrix} \mathbf{v} \\ \mathbf{W} \\ \dot{\mathbf{W}} \\ \mathcal{L} \\ \mathcal{F} \\ \mathcal{P} \\ \mathbf{s}_0^{\text{InSAR}} \end{bmatrix}_{t_k} + \boldsymbol{\epsilon}_k, \quad (5.6)$$

where $\Delta \mathbf{d}^{\text{InSAR}}$ is a $(N_p \times 1)$ vector of InSAR line-of-sight displacements, and \mathbf{d}^{GNSS} a $(3N_s \times 1)$ vector containing the three component GNSS displacements since t_0 . Here, we choose to minimize the Laplacian of the interseismic slip rate, slip, and transient slip rate separately. Alternative options can be included, such the slip ($\mathbf{s} = \mathbf{v}t + \mathbf{W}$) and/or slip rate ($\dot{\mathbf{s}} = \mathbf{v} + \dot{\mathbf{W}}$). Assuming that the fault is modeled using N_d dislocation patches, the state vector comprises of an interseismic rate vector \mathbf{v} , an integrated random walk vector \mathbf{W} (cumulative slip deviation from the interseismic), and a random walk vector $\dot{\mathbf{W}}$ (transient slip rate) – all of length N_d . Additional terms are defined in equations (5.4) and (5.6). The length of the state vector does not change and is identical in the state observation and state transition equations. As the slip rate does not have an influence on the observations, a column of zeros is included in the observation matrix. We assume that the InSAR network is defined or inverted with respect to the first acquisition at time t_0^{InSAR} . By doing so, we are able to estimate the reference slip with respect to t_0^{InSAR} . In cases of isolated networks in time on a single track, the sub-networks can be regarded as “new” tracks (see Appendix 5.6 for how to include multiple InSAR datasets). Initially the reference slip is assumed to be zero or a prior slip is assumed, which is updated to $\mathbf{s}_0^{\text{InSAR}} = \mathbf{v}t_k + \mathbf{W}_k$ at $t_k = t_0^{\text{InSAR}}$. We include, the reference slip at the time of the master acquisition by including a set of pseudo observations in the observation equation as $\mathbf{0} = \mathbf{v}t_k + \mathbf{W}_k - \mathbf{s}_0^{\text{InSAR}}$. Note, this is not shown in equation (5.7), and only applies at $t_k = t_0^{\text{InSAR}}$.

The observation variance-covariance matrix follows from the combination of GNSS, InSAR, and the weight of the Laplacian smoothing, κ_i^2 , assuming all to be uncorrelated

with each other, as:

$$\mathbf{R}_k = \begin{bmatrix} \sigma^2 \Sigma_k^{\text{GNSS}} & \mathbf{0} & \mathbf{0} & \mathbf{0} & \mathbf{0} \\ \mathbf{0} & \sigma^2 \Sigma_k^{\text{InSAR}} & \mathbf{0} & \mathbf{0} & \mathbf{0} \\ \mathbf{0} & \mathbf{0} & \kappa_1^2 \mathbf{I} & \mathbf{0} & \mathbf{0} \\ \mathbf{0} & \mathbf{0} & \mathbf{0} & \kappa_2^2 \mathbf{I} & \mathbf{0} \\ \mathbf{0} & \mathbf{0} & \mathbf{0} & \mathbf{0} & \kappa_3^2 \mathbf{I} \end{bmatrix}, \quad (5.7)$$

where an additional scale parameter σ of the observation variance-covariance matrices is included to account for uncertainty in the model. For simplicity, we assume the weight of the Laplacian smoothing to be the same for the interseismic rate, slip, and slip rate; thus $\kappa = \kappa_1 = \kappa_2 = \kappa_3$.

In the state transition equation (5.2), the interseismic slip rate is by definition constant in time and does not, therefore, change from epoch t_k to t_{k+1} . The transient slip (integrated random walk) at the new epoch, \mathbf{W}_{k+1} , follows from that of the previous epoch combined with the integration of the random walk between both epochs as $\mathbf{W}_{k+1} = \mathbf{W}_k + (t_{k+1} - t_k) \dot{\mathbf{W}}_k$. As indicated before, the GNSS benchmark motion follows a random walk. The GNSS reference frame correction is assumed to be independent from epoch to epoch (*Segall and Matthews, 1997*), i.e. white noise $\sim \mathcal{N}(0, \zeta^2 \mathbf{I}_{\mathcal{F}})$, where ζ is a scale parameter of the reference frame variance-covariance matrix $\mathbf{I}_{\mathcal{F}}$. Similarly, the InSAR orbit (plane) is assumed to be white noise $\sim \mathcal{N}(0, \varrho^2 \mathbf{I}_{\mathcal{P}})$. The full state transition equation can be written as:

$$\underbrace{\begin{bmatrix} \mathbf{v} \\ \mathbf{W} \\ \dot{\mathbf{W}} \\ \mathcal{L} \\ \mathcal{F} \\ \mathcal{P} \\ \mathbf{s}_0^{\text{InSAR}} \end{bmatrix}}_{\mathbf{X}_{k+1}} \Big|_{t_{k+1}} = \underbrace{\begin{bmatrix} \mathbf{I} & \mathbf{0} & \mathbf{0} & \mathbf{0} & \mathbf{0} & \mathbf{0} & \mathbf{0} \\ \mathbf{0} & \mathbf{I} & \mathbf{I}(t_{k+1} - t_k) & \mathbf{0} & \mathbf{0} & \mathbf{0} & \mathbf{0} \\ \mathbf{0} & \mathbf{0} & \mathbf{I} & \mathbf{0} & \mathbf{0} & \mathbf{0} & \mathbf{0} \\ \mathbf{0} & \mathbf{0} & \mathbf{0} & \mathbf{I}_{\mathcal{L}} & \mathbf{0} & \mathbf{0} & \mathbf{0} \\ \mathbf{0} & \mathbf{0} & \mathbf{0} & \mathbf{0} & \mathbf{0} & \mathbf{0} & \mathbf{0} \\ \mathbf{0} & \mathbf{0} & \mathbf{0} & \mathbf{0} & \mathbf{0} & \mathbf{0} & \mathbf{0} \\ \mathbf{0} & \mathbf{0} & \mathbf{0} & \mathbf{0} & \mathbf{0} & \mathbf{0} & \mathbf{I} \end{bmatrix}}_{\mathbf{T}_{k+1}} \Big|_{t_{k+1}} \underbrace{\begin{bmatrix} \mathbf{v} \\ \mathbf{W} \\ \dot{\mathbf{W}} \\ \mathcal{L} \\ \mathcal{F} \\ \mathcal{P} \\ \mathbf{s}_0^{\text{InSAR}} \end{bmatrix}}_{\mathbf{X}_k} \Big|_{t_k} + \boldsymbol{\delta}_{k+1}, \quad (5.8)$$

with $\mathbf{0}$ a zeros matrix, \mathbf{I} an identity matrix, both of size $(N_d \times N_d)$, and $\mathbf{I}_{\mathcal{L}}$ an identity matrix of size $(3N_s \times 3N_s)$.

For the process noise variance-covariance matrix, \mathbf{Q}_{t_k} , we follow e.g. *Segall and Matthews (1997)*, *Segall et al. (2000)*, for the interseismic slip rate, integrated random walk, random walk, GNSS benchmark motion, and GNSS reference frame errors. We apply the same methodology for the InSAR orbit (plane) with error distribution $\sim \mathcal{N}(0, \varrho^2 \mathbf{I}_{\mathcal{P}})$. Like the interseismic slip rate, the reference slip does not change in time.

The full process noise variance-covariance matrix \mathbf{Q}_{t_k} is therefore:

$$\mathbf{Q}_{t_k} = \begin{bmatrix} \mathbf{0} & \mathbf{0} & \mathbf{0} & \mathbf{0} & \mathbf{0} & \mathbf{0} & \mathbf{0} \\ \mathbf{0} & \omega^2 \frac{\Delta t^3}{3} \mathbf{I} & \omega^2 \frac{\Delta t^2}{2} \mathbf{I} & \mathbf{0} & \mathbf{0} & \mathbf{0} & \mathbf{0} \\ \mathbf{0} & \omega^2 \frac{\Delta t^2}{2} \mathbf{I} & \omega^2 \Delta t \mathbf{I} & \mathbf{0} & \mathbf{0} & \mathbf{0} & \mathbf{0} \\ \mathbf{0} & \mathbf{0} & \mathbf{0} & \tau^2 \Delta t \mathbf{I}_{\mathcal{L}} & \mathbf{0} & \mathbf{0} & \mathbf{0} \\ \mathbf{0} & \mathbf{0} & \mathbf{0} & \mathbf{0} & \zeta^2 \mathbf{I}_{\mathcal{F}} & \mathbf{0} & \mathbf{0} \\ \mathbf{0} & \mathbf{0} & \mathbf{0} & \mathbf{0} & \mathbf{0} & \varrho^2 \mathbf{I}_{\mathcal{P}} & \mathbf{0} \\ \mathbf{0} & \mathbf{0} & \mathbf{0} & \mathbf{0} & \mathbf{0} & \mathbf{0} & \mathbf{0} \end{bmatrix}, \quad (5.9)$$

with $\Delta t = (t_{k+1} - t_k)$. Like before, $\mathbf{0}$ and \mathbf{I} are the zero and identity matrices. The size of $\mathbf{I}_{\mathcal{P}}$ is (3×3) , while for $\mathbf{I}_{\mathcal{F}}$ the size depends on the parameters included; for example in case of translation, rotation, and scaling it has size (7×7) .

5.2.4 Kalman filter and backward smoothing procedure

The full description of the Kalman forward filtering and backward smoothing approach is contained in *Segall and Matthews (1997)*. During the forward filtering step, the observations up to (and including) that of the current epoch, t_k , are used to predict the state of the next epoch, $\hat{\mathbf{X}}_{k+1|k}$. We use the notation $\hat{\mathbf{X}}_{k+1|k}$, which reads $\hat{\mathbf{X}}$ at $k+1$ given k , and is the state at epoch $k+1$ given the data up to epoch k . The prediction is described by the state transition equation (5.2):

$$\begin{aligned} \hat{\mathbf{X}}_{k+1|k} &= \mathbf{T}_{k+1} \hat{\mathbf{X}}_{k|k} \\ \mathbf{\Omega}_{k+1|k} &= \mathbf{T}_{k+1} \mathbf{\Omega}_{k|k} \mathbf{T}_{k+1}^T + \mathbf{Q}_{k+1}. \end{aligned} \quad (5.10)$$

This is followed by an update to the estimated state, by including the actual observations of the predicted epoch as:

$$\begin{aligned} \hat{\mathbf{X}}_{k+1|k+1} &= \hat{\mathbf{X}}_{k+1|k} + \mathbf{K}_{k+1} (\mathbf{d}_{k+1} - \mathbf{H}_{k+1} \hat{\mathbf{X}}_{k+1|k}) \\ \mathbf{\Omega}_{k+1|k+1} &= \mathbf{\Omega}_{k+1|k} - \mathbf{K}_{k+1} \mathbf{H}_{k+1} \mathbf{\Omega}_{k+1|k}. \end{aligned} \quad (5.11)$$

The notation $\hat{\mathbf{X}}_{k+1|k+1}$, now reads $\hat{\mathbf{X}}$ at epoch $k+1$ given the data up to epoch $k+1$. \mathbf{K}_{k+1} is the Kalman filter gain at epoch t_{k+1} , defined as:

$$\mathbf{K}_{k+1} = \mathbf{\Omega}_{k+1|k} \mathbf{H}_{k+1}^T (\mathbf{R}_{k+1} + \mathbf{H}_{k+1} \mathbf{\Omega}_{k+1|k} \mathbf{H}_{k+1}^T)^{-1}. \quad (5.12)$$

The prediction and update procedure is applied in sequence to the whole time-series until the observations of the last epoch, N , are updated, yielding $\hat{\mathbf{X}}_{N|N}$. At this stage, the estimated state is conditional on the data up to that epoch. After performing the backward smoothing operation, an identical procedure to Kalman filtering but with time reversed (i.e. starting from the last epoch), all geodetic observations are used in

constraining the state vector at all epochs, yielding $\widehat{\mathbf{X}}_{k|N}$ for all k .

To initiate the Kalman filter, an *a priori* estimate of state vector given no data, $\widehat{\mathbf{X}}_{1|0}$, is assumed, which describes the state at the initial epoch without any constraint from the data. The corresponding uncertainties are specified in $\mathbf{\Omega}_{1|0}$. Larger uncertainty can be attributed when good *a priori* knowledge of the state vector is lacking.

5.2.5 Comparing the NIF with the earlier implementation

We modified the version of the NIF by [Bartlow et al. \(2014\)](#), which works with GNSS data only, to include also InSAR data. While the main changes are related to the InSAR data component, we also include the interseismic rate directly into the inverse problem, whereas, [Bartlow et al. \(2014\)](#) corrects the GNSS observations for the interseismic slip rate prior to ingestion in the NIF. To assess the impact of our modifications, we compared the results of our NIF version and that of [Bartlow et al. \(2014\)](#) when inverting GNSS observations of the 2011 Cascadia Slow Slip Event (SSE). This dataset is distributed as test-data for the earlier implementation of the NIF. Overall, we find that our implementation does not significantly alter the results obtained from the previous implementation; average transient slip differences are <1 cm, and slip rate differences are negligible (~ 0 cm/day).

5.3 Synthetic simulation of the Guerrero SSE

Our test dataset reflects the tectonic setting in southern Mexico (Figure 5.1), with a simulation of the 2006 Guerrero SSE. Our observations span a duration of 1.8 years, from June 2005 to April 2007, and include an 8 month inter-SSE period, prior to the start of the 2006 SSE in February 2006 (1 year duration). We simulate the SSE, guided by the time-dependent GNSS modeling results of [Radiguet et al. \(2011\)](#), who solved for the slow slip source time function. We adopt a similar source time parameterization scheme ([Liu et al., 2006](#)), where the location of slow slip initialization and the 0.8 km/day slip propagation velocity is from the best fit GNSS model by [Radiguet et al. \(2011\)](#). For simplicity we fix the slow slip function rise time, which is estimated to vary between 160 and 200 days ([Radiguet et al., 2011](#)), to be 183 days. For the maximum accumulated slip over the duration of the 2006 SSE, we use the results from [Bekaert et al. \(2015\)](#), which are similar to other studies of the same event (e.g. [Vergnolle et al., 2010](#), [Radiguet et al., 2011](#), [Cavalié et al., 2013](#)). A full mathematical description of our time-dependent slow slip model is contained in Appendix 5.6. We define the interseismic loading using a backslip formulation ([Savage, 1983](#)), where the slip deficit follows from the multiplication of the time with the MORVEL plate convergence rate of 6.1 cm/year ([DeMets et al., 2010](#)) and a simulated inter-SSE coupling. The latter only varies with depth; we assume the fault is freely slipping at shallow depths (coupling = 0), fully locked in the seismogenic zone between ~ 15 -25 km (coupling = 1), and that

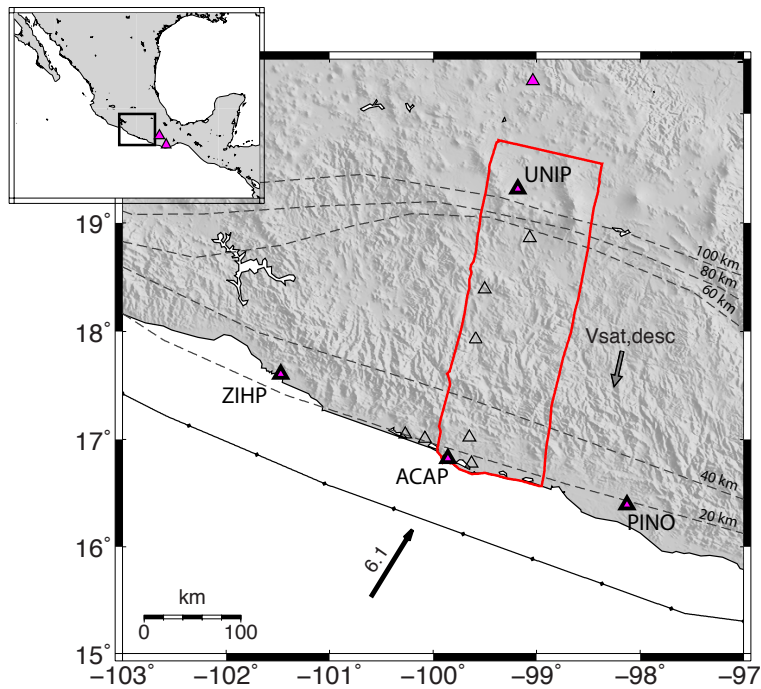


Figure 5.1: Overview map of the Guerrero region, where the seven magenta triangles indicate the location of the continuous GNSS sites used in our simulation. Black triangles show the other GNSS stations of the network that were not considered. The red polygon shows the extent of the InSAR track. The gray arrow indicates the MORVEL relative plate motion of the Cocos and the North America Plate (*DeMets et al., 2010*), with depth contours of the subducting slab indicated every 20 km (*Pardo and Suárez, 1995, Melgar and Pérez-Campos, 2011, Pérez-Campos and Clayton, 2014*).

there is a smooth transition region from 25-50 km depth, below which the fault is freely slipping.

We use the time-dependent cumulative simulated slip (interseismic and slow slip) on the subduction interface in combination with Green’s functions from triangular dislocations (*Thomas, 1993*), to infer the displacements over time at the surface. We use the real GNSS station distribution that was installed in 2006, but limit ourselves to seven stations, with six in the far field (magenta markers in Figure 5.1). We do this to show the impact of including InSAR more clearly in a typical region with sparse GNSS coverage. GNSS observations are simulated every 3 days, with random white noise of 1 mm uncertainty for the horizontal displacements, and 2 mm for the vertical displacements. A time-series with the north, east, and up components is shown for selected GNSS stations in Figure 5.2(a). The location of our simulated InSAR track corresponds to the location of the descending Envisat track 255 (red polygon in Figure 5.1), used in earlier slow slip studies over the region (e.g. *Bekaert et al., 2015, Cavalie et al., 2013*). In time, we fix our master SAR acquisition to be on 1 June 2005, with a simulated SAR acquisition every 2 months. We generate 10 interferograms, and include orbit errors by simulating the addition of a bilinear plane. We incorporate the effects of

residual atmosphere delays by including spatially-correlated noise according to [Lohman and Simons \(2005\)](#), which varies in magnitude and correlation length for each interferogram. Figure 5.2(b) shows the individually simulated components of the interferogram, and the interferograms as input to the NIF. Our simulated interferograms have similar signal magnitude as processed Envisat data over the region ([Bekaert et al., 2015](#)).

5.4 Results

We compare the NIF results when inverting for the GNSS observations only, and when jointly inverting GNSS and InSAR observations. InSAR covariance is often neglected in slip inversion studies. This should be avoided, as spatially-correlated atmospheric noise will be treated as if it were signal. To demonstrate the impact on the estimated slip, we also include a comparison between results when the InSAR covariance is included in the inversion, and when it is neglected. We do not change the initialization of the state vector parameters between the different cases. At $t = 0$, we assume the interseismic slip rate to be 0 cm/yr with a 6 cm/year uncertainty, the accumulative slip to be 0 cm with a 1 cm uncertainty, and the transient slip rate to be 0 cm/day with an uncertainty of 10^{-8} cm/day. These parameters are chosen assuming that the observations start in an inter-SSE period. We choose the reference frame and local station motion uncertainty such that local variations are allowed over time, but no clear tectonic leakage can be observed in time. This approach is needed for two main reasons: (1) the SSE is observed at only one GNSS station and therefore looks like an incoherent motion, while in reality it is a tectonic signal; (2) all GNSS stations are located on one side of the fault (hanging wall) and therefore the interseismic slip rate is quasi-uniform and will be partly mapped into the GNSS frame motion. The spatial and temporal smoothing hyperparameters vary between the different cases, and is selected through a maximum likelihood grid search, as proposed in the original NIF ([Segall and Matthews, 1997](#)) and applied in later studies (e.g. [Segall et al., 2000](#), [Bartlow et al., 2011, 2014](#)). As all GNSS observations are in the reference frame of the hanging wall, we are solving for the interseismic loading in a backslip framework ([Savage, 1983](#)). The transient slip has the opposite sense to the interseismic slip deficit. To avoid leakage of the interseismic slip rate into the transient slip rate, and vice-versa we enforce a negativity constraint on the interseismic slip rate consistent with the backslip formulation, while enforcing a positivity constraint on the transient slip rate. Identical to the approach by [Bartlow et al. \(2011\)](#), we use the PDCO (Primal-Dual interior method for Convex Objectives) package ([Saunders, 2015](#)) to optimize the state vector after imposing the sign constraint. Due to computation intensity, we do not run the PDCO optimization for the state vector as part of our hyperparameter grid search. However, after the Maximum Likelihood Estimation (MLE) of the hyperparameters, we compute the MLE slip solution including the PDCO optimization. Below, we report on the results from

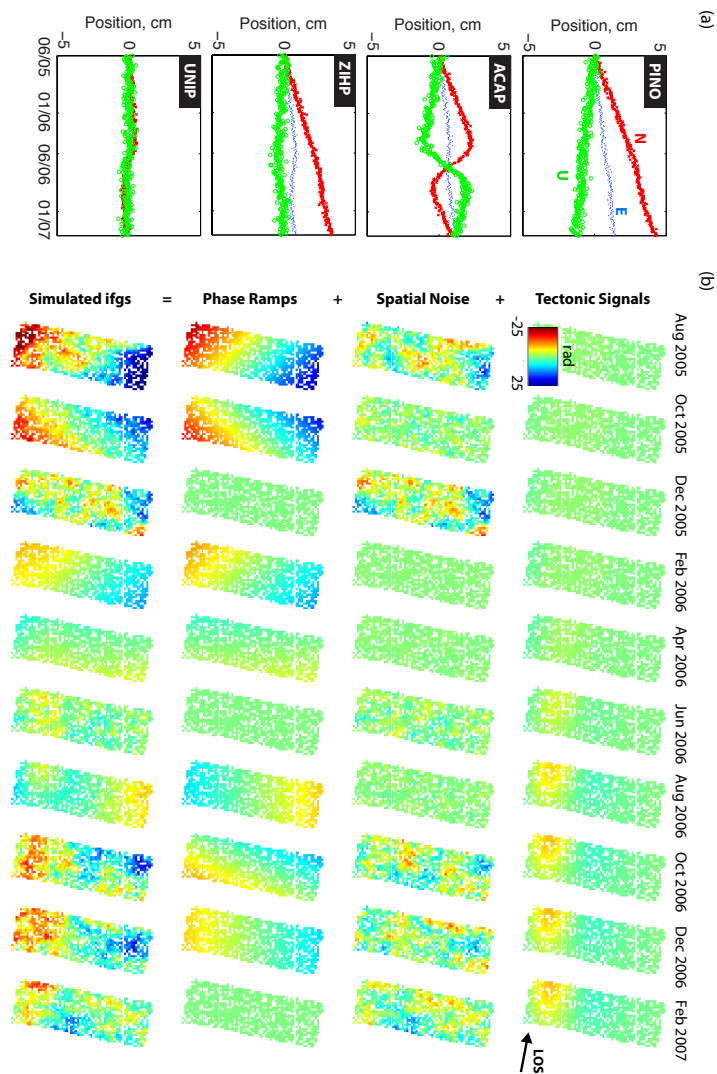


Figure 5.2: Overview of the simulated data. (a) Simulated surface displacement time-series for the labeled GNSS stations in Figure 5.1. (b) Simulated InSAR data, with (first row) the simulated tectonic signal, (second row) the simulated spatially-correlated noise, (third row) the InSAR orbit errors, and (bottom row) the interferograms as input in the NIF. 2π rad corresponds to 2.8 cm in the radar line of sight (LOS).

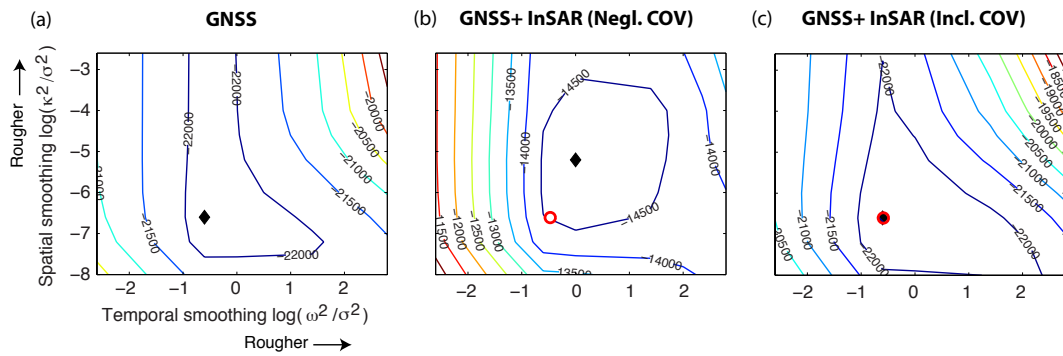


Figure 5.3: Likelihood surface ($-2L$) as function of the smoothing hyperparameters in space (κ^2/σ^2) and in time (ω^2/σ^2), obtained from a grid search. (a) In case of inverting for GNSS observations only, (b) when combining GNSS with InSAR while neglecting InSAR covariance, and (c) when combining GNSS and InSAR including full variance-covariance information. Black diamond markers represent the selected maximum likelihood solution, for which the inter-SSE locking rate is shown in Figure 5.4(b), the cumulative slip in Figure 5.5(b), and the slip rate history in Figure 5.6. The red circle marker in (b) and (c) corresponds to the maximum likelihood solution when using only GNSS (a).

the maximum likelihood solution for the three defined cases.

5.4.1 GNSS only

Figure 5.3(a) shows the results of the hyperparameter grid search, with a maximum likelihood value for spatial smoothing hyperparameter of $\kappa^2/\sigma^2 = 24 \cdot 10^{-8}$, temporal smoothing hyperparameter of $\omega^2/\sigma^2 = 0.24$, and estimated data variance-covariance scaling of $\hat{\sigma} = 0.97$. As expected, the latter is close to 1, indicating that the data uncertainty is well described by the inverse problem. The results of the maximum likelihood solution after forward filtering and backward smoothing are shown in Figure 5.4 for the inter-SSE locking rate, Figure 5.5 for the cumulative estimated slow slip, and Figure 5.6 for the transient slip rate history.

The coastal GNSS stations are located approximately above the locked part of the subduction interface, Figure 5.4(a), which is loaded in our simulation at a rate of ~ 6 cm/year. In our estimation we are capable of retrieving this same peak magnitude of 6 cm/year. We find that the locking rate on the fault is well estimated for patches close to (~ 20 km) the coastal GNSS sites, with a residual that falls within the ~ 1.5 cm/year estimated uncertainty (Figure 5.4(c)). While a similar strike-parallel pattern can be observed, we find the peak distribution to be located ~ 10 km shallower than that in the input simulation. We observe some smearing further down-dip, with an average residual of ~ 2.5 cm/year, which is likely due to the imposed smoothing constraint, and to compensate for the over-estimation near the trench. The poor resolution is not surprising given the very sparse GNSS coverage.

Our estimated cumulative slip, Figure 5.5(b), is a smeared version of the original simulation, Figure 5.5(a). This is to be expected, as the GNSS network is not well

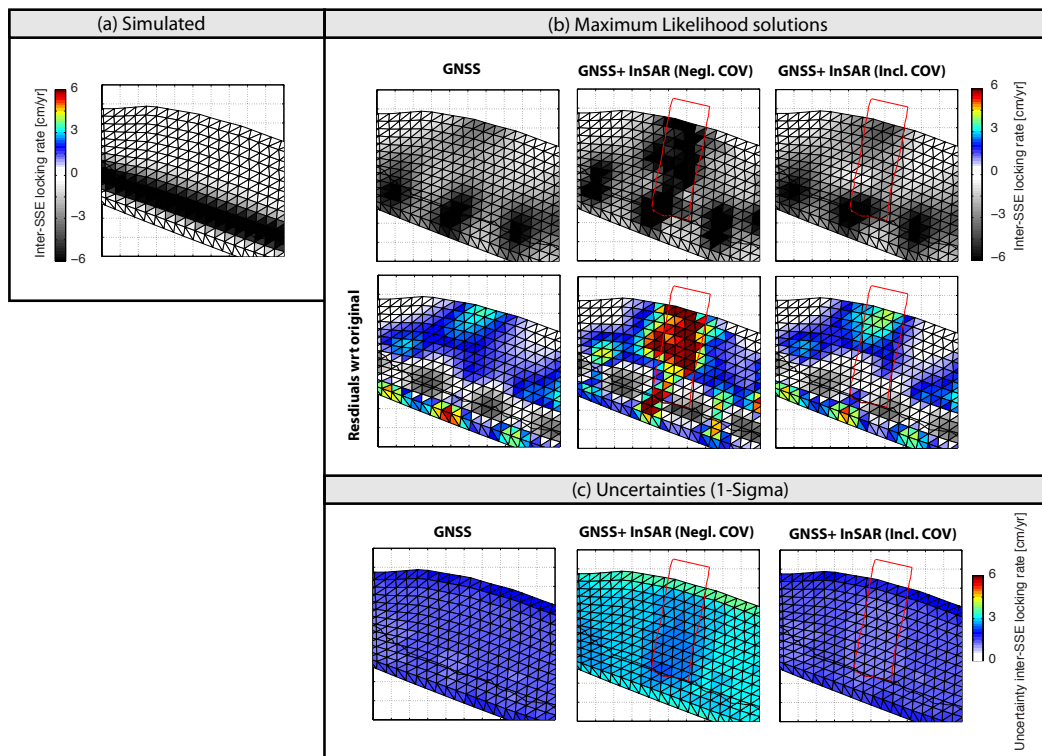


Figure 5.4: Comparison of the inter-SSE locking rate. (a) The simulated rate, (b) the Maximum Likelihood solutions, and the residuals with respect to the simulated value. (c) Estimated uncertainties. We show the Maximum Likelihood solution when using GNSS alone, and the joint inversion with InSAR, while neglecting and accounting for the InSAR covariance information.

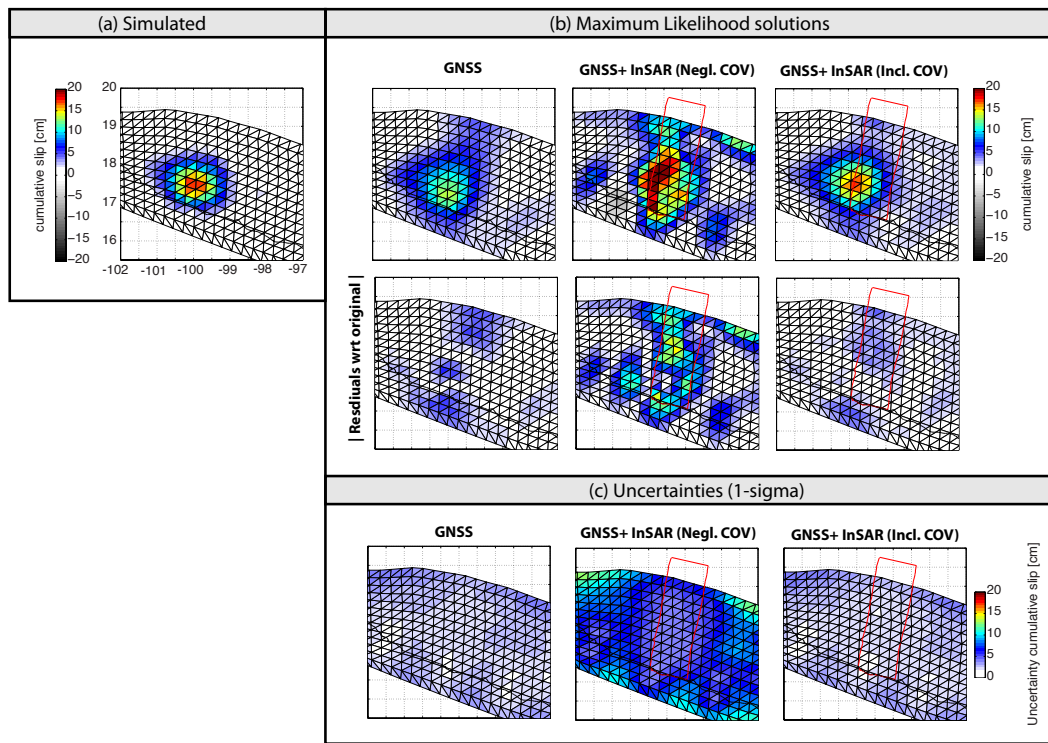


Figure 5.5: The same as Figure 5.4 but for the cumulative transient slip between January 2005 and April 2007.

distributed in order to resolve for the peak slow slip location, with only the ACAP station clearly capturing the SSE surface displacements. We find the peak slip to be under-estimated by ~ 7 cm, with an average estimated uncertainty of ~ 2 cm (Figure 5.5(c)). We also find some up-dip slip residuals, introduced by the mis-estimation of the inter-SSE loading. The latter also causes the slip uncertainty to grow over time.

We find the estimated slip rate (Figure 5.6 (second row)) to correlate in space and time with that of the simulation (Figure 5.6 (top row)). As for the cumulative slip, we find the estimated slip rate to be smoother than that of the simulation. On average, an under-estimation of ~ 0.06 cm/day is observed during the transient period (Figure 5.7 (top row)).

Original observations and those estimated are shown in the Supplemental material (Figure D.1). The modeled surface displacements fit the observations well, with a mean residual of around 0 mm, and an accuracy similar to that of the simulated observations: ~ 1 mm for horizontal and ~ 2 mm for the vertical components.

5.4.2 GNSS and InSAR (neglecting covariance)

Figure 5.3(b) shows the results of the grid search for the hyperparameters. Our estimated maximum likelihood value for the temporal smoothing hyperparameter ($\omega^2/\sigma^2 = 0.8$) is double that of the GNSS case. Compared to before, a much rougher spatial

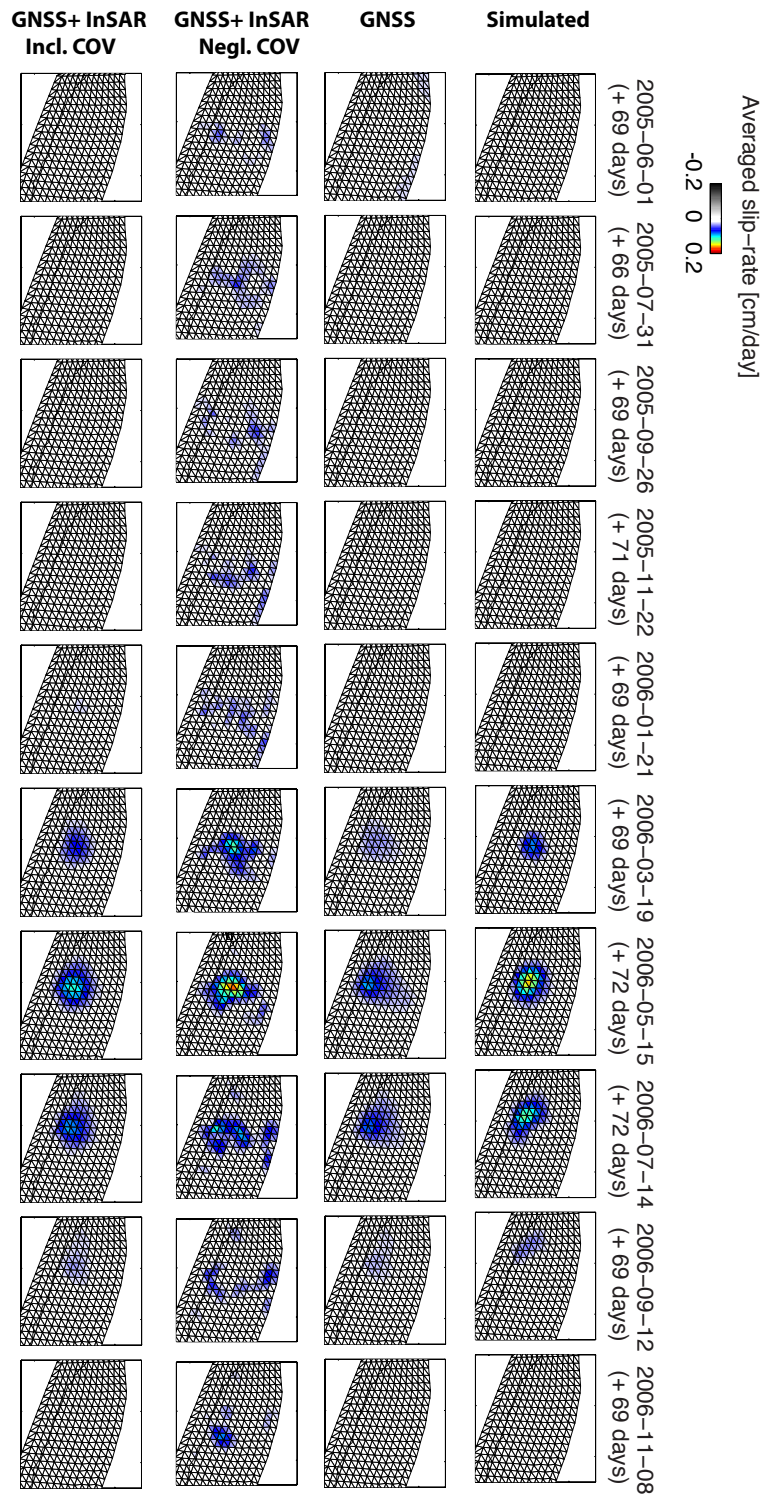


Figure 5.6: Transient slip rate history between January 2005 and April 2007, with a window each 2 months, averaged over ~ 70 days. The simulated slip rate (first row) is compared with the maximum likelihood solution when inverting for GNSS alone (second row), the combination of GNSS and InSAR while neglecting InSAR covariance (third row), and the joint inversion while including the InSAR covariance (bottom row). The averaging duration is indicated in the title as (+ # days).

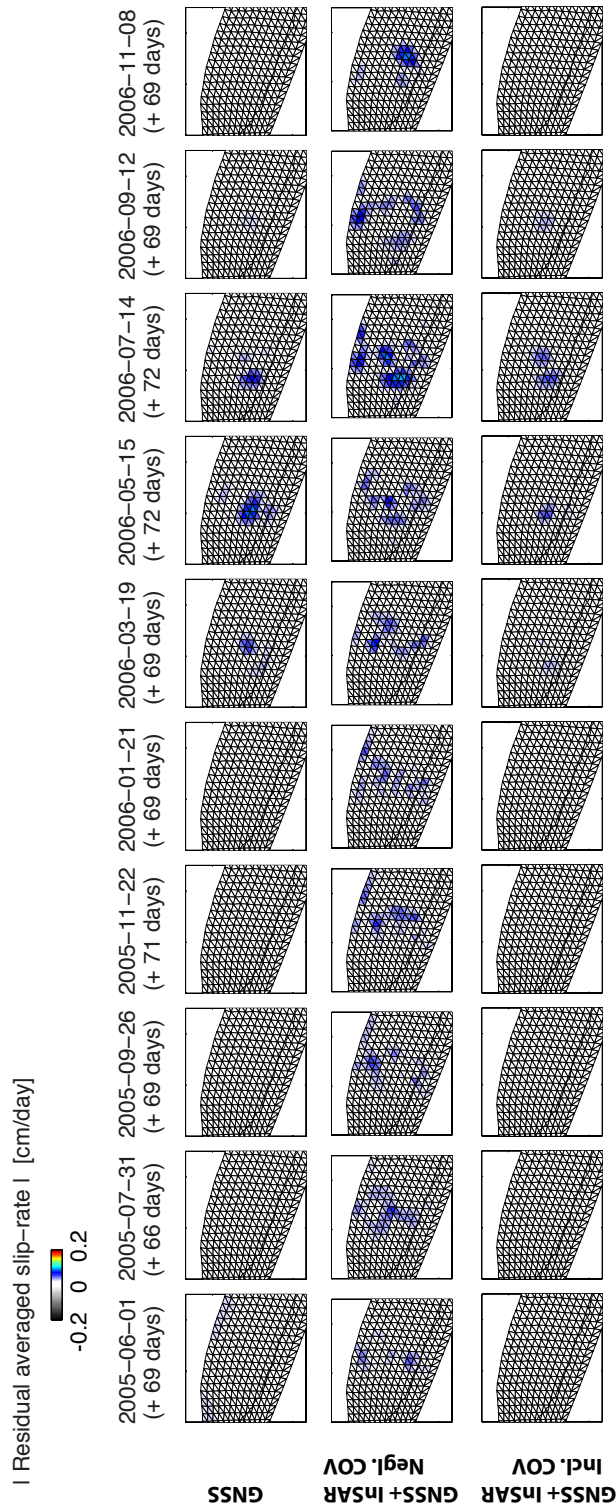


Figure 5.7: Absolute residual between the simulated and estimated slip rate history, when inverting for GNSS only (first row), combining GNSS and InSAR while neglecting InSAR covariance (second row), and the joint inversion while including the InSAR covariance (third row). The panel averaging window is indicated in the title as (+# days)

solution is preferred ($\kappa^2/\sigma^2 = 5 \cdot 10^{-6}$). We find a lower value for the estimated data variance-covariance scaling, $\hat{\sigma} = 0.89$, which implies that the model overfits the data.

As InSAR covariance information is not included, each of the $\sim 10^3$ InSAR observations are treated as if they are independent observations. A much rougher solution is therefore found for the maximum likelihood solution. In reality much of this roughness is fitting the spatially-correlated InSAR noise from the residual atmosphere. This results in apparent noise signals that propagate into the slip model. The estimated inter-SSE loading rate (Figure 5.4(b)) shows large residuals underneath the InSAR track, especially towards the down-dip extent of the subduction interface (up to 8 cm/year).

The cumulative transient peak slip is over-estimated by ~ 3 cm, Figure 5.5(b). Also large errors relative to the true input slip of on average ~ 12 cm can be observed at other locations, especially down-dip of the slow slip region. Because the solution is rougher than the GNSS only solution, we also find larger uncertainties for the estimated cumulative slip. The smallest uncertainty of ~ 4.5 cm can be found underneath the InSAR track and GNSS station locations, with larger values of on average ~ 8 cm elsewhere.

The slip rate history (Figure 5.6 (third row)) shows much more temporal variation over the whole time-period, even when there is no SSE taking place. These fluctuations reach an average magnitude of ~ 0.07 cm/day.

We find the GNSS residuals are within the uncertainty bounds of the original simulated observations (mean residual around zero mm), see Supplemental material Figure D.2(a). For the InSAR data, we find an average Root Mean Squared Error (RMSE) of ~ 3 rad (or ~ 1.3 cm). As we simulated the original tectonic signal and the InSAR orbit error (phase ramp), a direct comparison can be made with the NIF estimates. Supplemental material Figure D.2(b) gives the simulated tectonic signal and the misfit of the estimation. We find a mean RMSE of ~ 0.57 rad (or ~ 0.25 cm). The last three interferograms (Oct 2006, Nov 2006, and Feb 2007) show the largest residuals, with an average of ~ 1 rad (or ~ 0.45 cm). Over time, the spatial pattern of the residuals is enhanced; illustrating that mis-estimation is integrated over time. We find that the orbital planes are well estimated with small residuals, average RMSE of ~ 0.7 rad (or 0.3 cm); see Supplemental material Figure D.2(b).

5.4.3 GNSS and InSAR (including covariance)

By including the full InSAR variance-covariance information, we find that the combined GNSS and InSAR solution is more similar to the GNSS only case. This is expected as the InSAR observations add more information about the spatial extent of the slow slip surface observations. However, the InSAR contribution is down-weighted and provides only a lower-level constraint (e.g. [Bekaert et al., 2015](#)), as the simulated slow slip signal has a correlation length similar to that of the simulated residual atmosphere (i.e. ~ 2 -

50 km). By including the covariance, we find the estimated data variance-covariance scaling is close to 1, $\hat{\sigma} = 0.99$. We also find similar hyperparameters to the GNSS only case.

Overall an improvement can be observed when jointly inverting GNSS and InSAR, compared to the GNSS only case, while accounting properly for the InSAR covariance information. Apparent noise signals, introduced in the slip rate history when neglecting the covariance information, are now suppressed (Figure 5.6(b)). We find a significant improvement in the location and estimation of the peak cumulative transient slip, misfit of <1 cm compared to ~ 7 cm for the GNSS-only case, and with a similar uncertainty of ~ 2 cm. The inter-SSE loading is slightly different to the GNSS case. We find a residual rate of up to 4.5 cm/year underneath the InSAR track, down-dip of the slow slip region. When neglecting InSAR covariance, this residual was significantly larger (up to ~ 8 cm/year).

As before, we find small residuals for the GNSS and InSAR (Supplemental material Figure D.3). GNSS residuals are within the uncertainty bounds of the simulated data. For the InSAR, we find the estimated tectonic signal and orbital errors with similar magnitudes as when neglecting the InSAR covariance. The misfit between the tectonic simulation and the estimation indicates under-estimation of the slow slip signal.

5.5 Discussion

Our NIF results are a reasonable approximation of the simulated tectonic slow slip signal. We find that the InSAR observations provide an additional constraint on the slow slip signal at the fault interface, which is under-estimated when inverting sparsely distributed GNSS observations only.

Our NIF implementation is limited to a single spatial smoothing hyperparameter. We believe it will be more appropriate to include a separate smoothing hyperparameter for the inter-SSE locking rate, and also smooth differently in the dip and strike direction. For example, at subduction zones the interseismic slip rate is expected to vary with depth with a shorter wavelength than in the along strike direction. Including an additional hyperparameter in our current NIF implementation comes at the cost of an extra dimension to the grid search.

With increasing step size, and with more hyperparameters to solve for, the grid search becomes a time consuming operation. An alternative approach to the grid search is included in the Extended NIF by *McGuire and Segall (2003)*, where the hyperparameters are included directly in the state vector. As in our study, the hyperparameters remain constant over time. Assuming constant hyperparameters can form a limitation in a complex time-series with a mixture of interseismic, coseismic, postseismic, aseismic, and slow slip processes. In particular, the rapid displacement change during a short-term SSE might be suppressed when the smoothing hyperparameters are solved toward

interseismic slip rate. Developments by *Fukuda et al.* (2004, 2008) allow for a time-varying spatial and temporal smoothing parameter. This is achieved by including the hyperparameters as stochastic variables using the Monte Carlo Mixture Kalman Filter or the hierarchical Bayesian state space approach. None of the above NIF modifications currently include InSAR capability. We believe that our presented methodology can be adopted straightforwardly into the other methods.

In our simulation, significant spatially-correlated atmospheric noise (simulated variance between 1-3 cm², and correlation lengths up to 50 km) is added. InSAR covariance information is often neglected in tectonic slip inversion studies. This should be avoided, as spatially correlated noise will be treated as signal. This becomes of special importance in studies where the tectonic signals have a similar correlation length as the noise, as is the case for our simulation here. Recently, different efforts and promising progress has been made on the quantification and construction of InSAR variance-covariance matrices (e.g. *González and Fernández, 2011, Agram and Simons, 2015, Fattahi, 2015, Bekaert et al., 2015*). Future modeling studies should aim to include InSAR covariance information as part of regular inversion procedures.

The quality of the InSAR observations are expected to improve with more regular SAR acquisitions. Our simulation included a SAR acquisition every 60 days. With Sentinel 1 acquisitions are currently every 12 days, which will further decrease to every 6 days once Sentinel 1B is launched. With a swath width of ~ 250 km and a spatial resolution of 5x20 m, large areas can be covered at high resolution and with short repeat times. Having a larger amount of independent InSAR observations will lead to a further reduction in the influence of atmospheric noise. Being able to ingest this data for time-dependent modeling in the NIF could provide invaluable information in a variety of applications, such as volcano inflation and deflation, and fault creep, as well as coseismic and postseismic events.

5.6 Conclusions

Vast amounts of geodetic data have been acquired over the last two decades. The acquisition rate will continue to increase exponentially with further expansion of GNSS networks and the acquisition of InSAR data from Sentinel 1, NISAR, and ALOS 2. Simultaneous inversion of all geodetic data to solve for the time-dependent history of fault slip is a computationally-intensive process, for which an alternative is the Network Inversion Filter. Different versions exist of this method, but to date, none of these include Interferometric Synthetic Aperture (InSAR) observations. In this study, we have provided and applied the Network Inversion Filter methodology to include InSAR. To validate the approach we simulated the 2006 Guerrero SSE for a subset of the existing GNSS sites (mainly far-field) and for the descending Envisat track 255. We find that GNSS can retrieve the cumulative SSE at approximately the same location as

the input simulation, but with a smaller peak slip, due to spatial smoothing. Inclusion of high resolution InSAR further improves the recovery of the transient slip. InSAR covariance is often neglected in slip inversion studies. This should be avoided, as spatially-correlated atmospheric noise will be treated as if it was signal, introducing apparent slip signals at depth. We compare the joint GNSS and InSAR inversion while neglecting and including InSAR covariance information. When including InSAR covariance, we find a solution that has similar smoothing hyperparameters to that of GNSS. We find that InSAR provides an improved constraint with its high-resolution observations above the slow slip region. Our study demonstrates the use of InSAR data to retrieve time-dependent slip, which can provide invaluable information for a wide variety of applications.

Symbols

Subscript

InSAR	Interferometric Synthetic Aperture Radar
GNSS	Global Navigation Satellite System
$k + 1 k$	Epoch $k + 1$ given all data up to epoch k
k	Epoch k given all data up to epoch k

Symbols

α, β, γ	Coefficients of the InSAR orbit error (plane)
δ	Residual of state vector in the state transition equation
$\epsilon^{\text{GNSS}}, \epsilon^{\text{InSAR}}$	GNSS and InSAR observation errors
\mathcal{F}	GNSS reference frame coefficients (e.g. translation, rotation, and or scaling)
\mathcal{L}	Local GNSS benchmark motions for each component (ENU)
\mathcal{P}	InSAR orbit (plane) coefficients ($[\alpha, \beta, \gamma]^\top$)
∇^2	Laplacian operator
Ω	State variance-covariance matrix
I	Identity matrix
O	Zero matrix
R, Σ	Total and individual dataset observation variance-covariance matrices
Q	Process noise variance-covariance matrix
$\Delta \mathbf{d}^{\text{InSAR}}$	InSAR radar line-of-sight surface displacements
Δt	Time difference between epochs
\dot{W}	slip rate or Random walk $\sim \mathcal{N}(0, \omega^2)$
κ	Spatial smoothing parameter
\mathbf{d}	Observations of surface displacements
\mathbf{F}	Linearized Helmert transformation matrix of GNSS reference frame
\mathbf{G}	Greens coefficients
\mathbf{H}	Observation matrix
\mathbf{K}	Kalman filter gain
\mathbf{P}	InSAR orbit (plane) matrix ($[\mathbf{x}_1, \mathbf{x}_2, \mathbf{1}]$)
s	Fault slip
s_0^{InSAR}	Reference slip at the InSAR reference time
\mathbf{T}	State transition matrix
\mathbf{X}	State vector
\mathcal{N}	Normal distribution
ω	Random walk scale parameter controlling temporal smoothing
σ	Scaling parameter of the data observation variance-covariance matrix
τ	Scale parameter of the brownian random walk of the local GNSS benchmark motion

ζ	Scale parameter of the GNSS reference frame variance-covariance matrix
N_s, N_p, N_I	Number of GNSS stations, InSAR pixels on a single track, and InSAR interferograms on a single track
$t_0^{\text{GNSS}}, t_0^{\text{INSAR}}$	GNSS and InSAR reference time
t	Time
v	Interseismic slip rate
W	Integrated random walk or Cumulative slip deviated from the steady-state interseismic slip rate

Acknowledgments

We thank Noel Bartlow for stimulating discussions. One figure was prepared using the public domain GMT software ([Wessel and Smith, 1991](#)). This work was supported by the Royal Astronomical Society grant. COMET is the NERC Centre for the Observation and Modelling of Earthquakes, Volcanoes and Tectonics. Results can be obtained by contacting the corresponding author (eedpsb@leeds.ac.uk).

Appendix Time-dependent slow slip simulation

Following [Liu et al. \(2006\)](#), we define the source time function of transient slip-rate as:

$$v = \begin{cases} A \sin\left(\frac{\pi t}{t_{\text{SSE}}}\right) & 0 \leq t < t_{\text{SSE}}/2, \\ \frac{A}{2} \left[1 + \cos\left(\frac{2\pi t}{t_{\text{SSE}}} - \pi\right)\right] & t_{\text{SSE}}/2 \leq t < t_{\text{SSE}} \end{cases} \quad (5.13)$$

where t is time, t_{SSE} the rise time and duration of the slow slip event, and A the amplitude of the source function. We assume the acceleration and deceleration rise time have equal duration. The time-evolution of slip, s , follows from the integration of transient slip-rate, where we define the integration constants and A such $s=0$ at $t=0$, and $s=s_0^{\text{SSE}}$ at $t=t_{\text{SSE}}$, leading to:

$$s = \begin{cases} \frac{4s_0^{\text{SSE}}}{\pi+4} \left[1 - \cos\left(\frac{\pi t}{t_{\text{SSE}}}\right)\right] & 0 \leq t < t_{\text{SSE}}/2, \\ \frac{s_0^{\text{SSE}}}{\pi+4} \left[\frac{2\pi t}{t_{\text{SSE}}} + 4 - \pi - \sin\left(\frac{2\pi t}{t_{\text{SSE}}}\right)\right] & t_{\text{SSE}}/2 \leq t < t_{\text{SSE}} \end{cases} \quad (5.14)$$

An example is contained in Supplemental Figure [D.4](#).

Appendix NIF model for GNSS and multiple InSAR tracks

Here we expand the observation equation to include two InSAR tracks.

$$\begin{bmatrix} \mathbf{d}^{\text{GNSS}} \\ \Delta \mathbf{d}^{\text{InSAR},1} \\ \Delta \mathbf{d}^{\text{InSAR},2} \\ \mathbf{0} \\ \mathbf{0} \\ \mathbf{0} \end{bmatrix}_{t_k} = \underbrace{\begin{bmatrix} \mathbf{G}^{\text{GNSS}}(t_k - t_0^{\text{GNSS}}) & \mathbf{0} & \mathbf{I} & \mathbf{F} & \mathbf{0} & \mathbf{0} & \mathbf{0} & \mathbf{0} \\ \mathbf{G}^{\text{InSAR},1,t_k} & \mathbf{G}^{\text{InSAR},1} & \mathbf{0} & \mathbf{0} & \mathbf{0} & \mathbf{P}^{\text{InSAR},1} & -\mathbf{G}^{\text{InSAR},1} & \mathbf{0} \\ \mathbf{G}^{\text{InSAR},2,t_k} & \mathbf{G}^{\text{InSAR},2} & \mathbf{0} & \mathbf{0} & \mathbf{0} & \mathbf{0} & \mathbf{P}^{\text{InSAR},2} & -\mathbf{G}^{\text{InSAR},2} \\ \mathbf{\nabla}^2 & \mathbf{0} \\ \mathbf{0} & \mathbf{\nabla}^2 & \mathbf{0} & \mathbf{0} & \mathbf{0} & \mathbf{0} & \mathbf{0} & \mathbf{0} \\ \mathbf{0} & \mathbf{0} & \mathbf{\nabla}^2 & \mathbf{0} & \mathbf{0} & \mathbf{0} & \mathbf{0} & \mathbf{0} \end{bmatrix}}_{\mathbf{H}_k} + \boldsymbol{\epsilon}_k,$$

$$\begin{bmatrix} \mathbf{v} \\ \mathbf{W} \\ \dot{\mathbf{W}} \\ \mathcal{L} \\ \mathcal{F} \\ \mathcal{P}^{\text{InSAR},1} \\ \mathbf{s}_0^{\text{InSAR},1} \\ \mathcal{P}^{\text{InSAR},2} \\ \mathbf{s}_0^{\text{InSAR},2} \end{bmatrix}_{t_k}$$

References

- Agram, P. S., and M. Simons (2015), A noise model for InSAR time series, *J. Geophys. Res.*, *120*(4), 2752 – 2771, doi:[10.1002/2014JB011271](https://doi.org/10.1002/2014JB011271). 5.5
- Bartlow, N. M., S. Miyazaki, A. M. Bradley, and P. Segall (2011), Space-time correlation of slip and tremor during the 2009 Cascadia slow slip event, *Geophys. Res. Lett.*, *38*(18), doi:[10.1029/2011GL048714](https://doi.org/10.1029/2011GL048714). 5.4
- Bartlow, N. M., L. M. Wallace, R. J. Beavan, S. Bannister, and P. Segall (2014), Time-dependent modeling of slow slip events and associated seismicity and tremor at the Hikurangi subduction zone, New Zealand, *J. Geophys. Res.*, *119*(1), 734 – 753, doi:[10.1002/2013JB010609](https://doi.org/10.1002/2013JB010609). 5.1, 5.2.5, 5.4
- Bedford, J., M. Moreno, J. C. Baez, D. Lange, F. Tilmann, M. Rosenau, O. Heidbach, O. Oncken, M. Bartsch, A. Rietbrock, A. Tassara, M. Bevis, and C. Vigny (2013), A high-resolution, time-variable afterslip model for the 2010 Maule Mw = 8.8, Chile megathrust earthquake, *Earth and Planetary Science Letters*, *383*(0), 26 – 36, doi:<http://dx.doi.org/10.1016/j.epsl.2013.09.020>. 5.1
- Bekaert, D., A. Hooper, and T. Wright (2015), Reassessing the 2006 Guerrero Slow Slip Event, Mexico: implications for large earthquakes in the Guerrero Gap, *J. Geophys. Res.*, *120*, doi:[10.1002/2014JB011557](https://doi.org/10.1002/2014JB011557). 5.2.2, 5.3, 5.3, 5.4.3, 5.5
- Cavalié, O., E. Pathier, M. Radiguet, M. Vergnolle, N. Cotte, A. Walpersdorf, V. Kostoglodov, and F. Cotton (2013), Slow slip event in the Mexican subduction zone: Evidence of shallower slip in the Guerrero seismic gap for the 2006 event revealed by the joint inversion of InSAR and GPS data, *Earth and Planetary Science Letters*, *367*, doi:[10.1016/j.epsl.2013.02.020](https://doi.org/10.1016/j.epsl.2013.02.020). 5.3, 5.3
- Cervelli, P., P. Segall, K. Johnson, M. Lisowski, and A. Miklius (2002), Sudden aseismic fault slip on the south flank of Kilauea volcano, *Nature*, *414*(6875), 1014 – 1018, doi:[10.1038/4151014a](https://doi.org/10.1038/4151014a). 5.1
- DeMets, C., R. Gordon, and D. Argus (2010), Geologically current plate motions, *Geophys. J. Int.*, *181*(1), 1 – 80, doi:[10.1111/j.1365-246X.2009.04491.x](https://doi.org/10.1111/j.1365-246X.2009.04491.x). 5.3, 5.1
- Fattahi, H. (2015), InSAR bias and uncertainty due to the systematic and stochastic tropospheric delay, abstract id 79726, presented at 2015 Fall Meeting, AGU, San Francisco, Calif. 5.5
- Fukuda, J., T. Higuchi, S. Miyazaki, and T. Kato (2004), A new approach to time-dependent inversion of geodetic data using a Monte Carlo mixture Kalman filter, *Geophysical Journal International*, *159*(1), 17 – 39, doi:[10.1111/j.1365-246X.2004.02383.x](https://doi.org/10.1111/j.1365-246X.2004.02383.x). 5.5
- Fukuda, J., S. Miyazaki, T. Higuchi, and T. Kato (2008), Geodetic inversion for space-time distribution of fault slip with time-varying smoothing regularization, *Geophysical Journal International*, *173*(1), 25 – 48, doi:[10.1111/j.1365-246X.2007.03722.x](https://doi.org/10.1111/j.1365-246X.2007.03722.x). 5.5

- González, P. J., and J. Fernández (2011), Error estimation in multitemporal InSAR deformation time series, with application to Lanzarote, Canary Islands, *J. Geophys. Res.*, *116*(B10), doi:[10.1029/2011JB008412](https://doi.org/10.1029/2011JB008412). 5.5
- Hooper, A., D. Bekaert, K. Spaans, and M. Arikani (2012), Recent advances in SAR interferometry time series analysis for measuring crustal deformation, *Tectonophysics*, *514*517, 1 – 13, doi:<http://dx.doi.org/10.1016/j.tecto.2011.10.013>. 5.2.2
- Hsu, Y.-J., M. Simons, J.-P. Avouac, J. Galetzka, K. Sieh, M. Chlieh, D. Natawidjaja, L. Prawirodirdjo, and Y. Bock (2006), Frictional Afterslip Following the 2005 Nias-Simeulue Earthquake, Sumatra, *Science*, *312*(5782), 1921 – 1926, doi:[10.1126/science.1126960](https://doi.org/10.1126/science.1126960). 5.1
- Jónsson, S., H. Zebker, P. Segall, and F. Amelung (2002), Fault slip distribution of the 1999 mw 7.1 Hector mine, California, earthquake, estimated from satellite radar and gps measurements, *Bulletin of the Seismological Society of America*, *92*(4), 1377 – 1389, doi:[10.1785/0120000922](https://doi.org/10.1785/0120000922). 5.1
- Kositsky, A. P., and J.-P. Avouac (2010), Inverting geodetic time series with a principal component analysis-based inversion method, *J. Geophys. Res.*, *115*(B3), doi:[10.1029/2009JB006535](https://doi.org/10.1029/2009JB006535). 5.1
- Langbein, J., and H. Johnson (1997), Correlated errors in geodetic time series: Implications for time-dependent deformation, *J. Geophys. Res.*, *102*(B1), 591 – 603, doi:[10.1029/96JB02945](https://doi.org/10.1029/96JB02945). 5.2.1
- Liu, P., S. Custódio, and R. J. Archuleta (2006), Kinematic Inversion of the 2004 M 6.0 Parkfield Earthquake Including an Approximation to Site Effects, *Bulletin of the Seismological Society of America*, *96*(4B), 143 – 158, doi:[10.1785/0120050826](https://doi.org/10.1785/0120050826). 5.3, 5.6
- Lohman, R. B., and M. Simons (2005), Some thoughts on the use of InSAR data to constrain models of surface deformation: Noise structure and data downsampling, *Geochem. Geophys. Geosyst.*, *6*(1), doi:[10.1029/2004GC000841](https://doi.org/10.1029/2004GC000841). 5.1, 5.3
- Mavrommatis, A. P., P. Segall, and K. M. Johnson (2014), A decadal-scale deformation transient prior to the 2011 Mw 9.0 Tohoku-oki earthquake, *Geophys. Res. Lett.*, *41*(13), 4486 – 4494, doi:[10.1002/2014GL060139](https://doi.org/10.1002/2014GL060139). 5.1, 5.2.1
- McGuire, J. J., and P. Segall (2003), Imaging of aseismic fault slip transients recorded by dense geodetic networks, *Geophysical Journal International*, *155*(3), 778 – 788, doi:[10.1111/j.1365-246X.2003.02022.x](https://doi.org/10.1111/j.1365-246X.2003.02022.x). 5.1, 5.5
- Melgar, D., and X. Pérez-Campos (2011), Imaging the Moho and subducted oceanic crust at the Isthmus of Tehuantepec, Mexico, from receiver functions, *Pure and Applied Geophysics*, *168*(8-9), 1449 – 1460, doi:[10.1007/s00024-010-0199-5](https://doi.org/10.1007/s00024-010-0199-5). 5.1
- Miyazaki, S., J. J. McGuire, and P. Segall (2003), A transient subduction zone slip episode in southwest Japan observed by the nationwide GPS array, *J. Geophys. Res.*, *108*(B2), doi:[10.1029/2001JB000456](https://doi.org/10.1029/2001JB000456). 5.2.1
- Miyazaki, S., P. Segall, J. Fukuda, and T. Kato (2004), Space time distribution of afterslip following the 2003 Tokachi-oki earthquake: Implications for variations in fault zone frictional properties, *J. Geophys. Res.*, *31*(6), doi:[10.1029/2003GL019410](https://doi.org/10.1029/2003GL019410). 5.1
- Okada, Y. (1985), Surface deformation due to shear and tensile faults in a half-space, *Bulletin of the Seismological Society of America*, *75*(4), 1135 – 1154. 5.2
- Pardo, M., and G. Suárez (1995), Shape of the subducted Rivera and Cocos Plates in southern Mexico: Seismic and tectonic implications, *J. Geophys. Res.*, *100*(B7), 12,357 – 12,373, doi:[10.1029/95JB00919](https://doi.org/10.1029/95JB00919). 5.1

- Pérez-Campos, X., and R. W. Clayton (2014), Interaction of cocos and rivera plates with the upper-mantle transition zone underneath central mexico, *Geophys. J. Int.*, *197*(3), 1763 – 1769, doi:[10.1093/gji/ggu087](https://doi.org/10.1093/gji/ggu087). 5.1
- Pritchard, M. E., M. Simons, P. A. Rosen, S. Hensley, and F. H. Webb (2002), Co-seismic slip from the 1995 July 30 Mw= 8.1 Antofagasta, Chile, earthquake as constrained by InSAR and GPS observations, *Geophys. J. Int.*, *150*(2), 362 – 376, doi:[10.1046/j.1365-246X.2002.01661.x](https://doi.org/10.1046/j.1365-246X.2002.01661.x). 5.1
- Radiguet, M., F. Cotton, M. Vergnolle, M. Campillo, B. Valette, V. Kostoglodov, and N. Cotte (2011), Spatial and temporal evolution of a long term slow slip event: the 2006 Guerrero Slow Slip Event, *Geophys. J. Int.*, *184*(2), 816 – 828, doi:[10.1111/j.1365-246X.2010.04866.x](https://doi.org/10.1111/j.1365-246X.2010.04866.x). 5.1, 5.3
- Saunders, M. (2015), PDCO convex optimization software, [Version downloaded August 2015]. 5.4
- Savage, J. C. (1983), A dislocation model of strain accumulation and release at a subduction zone, *J. Geophys. Res.*, *88*(B6), 4984 – 4996, doi:[10.1029/JB088iB06p04984](https://doi.org/10.1029/JB088iB06p04984). 5.3, 5.4
- Schmidt, D. A., and H. Gao (2010), Source parameters and time-dependent slip distributions of slow slip events on the Cascadia subduction zone from 1998 to 2008, *J. Geophys. Res.*, *115*(B4), doi:[10.1029/2008JB006045](https://doi.org/10.1029/2008JB006045). 5.1
- Segall, P., and M. Matthews (1997), Time dependent inversion of geodetic data, *J. Geophys. Res.*, *102*(B10), 22,391 – 22,409, doi:[10.1029/97JB01795](https://doi.org/10.1029/97JB01795). 5.1, 5.2, 5.2, 5.2.1, 5.2.3, 5.2.3, 5.2.4, 5.4
- Segall, P., R. Bürgmann, and M. Matthews (2000), Time-dependent triggered afterslip following the 1989 Loma Prieta earthquake, *J. Geophys. Res.*, *105*(B3), 5615 – 5634, doi:[10.1029/1999JB900352](https://doi.org/10.1029/1999JB900352). 5.2, 5.2.3, 5.4
- Segall, P., E. K. Desmarais, D. Shelly, A. Miklius, and P. Cervelli (2006), Earthquakes triggered by silent slip events on Kilauea volcano, Hawaii, *Nature*, *442*(7098), 71 – 74, doi:[10.1038/nature04938](https://doi.org/10.1038/nature04938). 5.1
- Simons, M., Y. Fialko, and L. Rivera (2002), Coseismic Deformation from the 1999 Mw 7.1 Hector Mine, California, Earthquake as Inferred from InSAR and GPS Observations, *Bulletin of the Seismological Society of America*, *92*(4), 1390 – 1402, doi:[10.1785/0120000933](https://doi.org/10.1785/0120000933). 5.1
- Thomas, A. (1993), Poly3D: A Three-Dimensional, Polygonal Element, Displacement Discontinuity Boundary Element Computer Program with Applications to Fractures, Faults, and Cavities in the Earth's Crust, Master's thesis, Stanford University. 5.2, 5.3
- Vergnolle, M., A. Walpersdorf, V. Kostoglodov, P. Tregoning, J. Santiago, N. Cotte, and S. Franco (2010), Slow slip events in Mexico revised from the processing of 11-year GPS observations, *J. Geophys. Res.*, *115*(B8), doi:[10.1029/2009JB006852](https://doi.org/10.1029/2009JB006852). 5.3
- Wessel, P., and W. Smith (1991), Free Software helps Map and Display Data, *Eos Trans. AGU*, *72*(41), 445 – 446, doi:[10.1029/90EO00319](https://doi.org/10.1029/90EO00319). 5.6
- Wright, T., Z. Lu, and C. Wicks (2004), Constraining the Slip Distribution and Fault Geometry of the Mw 7.9, 3 November 2002, Denali Fault Earthquake with Interferometric Synthetic Aperture Radar and Global Positioning System Data, *Bulletin of the Seismological Society of America*, *94*(6B), doi:[10.1785/0120040623](https://doi.org/10.1785/0120040623). 5.1

Chapter 6

Discussion and conclusions

6.1 Discussion

The Mexican SSEs compared to others

An overview of the world's subduction zone SSEs is given in Figure 6.1. In total there are six known locations including: Mexico, Cascadia, Japan, Costa Rica, Alaska, and New Zealand. Between all these, the Mexican SSEs compare best with the long-term SSEs in Japan. They have a similar peak slip magnitude, duration, and recurrence interval. For both regions, SSEs are located at a similar depth, but the Mexican SSEs extend ~ 10 km deeper and also enter into the seismogenic zone. In both cases, tremor is concentrated towards the down-dip extent of slow slip region. Below, I provide a summary for the characteristic SSE parameters for the six known SSE subduction zone locations:

- **Mexico** has large and small magnitude SSEs. The larger SSEs repeat approximately every 3-5 years, have a duration of up to a year, and reach a magnitude of up to M_w 7-7.4 (e.g. [Vergnolle et al., 2010](#), [Larson et al., 2004](#)). These SSEs have been shown to enter into the seismogenic zone, and reach depths of up to 40 km. On average, they have a peak slip value of ~ 15 -20 cm, located at a depth of ~ 35 km (e.g. [Radiquet et al., 2012](#), [Bekaert et al., 2015a](#)). The smaller SSEs, only discovered recently by [Frank et al. \(2015\)](#), repeat every 3 months and are observed just down-dip of the larger SSEs. They have a duration of ~ 1 month, reach a peak slip of ~ 6 mm, and are on average equivalent to $M_w \sim 6.4$ ([Frank et al., 2015](#)). Non-volcanic tremor in Mexico is located on the down-dip edge of the small magnitude SSEs.
- **Japan** has short and long-term SSEs. Its long-term events occur in the Bungo Channel (southwest of Shikoku) at depths of 20-30 km, with duration of a few months up to 2 years (e.g. [Hirose et al., 1999](#), [Yoshioka et al., 2015](#)), and a recurrence interval of 5 to 7 years ([Kobayashi and Yamamoto, 2011](#)). Peak cu-

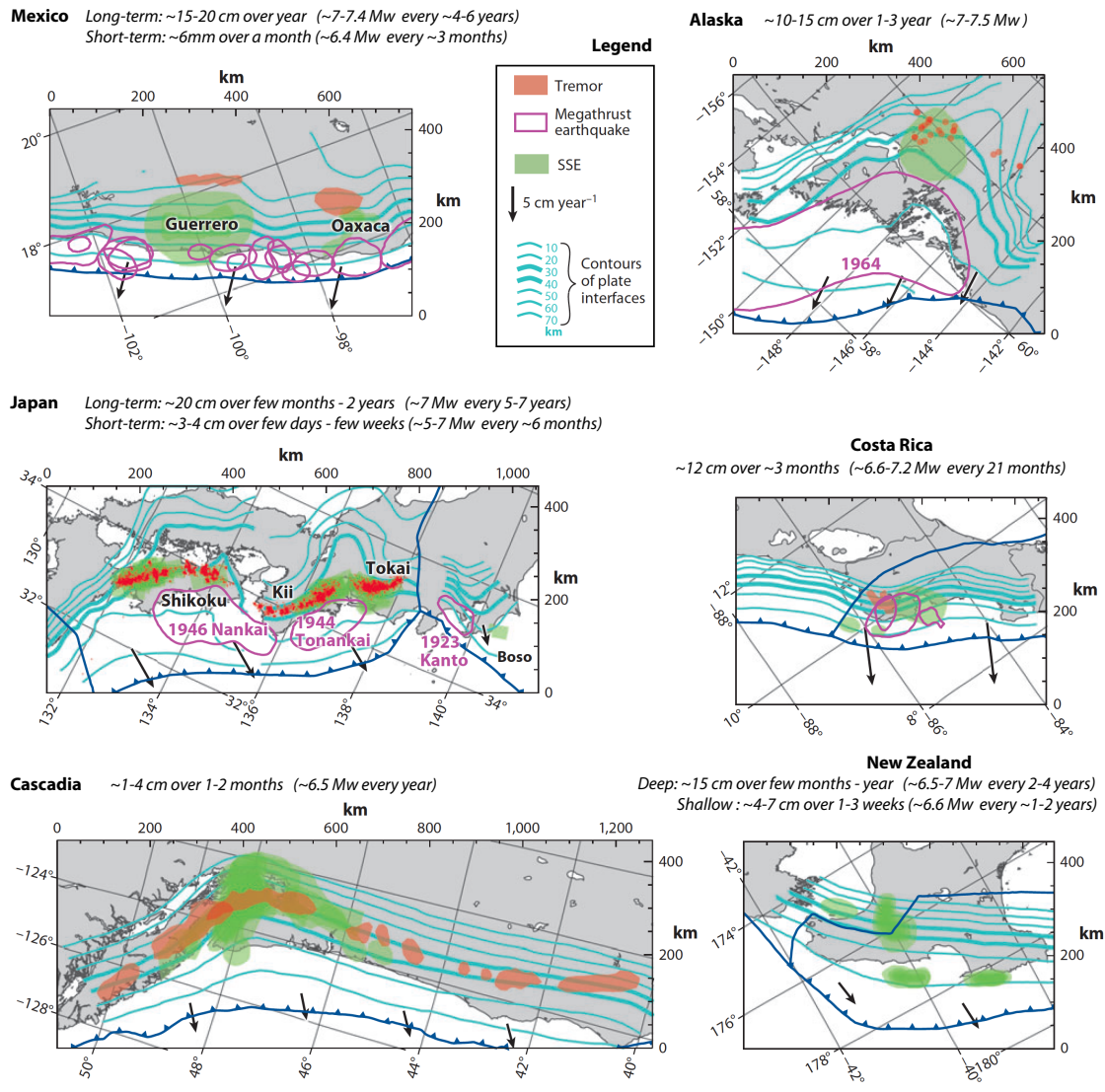


Figure 6.1: Map overview of slow slip solutions at subduction zones, modified from *Beroza and Ide (2011)*. Individual panels show the location of the SSEs (green polygons), with respect to the subduction zone geometry (cyan depth contours), non-volcanic tremor (orange polygon), and past co-seismic rupture areas (purple polygons). The title contains characteristic SSE information for each region (see text for references).

mulative slip reaches 5 to 20 cm, and give a magnitude of $M_w \sim 7$. Short-term SSEs with a duration of a few days to a week have been detected down-dip of the long-term SSEs, reaching depths between 10-60 km (e.g. [Hirose and Obara, 2005](#), [Nishimura, 2014](#)). The recurrence is shorter with an interval of up to half a year. On average the short-term SSEs reach equivalent earthquake magnitudes of M_w 5-7, with slip magnitudes up to 4 cm. Tremor is observed to coincide with these short-term SSEs, and is located on the down-dip edge of the long-term SSEs ([Nishimura, 2014](#)).

- The **Cascadia** SSEs span a wide range of durations and recurrence intervals (e.g. [Brudzinski and Allen, 2007](#)). On average SSEs have a duration up to 40 days, and repeat each 10-14 months. A shorter recurrence interval is observed between 41°N - 46°N (e.g. [Schmalzle et al., 2014](#)). SSE slip magnitudes are small, with on average 1-4 cm slip, equivalent to on average $M_w \sim 6.2$ - 6.8 (e.g. [Dragert et al., 2004](#), [Schwartz and Rokosky, 2007](#)). SSEs have been collocated in space and time with tremor (e.g. [Bartlow et al., 2011](#)).
- **New Zealand** has deep and shallow SSEs. The deep SSEs are located at the down-dip extent of the locked region at 25-60 km depth. They have a recurrence interval of 2-4 years, and a duration varying from a couple of months to a year (e.g. [Wallace and Beavan, 2006](#)). With slip magnitudes of up to 10-20 cm, the deep SSEs are approximately equivalent to a M_w 6.5-7 earthquake. The shallow SSEs are located at 15 km depth, have a duration of 1-3 weeks, and a shorter 1-2 years repeat interval. The slip magnitude ranges from 4-7 cm, corresponding to an equivalent M_w 6.5-6.8 (e.g. [Bartlow et al., 2014](#)).
- So far 3 SSEs have been observed in **Alaska** ([Ohta et al., 2006](#), [Wei et al., 2012](#), [Fu and Freymueller, 2013](#)). The duration of the SSEs varies between 1 and 3 years, with no regular repeat interval. The last two SSEs are offset by 8 and 9 years from the first SSE. Slip magnitudes of 10-18 cm have been modelled, with an earthquake like magnitude of $M_w \sim 7$ - 7.5 .
- **Costa Rica** has large SSEs, which repeat approximately every ~ 21 months, and small SSEs in northern part of the peninsula, which have a shorter recurrence interval of 1 year ([Jiang et al., 2012](#)). The larger SSEs reach a peak slip of 12 cm over a 3 month duration, and are equivalent to M_w 6.6-7.2 ([Outerbridge et al., 2010](#)). [Outerbridge et al. \(2010\)](#) showed tremor and SSEs to temporally-correlated, but could not find a spatial correlation.

Geodetic observations of SSEs

Today, geodetic observations of SSEs have mainly relied on continuous GNSS networks. Figure 6.2 gives an overview of the GNSS sites around the Pacific Ocean from [Kreemer](#)

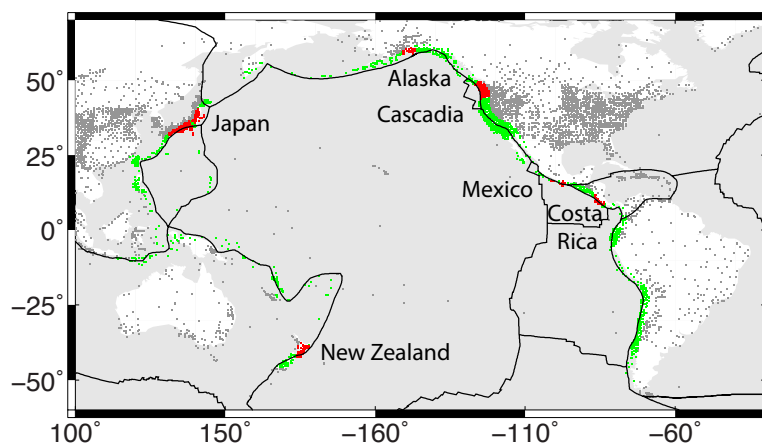


Figure 6.2: Map of the GNSS station distribution around the Circum-Pacific belt - Ring of Fire. Markers show the GNSS stations from the Global strain rate model (*Kreemer et al., 2014*) gridded at 0.5° spacing. GNSS stations within the Ring of Fire, 2.5° region around the closest plate, are colored green and red, where the red show those GNSS stations within a known SSE region.

et al. (2014), with those around Circum-Pacific belt, also know as the “Ring of Fire”, shown in green and red. To estimate how well monitored SSEs are around the Pacific, I grid the GNSS station locations at a resolution of 0.5° (~ 55 km along the equator), and I assume that this resolution is enough to capture slow slip surface displacements. As most of the deformation takes place in the first 250 km of the hanging wall, I limit my analysis to the hanging wall side of Circum-Pacific belt, and label the region within 2.5° as part of the “Ring of Fire”. In total $\sim 25\%$ of the Circum-Pacific belt is covered by GNSS (red and green markers in Figure 6.2) at 0.5° resolution. This means that we do not know whether slow slip occurs in $\sim 75\%$ of the Circum-Pacific belt. This observation gap could be covered by combining InSAR ($\sim 38\%$) and seafloor geodesy ($\sim 37\%$).

Today, slow slip regions cover roughly $\sim 9\%$ of the Circum-Pacific belt. Regions with known SSEs are $\sim 56\%$ covered by GNSS (red markers in Figure 6.2) at 0.5° resolution. Clearly, a good GNSS density can be observed over Japan and Cascadia, with a much lower coverage in Mexico and Costa Rica. Additional InSAR and sea-floor geodesy observations would allow us to better constrain existing models, especially in regions with offshore SSEs, as in New Zealand. About half of the missing coverage at known SSE sites is offshore, requiring seafloor geodesy.

Observing SSEs with InSAR around the world

The Mexican SSEs are some of the largest around the world, and due to a favourable setting of the tectonic interface also give one of the largest surface displacements associated with slow slip. For the feasibility of InSAR as observation technique for slow

slip, many factors need to be considered which will vary on a case-by-case basis. I identified the following three factors that can play a key role in InSAR success for slow slip purposes.

1. The amount of cumulative slow slip expected in the radar line-of-sight, which is dependent on the SAR platform acquisition geometry and the orientation of the surface displacements.
2. The amount of tropospheric and ionospheric InSAR noise. The latter is more prominent for the longer wavelengths SAR platforms (e.g. L-band) such as ALOS 1/2, and the future NISAR mission.
3. The SAR repeat interval, the duration of the InSAR time-series, and the duration of the SSE. All these play a role for time-dependant modelling objectives as well as how much atmospheric variability can be further decreased.

The larger the Signal-to-Noise Ratio (SNR), described by (1)-(2), the easier it will be to extract the signal from the InSAR data. Sophisticated time-series InSAR methods and atmospheric noise corrections can be used to decrease the noise-level further.

Below, I summarize the results for a C-band InSAR feasibility study, assuming Envisat and Sentinel 1 geometries, for the August 2009 Cascadia SSE. The applied methodology can be found in Appendix E. For simplicity the perpendicular baseline component was neglected here. The 2009 Cascadia SSE has a ~ 1 month duration, with cumulative GNSS slow slip surface displacements of maximum ~ 7 mm towards the southwest, and with a small ~ 1 -2 mm upward motion. With a focus on C-band SAR platforms, I neglect the ionospheric noise. For the troposphere I consider two cases, one where the noise level is 2 cm, and another one of 4 cm. For simplicity, I assume a 3-year InSAR observation period with the SSE occurring halfway in time. Table 6.1 gives an overview of the SNR for the various acquisition geometries and the for the two noise cases. It can be observed that the ascending acquisition mode has a favourable geometry with respect to the surface displacement field, with an SNR 5-8 times larger than the descending case. Nonetheless, over the 3-year time-period none of the SAR platforms get a SNR larger than 1. Based on the assumed noise levels, InSAR will therefore not be feasible to observation technique. Potentially InSAR can be successful if a longer time-series is considered, or in case the noise-levels are further decreased using improved tropospheric correction methods. Which correction method gives the largest reduction in tropospheric noise depends on your region. I elaborated on this in chapter 3 and summarize the findings below in the conclusions. Another consideration can be to capture the superposition of multiple SSEs, which will increase the signal level further.

Table 6.1: Envisat and Sentinel 1 InSAR feasibility for the 2009 Cascadian SSE. The table gives the Signal-to-Noise Ratio for a 3-year duration InSAR time-series, assuming ascending and descending geometries, with a tropospheric noise level of 2 and 4 cm (columns). The analysis includes the aimed Sentinel 1 and Envisat repeat times (rows), with a more realistic case included for Envisat.

SAR repeat interval	2 cm		4 cm	
	Descending	Ascending	Descending	Ascending
Sentinel 1A/B - 6 days	0.19	0.94	0.09	0.47
Sentinel 1A - 12 days	0.13	0.66	0.07	0.33
Envisat - 35 days	0.03	0.29	0.01	0.15
Envisat - 70 days (realistic)	0.02	0.21	0.01	0.10

6.2 Conclusions

My thesis has demonstrated that advanced time-series processing and atmospheric correction methods enable the use of Interferometric Synthetic Aperture Radar for the observation of slow slip surface displacements at high spatial resolution, and in combination with GNSS, for subsequent slow slip modelling on the subducting interface. In fact, the atmospheric noise correction still forms one of the largest challenges facing the InSAR community today and therefore formed a focus in my thesis. The development of a novel tropospheric correction method facilitated slow slip modelling in a static inversion. Subsequently, I developed a refined approach using a time-dependent slip inversion combining GNSS and InSAR. While further work is required, this will provide valuable insight into the physics of slow slip events. Below, I provide an overview of the key findings of my thesis, together with more detailed conclusions.

Key Finding 1: Topography-correlated SAR delays can be described by a power-law function, which unlike previous methods allows for spatial variation of the troposphere. The power-law can be applied in presence of deformation by applying spatial band filtering to separate tectonic signals from tropospheric delays.

Chapter 2 of my PhD thesis focuses on a new phase-based method for tropospheric delay estimation. Typically, phase-based tropospheric corrections have been estimated over a full interferogram, a non-deforming region, or from a band insensitive to deformation. Some studies have applied the linear correction locally and reported good results, with a significant decrease in topography-correlated signals. Applying the linear estimation locally should be avoided as the intercept of the linear function will be biased by other signals, leading to an incorrect estimate of the tropospheric delay. In response to this, I developed a power-law relationship that can be applied locally, and which allows to estimate a spatially-varying signal from the interferometric phase. Accounting for spatial variation becomes more important for larger spatial datasets (>10s of km) as pressure, temperature, and relative humidity can change significantly over these spatial

scales. I performed a case study correction over Mexico using C-band Envisat data, where large tropospheric signals are present and masking smaller magnitude slow slip surface displacements. After the power-law tropospheric correction, I find a reduction in the topography-correlated signals, and an improved correlation between the GNSS and InSAR. In chapter 4, I use these derived surface deformation in the modelling of the 2006 Guerrero SSE.

Key Finding 2: From all available tropospheric correction methods, space-based spectrometers give the largest noise reduction. In the presence of clouds, all correction methods perform 10-20% worse. Phase-based methods perform well when the tropospheric delay is topography-correlated. On average, global weather models perform better than local high-resolution models.

In chapter 3, I performed a statistical comparison of all the current available tropospheric correction methods over Mexico, Italy and El Hierro. I found that none of the tropospheric correction methods can be labeled the best in reducing tropospheric InSAR noise in a consistent manner over different regions, and at different instants. I came to this conclusion after an analysis where I compared tropospheric delay estimates based on spectrometer measurements from MERIS and MODIS, output of low and high spatial resolution weather models, and using the empirical linear and power-law interferometric phase-based methods. All these methods are now included in my open source Toolbox for Reducing Atmospheric InSAR Noise (TRAIN). As anticipated, I confirmed that the auxiliary data methods are limited by the spatial and temporal resolution of the source data, while for the phase-based methods the limitation lies in separating tropospheric delays signals from other phase contributors such as tectonic and man-induced signals. In my analysis I found that spectrometers gave consistently the largest RMSE reduction, but this was only when the data were available during day-time and cloud-free conditions, which represented a strong limitation. As MERIS was acquired simultaneously with the Envisat radar data, thus capturing the true troposphere at the right moment, it performed the best, decreasing the residual noise level close to the theoretical accuracy of MERIS as determined in earlier literature. While MODIS requires an interpolation in space and time, I found its accuracy to be at best equal to that of MERIS, and in the worst case twice that of MERIS. The phase-based methods performed better than the weather model in those instances where the tropospheric delay was mainly topography-correlated. In presence of additional coherent features in the atmosphere (e.g. gravity waves), weather models have the potential to provide an improved delay estimation. Turbulent features are less well resolved, therefore mis-estimation in weather models result often in an increased RMSE. I did not observe a clear improvement by using a high-resolution weather model (7 km and 2 km versus ~ 70 km). High-resolution models allow for more complexity in the local tropospheric

delay, but when estimated incorrectly are directly penalized with an increased RMSE. Considering a longer required runtime, local weather models are less suitable for near real-time InSAR applications. From a cloud cover analysis, I found the performance of the different correction methods to worsen consistently with increasing cloud cover, with a $\sim 20\%$ increase in RMSE for each cloudy SAR date. Clearly each method has its own limitations and sensitivities to different components of the tropospheric delay (e.g. only a wet component can be estimated from spectrometer observations, and a topography-correlated component for the phase-based methods), therefore further developments should aim for an integration of the different correction methods in an optimal manner. Suggestions for this are included in the recommendations section.

Key Finding 3: Slow slip entered the Guerrero seismic gap during the 2006 SSE. Since 1911, the Guerrero Gap has accumulated a Mw 8 equivalent slip deficit, imposing a large seismic hazard for Mexico City and surrounding. This hazard has not been decreased significantly by the 2014 Guerrero earthquakes.

In chapter 4, I combined GNSS observations and tropospheric corrected InSAR data with an objective to develop a slip model inversion strategy, and to refine the estimate of the slow slip model for the 2006 Guerrero SSE. I achieved this by formulating the joint inverse problem in a Bayesian framework, where all unknowns such as slip, rake, smoothness, and InSAR plane are sampled using Markov Chain Monte Carlo methods. I found that high-resolution InSAR observations have a strong impact on the spatial extent of slow slip on the subduction interface. However, careful attention should be given to InSAR noise-covariance information. When I included the InSAR noise covariance information, the slip solution tended towards the GNSS-only solution. In this instant InSAR provided only a conservative constraint on the slip solution, as residual atmospheric signals had a similar covariance structure to the actual slow slip surface displacements. When neglecting covariance, as done frequently in the InSAR community, more emphasis was put on the InSAR data, and thus also on potential residual noise signals. When neglecting covariance information, I found that the joint GNSS and InSAR solution extended further East underneath the InSAR track.

Independently when inverting the GNSS observations alone, combining GNSS and InSAR when neglecting or including the covariance information, all slow slip solutions give an equivalent earthquake magnitude of M_w 7.3, and where most of the seismic moment ($\sim 75\%$) is released in the transition zone (25-40 km depths), with a peak slip of ~ 17 cm just down-dip of the transition on the sub-horizontal section of the subducting interface. Compared to earlier studies, I found larger slip magnitudes (~ 5 cm) to occur in the seismogenic zone (10-25 km depths); part of this can be attributed to a variation in smoothness. From my slow slip model analysis, I found the 2006 slow slip event to release about 19-25% of its total seismic moment within the locked part of the

Guerrero Gap, with a moment release equivalent to an earthquake magnitude of $M_w \sim 6.9$. From the end of the 2002 SSE to the end of the 2006 SSE, including the 2006 slow slip release, the Guerrero Gap has been loaded by $M_w \sim 6.8$ each year. In order to assess the seismic potential of the Guerrero gap since the 1911 earthquake, I assumed that stress has been only released by earthquakes and slow slip, and that SSEs repeat every 4 years. Based on this I found that the Guerrero gap has accumulated a potential of a $M_w \sim 8$ earthquake over the last century. Even the two recent April and May 2014 ($M_w \sim 7$) earthquakes, that occurred on the western edge of the Guerrero Gap, do not change this potential significantly.

Key Finding 4: High spatial-resolution InSAR observation and continuous GNSS can be combined together in a NIF framework to retrieve time-dependant slip history of SSEs at better resolution than before. It is of importance to account for InSAR covariance information, as otherwise spatially-correlated noise will be treated as if it were signal.

Having good knowledge on the slip history of slow slip events in combination with other observations from seismology can provide valuable information about the physics involved. The slip history can be retrieved through a simultaneous inversion of all geodetic data. This however is a computational intensive process, for which the Network Inversion Filter is an alternative. Several versions of the NIF exist, but none of the methods include InSAR observations. In chapter 5, I developed and applied the methodology to include InSAR and GNSS together in the Network Inversion Filter (NIF) framework. In my study, I demonstrated the importance of including InSAR covariance information. This is of particular importance for tectonic modeling of signal such as slow slip events that have a similar correlation length as tropospheric signals. Indeed, when neglected, spatially correlated noise will be treated as if it were signal. When the InSAR covariance is included, more emphasis is put on the GNSS data, while InSAR still provides a lower-level constraint. The NIF combining GNSS and InSAR will be a powerful tool for researchers across multiple disciplines to study time-dependant tectonic processes.

6.3 Recommendations and Future work

InSAR noise

Surface deformation associated with pre- and post- event processes around tectonic faults (e.g. creep, interseismic and postseismic deformation) is often of small magnitude, and can be masked by noise in the InSAR measurements. Hence, the accuracy of InSAR surface deformation measurements depends on how well we correct the data for various noise components. These include tidal motion (1-2 cm displacement in the radar line-

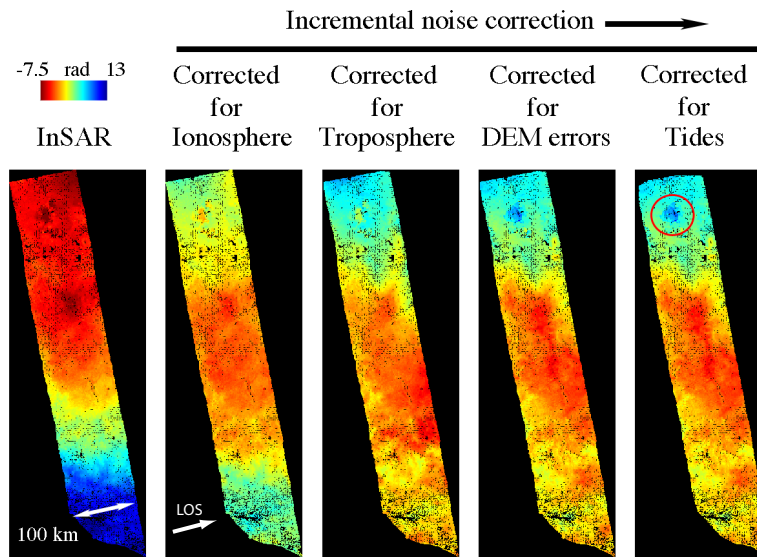


Figure 6.3: Noise masking the subsidence signal over Mexico City (red circle) in an L-band ALOS interferogram from 1 October 2008 to 16 February 2009 (138 days) on track 186. Incremental noise correction from left to right for the ionosphere, the troposphere, DEM errors, and tides. Each 6.28 rad corresponds to 11.5 cm displacement in the radar line-of-sight.

of-sight), satellite orbit errors (a smooth trend), residual topography (DEM) errors (up to a few cm), the ionosphere (up to 5m for L-band), and the troposphere (up to 20-30 cm). Correcting for all these components should become a standard practice of the InSAR processing chain. An example of an incremental correction for an L-band ALOS interferogram is shown in Figure 6.3. The ionosphere and troposphere are the largest and most important noise sources. While tidal motion can be modeled (*DiCaprio and Simons, 2008*), and InSAR orbit and DEM errors can be addressed by integration with GPS and application of time-series InSAR methods (e.g. *Hooper et al., 2012*), correcting for atmospheric noise remains one of the most significant challenges for the InSAR community (*Hooper et al., 2012, Bekaert et al., 2015b,c*). Below I comment on future projects that aim to progress the field.

Tropospheric InSAR correction

Tropospheric corrections are often applied without quality control. While uncertainties in weather models are not well defined, specific metrics can be thought that describe whether weather models are likely to provide an accurate tropospheric correction. For example under what conditions will there be more turbulence, which is not physically described in weather model but treated as a stochastic process. In a co-authored study (*Walters et al., 2015*), we show that humidity, temperature, or complexity in local topography, can be used as indicator for weather model performance. Similarly, spectrometers products of Precipitable Water Vapor are made for a specific time, but no quality measure is provided in terms of the impact of temporal interpolation to the

SAR acquisition time, or with respect to a bias from an incorrect cloud mask. For example variable wind speed would impact a linear weighted temporal interpolation. Being able to quantify the accuracy of the different atmospheric correction methods will be of direct benefit when propagating uncertainties in time-series processing (see below on Inversion of GNSS and InSAR for tectonic signals), and when performing a weighted joint inversion of different tropospheric observations. The latter is another project for future research. As weather models, spectrometers, and InSAR have a different sensitivity to the troposphere, a joint inversion of all the datasets will help to constrain the tropospheric noise.

Ionospheric InSAR correction

Opportunities exist to further progress the field in developing and expanding ionospheric correction methods for InSAR data. This is of particular importance for L-band SAR missions, such ALOS 1 mission, the current ALOS 2 mission, and the future NASA/ISRO NISAR mission. *Meyer et al. (2015)* showed that the ALOS 1/2 ascending orbit configuration is especially sensitive for equatorial ionospheric scintillation, mainly related to the time of day and the mission operation with respect to the solar cycle. In terms of ionospheric InSAR corrections, phase-based estimation methods are limited by decorrelation of the interferograms. Currently, ionospheric weather models of TEC are often too coarse (2-2.5 degrees) for the purpose of correcting InSAR data for ionospheric noise. However, this field is undergoing continuous development, and an up-to-date study would prove invaluable to assess the current state-of-the-art. This would benefit from collaboration with expert groups such as at the University of Bath, which have in house capabilities of running dedicated models. Alternatively, GPS can be used, but is often limited by the spatial resolution. Auxiliary based corrections alone will likely currently not be enough to correct for high scintillation effects in InSAR data. However the combination of auxiliary data and phase-based methods might provide a useful constraint.

Inversion of GNSS and InSAR for tectonic signals

InSAR is an attractive technique that can provide observations of tectonic deformation at high spatial resolution. Joint inversion of GNSS and InSAR often neglect the InSAR covariance information. This should be avoided, as spatially correlated InSAR noise will be treated as if it were signal. The challenge of including covariance information lies in the construction of an accurate noise covariance matrix. As part of my research, I have attempted to construct the covariance matrix for the estimated slow slip signal from a statistical analysis of the InSAR time-series (*Bekaert et al., 2015a*). *Fattahi (2015)* proposes to split the tropospheric noise into a stochastic and analytical component, where the latter represents seasonal and annual variability that can be mathematically

described. Another approach is to account for the temporal noise correlation between interferograms during a weighted InSAR time-series inversion, and propagate the full uncertainties to estimate the accuracy of the different time-series components (e.g. *González and Fernández, 2011*). Up to today, the methodology for the estimation of the InSAR covariance matrix, and its application for tectonics studies, remains an ongoing research topic that will have a big impact on future modeling.

Seafloor geodesy for constraining SSE

Up until now, slow slip modeling has mainly relied on InSAR and GNSS observations. This means that geodetic observations have been limited to those on the continents. A powerful complement to satellite geodesy is the use of seafloor geodesy. It provides the means to constrain regions with offshore SSEs such as in New Zealand, Japan (Boso), and Costa Rica. In other regions such as Mexico, seafloor geodesy can constrain the up-dip extent of the slow slip solution. This year's HOBITSS project in New Zealand is the first attempt on using seafloor geodesy to study offshore SSEs (*Wallace, 2015*). From May 2014 till June 2015, 24 Absolute Pressure Gauges (APG) and 15 Ocean Bottom Seismometers (OBS) were operated at less than 10 km spacing, directly above a known slow slip region offshore in Gisborne. At the moment of writing, results have not yet been announced. In future, I expect further deployment of seafloor geodesy to other slow slip subduction zones could provide valuable observations that can help us in getting a better understanding of SSEs.

A global online SSE catalogue

Comparing all slow slip regions known today helps in the search for common features when slow slip occurs. This can be facilitated by a global catalogue of slow slip models. Such a research effort is currently underway by Priyamvada Nanjundiah and Sylvain Barbot at Earth Observation Singapore (EOS) (*Nanjundiah, 2015*). Their Source Characteristics of EarthQuakes (SCEQ) catalogue is a layer for google earth, which can be added by including the following link <https://bitbucket.org/sbarbot/sceq/raw/default/sceq.kml>. An online catalogue is of direct benefit for the research community. It could be used as an online distribution of results, but also to perform analysis across different regions. When comparing different regions it would be beneficial to include different layers of geospatial information such as isotherms, subduction interfaces, interface segmentation, plate age, convergence rates, earthquake locations, tremor locations, results from receiver functions and magnetotelluric studies, and many more. Being able to synthesise this information in an online geospatial framework will allow detailed comparison of different slow slip regions with an invaluable database of information for researchers around the world. A global approach towards the slow slip phenomena will be the future direction to take in order to address some of the key

questions, one of which is: Why does slow slip occur in some regions and not in others?

6.4 Concluding Remarks

In this thesis, I developed the required methodology to use InSAR as an observation technique for slow slip, and demonstrated its use with a slow slip study over Mexico. My methodology has a wide impact as it provides the general InSAR framework for other slow slip regions. In addition, my expansion to include InSAR in the Network Inversion Filter allows for time-dependant slip modelling, not just limited to slow slip, but also for fault creep and other time-dependent slip processes. Finally, I developed the Toolbox for Reducing Atmospheric InSAR Noise (TRAIN), which includes all state-of-the-art tropospheric InSAR correction methods. This includes my newly developed phase-based power-law tropospheric correction method, which unlike previous methods accounts for spatially variable tropospheric properties. All these tools are of wide interest for the InSAR community and can be applied across many disciplines, and moreover are easily integrated in the default InSAR processing chain. Being able to decrease the atmospheric noise levels for InSAR, improves the retrieval of small magnitude signals such as inter-seismic, post-seismic, and slow slip signals, and moreover has the potential to uncover new undetected deformation signals that otherwise would have been masked by noise.

References

- Bartlow, N. M., S. Miyazaki, A. M. Bradley, and P. Segall (2011), Space-time correlation of slip and tremor during the 2009 Cascadia slow slip event, *Geophys. Res. Lett.*, *38*(18), doi:[10.1029/2011GL048714](https://doi.org/10.1029/2011GL048714). 6.1
- Bartlow, N. M., L. M. Wallace, R. J. Beavan, S. Bannister, and P. Segall (2014), Time-dependent modeling of slow slip events and associated seismicity and tremor at the Hikurangi subduction zone, New Zealand, *J. Geophys. Res.*, *119*(1), 734 – 753, doi:[10.1002/2013JB010609](https://doi.org/10.1002/2013JB010609). 6.1
- Bekaert, D., A. Hooper, and T. Wright (2015a), Reassessing the 2006 Guerrero Slow Slip Event, Mexico: implications for large earthquakes in the Guerrero Gap, *J. Geophys. Res.*, *120*, doi:[10.1002/2014JB011557](https://doi.org/10.1002/2014JB011557). 6.1, 6.3
- Bekaert, D., A. Hooper, and T. Wright (2015b), A spatially-variable power-law tropospheric correction technique for InSAR data, *J. Geophys. Res.*, *120*, doi:[10.1002/2014JB011558](https://doi.org/10.1002/2014JB011558). 6.3
- Bekaert, D., R. Walters, T. Wright, A. Hooper, and D. Parker (2015c), Statistical comparison of insar tropospheric correction techniques, *Remote Sensing of Environment*, *170*, 40 – 47, doi:<http://dx.doi.org/10.1016/j.rse.2015.08.035>. 6.3
- Beroza, G. C., and S. Ide (2011), Slow Earthquakes and Nonvolcanic Tremor, *Annual Review of Earth and Planetary Sciences*, *39*(1), 271 – 296, doi:[10.1146/annurev-earth-040809-152531](https://doi.org/10.1146/annurev-earth-040809-152531). 6.1
- Brudzinski, M. R., and R. M. Allen (2007), Segmentation in episodic tremor and slip all along Cascadia, *Geology*, *35*(10), 907 – 910, doi:[10.1130/G23740A.1](https://doi.org/10.1130/G23740A.1). 6.1
- DiCaprio, C. J., and M. Simons (2008), Importance of ocean tidal load corrections for differential InSAR, *Geophys. Res. Lett.*, *35*(22), doi:[10.1029/2008GL035806](https://doi.org/10.1029/2008GL035806). 6.3
- Dragert, H., K. Wang, and G. Rogers (2004), Geodetic and seismic signatures of episodic tremor and slip in the northern Cascadia subduction zone, *Earth, Planets and Space*, *56*(12), 1143 – 1150, doi:[10.1186/BF03353333](https://doi.org/10.1186/BF03353333). 6.1
- Fattahi, H. (2015), InSAR bias and uncertainty due to the systematic and stochastic tropospheric delay, abstract id 79726, presented at 2015 Fall Meeting, AGU, San Francisco, Calif. 6.3
- Frank, W. B., M. Radiguet, B. Rousset, N. M. Shapiro, A. L. Husker, V. Kostoglodov, N. Cotte, and M. Campillo (2015), Uncovering the geodetic signature of silent slip through repeating earthquakes, *Geophys. Res. Lett.*, *42*(8), 2774 – 2779, doi:[10.1002/2015GL063685](https://doi.org/10.1002/2015GL063685). 6.1
- Fu, Y., and J. T. Freymueller (2013), Repeated large Slow Slip Events at the southcentral Alaska subduction zone, *Earth and Planetary Science Letters*, *375*, 303 – 311, doi:[10.1016/j.epsl.2013.05.049](https://doi.org/10.1016/j.epsl.2013.05.049). 6.1
- González, P. J., and J. Fernández (2011), Error estimation in multitemporal InSAR deformation time series, with application to Lanzarote, Canary Islands, *J. Geophys. Res.*, *116*(B10), doi:[10.1029/2011JB008412](https://doi.org/10.1029/2011JB008412). 6.3

- Hirose, H., and K. Obara (2005), Repeating short- and long-term slow slip events with deep tremor activity around the Bungo channel region, southwest Japan, *Earth, Planets and Space*, *57*(10), 961 – 972, doi:[10.1186/BF03351875](https://doi.org/10.1186/BF03351875). 6.1
- Hirose, H., K. Hirahara, F. Kimata, N. Fujii, and S. Miyazaki (1999), A slow thrust slip event following the two 1996 Hyuganada earthquakes beneath the Bungo Channel, southwest Japan, *J. Geophys. Res.*, *26*(21), 3237 – 3240, doi:[10.1029/1999GL010999](https://doi.org/10.1029/1999GL010999). 6.1
- Hooper, A., D. Bekaert, K. Spaans, and M. Arikani (2012), Recent advances in SAR interferometry time series analysis for measuring crustal deformation, *Tectonophysics*, *514517*, 1 – 13, doi:<http://dx.doi.org/10.1016/j.tecto.2011.10.013>. 6.3
- Jiang, Y., S. Wdowinski, T. H. Dixon, M. Hackl, M. Protti, and V. Gonzalez (2012), Slow slip events in Costa Rica detected by continuous GPS observations, 20022011, *Geochem. Geophys. Geosyst.*, *13*(4), doi:[10.1029/2012GC004058](https://doi.org/10.1029/2012GC004058). 6.1
- Kobayashi, A., and T. Yamamoto (2011), Repetitive long-term slow slip events beneath the Bungo Channel, southwestern Japan, identified from leveling and sea level data from 1979 to 2008, *J. Geophys. Res.*, *116*(B4), doi:[10.1029/2010JB007822](https://doi.org/10.1029/2010JB007822). 6.1
- Kreemer, C., G. Blewitt, and E. C. Klein (2014), A geodetic plate motion and Global Strain Rate Model, *Geochemistry, Geophysics, Geosystems*, *15*(10), 3849 – 3889, doi:[10.1002/2014GC005407](https://doi.org/10.1002/2014GC005407). 6.1, 6.2
- Larson, K., A. Lowry, V. Kostoglodov, W. Hutton, O. Sánchez, K. Hudnut, and G. Suárez (2004), Crustal deformation measurements in Guerrero, Mexico, *J. Geophys. Res.*, *109*(B4), doi:[10.1029/2003JB002843](https://doi.org/10.1029/2003JB002843). 6.1
- Meyer, F., K. Chotoo, S. Chotoo, B. Huxtable, and C. Carrano (2015), The Influence of Equatorial Scintillation on L-Band SAR Image Quality and Phase, *Geoscience and Remote Sensing, IEEE Transactions on*, *PP*(99), 1–12, doi:[10.1109/TGRS.2015.2468573](https://doi.org/10.1109/TGRS.2015.2468573). 6.3
- Nanjundiah, P. (2015), Depth dependence of source characteristics of slow slip events and earthquakes on thrust faults, abstract id 76574, presented at 2015 Fall Meeting, AGU, San Francisco, Calif. 6.3
- Nishimura, T. (2014), Short-term slow slip events along the Ryukyu Trench, southwestern Japan, observed by continuous GNSS, *Progress in Earth and Planetary Science*, *1*(1), doi:[10.1186/s40645-014-0022-5](https://doi.org/10.1186/s40645-014-0022-5). 6.1
- Ohta, Y., J. T. Freymueller, S. Hreinsdóttir, and H. Suito (2006), A large slow slip event and the depth of the seismogenic zone in the south central Alaska subduction zone, *Earth and Planetary Science Letters*, *247*(12), 108 – 116, doi:<http://dx.doi.org/10.1016/j.epsl.2006.05.013>. 6.1
- Outerbridge, K. C., T. H. Dixon, S. Y. Schwartz, J. I. Walter, M. Protti, V. Gonzalez, J. Biggs, M. Thorwart, and W. Rabbel (2010), A tremor and slip event on the Cocos-Caribbean subduction zone as measured by a global positioning system (GPS) and seismic network on the Nicoya Peninsula, Costa Rica, *J. Geophys. Res.*, *115*(B10), doi:[10.1029/2009JB006845](https://doi.org/10.1029/2009JB006845), b10408. 6.1
- Radiguet, M., F. Cotton, M. Vergnolle, M. Campillo, A. Walpersdorf, N. Cotte, and V. Kostoglodov (2012), Slow slip events and strain accumulation in the Guerrero gap, Mexico, *J. Geophys. Res.*, *117*(B4), doi:[10.1029/2011JB008801](https://doi.org/10.1029/2011JB008801). 6.1
- Schmalzle, G. M., R. McCaffrey, and K. C. Creager (2014), Central Cascadia subduction zone creep, *Geochemistry, Geophysics, Geosystems*, *15*(4), 1515 – 1532, doi:[10.1002/2013GC005172](https://doi.org/10.1002/2013GC005172). 6.1

- Schwartz, S., and J. Rokosky (2007), Slow slip events and seismic tremor at circum-pacific subduction zones, *Review of Geophysics*, *45*(3), doi:[10.1029/2006RG000208](https://doi.org/10.1029/2006RG000208). [6.1](#)
- Vergnolle, M., A. Walpersdorf, V. Kostoglodov, P. Tregoning, J. Santiago, N. Cotte, and S. Franco (2010), Slow slip events in Mexico revised from the processing of 11-year GPS observations, *J. Geophys. Res.*, *115*(B8), doi:[10.1029/2009JB006852](https://doi.org/10.1029/2009JB006852). [6.1](#)
- Wallace, L. M. (2015), Seafloor Geodetic and Ocean Bottom Seismometer Investigation of Shallow Slow Slip Events at the Hikurangi Subduction Margin, New Zealand, abstract id 71324, presented at 2015 Fall Meeting, AGU, San Francisco, Calif. [6.3](#)
- Wallace, L. M., and J. Beavan (2006), A large slow slip event on the central Hikurangi subduction interface beneath the Manawatu region, North Island, New Zealand, *Geophys. Res. Lett.*, *33*(11), doi:[10.1029/2006GL026009](https://doi.org/10.1029/2006GL026009). [6.1](#)
- Walters, R., D. Bekaert, T. Wright, D. Parker, A. Hooper, P. Crippa, and Z. Li (2015), A Global Validation of ERA-Interim Atmospheric Correction for InSAR, *Proceedings Fringe 2015*. [6.3](#)
- Wei, M., J. J. McGuire, and E. Richardson (2012), A slow slip event in the south central Alaska Subduction Zone and related seismicity anomaly, *Geophys. Res. Lett.*, *39*(15), doi:[10.1029/2012GL052351](https://doi.org/10.1029/2012GL052351). [6.1](#)
- Yoshioka, S., Y. Matsuoka, and S. Ide (2015), Spatiotemporal slip distributions of three long-term slow slip events beneath the Bungo Channel, southwest Japan, inferred from inversion analyses of GPS data, *Geophysical Journal International*, *201*(3), 1437–1455, doi:[10.1093/gji/ggv022](https://doi.org/10.1093/gji/ggv022). [6.1](#)

Appendix A

Supplemental material Chapter 2

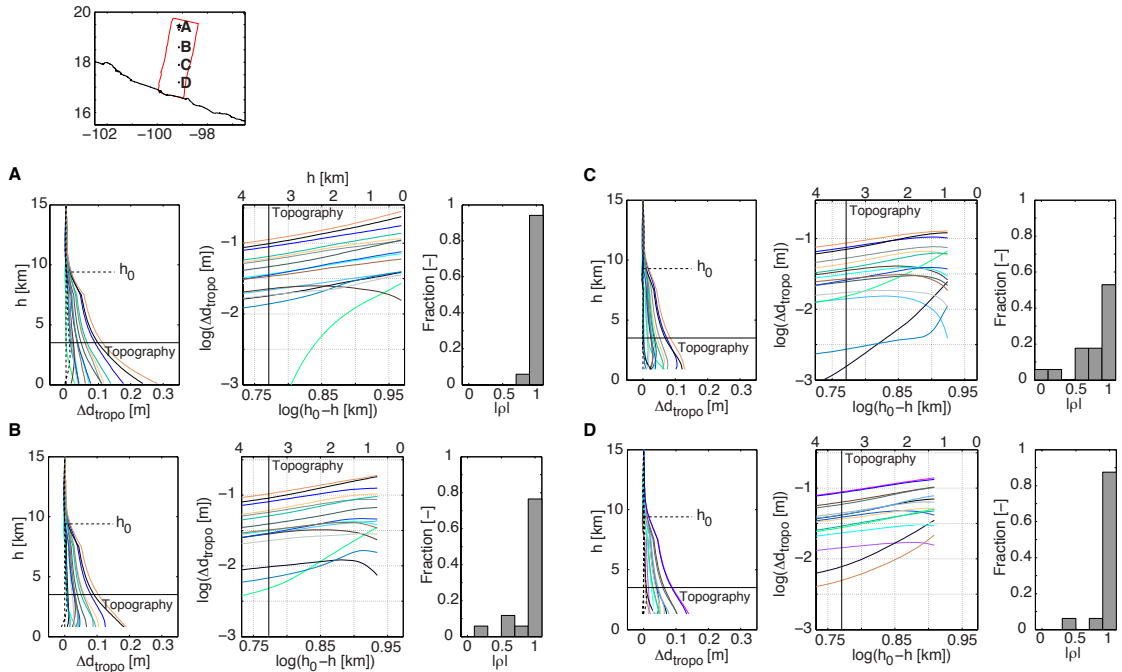


Figure A.1: Top, overview map of the locations A-D considered in this analysis. First panel of (a)-(d), radar line-of-sight relative delays computed for each interferogram using the ERA-I ECMWF weather model. The dashed solid line indicates the estimated h_0 , while the solid black line gives the maximum elevation over the InSAR region. Second panel, log-log plots of the delay curves shown in the first panel, for which the colours are kept consistent. Only the height range up to 4 km is shown. A near-linear behaviour indicates the net delay curve can be well approximated by a power-law function. The dashed delays (first panel) are not included as they contain negative components for which the log cannot be taken, and in any case represent cases where the difference in delay is close to zero and the troposphere therefore has negligible effect. Third panel, histogram of the correlation coefficients for each line in the second panel.

Appendix B

Supplemental material Chapter 3

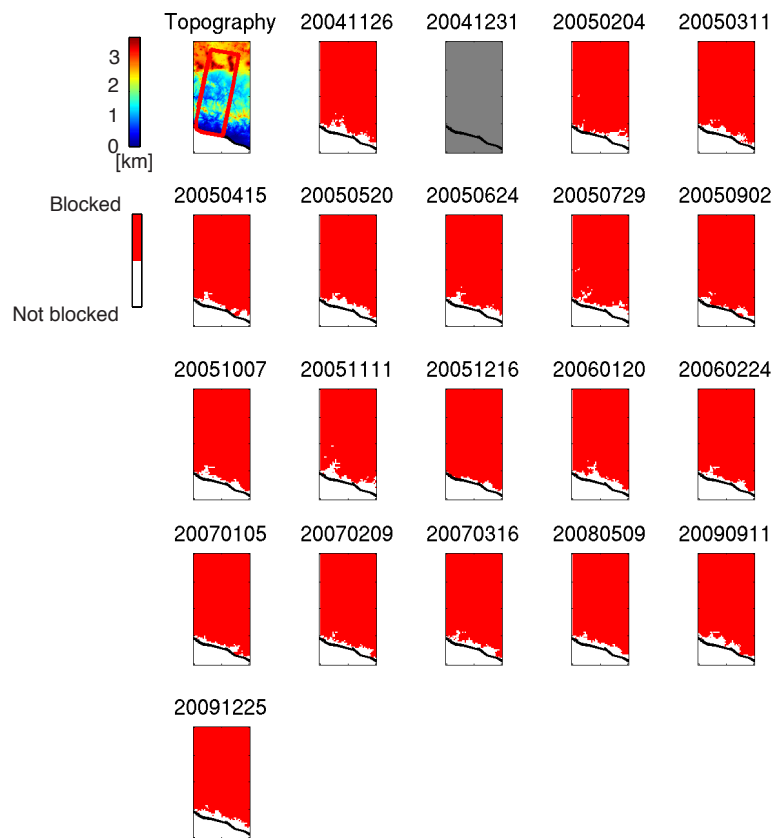


Figure B.1: Mountain wind blockage over Mexico based on the WRF 850 hPa horizontal wind velocities, perpendicular to the mountain ridge, at the time of each SAR acquisition. Maximum stagnation height is compared with the local topography, and shown as binary, with red colors represent blocking, and white no blocking. Gray refers to absence of data. The first figure panel shows the local topography, the extent of the InSAR area (red outline).

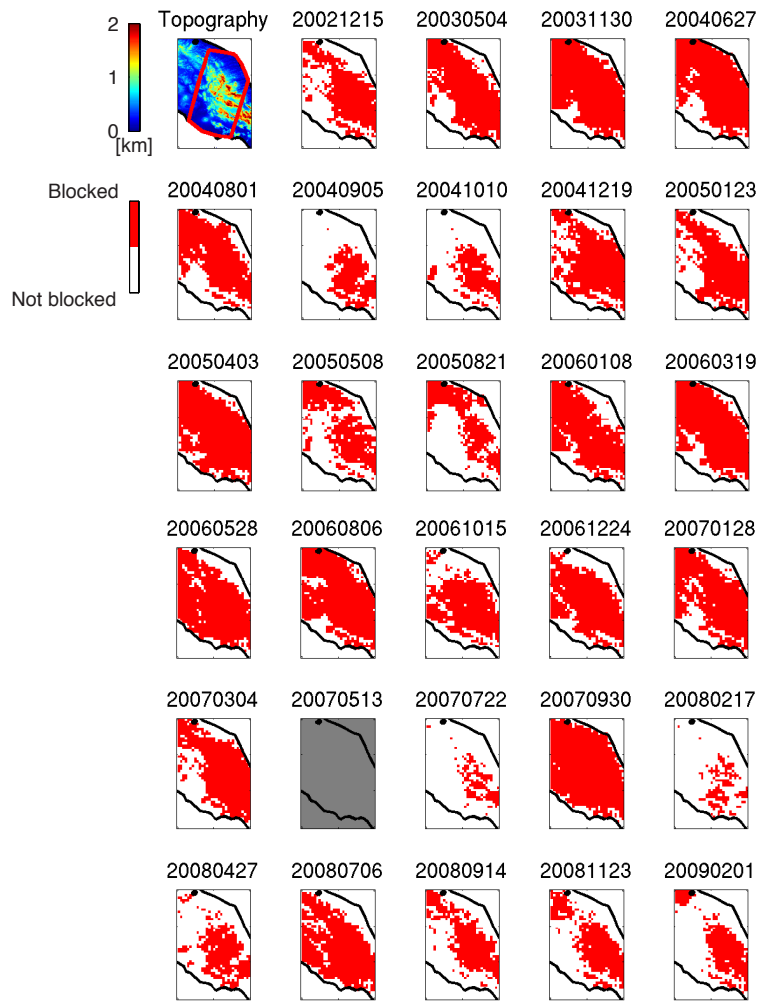


Figure B.2: Same as Figure B.1, but for Italy.

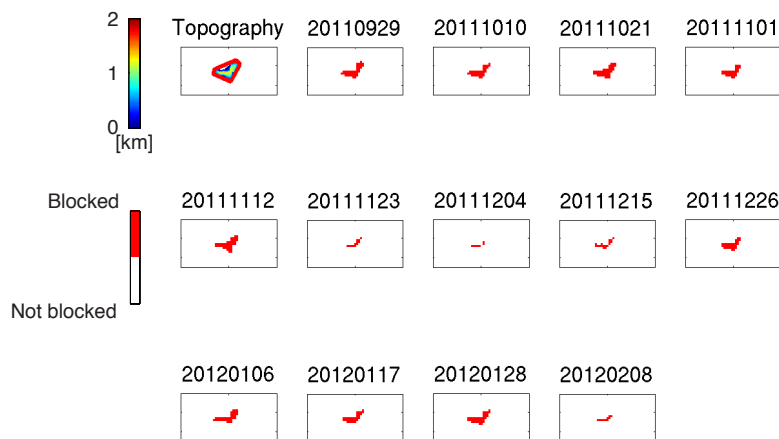


Figure B.3: Same as Figure B.1, but for El Hierro.

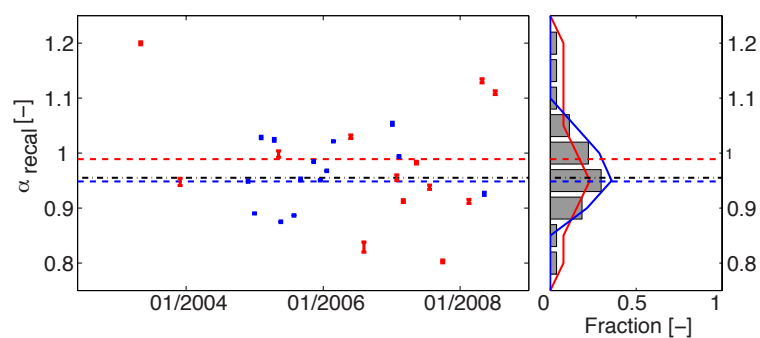


Figure B.4: MODIS recalibration factors α_{reca} , estimated from a linear relationship between MERIS and MODIS PWV. Left, variation of the estimated calibration factors in time with corresponding 2σ uncertainty, and where the weighted mean is indicated by the dashed line. Red colors relate to the observations over Italy, blue over Mexico, and black shows the combined datasets. Right, the histogram of the calibration factors, where gray bars shows the combined dataset with a weighted average calibration factor of 0.95. Only acquisitions with more than 50% mutual MERIS and MODIS pixels are considered in this analysis.

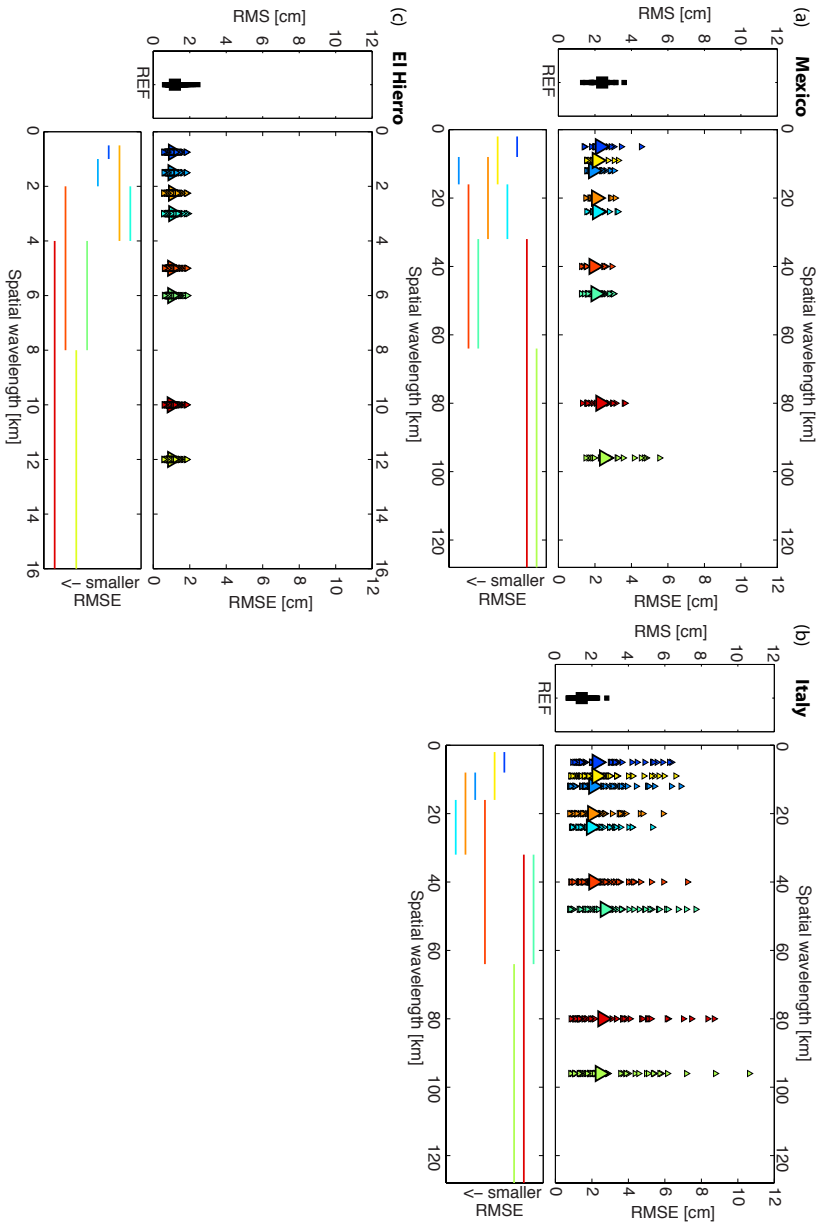


Figure B.5: Power-law spatial band selection for (a) Mexico, (b) Italy, and (c) El Hierro. Left panel, Root Mean Squared (RMS) of the tropospheric signal of the reference technique, corresponding to the unwrapped interferograms corrected for DEM errors and tectonic signals. Right panel, RMS Errors after correction of the reference signal using tropospheric estimates of the power-law for different spatial bands (colored markers). Small colored markers represent individual interferograms, while the thicker marker represents the average of all interferograms.

Table B.1: Interferometric Envisat dataset over Mexico (track 255)

	Date pair	Perp. baseline [m]		Date pair	Perp. baseline [m]
Ifig 1	16-Dec-2005 - 26-Nov-2004	209.7	Ifig 11	16-Dec-2005 - 11-Nov-2005	689.8
Ifig 2	16-Dec-2005 - 31-Dec-2004	134	Ifig 12	16-Dec-2005 - 20-Jan-2006	-864.4
Ifig 3	16-Dec-2005 - 04-Feb-2005	-119.5	Ifig 13	16-Dec-2005 - 24-Feb-2006	-282.4
Ifig 4	16-Dec-2005 - 11-Mar-2005	283.1	Ifig 14	16-Dec-2005 - 05-Jan-2007	430.1
Ifig 5	16-Dec-2005 - 15-Apr-2005	561	Ifig 15	16-Dec-2005 - 09-Feb-2007	85.8
Ifig 6	16-Dec-2005 - 20-May-2005	122.8	Ifig 16	16-Dec-2005 - 16-Mar-2007	348.8
Ifig 7	16-Dec-2005 - 24-Jun-2005	700	Ifig 17	16-Dec-2005 - 09-May-2008	138.3
Ifig 8	16-Dec-2005 - 29-Jul-2005	304.6	Ifig 18	16-Dec-2005 - 11-Sep-2009	352.1
Ifig 9	16-Dec-2005 - 02-Sep-2005	651.8	Ifig 19	16-Dec-2005 - 25-Dec-2009	83.2
Ifig 10	16-Dec-2005 - 07-Oct-2005	-110.2			

Table B.2: Interferometric Envisat dataset over Italy (track 79)

	Date pair	Perp. baseline [m]		Date pair	Perp. baseline [m]
Fig 1	15-Dec-2002 - 30-Nov-2003	-320	Fig 26	28-May-2006 - 15-Oct-2006	235.5
Fig 2	15-Dec-2002 - 01-Aug-2004	-176.4	Fig 27	28-May-2006 - 28-Jan-2007	33.4
Fig 3	30-Nov-2003 - 01-Aug-2004	143.6	Fig 28	15-Oct-2006 - 28-Jan-2007	-202.1
Fig 4	30-Nov-2003 - 10-Oct-2004	205.1	Fig 29	15-Oct-2006 - 13-May-2007	152.7
Fig 5	30-Nov-2003 - 19-Dec-2004	-65.4	Fig 30	24-Dec-2006 - 04-Mar-2007	-124.1
Fig 6	30-Nov-2003 - 23-Jan-2005	-235.2	Fig 31	28-Jan-2007 - 13-May-2007	354.8
Fig 7	01-Aug-2004 - 10-Oct-2004	61.5	Fig 32	28-Jan-2007 - 17-Feb-2008	60.8
Fig 8	01-Aug-2004 - 19-Dec-2004	-209	Fig 33	28-Jan-2007 - 14-Sep-2008	44.3
Fig 9	10-Oct-2004 - 08-Jan-2006	267.2	Fig 34	13-May-2007 - 22-Jul-2007	148.6
Fig 10	10-Oct-2004 - 19-Mar-2006	217.5	Fig 35	13-May-2007 - 30-Sep-2007	-43.9
Fig 11	19-Dec-2004 - 23-Jan-2005	-169.8	Fig 36	13-May-2007 - 17-Feb-2008	-294
Fig 12	23-Jan-2005 - 03-Apr-2005	-345	Fig 37	22-Jul-2007 - 30-Sep-2007	-192.5
Fig 13	23-Jan-2005 - 15-Oct-2006	-131.7	Fig 38	22-Jul-2007 - 27-Apr-2008	-126.7
Fig 14	03-Apr-2005 - 28-May-2006	-22.2	Fig 39	30-Sep-2007 - 17-Feb-2008	-250.1
Fig 15	03-Apr-2005 - 15-Oct-2006	213.3	Fig 40	30-Sep-2007 - 27-Apr-2008	65.8
Fig 16	03-Apr-2005 - 28-Jan-2007	11.2	Fig 41	17-Feb-2008 - 27-Apr-2008	315.9
Fig 17	08-May-2005 - 08-Jan-2006	-109.1	Fig 42	17-Feb-2008 - 14-Sep-2008	-16.5
Fig 18	08-May-2005 - 24-Dec-2006	-138.1	Fig 43	17-Feb-2008 - 23-Nov-2008	123.3
Fig 19	21-Aug-2005 - 08-Jan-2006	118.6	Fig 44	17-Feb-2008 - 01-Feb-2009	134.9
Fig 20	21-Aug-2005 - 19-Mar-2006	68.9	Fig 45	27-Apr-2008 - 23-Nov-2008	-192.6
Fig 21	08-Jan-2006 - 19-Mar-2006	-49.7	Fig 46	27-Apr-2008 - 01-Feb-2009	-181
Fig 22	08-Jan-2006 - 24-Dec-2006	-29	Fig 47	14-Sep-2008 - 23-Nov-2008	139.8
Fig 23	08-Jan-2006 - 04-Mar-2007	-153.1	Fig 48	14-Sep-2008 - 01-Feb-2009	151.4
Fig 24	19-Mar-2006 - 24-Dec-2006	20.7	Fig 49	23-Nov-2008 - 01-Feb-2009	11.6
Fig 25	19-Mar-2006 - 04-Mar-2007	-103.4			

Table B.3: Interferometric TerraSAR-X dataset over El Hierro (track 79)

	Date pair	Perp. baseline [m]	Date pair	Perp. baseline [m]	
Ifg 1	29-Sep-2011 - 10-Oct-2011	-118.2	Ifg 40	01-Nov-2011 - 17-Jan-2012	-165.4
Ifg 2	29-Sep-2011 - 21-Oct-2011	-61.4	Ifg 41	01-Nov-2011 - 28-Jan-2012	-190.2
Ifg 3	29-Sep-2011 - 01-Nov-2011	24.7	Ifg 42	01-Nov-2011 - 08-Feb-2012	-38.4
Ifg 4	29-Sep-2011 - 12-Nov-2011	-37.2	Ifg 43	12-Nov-2011 - 23-Nov-2011	-34.7
Ifg 5	29-Sep-2011 - 23-Nov-2011	-71.9	Ifg 44	12-Nov-2011 - 04-Dec-2011	32.2
Ifg 6	29-Sep-2011 - 04-Dec-2011	-5	Ifg 45	12-Nov-2011 - 15-Dec-2011	2.2
Ifg 7	29-Sep-2011 - 15-Dec-2011	-35	Ifg 46	12-Nov-2011 - 26-Dec-2011	172.5
Ifg 8	29-Sep-2011 - 26-Dec-2011	135.3	Ifg 47	12-Nov-2011 - 06-Jan-2012	-32.4
Ifg 9	29-Sep-2011 - 06-Jan-2012	-69.6	Ifg 48	12-Nov-2011 - 17-Jan-2012	-103.5
Ifg 10	29-Sep-2011 - 17-Jan-2012	-140.8	Ifg 49	12-Nov-2011 - 28-Jan-2012	-128.3
Ifg 11	29-Sep-2011 - 28-Jan-2012	-165.5	Ifg 50	12-Nov-2011 - 08-Feb-2012	23.5
Ifg 12	29-Sep-2011 - 08-Feb-2012	-13.8	Ifg 51	23-Nov-2011 - 04-Dec-2011	66.9
Ifg 13	10-Oct-2011 - 21-Oct-2011	56.8	Ifg 52	23-Nov-2011 - 15-Dec-2011	36.9
Ifg 14	10-Oct-2011 - 01-Nov-2011	142.9	Ifg 53	23-Nov-2011 - 26-Dec-2011	207.2
Ifg 15	10-Oct-2011 - 12-Nov-2011	81	Ifg 54	23-Nov-2011 - 06-Jan-2012	2.3
Ifg 16	10-Oct-2011 - 23-Nov-2011	46.3	Ifg 55	23-Nov-2011 - 17-Jan-2012	-68.9
Ifg 17	10-Oct-2011 - 04-Dec-2011	113.2	Ifg 56	23-Nov-2011 - 28-Jan-2012	-93.6
Ifg 18	10-Oct-2011 - 15-Dec-2011	83.2	Ifg 57	23-Nov-2011 - 08-Feb-2012	58.1
Ifg 19	10-Oct-2011 - 26-Dec-2011	253.5	Ifg 58	04-Dec-2011 - 15-Dec-2011	-30
Ifg 20	10-Oct-2011 - 06-Jan-2012	48.6	Ifg 59	04-Dec-2011 - 26-Dec-2011	140.3
Ifg 21	10-Oct-2011 - 17-Jan-2012	-22.5	Ifg 60	04-Dec-2011 - 06-Jan-2012	-64.6
Ifg 22	10-Oct-2011 - 28-Jan-2012	-47.3	Ifg 61	04-Dec-2011 - 17-Jan-2012	-135.7
Ifg 23	10-Oct-2011 - 08-Feb-2012	104.5	Ifg 62	04-Dec-2011 - 28-Jan-2012	-160.5
Ifg 24	21-Oct-2011 - 01-Nov-2011	86.1	Ifg 63	04-Dec-2011 - 08-Feb-2012	-8.7
Ifg 25	21-Oct-2011 - 12-Nov-2011	24.2	Ifg 64	15-Dec-2011 - 26-Dec-2011	170.3

Table B.3: (Continued)

	Date pair	Perp. baseline [m]		Date pair	Perp. baseline [m]
Fig 26	21-Oct-2011 - 23-Nov-2011	-10.5	Fig 65	15-Dec-2011 - 06-Jan-2012	-34.6
Fig 27	21-Oct-2011 - 04-Dec-2011	56.4	Fig 66	15-Dec-2011 - 17-Jan-2012	-105.8
Fig 28	21-Oct-2011 - 15-Dec-2011	26.4	Fig 67	15-Dec-2011 - 28-Jan-2012	-130.5
Fig 29	21-Oct-2011 - 26-Dec-2011	196.7	Fig 68	15-Dec-2011 - 08-Feb-2012	21.2
Fig 30	21-Oct-2011 - 06-Jan-2012	-8.2	Fig 69	26-Dec-2011 - 06-Jan-2012	-204.9
Fig 31	21-Oct-2011 - 17-Jan-2012	-79.3	Fig 70	26-Dec-2011 - 17-Jan-2012	-276
Fig 32	21-Oct-2011 - 28-Jan-2012	-104.1	Fig 71	26-Dec-2011 - 28-Jan-2012	-300.8
Fig 33	21-Oct-2011 - 08-Feb-2012	47.7	Fig 72	26-Dec-2011 - 08-Feb-2012	-149
Fig 34	01-Nov-2011 - 12-Nov-2011	-61.9	Fig 73	06-Jan-2012 - 17-Jan-2012	-71.1
Fig 35	01-Nov-2011 - 23-Nov-2011	-96.6	Fig 74	06-Jan-2012 - 28-Jan-2012	-95.9
Fig 36	01-Nov-2011 - 04-Dec-2011	-29.7	Fig 75	06-Jan-2012 - 08-Feb-2012	55.9
Fig 37	01-Nov-2011 - 15-Dec-2011	-59.7	Fig 76	17-Jan-2012 - 28-Jan-2012	-24.7
Fig 38	01-Nov-2011 - 26-Dec-2011	110.6	Fig 77	17-Jan-2012 - 08-Feb-2012	127
Fig 39	01-Nov-2011 - 06-Jan-2012	-94.3	Fig 78	28-Jan-2012 - 08-Feb-2012	151.7

Appendix C

Supplemental material Chapter 4

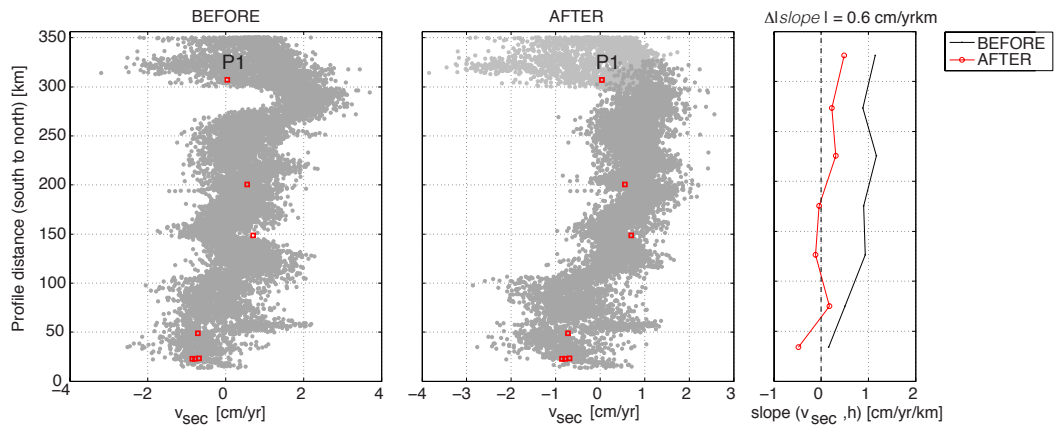


Figure C.1: Comparison between inter-SSE velocities from InSAR (gray points) and GPS (red squares), before (left panel) and after (middle panel) tropospheric correction. The light gray scatters indicate the region around Mexico City where tectonic deformation contaminates the tropospheric correction. The right panel shows the local correlation with topography. On average, applying the power-law method reduces the local correlation by 0.6 cm/yr per km.

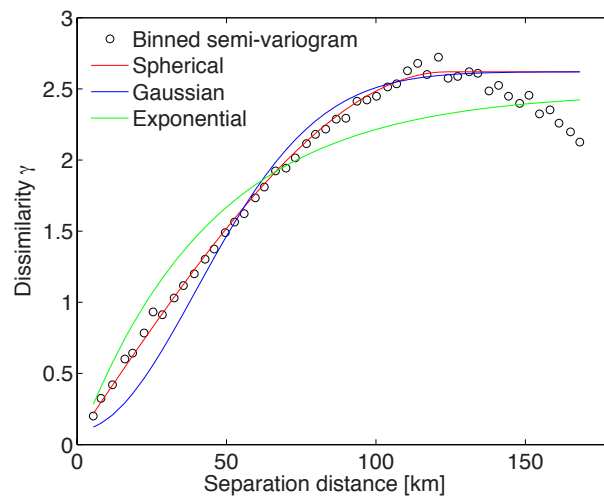


Figure C.2: Experimental variogram estimated from InSAR for the slow slip component after tropospheric correction (circular markers). Lines correspond to different fitted covariance functions, for which the spherical function shows the best fit.

Appendix D

Supplemental material Chapter 5

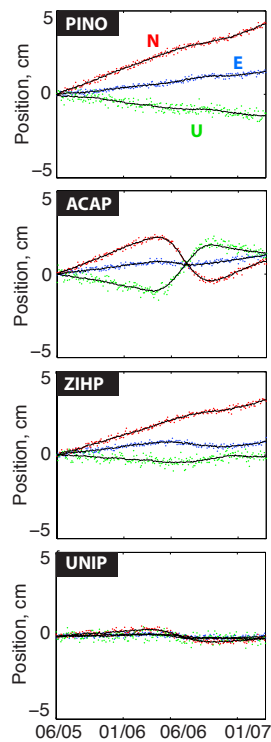


Figure D.1: Comparing simulated GNSS surface displacements (colored points) with those estimated from the NIF (solid black lines) when inverting for only GNSS observations. GNSS station locations are indicated in Figure 5.1.

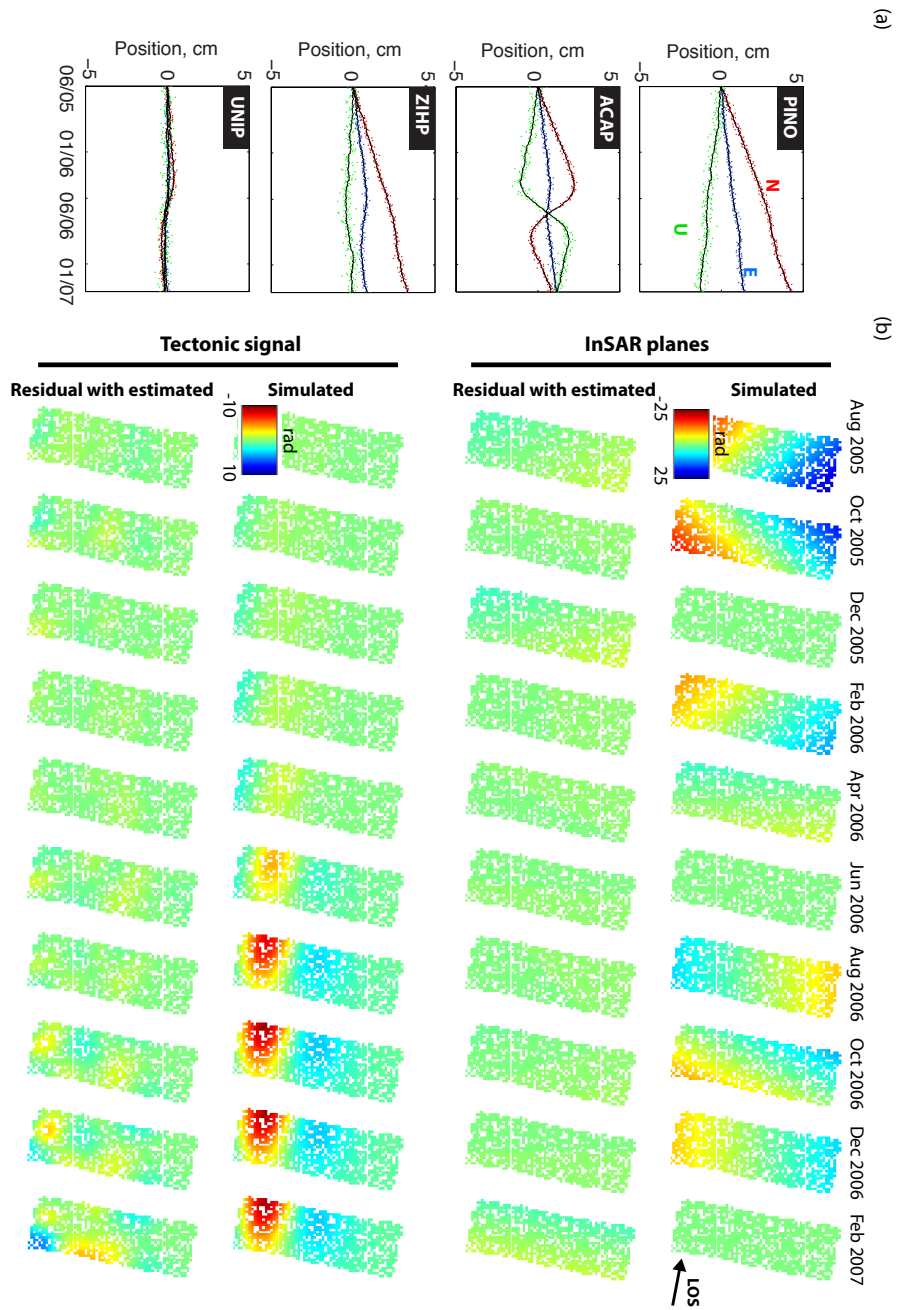


Figure D.2: Surface observations estimated from the NIF after a joint GNSS and InSAR inversion, while neglecting InSAR covariance. (a) Comparing simulated GNSS surface displacements (colored points) with those estimated from the NIF (solid black lines). GNSS station locations are indicated in Figure 5.1. (b) Comparing the estimated tectonic signal and orbital ramps with the original simulation. 2π rad corresponds to 2.8 cm in the radar line of sight (LOS).

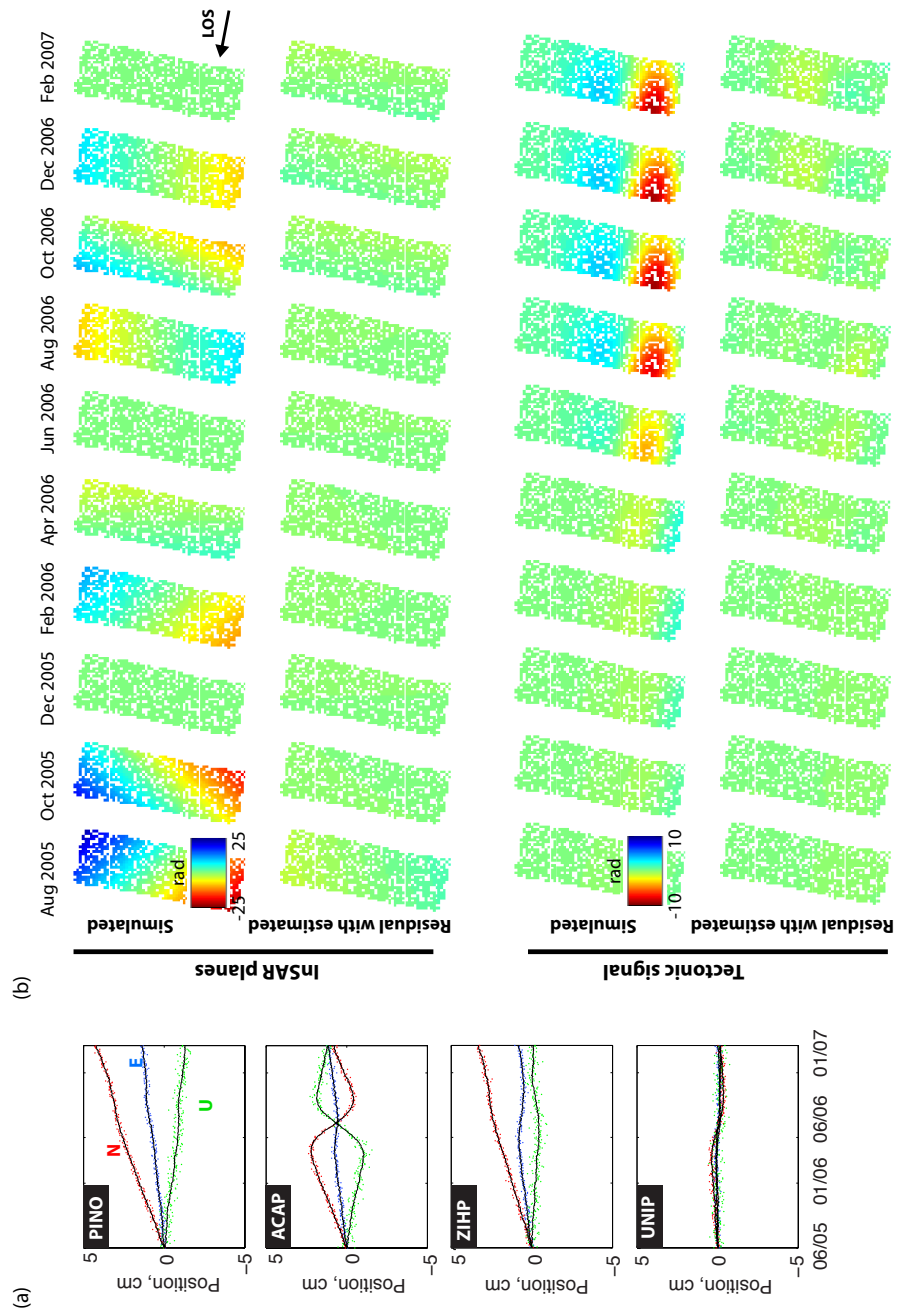


Figure D.3: Same as Figure D.2 but for the joint inversion of GNSS and InSAR, while including InSAR covariance.

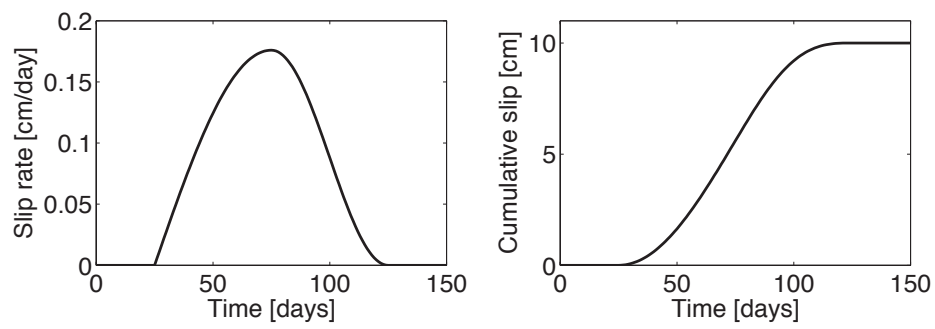


Figure D.4: (a) Slip-rate and (b) slip over time for our simulated SSE. This example shows a SSE started after 25 days, with a duration of 100 days, and an accumulated slip of 10 cm.

Appendix E

Methodology for InSAR feasibility study of slow slip events

Slow slip surface displacements are often masked by tropospheric noise in the interferograms, and therefore require advanced tropospheric corrections in combination with sophisticated time-series InSAR processing method to decrease the InSAR noise levels. The feasibility of InSAR to observe SSE can be investigated by comparing the Signal-to-Noise (SNR) ratio. When the $SNR > 1$, InSAR is likely to be successful. The signal follows by projecting an estimate of the cumulative slow slip surface displacements (e.g. from GNSS) into the radar line-of-sight. The magnitude will thus be depending on the specific satellite acquisition geometry. The noise-level as found after time-series InSAR processing can be computed by propagating the interferogram uncertainties using the inverse problem as will be used in the time-series approach. Let us assume that the inverse problem is defined as:

$$E \{ \underline{\Delta\phi} \} = \mathbf{A}\underline{x}, \quad (\text{E.1})$$

with \mathbf{A} the design matrix of the inverse problem, $\underline{\Delta\phi}$ an observation vector with the interferograms, \underline{x} a vector of unknowns which includes the slow slip signal, and $E\{\cdot\}$ the expectation operator. The covariance matrix of the observations is defined as $\mathbf{Q}_{\Delta\phi}$. By applying the variance propagation law, the estimated covariance matrix of the unknowns $\mathbf{Q}_{\hat{\underline{x}}}$ follows as:

$$\mathbf{Q}_{\hat{\underline{x}}} = \left(\mathbf{A}^T \mathbf{Q}_{\Delta\phi}^{-1} \mathbf{A} \right)^{-1} \quad (\text{E.2})$$

Below, I elaborate on how the design matrix for a Single Master (SM) time-series approach is defined. This is a modification to *Hooper et al.* (e.g. 2004) where a steady-state velocity model is assumed. Surface displacements d_{tect} introduced from a subduction process and the occurrence of a slow slip event, can be modeled as a steady-state ve-

locity in combination with a sigmoid function (e.g [Larson et al., 2004](#), [Franco et al., 2005](#)) as:

$$d_{tect}(t) = d_0 + v_{int}t + d_{SSE} \left[1 + \exp\left(\frac{t - t_{0,SSE}}{\tau_{SSE}}\right) \right]^{-1}, \quad (\text{E.3})$$

with t the time, d_0 the reference tectonic deformation at $t=0$, v_{int} the interseismic velocity, d_{SSE} the cumulative slow slip displacements, $t_{0,SSE}$ the center time of the SSE, and τ_{SSE} the duration of the SSE. For an interferogram with a master acquisition at t_m , and a slave acquisition at t_s , the relative displacement becomes:

$$\Delta d_{tect} = v_{int}\Delta t + d_{SSE}\alpha_{(t_m,t_s)}, \quad (\text{E.4})$$

with $\alpha_{(t_m,t_s)}$ a scaling factor with its magnitude depending on the master and slave acquisition times. Including equation (E.4) for n interferograms, into the SM time-series framework (e.g. [Hooper et al., 2004](#)) leads to:

$$E \{ \underline{\Delta\phi} \} = \mathbf{A}\underline{x} \quad (\text{E.5})$$

$$E \left\{ \begin{bmatrix} \Delta\phi_{t_1} \\ \vdots \\ \Delta\phi_{t_k} \\ \vdots \\ \Delta\phi_{t_n} \end{bmatrix} \right\} = \frac{-4\pi}{\lambda} \begin{bmatrix} \Delta t_1 & \alpha_{(t_m,t_1)} & B_{\perp t_1} & 1 \\ \vdots & \vdots & \vdots & \vdots \\ \Delta t_i & \alpha_{(t_m,t_k)} & B_{\perp t_i} & 1 \\ \vdots & \vdots & \vdots & \vdots \\ \Delta t_n & \alpha_{(t_m,t_n)} & B_{\perp t_n} & 1 \end{bmatrix} \begin{bmatrix} v_{int} \\ d_{SSE} \\ c_{topo} \\ a_m \end{bmatrix},$$

with Δt_i the time difference between the master and the i^{th} slave acquisition, $B_{\perp t_i}$ the corresponding perpendicular baseline, c_{topo} the DEM-correlated errors, and a_m the residual master atmosphere and noise. $-4\pi/\lambda$ is a conversion factor to convert interferometric phase to LOS deformation. The errors after applying time-series processing can now be computed by substituting \mathbf{A} into equation (E.2).

References

- Franco, S., V. Kostoglodov, K. Larson, V. Manea, M. Manea, and J. Santiago (2005), Propagation of the 20012002 silent earthquake and interplate coupling in the Oaxaca subduction zone, Mexico, *Earth, Planets and Space*, *57*(10), 973 – 985, doi:[10.1186/BF03351876](https://doi.org/10.1186/BF03351876). [E](#)
- Hooper, A., H. Zebker, P. Segall, and B. Kampes (2004), A new method for measuring deformation on volcanoes and other natural terrains using InSAR persistent scatterers, *Geophys. Res. Lett.*, *31*(23), doi:[10.1029/2004GL021737](https://doi.org/10.1029/2004GL021737). [E](#), [E](#)
- Larson, K., A. Lowry, V. Kostoglodov, W. Hutton, O. Sánchez, K. Hudnut, and G. Suárez (2004), Crustal deformation measurements in Guerrero, Mexico, *J. Geophys. Res.*, *109*(B4), doi:[10.1029/2003JB002843](https://doi.org/10.1029/2003JB002843). [E](#)

